STUDIES OF
AXI-ASYMMETRIC DIELECTRIC WAVEGUIDES:

A thesis submitted for the degree Doctor of Philosophy

BY   IAIN MURRAY SKINNER

The Australian National University

Canberra

March, 1985

DECLARATION

This thesis is an account of research undertaken in the Department of Applied Mathematics within the Research School of Physical Sciences at The Australian National University between February 1982 and March 1985, while I was enrolled for the degree Doctor of Philosophy.

Drs J.D.Love and C.Pask supervised the work in part I, but unless specifically disowned, the material presented therein is my own. The content of part II is the result of close collaboration with Dr C.Pask.

None of the work reported here has ever been submitted for any other degree at this or any other institution of learning.

Iain Skinner

THIS WORK IS DEDICATED

TO THE GLORY OF GOD

ACKNOWLEDGEMENTS

Over three years ago, when I decided to become a climatic refugee from the Sunshine State and venture southwards to these frozen wastelands, it was in the hope that my health would improve. I thank God that this occurred, and also that, upon arriving in Canberra, I was welcomed by this friendly Department of Applied Mathematics. The zestful leadership and enthusiasm for research of Barry Ninham and Allan Snyder is infectious and contributes significantly to the ethos of this place, and enabled this thesis to reach its consummation.

I cannot express the debt of gratitude I owe Colin Pask. His patience and readiness to explain, again and again, is valued; but it is more for personal friendship and genuine interest in matters other than work, that he earns the respect and thanks of this student. For his belief in my ability and encouragement to persist to the end of the most tedious analysis, John Love deserves thanks. Also, I am grateful for the assistance he provided during the preparation of thesis.

My close friend and fellow pilgram for three years, Frank Rühl, deserves special thanks. As a fellow traveller, his company was always welcome on the lonely trail and his pacing made it easier to continue. I am indebted to Richard Black, who guided me to the computing resources and then permitted me to explore unhindered, to Stephen Garth, whose explanations of physical phenomena were interesting, and Derek Bertilone, who meticulously proof-read the manuscript.

Together with Frank and Stephen, I shared an office with Bryan Beresford-Smith. Thanks, fellas, for the many debates, in which no subject was forbidden - except mathematics! - numerous indoor cricket - a real turning wicket - and football matches, and lunchtime concertos for string and woodwind ensembles.

Thanks are due to Diana Wallace who patiently instructed me in the mystique of word processing and Cathy Miller who miraculously converted my bewildering notes into a presentable manuscript.

To the remaining members of the Department of Applied Mathematics, especially those of the optics group, thank you for many enlightening and enlivening discussions about ... . Unfortunately the late Departmental Cat did not live to see the final form of those numbers she

forced from the reluctantly co-operative siliconized simpleton during long, cold vigils at the terminal.

I wish to thank my family and friends in Queensland for their encouragement to persist and my Canberran friends, in particular Peter and Linda Rossiter, whose generous hospitality significantly aided the endurance of separation from my beloved Queensland.

Thanks are extended to Dr R.A.Sammut for providing the results mentioned in §4.3.3.

Finally, for financial support I thank the Australian Federal Government (1982-83), the Autralian National University (1982-83), and the Australian Radio Research Board (1983-85).

PREFACE

Dear Reader,

Having woken this volume from its slumber, idly lifted it from its bed among its colleagues, blown the accumulated dust from its cover, and curiously opened the same, you will be relieved to learn that the arrangement of the contents is subject to systematic conventions.

Equations are numbered consecutively in each chapter, where they are referenced by number, e.g. (123). Elsewhere, they are called by chapter and number, e.g. (12.345). Figures and tables are numbered consecutively in each chapter, and are always given by their full names, e.g. figure 12.345. References are consolidated in one list, located at the end of this thesis. Authors are cited by name and year, with the exception of Abramowitz & Stegun (1965) which is abbreviated to A&S.

While I have endeavoured to define all symbols, there may be isolated occasions of confusion and ambiguity. Since my notation is consistent with standard mathematical usage, functions are as specified in A&S, and waveguide parameters are as defined in Snyder & Love (1983) – with the exception of Δ, which is discussed in §P.2.1 – such cases should not present insurmountable difficulties.

ABSTRACT

The major concern of this thesis is the effects which asymmetry about the axis of propagation have on the performance of dielectric waveguides. In particular, weakly guiding waveguides are investigated.

A brief Prologue outlines the assumptions and formalism of the weak guidance approximation, and introduces some of the phenomena seen on waveguides. Chapter 1 surveys the general methods employed to solve - exactly or approximately - for properties of axi-asymmetric waveguides. Examples of solutions are included: the clad-parabolic elliptical fibre and the infinite linear waveguide.

A general method, to solve exactly for properties of a step fibre with a cross-section of arbitrary shape, is developed in chapter 2. This method is used in chapters 3 and 4 to decsribe the step elliptical and step retangular waveguides. As well as these exact values, quantities are estimated using standard and new approximation techniques. Thus the accuracy of certain methods is established.

Since the exact analysis of single-moded single-polarization fibres is difficult, these structures are modelled in chapter 5 by the butterfly profile for which parameters are easily obtained. It is shown how the observed behaviour of bow-tie fibres is described by this model.

In chapter 6 the effect of a waveguide's core on the radiation loss caused by a bend is established. This enables the description, using some model profiles, of the way the loss from an axi-asymmetric waveguide will vary with the relative orientations of the plane of the bend and core's axes of symmetry.

Chapter 7 presents an alternative formalism for the weak guidance approximation. This is in terms of Fourier optics, and thus an integral equation rather than a differential equation is obtained. Using this new method, an attempt is made to relate the structure of the fibre's far field pattern to the details of the refractive index.

Finally, chapter 8 discusses a mathematical curiosity suggested by the analysis of chapter 7. How are zeroes of the eigenfunctions of an integral operator related to the structure of the operator's kernel?

PUBLICATIONS

Papers (in preparation) :

J.D.LOVE, C.PASK & I.M.SKINNER, *Approximation Methods for Noncircular Optical Fibres*

I.M.SKINNER, *Asymptotic Approximation Techniques and Elliptical Waveguides*

I.M.SKINNER & J.D.LOVE, *Butterfly Model of Single Polarization Fibres*

C.PASK & I.M.SKINNER, *Fourier Fibre Optics*

I.M.SKINNER & J.D.LOVE, *Clad-Parabolic Elliptical Fibres*

J.D.LOVE & I.M.SKINNER, *Bend Loss from a Finite Waveguide*

Conference Presentations:

J.D.LOVE, C.PASK, I.M.SKINNER & R.J.BLACK, *Noncircular Fibres and Waveguides*, 8th Australian Workshop on Optical Communication, Adelaide, 1983

I.M.SKINNER, *Eigenfunctions of Integral Operators*, 20th Australian Applied Mathematics Conference, Merimbula, 1984

I.M.SKINNER, *Bow-Ties and Butterflies*, 21st Australian Applied Mathematics Conference, Launceston, 1985

CONTENTS

PROLOGUE

"Yes, Eeyore. He's clever, Rabbit is," said
Piglet.
"Clever!" said Eeyore scornfully, putting a foot
heavily on his three sticks. "Education!" said
Eeyore bitterly, jumping on his six sticks.
"What **is** Learning?" asked Eeyore as he kicked
his twelve sticks into the air. "A thing **Rabbit**
knows! Ha!"

A.A.Milne, "The House at Pooh Corner"

This chapter introduces the concepts which are exploited and developed
in the remainder of this thesis. Firstly, the formalism and basic
equation of the weak guidance approximation are outlined, and then the
way corrections can be incorporated to better describe phenomena in an
axi-asymmetric fibre. These are the basic materials for part I. A
brief discussion of the physically observable quantities, which motivate
the alternate formalism for the weak guidance approximation presented in
part II, concludes this chapter.

§P.1   Electromagnetic waves in dielectric waveguides

Comprising both optical fibres and planar integrated optical
components, dielectric waveguides are assuming fundamental importance in
modern information gathering and transfer.

The description of an electromagnetic waveguide is not new, dating
from the work of Thomson (1893) and Rayleigh (1897) who investigated
metallic guides. In 1910 Hondros & Debye described the propagation of
an electromagnetic wave along a cylindrical, dielectric waveguide, but
it was not until after the Second World War that intensive interest
returned to these devices.

A proliferation of results and suggestions climaxed with the
realization (Kao & Hockman, 1966) that newly developed, highly pure

silica could transmit light signals over significant distances. This telecommunication application provided the motivation for extensive studies of dielectric waveguides.

Figure P.1 is a schematic representation of the main features of such a device. There is an inner region — the core — and an outer region — the cladding — finite in extent and generally with a refractive index lower than the core's. Throughout this thesis, it is assumed that the waveguides are translationally invariant, i.e. that the refractive index structure is independant of z, the axial co-ordinate. Also, it is assumed that the propagating wave travels along this z-axis.

Most of the results obtained in this subject are restricted to axisymmetric waveguides. Frequently even these are approximations. The reason is the mathematical complexity and intractability of the set of equations modelling the system. In this thesis, non-axisymmetric waveguides are examined.

An electromagnetic wave's behaviour is described by the Maxwell equations (e.g. Landau & Lifshitz, 1971, ch.4):

$$(\nabla \wedge E) = - \mu \frac{\partial H}{\partial t} \, ,$$

$$\nabla . (\mu H) = 0 \, ,$$

$$\nabla \wedge H = \varepsilon \frac{\partial E}{\partial t} + 4 \pi J \, ,$$

and

$$\nabla . (\varepsilon E) = 4 \pi \rho \, ,$$

where μ and ε, the magnetic permeability and electric permittivity, respectively, are assumed time-independent but not spatially invariant, E and H are the electric and magnetic field vectors, respectively, J is the current density vector, ρ is the volumetric charge density, and the

Figure   P.1

(a)   A schematic representation of an axially invariant, dielectric waveguide.
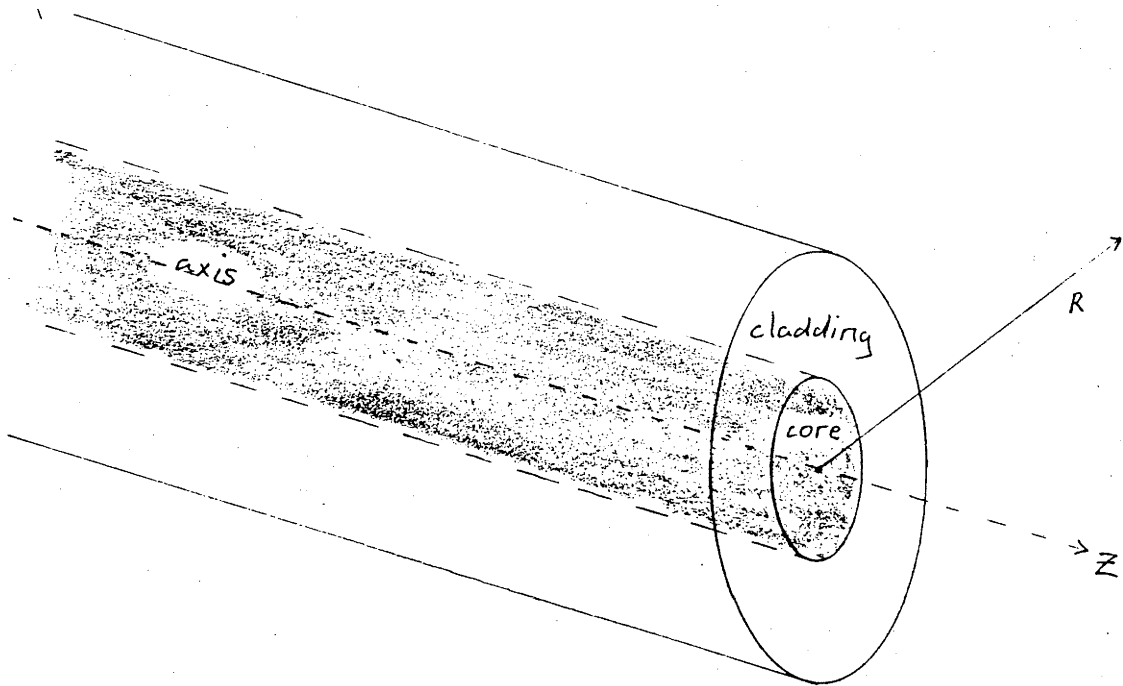
(b) Motivation of the weak guidance approximation. The heavy line indicates most of the energy is near the core. Hence the cladding is assumed infinite, leaving a small total variation in the refractive index, n.
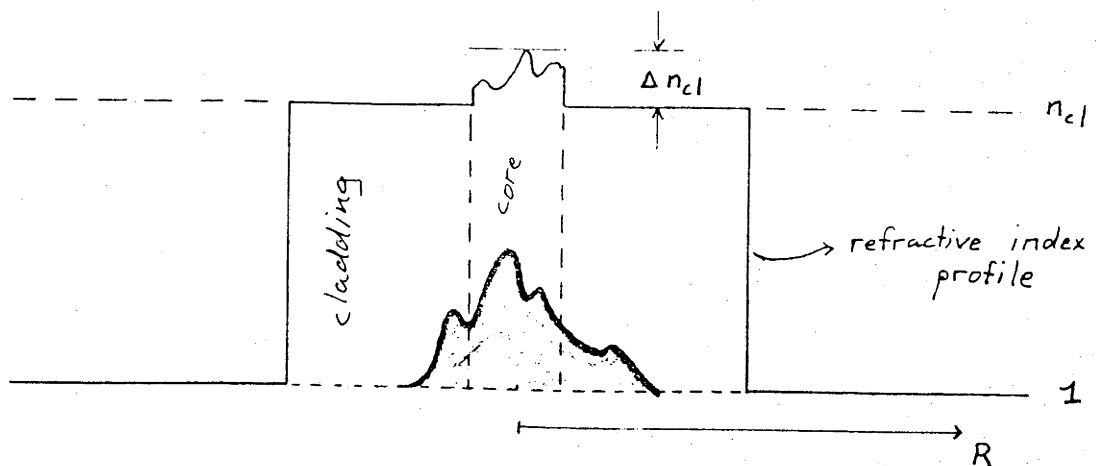
gradient operator involves the three Cartesian position co-ordinates. The solution of these partial differential equations, together with the appropriate boundary and continuity conditions, is difficult. Fortunately a telecommunication fibre has only a small variation in its refractive index, $n = \sqrt{\varepsilon/\varepsilon_0}$. This motivated the development of an approximate theory, that of weak guidance (Snyder, 1969; Gloge, 1971).

§P.2 Weak guidance formalism

§P.2.1 Basic Assumptions

Most of the energy confined to and travelling along the waveguide is concentrated near the core. Typically the core's radius is less than a fifth of the width of the cladding. Thus, to a first approximation, little difference will appear between the guidance properties of the physical waveguide and the model produced by extending the cladding to an infinite distance from the axis. These two forms are indicated by the solid and broken curves, respectively, of figure 6.1(b).

This unphysical, infinite refractive index profile across the infinite cross-section of the waveguide is described by the function $n(x,y)$. It is useful to write this so that the variation from $n_{c\ell}$, the refractive index of the infinite cladding, is apparent. Also, because $\varepsilon = n^2 \varepsilon_0$ is the physical quantity, it is more appropriate to describe n^2. Thus,

$$n^2(x,y) = n_{c\ell}^2 + \left[n^2(x,y) - n_{c\ell}^2 \right]$$

where the variation appears in the square brackets. By defining

$$2\Delta = \frac{n_0^2 - n_{c\ell}^2}{n_{c\ell}^2},$$

where n_0 is the maximum value of n over the infinite cross-section, this variation can be normalized;

$$n^2(x,y) - n_{c\ell}^2 = 2\Delta\, n_{c\ell}^2\, g(x,y), \tag{1}$$

with the maximum value of g being 1. g(x,y) is termed the profile's shape-function. This choice of $n_{c\ell}$, to normalize the variation in n, differs from the usual choice n_0 (e.g. Snyder & Love, 1983). However, within the weak guidance assumption $n_{c\ell} \approx n_0$, so no effective difference occurs. The base index of the infinite cladding is the more natural choice. In practical waveguides dopants are added to create a variation from the refractive index of a uniform substrate.

The maximum relative variation of n^2 from $n_{c\ell}^2$ is given by 2Δ. This definition gives Δ as the relative difference between $n_{c\ell}$ and n_0, when $\Delta \ll 1$. Typically Δ is between 10^{-3} and 10^{-2}. Because of this small size, it is possible to obtain a series solution in $\Delta^{1/2}$ of the Maxwell equations (e.g. Snyder & Love, 1983, ch.32).

This thesis is concerned only with weakly guiding, dielectric waveguides, i.e. those for which the assumptions outlined above are an excellent approximation.

§P.2.2 Scalar wave equation

The key feature of the weak guidance theory is that the electric field within a non-axisymmetric waveguide can be approximated as

$$\mathbf{E} \approx A\psi e^{i(\beta z - \omega t)}\, \hat{\mathbf{p}} + O(\Delta^{1/2}), \tag{2}$$

where A is a physical amplitude constant, ψ is a function describing the variation of E across the infinite cross-section and termed the modal field, β is the propagation constant of the mode, ω the angular

frequency of the electromagnetic wave, and **p** the direction of the electric field, ie. the state of polarization of the wave. There are two natural, orthogonal directions for **p**. These are the optical axes. In this thesis these are always taken to be co-incident with the Cartesian axes. Of course **H** can be constructed from **E**, and shows a similar form. As discussed in §P.2.4, Snyder & Young (1978) showed that (2) is not a perfect description. In this thesis, ψ is assumed to be real, corresponding to non-absorbing dielectrics.

Rather than the derivation of the solution of the Maxwell equations for the vector fields **E** and **H**, the problem is reduced to the search for a scalar field ψ and its associated propagation constant, β. These follow from the well-known scalar wave equation:

$$\left(\nabla^2 + k^2 n^2(x,y) - \beta^2\right) \psi = 0,$$

where ∇^2 is the two-dimensional Laplacean operator defined by the co-ordinates of the cross-section, and $k=2\pi/\lambda$ is the wavenumber in a vacuum. Substitution of (1) gives

$$\left(\nabla^2 + V^2 g(x,y) - W^2\right) \psi = 0, \tag{3}$$

where V, defined by

$$V^2 = \rho^2 k^2 n_{cl}^2 \, 2\Delta, \tag{4}$$

is the normalized frequency. Modal parameters W and U, defined by

$$W^2 = \rho^2 \left(\beta^2 - k^2 n_{cl}^2\right) \tag{5a}$$

and

$$U^2 = V^2 - W^2 = \rho^2 \left(k^2 n_0^2 - \beta^2\right), \tag{5b}$$

are the normalized propagation constants. A length scale, ρ, is introduced to normalize quantities, including the derivatives in ∇^2.

Equation (3) can be re-arranged as

$$\left(\nabla^2 + gV^2\right) \psi = W^2\psi ,$$

which is the standard form of the two-dimensional eigenvalue problem for a differential operator. A given pair V and g uniquely specifies an operator, corresponding to a specific profile and operating frequency. This operator has discrete eigenfunctions, the modes ψ, and associated eigenvalues, W^2, which is a normalized form of β^2.

§P.2.3 Dimensionless parameters

The lengths are normalized with ρ, a characteristic length of the waveguide's core. On an axisymmetric structure, the natural dimension is the core's radius. However, for a non-axisymmetric arrangement, an ambiguity occurs. For example, with an elliptical core, should one select the semiminor axis, the semimajor axis, or the geometric mean of the two? This inherent abmiguity has caused some confusion within the literature, and is explained in more detail in chapters 3 and 4.

Hussey & Pask (1982) showed the utility of the profile volume in comparing waveguides with different shape-functions. With this motivation, the canonical length $\bar{\rho}$, is defined:

$$\bar{\rho}^2 \equiv \frac{1}{\pi} \int_{R^2} g(x,y) \ dx \ dy. \tag{6}$$

For a circular step-profile, this returns the value of the radius; for an elliptical step, it is the geometric mean of the semimajor and semiminor axes; for a clad parabolic profile divide these expressions by $\sqrt{3}/2$.

Employing the canonical length in (4) and (5), the value of V is defined to be the **canonical frequency**, and U and W are the **canonical propagation constants.**

§P.2.4 Scalar modes and modal nomenclature

The form of E given by (2) is linearly polarized (LP), and the associated solutions of (3) are termed the LP-modes. It is often thought that these correspond to the true modes of a waveguide. Snyder & Young (1978) showed this not to be the case.

The fundamental mode (HE_{11}) is virtually an LP-mode, LP_{01}. It is also interesting that Sturm-Louiville theory (e.g. Ince, 1926a, ch.10) shows that for this mode, which has the lowest value of U (highest value of W), ψ has the same sign throughout the infinite cross-section.

On axisymmetric waveguides, higher-order modes are not LP-modes. Here, solutions of (3) are of the form

$$\psi_\ell^\pm = F_\ell(R) \begin{Bmatrix} \cos \\ \sin \end{Bmatrix} (\ell\theta).$$

The choice of the trigonometric function does not influence the value of U and W. Snyder & Young showed that, in this case, the true modes are radially and azimuthally polarized, rather than polarized along the optical axes. These true states of polarization are obtained by adding different, degenerate LP-modes. For example,

$$E \approx A \left(a_1 F_\ell \cos \ell\theta \, \hat{x} + a_2 F_\ell \sin \ell\theta \, \hat{y} \right)$$

where a_1 and a_2 are real constants.

On a non-axisymmetric profile, the degeneracy of the propagation constants for the two different trigonometric functions is broken. While the true modes are still the sum of two different LP-modes, even
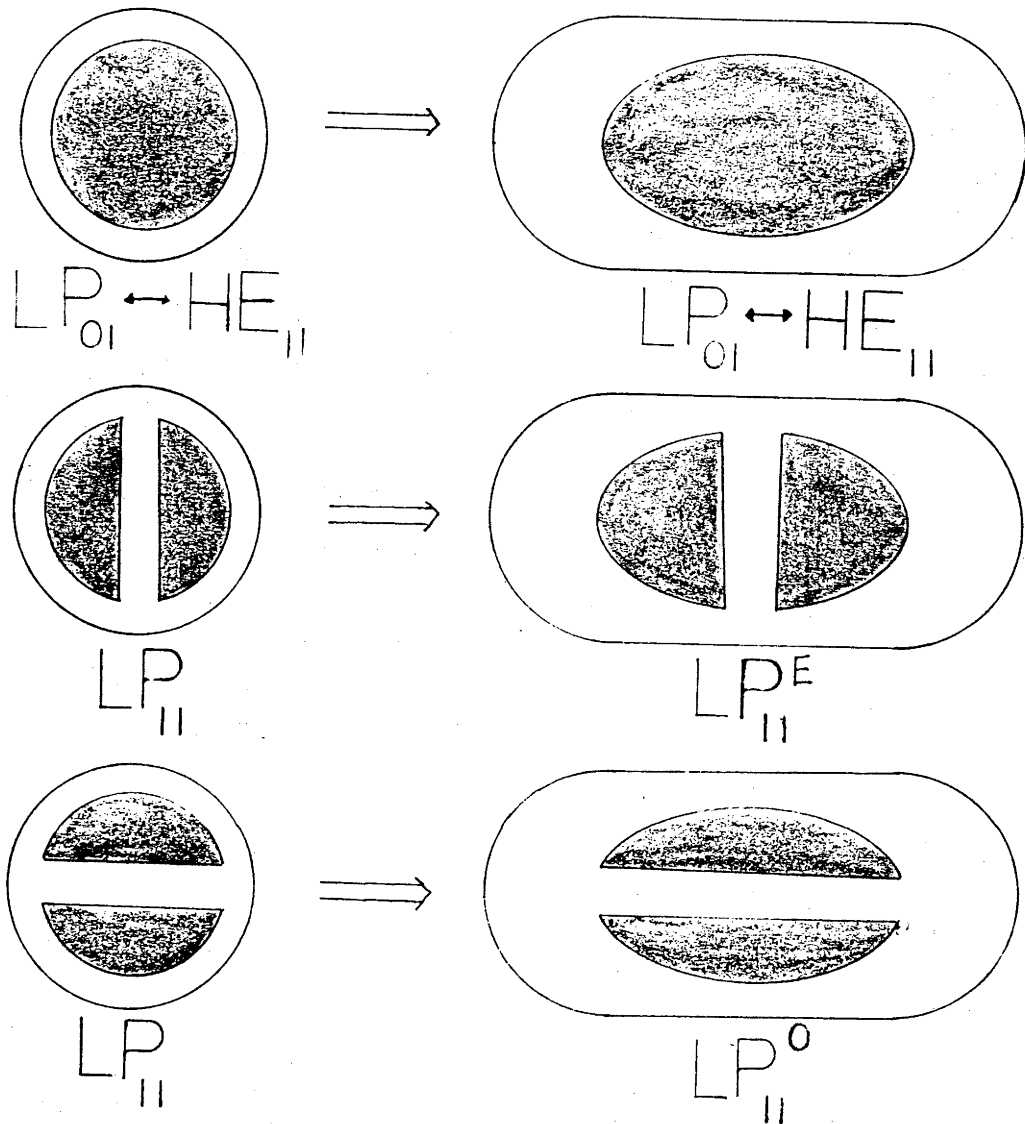
Figure P.2

A schematic representation of the variation of standard LP-modes as a
waveguide's cross-section varies from circular. Notice how the
degeneracy of the LP_{11}-mode is broken

for slight non-axisymmetry, one particular LP-mode will dominate. Thus, on a non-axisymmetric guide, the higher-order modes are also essentially LP-modes. In this thesis, all analysis of the non-axisymetric wavegides will be in terms of LP-modes. (For an explanation of the numbering of LP-modes, see Gloge, 1971.)

On the axisymmetric waveguide the two trigonometric functions give two distinct symmetry patterns for the modal field of the LP_{11}-mode (refer figure P.2). On the non-axisymmetric waveguide, this degeneracy is destroyed and modal nomenclature becomes more complicated. The usual notation (eg. Marcatili, 1969a; Goell, 1969; Eyges et al, 1979) divides the modal fields into symmetry groups and number from 1 with increasing value of U, i.e. increasing order of the mode. In this thesis, the LP_{11} notation is retained, and the superscripts E and O are employed to indicate symmetry or anti-symmetry about the X-axis.

For the refractive index profiles studied in this thesis, the fundamental mode and only the first two higher-order modes, the LP_{11}^{0}- and LP_{11}^{E}-mode are examined in any detail; i.e. interest is primarily in single-moded waveguides.

§P.2.5 Modal cut-off

As mentioned at the end of §P.2.2, the solution of (3) produces eigenvalues W^2. It is only positive values of W^2, producing real values of W, that correspond to bound modes on the waveguide. That there is this transition, called cut-off, has a semi-intuitive explanation. Consideration of (5a) shows that negative W^2 means

$$\beta < kn_{c\ell}$$

$$\Rightarrow \frac{\omega}{\beta} > c/n_{c\ell} \, ,$$

which is equivalent to claiming the wave's phase velocity exceeds the speed of light in the medium forming the cladding.

From (3) it is apparent that, for a given function g and a nominated ψ, a variation in V causes a change in W. As V decreases, so does W. It may be that W=0 for some special value V_{co} which is termed the normalized cut-off frequency of the mode. On practical fibre's, all higher-order modes have non-zero cut-off frequencies; the fundamental mode **may** have a non-zero cut-off frequency. For some unphysical refractive index profiles no mode is cut-off.

The value V_{co} of a particular mode depends only on the shape function g. For single-moded operation of a fibre, the constant V, defined in (4) needs to be in the region where the fundamental mode exists as a bound state, but higher-order modes do not. The first higher modal cut-off is thus an important parameter of a fibre, and in thesis it is evaluated for several non-axisymmetric profiles. In particular it is shown how the degeneracy of the first higher scalar modal cut-off frequency, that of the LP_{11}-mode, is destroyed when the degeneracy of the LP_{11}^{E}- and LP_{11}^{O}-modes is destroyed.

Finally it is worth noting that as $V \rightarrow V_{co}$, the mode's energy spreads further and further into the cladding, thus invalidating the basic assumption described in §P.2.1. However, this occurs only very, very close to V_{co}, and the infinite cladding assumption is still useful in fixing the limiting behaviour of the mode.

§P.2.6 Radiation and bent waveguides

Bends in waveguides arise for various reasons. In itegrated optics, the bends are a designed feature of the device. On the other hand, frequently the inherent microbending of optical fibres detracts from their performance.

When a dielectric waveguide is bent, energy radiates from the bound modes. It is important to assess this loss. In chapter 6 it is examined, with particular interest in how the asymmetry of the cross-section influences the loss from bends which are sufficiently gradual that the waveguide locally is axially invariant.

§P.3   Axi-asymmetry and polarization

Why study non-axisymmetric waveguides? There is the prosaic reason that a perfectly axisymetric waveguide can never be constructed. However, rather than restrict attention to slight imperfections on an ideal structure, this thesis is concerned with significant departures from axisymmetry.

As explained in §P.2.4 and §P.2.5, on a circularly symmetric waveguide, there is a degeneracy between the LP^E_{11}- and LP^O_{11}-modes. A Non-axisymmetric profile produces distinct behaviour for these, and other degenerate pairs of modes. But a non-axisymmetric waveguide also separates a more important degeneracy, that of the two states of polarization which correspond to the same scalar mode.

§P.3.1 Geometric birefringence

One of the features which exists on a non-circular waveguide is birefringence. The nature of this is now explained. Within any dielectric waveguide, there are always two distinct states of polarization, as mentioned below (2). These two directions cause the appearance of two distinct modes which are identical within the scalar analysis. The correction term in (2) depends on the direction of $\hat{p}$. It is emphasized that polarization is a phenomena which can only be described using vector analysis.

Furthermore, the distinct polarization states, corresponding to the same scalar modes, do not have the same propagation constants. The propagation constant yielded by (3) is not the true propagation constant of the mode. To correct for the latter, it is necessary to add a vector-dependent correction term of order Δ to the scalar value. The value of this correction term is dependent on the polarization of the mode. This difference in the propagation constants is entirely due to the shape of the waveguide, and is not present on axisymmetric fibres. The corrected propagation constants of the X- and Y-polarized modes are β_x and β_y, respectively.

As a wave travels along the waveguide, it is scattered by the microscopic imperfections which inevitably occur in any real structure. This means that some energy in one mode is transferred to another mode. The probability of this transition increases as the difference between propagation constants of the two modes decreases. Thus, an investigation of the difference between the corrected propagation constants of the two polarization states of the same scalar mode reveals the likelihood of a given state of input poarization being preserved during transmission. The difference between β_x and β_y is very much less than the difference between the values of β for different scalar, and hence unrelated vector, modes.

The difference $\beta_x - \beta_y$ is known as the modal birefringence. For the axisymmetric waveguide, it is caused by the shape of the cross-section of the fibre, and is termed geometric birefringence to distinguish it from anisotropic birefringence, discussed in §P.4.

Consideration of the argument of the phase factor in (2), shows that the difference between β_x and β_y is

$$\beta_x - \beta_y = 2\pi/L,$$

where L, the beat-length, has a simple physical interpretation. It is the length after which the two modes are again in phase.

§P.3.2 Dimensionless parameters

To facilitate analysis, the birefringence $\beta_x - \beta_y$ is normalized so that a dimensionless parameter of order 1 is obtained. For this thesis, the parameter is chosen to be

$$B_p = \frac{\beta_x - \beta_y}{\Delta^2 k n_{c\ell}}. \tag{7}$$

Unfortunately within the literature there are several different measures of birefringence. The simplest (e.g. Rashleigh, 1982) is merely

$$B = \beta_x - \beta_y = B_p \Delta^2 k n_{c\ell}.$$

This remains very small, indicated by the presence of the square of Δ, and also retains the inverse-length measurement. To remove this, some authors (e.g. Varnham et al, 1983 a) divide by k, giving

$$B = \frac{\beta_x - \beta_y}{k} = B_p \Delta^2 n_{c\ell}.$$

However, the presence of Δ^2 shows that this, too, is an exceedingly small number. The $n_{c\ell}\Delta^2$ factor has its use in the conventional analysis of anisotropic birefringence, as will be shown in §P.4. Wishing to recover numbers of order one, other authors (e.g. Dyott et al, 1979) employ

$$B = \frac{\beta_x - \beta_y}{\Delta^2 n_{co}^2 k} \approx \frac{B_p}{n_{c\ell}}.$$

§P.3.3 Calculation of birefringence

The corrections to the scalar propagation constants were obtained by Snyder & Young (1978) in terms of the scalar modal field, ψ, and the scalar propagation constant, β. Their expression becomes (see Snyder & Love, 1983, p.286), with p being x or y,

$$\beta_p = \beta - \frac{\Delta^{3/2} \sqrt{2}}{\rho \bar{V} \|e_t\|^2} \int_{\mathcal{S}_\infty} dS \ (\mathbf{\nabla} \cdot e_t)(e_t \cdot \mathbf{\nabla} g) \tag{8}$$

where $\mathbf{\nabla}$ is a non-dimensionalized, gradient operator defined with respect to the cross-section's co-ordinates,

$$\|e_t\|^2 = \int_{\mathcal{S}_\infty} |e_t|^2 \ dS \tag{9a}$$

$\mathcal{S}_\infty$ indicates the integrals are over the infinite cross-section, and e_t is the component of $\mathbf{E}$ in the plane of the cross-section. As well as (9), another standard notational device used in this thesis is for two functions f_1 and f_2 and is defined on the infinite cross-section

$$\langle f_1, f_2 \rangle = \int_{\mathcal{S}_\infty} dS \ f_1 f_2 \tag{9b}$$

As explained in §P.2.4, for non-axisymmetric profiles,

$$e_t \approx A \psi \hat{p},$$

so that (8) becomes

$$\beta_p = \beta - \frac{\sqrt{2} \ \Delta^{3/2}}{\rho \bar{V} \|\psi\|^2} \int_{\mathcal{S}_\infty} dS \ \frac{\partial \psi}{\partial p} \psi \frac{\partial g}{\partial p} \ .$$

When this is used in (7), the normalized birefringence is

$$B_p = \frac{1}{\bar{V}^2 \|\psi\|^2} \int_{\mathcal{S}_\infty} dS \ (g_Y \psi_Y^2 - g_X \psi_X^2), \tag{10a}$$

where co-ordinate subscripts denote the partial derivative with respect to that co-ordinate. In (10a) differentiation is with respect to the Cartesian co-ordinates. In many applications, for example the butterfly profile of chapter 5, polar co-ordinates are used to define g and ψ. Standard formulae for changing co-ordinates produce

$$B_p = \frac{1}{\bar{V}^2 \|\psi\|^2} \oint_\infty dS \left[\frac{\cos 2\theta}{R^2} (g_\theta \psi_\theta^2 - R^2 g_R \psi_R^2) + \frac{\sin 2\theta}{R^2} (g_R \psi_\theta^2 + g_\theta \psi_R^2) \right]. \quad (10b)$$

In the special case when the waveguide has a step-profile, i.e.

$$g = \begin{cases} 1 \text{ , inside core} \\ 0 \text{ , outside core,} \end{cases}$$

then (8) simplifies greatly (Snyder & Love, p.287) to become

$$\beta_p = \beta + \frac{\sqrt{2} \ \Delta^{3/2}}{\rho \ \bar{V}^2 \ \|e_t\|^2} \oint_C (\nabla \cdot e_t) \ e_t \cdot \hat{n} \ d\ell,$$

where C is the core-cladding interface and $d\ell$ is the elemental arclength on this curve to which $\hat{n}$ is the outwardly directed unit, normal vector. Proceeding as before, this can be used in definition (7) to yield

$$B_p = \frac{1}{\bar{V}^2 \|\psi\|^2} \oint_C d\ell \ (\psi_X n_X^2 - \psi_Y n_Y^2), \quad (11)$$

where n_X and n_Y are the obvious Cartesian components of $\hat{n}$.

§P.3.4 Vector corrections to scalar cut-off frequencies

Snyder & Young (1978) derived vector corrections to the scalar quantities obtained from the weak guidance approximation. Similarly, vector corrections to the scalar cut-off frequencies can be obtained. This is important because the two polarization states, corresponding to the same scalar mode, have different cut-off frequencies.

On a weakly guiding fibre with shape-function g and profile height parameter Δ, a scalar modal field ψ and a normalized cut-off frequency V_{co} gives a normalized cut-off frequency for the p-polarized mode of

$$V_{co}^{(p)} = V_{co} - \frac{\Delta}{2V_{co}} \frac{\int_{S_\infty} dS \frac{\partial g}{\partial p} \frac{\partial \psi}{\partial p}^2}{\int_{S_\infty} dS \, g \, \psi^2} .$$ (12)

A similar argument, to that used to obtain this correction, is outlined in §1.A.

§P.4 Anisotropic birefringence

As well as the shape of the waveguide, anisotropy of the dielectric material itself can cause birefringence. If the material is anisotropic, the distinct, orthogonal otical axes will be defined by a combination of material and geometric properties. Again β_X and β_Y will differ, because the two different polarization states will be guided by effectively different refractive index profiles, $n^{(X)}(x,y)$ and $n^{(Y)}(x,y)$ (e.g. Snyder & Rühl, 1983).

The total birefringence consists of geometric and anisotropic components:

$$B_p = B_a + B_g .$$

Kaminow & Ramaswamy (1979) showed that, in general, $B_a \gg B_g$.

Usually it is assumed that

$$n^{(X)} - n^{(Y)} = \delta n_{c\ell},$$

which is constant throughout the cladding. If this is so, Black (1984)

showed that the approximation

$$\beta_x - \beta_y = k \, \delta n_{c\ell}$$
$$\Rightarrow B_a = \delta/\Delta^2$$

is very good. This V-independent value of B_a is 30 for the typical

values $\Delta = 1/3\%$ and $\delta/\Delta = 1/10$. However, on a real

waveguide, $n^{(X)} - n^{(Y)}$ will vary over the cross-section, vanishing at

the boundaries. Under these conditions, B_a decreases as $V \to 0$.

As $V \to 0$, ψ spreads more into the cladding where the anisotropy

decreases. It is useful to define a correction factor

$$H_B = \frac{\beta_x - \beta_y}{k \left(\delta n_{c\ell} \right)} \, , \tag{13}$$

which quantifies this change. Here $\delta n_{c\ell}$ is taken to be the maximum

difference between $n^{(X)}$ and $n^{(Y)}$.

§P.5 Axi-asymmetry and approximation techniques

Although the analysis of non-axisymmetric waveguides has received

much attention, it is beset by a major problem. As explained in §P.1,

one reason why so much attention has been directed at axisymmetric

waveguides is that the solution of a non-axisymmetric structure is not

easy. Chapter 1 lists a few profiles for which simple solutions are

available. This general intractability has motivated the development of

several approximation techniques. These are reviewed in chapter 1.

However, like an experimental result, an approximation method is

only useful if one has an estimate of the error involved. Thus, it is

necessary to assess the accuracy of the standard approximation methods

when applied to several reference profiles, for which exact results are

available. In particular, in chapters 3 and 4, extensive examination of the accuracy of the standard approximation methods for rectangular and elliptical step-profiles occurs, and, having evaluated the exact solution of the butterfly profile in chapter 5, this is compared with a solution obtained by perturbing an axisymmetric profile.

Also, the form of exact results can suggest a new approximation of greater accuracy than existing methods. This idea is developed in chapter 3.

Perhaps the most powerful approximation method for an axi-axymmetric waveguide is to consider an appropriate measure of the axi-symmetry as the guide varies from one solvable form to another. In particular, several classes of waveguides, e.g. elliptical, vary continuously from a circular to an infinite planar waveguide. Both of these forms are very simple to analyze. In chapter 3 it is shown how the known limiting forms of a family of non-axisymmetric waveguides can be exploited to give excellent approximation formulae for most quantities of interest.

§P.6   Fourier fibre optics

In §P.2 the standard formalism of the theory of weak guidance was presented. This reduced to solving the scalar wave equation – a differential equation – for the modal field ψ which describes the energy distribution over the cross-section. Is there an alternative way of formulating weak guidance? This question is answered in detail in chapter 7.

Experimentalists are interested always in the quantities which are easiest to measure. Thus, the theoretical analysis incorporating these is more useful to them. Unfortunately, ψ, which is termed the near-

field pattern, is not the easiest quantity to measure. This distinction belongs to Ψ, the far-field pattern, which is the field seen when the light is projected from the end of the waveguide onto a distant screen.

It is clear (e.g. Born & Wolf, 1970) that Ψ is the Fourier transform of ψ. The Fourier transformation of a differential equation produces an integral equation. Thus, (3) can be converted to a scalar wave integral equation which, when solved, gives Ψ. This is an alternate formal structure for the weak guidance approximation.

Whether this new formalism facilitates the analysis of non-axisymmetric waveguides is difficult to answer. Certainly the problem again is simpler if g is an axisymmetric distribution. However, the new formulation is certain to be fruitful, if only because it utilizes the more easily observed quantity Ψ.

CHAPTER ONE

Solutions for Axi-Asymmetric Waveguides

Pooh thought for a long time and then added
sadly, "It isn't as easy as I thought. I
suppose that's why Heffalumps hardly **ever** get
caught."
"That must be it," said Piglet.
They sighed and got up; and when they had taken
a few gorse prickles out of themselves they sat
down again; and all the time Pooh was saying to
himself, "If only I could **think** of something!"
For he felt sure that a Very Clever Brain could
catch a Heffalump if only he knew the right way
to go about it.

A.A. Milne, "Winnie-the-Pooh"

This chapter surveys the general methods used to determine guidance

properties of non-axisymmetric waveguides. Some examples of solutions

of the scalar wave equation are mentioned, and some applications of

approximation methods are given. Comments about the strengths and

weaknesses of each appoach are included.

§1.1   Explicit exact solutions

For circular and planar waveguides, the symmetry and invariance

properties of the refractive index profile allows the reformulation of

the scalar wave equation

$$\left(\nabla^2 + V^2 g - W^2\right)\psi = 0 \tag{1}$$

as an ordinary differential equation for the normalized propagation

constant W and modal field ψ in terms of the profile's shape-function g

and the waveguide's normalized frequency V. However, for a general,

non-axisymmetric profile, this equation remains a non-separable

differential equation and solution is difficult.

There are only a few exceptions. For example, if the shape function is homogeneous (Snyder & Love, §16.5) - i.e., $\forall \alpha \varepsilon \mathbf{R}$, it satisfies

$$1 - g(\alpha X, \alpha Y) = \alpha^q \left(1 - g(X,Y)\right)$$

for some g-dependent constant q - then analytic expressions exist for the propagation constant, group velocity and distortion parameter of each mode. Infinite power-law profiles with elliptic or hyperbolic contours are of this form.

Another example requires g to be a separable function (Snyder & Love, §16.6) of the Cartesian co-ordinates, i.e.

$$g(X,Y) = g_1(X) + g_2(Y)$$

where g_1 is independent of Y, and g_2 of X. In this case (1) is separable in the co-ordinates X and Y, uncoupling to the two ordinary differential equations for $\psi_1(X)$ and $\psi_2(Y)$:

$$\ddot{\psi}_1 + \left(V^2 g_1 - \frac{W^2}{2} + \mu\right)\psi_1 = 0 \qquad (2a)$$

$$\ddot{\psi}_2 + \left(V^2 g_2 - \frac{W^2}{2} - \mu\right)\psi_2 = 0 \qquad (2b)$$

where μ is the separation constant. Examples of this form include the pseudo-rectangular profile (Kumar & Varshney, 1984) and similar refractive index distributions used to study rectangular waveguides.

Perhaps the simplest non-axisymmetric profile to solve is the infinite, parabolic, elliptical waveguide (Snyder & Love, p.355f). Because of its simplicity, this is useful in understanding the general properties of non-circular, refractive index distributions.

§1.1.E Example: Infinite linear profile

As an example of an exact, explicit solution, consider the profile, which is both homogeneous and separable, defined on the infinite cross-section by

$$g = 1 - \left|x/\rho_x\right| - \left|y/\rho_y\right|. \tag{3}$$

Contours of constant refractive index are shown in figure 1.1(a). The contour $n=n_{c\ell}$ is defined by $\left|x/\rho_x\right| + \left|y/\rho_y\right| = 1$.

Using the co-ordinate transformation given in Snyder & Love §16-7, it is straightforward to show that the normalized propagation constant, U, is given by

$$U_{jk} = \Lambda_{jk} V^{2/3} \quad , \quad j,k \geqslant 0 \tag{4a}$$

and the subscripts j and k label the modes. V is the normalized frequency. The scaling length is

$$\rho = \sqrt{\rho_x \rho_y};$$

$$\Lambda_{jk}^2 = \lambda_j \, \varepsilon^{1/3} + \lambda_k \, \varepsilon^{-1/3}; \tag{4b}$$

$$\varepsilon = \rho_x/\rho_y;$$

$$\lambda_{2j} = -a_j' \quad , \quad j \geqslant 0,$$

$$\lambda_{2j+1} = a_j \quad , \quad j \geqslant 0,$$

a_j and a_j' are the jth zeroes of Ai and Ai$'$, respectively, where Ai is the Airy function of the first kind (A&S, 10.4). The corresponding modal field, also labelled by jk, is

$$\psi_{jk} = \pm Ai\left(s_X^j\right) Ai\left(s_Y^k\right)$$

Figure 1.1

(a) Refractive index contours of the infinite linear profile of (3). The shaded region, being inside $n=n_{c\ell}$, indicates the core. The shape is measured by the inverse aspect ratio, $\varepsilon=\rho_y/\rho_x$.
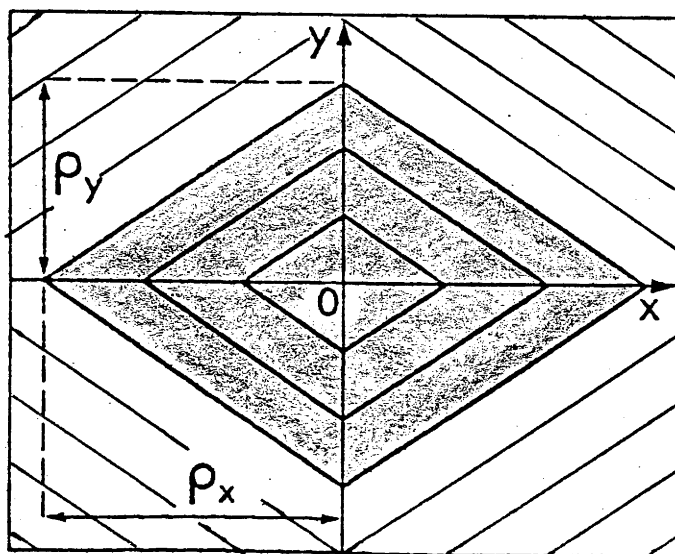
(b) Refractive index contours of the clad elliptical profile of (6). The shape is measured by the inverse aspect ratio, $\varepsilon=\rho_y/\rho_x$.

where the sign of ψ may vary from quadrant to quadrant, and

and

$$s_X^j = |X| \, V^{2/3} \, \varepsilon^{1/6} + \lambda_j$$

$$s_Y^k = |Y| \, V^{2/3} \, \varepsilon^{-1/6} + \lambda_k.$$

From (4), the distortion parameter (e.g. Snyder & Love, p.294) is

$$D = \frac{1}{9} \, \Lambda_{jk}^2 \, V^{-5/3} \qquad\qquad (5)$$

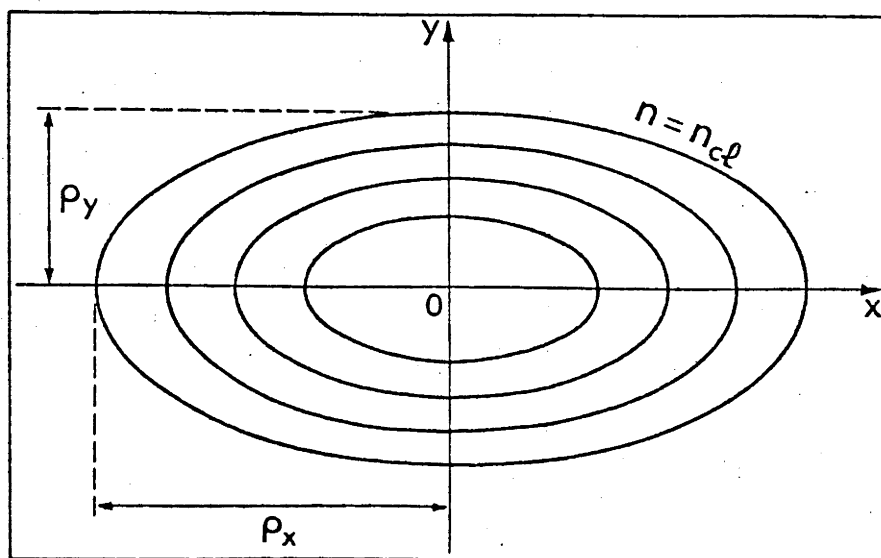which increases and becomes unbounded as $V \to 0$.

While unphysical, this profile shows some of the features of more realistic profiles. In particular, by considering a family of infinite linear profiles with identical core area, it is interesting to see how degeneracies amongst the modes change. A sequence of profiles of equal area is characterized by constant V and variable ε.

As ε changes, from (4), U_{jk} varies through Λ_{jk}, whose dependence on ε is shown in figure 1.2. As expected from symmetry considerations, $\Lambda_{jo} = \Lambda_{oj}$ at $\varepsilon=1$. However, if $\varepsilon \neq 1$, this degeneracy is broken. Also, as $\varepsilon \to 0$, the $\varepsilon^{-1/6}$ singularity in (4b) dominates and $\Lambda_{jk} \to \Lambda_{ok}$, $\forall \, j \geqslant 0$. The modes are infinitely degenerate in the $\varepsilon=0$ limit. In particular, an infinite number of modes have U_{00} as a limiting value!

Conventionally modes are ordered by increasing values of U. Thus as ε changes, the order of the mode changes, although the $(0,0)$ is always the first, or fundamental, mode. For example, at $\varepsilon=0.9$,

$$U_{00} < U_{10} < U_{01} < U_{20} < U_{02} < U_{11} < \cdots \; ,$$

whereas at $\varepsilon=0.1$,

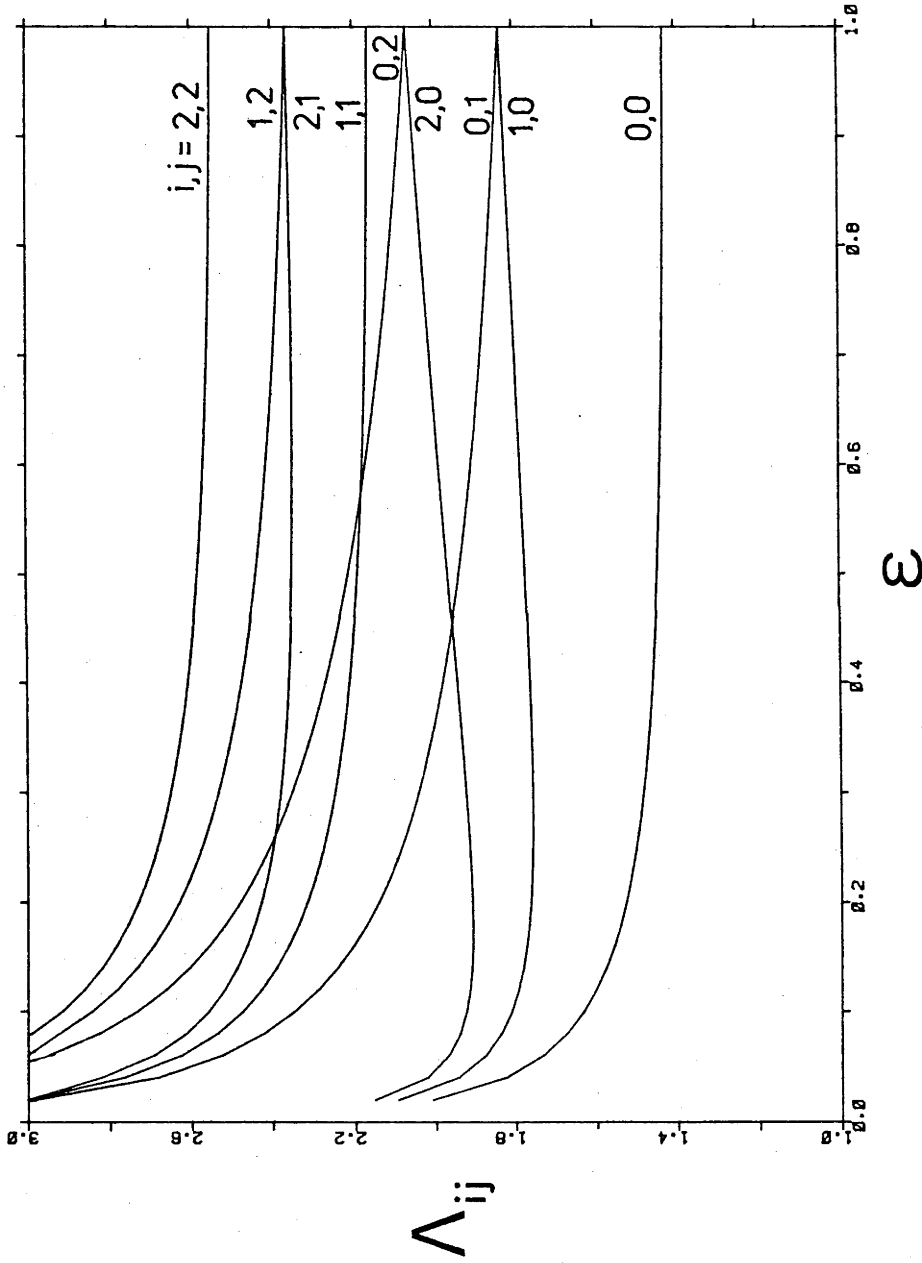$$U_{00} < U_{10} < U_{20} < U_{01} < U_{11} < U_{21} < \cdots \; .$$

Figure 1.2

Scaling parameters, Λ_{ij}, relating the normalized frequency, V, and normalized propagation constant, U, of the infinite linear profile. It is apparent how the ordering of the modes changes as the shape, measured by ε, varies.

This reshuffling of modes, as the shape of the cross-section varies, is characteristic of non-axisymmetric waveguides.

§1.2   Series solutions

If a simple closed form of solution for the field, ψ, given in (1), is not possible, sometimes a series solution can be obtained. For a physically meaningful answer, ψ needs to have no singularities and must vanish as $R \to \infty$. Hence a two dimensional analogue of the Frobenius method can be utilized to solve (1). ψ, a function of the planar coordinates R and θ, can be constructed as a doubly infinite expansion in simple functions of R and θ (e.g. (9)).

This method is versatile and quasi-analytic, but cumbersome to implement, ultimately requiring numerical computation. However, if (·1) is separable, the expansion of ψ is only singly infinite. This method is used extensively in this thesis (chapters 2 and 5).

§1.2.E Example: Clad-parabolic elliptical profile

As an example of this method, consider the solution of the clad-parabolic elliptical profile, defined by the shape-function

$$g(R,\theta) = \begin{cases} 1 - R^2(\varepsilon^2\cos^2\theta + \sin^2\theta) , & \text{inside core} \qquad (6a) \\ 0 & , \quad \text{outside core,} \qquad (6b) \end{cases}$$

where lengths are scaled by ρ_y,

$$\varepsilon = \rho_y / \rho_x ,$$

and ρ_x and ρ_y are the ellipse's semimajor and semiminor axes, respectively. The core's boundary is given by

$$R_B = \left(\varepsilon^2\cos^2\theta + \sin^2\theta\right)^{-1/2} .$$

The contours of constant refractive index, defined by (6), are shown in figure 1.1(b).

Putting (6) in (1) gives, inside and outside the core, respectively,

$$\left[\nabla^2 + R^2 U^2 - \frac{R^2 V^2}{2}((\epsilon^2+1) + (\epsilon^2-1) \cos 2\theta)\right]\psi = 0 \qquad (7a)$$

and

$$\left[\nabla^2 - R^2 W^2\right]\psi = 0 . \qquad (7b)$$

Since g is symmetric about both the X- and Y-axes, for the fundamental mode, ψ will have this property also. Thus, the field in the cladding is the solution of (7b) and can be written as

$$\psi_{c\ell} = \sum_{n=0}^{\infty} \beta_n \frac{K_{2n}(WR)}{K_{2n}(W)} \cos(2n\theta), \qquad (8)$$

since it is required that $\psi \to 0$ as $R \to \infty$. Here K_ℓ is a modified Hankel function of the third kind, and the β_n are constants.

To obtain ψ inside the core, the expansion is in a more elementary basis:

$$\psi_{co} = \sum_{m=0}^{\infty} \sum_{n=m}^{\infty} A_{nm}(\epsilon R)^{2n}\cos(2m\theta) \qquad (9)$$

where the A_{nm} are constants. Replacement of this form in (7a) produces recurrence relations for the elements of the matrix A, which is, as (9) assumed, lower triangular. With the identification

$$A_{nn} = \alpha_n, \quad n \geqslant 0,$$

these relations reduce to

$$A_{p+m,m} = \sum_{j=0}^{\infty} C_{pmj} \; \alpha_j \quad , \quad p,m \geqslant 0, \tag{10}$$

where the C_{pmj} depend on ε, V and U, and the α_n need to be determined form continuity requirements.

Because ψ and $\partial\psi/\partial R$ are continuous at the core-cladding interface, (8) - (10) yield

$$\sum_{p,j,m=0}^{\infty} C_{pmj} \; \alpha_j \; \varepsilon^{2p+2m} \; R_B^{2p+2m}(\theta) \; \cos 2m\theta$$

$$= \sum_{n=0}^{\infty} \beta_n \frac{K_{2n}\bigl(WR_B(\theta)\bigr)}{K_{2n}(W)} \cos 2n\theta \tag{11}$$

and

$$\sum_{m,p,j=0}^{\infty} C_{pmj} \; \alpha_j \; \varepsilon^{2p+2m} \; 2(p+m) \; R_B^{2p+2m-1}(\theta) \; \cos 2m\theta$$

$$= \sum_{n=0}^{\infty} W\beta_n \frac{K_{2n}'\bigl(WR_B(\theta)\bigr)}{K_{2n}(W)} \cos 2n\theta, \tag{12}$$

where prime denotes differentiation with respect to the argument. Clearly $R_B(\theta)$ is an even, π-periodic function so the following Fourier series exist. For $\ell \geqslant 0$,

$$\varepsilon^{2\ell} \; R_B^{2\ell}(\theta) = \sum_{m=0}^{\infty} a_{\ell m} \cos 2m\theta \; ; \tag{13a}$$

$$\frac{K_{2\ell}\bigl(WR_B(\theta)\bigr)}{K_{2\ell}(W)} = \sum_{m=0}^{\infty} b_{\ell m} \cos 2m\theta \; ; \tag{13b}$$

$$\varepsilon^{2\ell+1} \; R_B^{2\ell+1}(\theta) = \sum_{m=0}^{\infty} c_{\ell+1,m} \cos 2m\theta \; ; \tag{13c}$$

$$\frac{W \; K_{2\ell}'\bigl(WR_B(\theta)\bigr)}{K_{2\ell}(W)} = \sum_{m=0}^{\infty} d_{\ell m} \cos 2m\theta \; . \tag{13d}$$

Substituting (13) into (11) and (12), matching the components of cos(2jθ), and defining the matrices

$$E_{ij} = \sum_{m,p=0}^{\infty} C_{pmj} \left(a_{m+p,m+i}(1-\delta_{io}) + (1+\delta_{mi}) a_{m+p,|m-i|} \right) ,$$

$$F_{ij} = b_{j,j+i}(1-\delta_{oi}) + b_{j|j-i|}(1+\delta_{ij}) ,$$

$$G_{ij} = \sum_{m,p=0}^{\infty} C_{pmj} \, 2\varepsilon(p+m) \left(C_{m+p,m+i}(1-\delta_{io}) + (1+\delta_{mi}) C_{m+p,|m-i|} \right) ,$$

$$H_{ij} = d_{j,j+i}(1-\delta_{oi}) + d_{j|j-i|}(1+\delta_{ij}) ,$$

produces the two simultaneous matrix equations

$$E\alpha = F\beta \qquad\qquad (14)$$

$$G\alpha = H\beta, \qquad\qquad (15)$$

where the constants α_n and β_n are the components of the vectors α and β, respectively.

For a non-trivial solution of this system, the determinant of the augmented matrix

$$Q = \begin{bmatrix} E & -F \\ \hline -G & H \end{bmatrix}$$

must vanish. Indeed, det(Q) does vanish for a countable set of values of U, corresponding to the normalized propagation constants of all bound modes whose field, ψ, has the postulated symmetry about both Cartesian axes. The lowest value of U corresponds to the fundamental mode. Having calculated U, it is straightforward to solve (14) and (15) for the α_n and β_n, which fully describe ψ.

Comparison was made between the exact propagation constant, U, of a clad-parabolic elliptical fibre, and U estimated from the equivalent step elliptical fibre, defined by the moment method (Black & Pask, 1984). For $\epsilon=2/3$ and $v=2.828$, U is overestimated by 2.7%.

In the limit $V \to \infty$, the behaviour of this profile is identical to that of the infinite, parabolic profile. The power, concentrated in the core, is not influenced by the cladding.

§1.3   Variational methods

The field, ψ, of the fundamental mode is relatively insensitive to the variation of the refractive index, n. This observation inspired several schemes which identify equivalences between waveguides. Because of its simplicity, the step-index fibre is frequently used in this identification, so that ψ approximated by ψ_0, which, defined in terms of Bessel functions, is the fundamental modal field of a circular, stepped waveguide. The method of selection of ψ_0 optimizes the matching of some guidance property of the two different profiles.

Near the axis of proagation for the fundamental mode of most waveguides, ψ is approximately Gaussian in shape. Snyder & Sammut (1979) employed a variational expression to optimize the choice of a Gaussian function to match ψ:

$$\psi \approx \psi_G = \exp\left(-R^2/2R_0^2\right)$$

where R_0 is the spot-size, chosen so that $\frac{\partial U}{\partial R_0} = 0$. Subsequently, this method was extended to both non-axisymmetric profiles (Snyder, 1981), with two free spot-sizes, and higher-order modes (Love & Hussey, 1984). The Gaussian approximation is a simpler analysis of the behaviour of a non-axisymmetric waveguide than existing equivalent step-

index methods. Sometimes it is exceptionally accurate (e.g. §1.3.E).

Its great advantage is that simple expressions can be obtained for

various properties which depend on ψ, e.g. birefringence.

However, the Gaussian approximation does have a major deficiency.

While ψ resembles a Gaussian function in the core, as $R \to \infty$, this

similarity diminishes. As a mode approaches cut-off, more power travels

in the cladding, i.e. ψ spreads further from the axis, and this

approximation's accuracy deteriorates. Physically this can be

appreciated by recognizing that the Gaussian approximation defines an

equivalent waveguide which is based on an infinitely, parabolic,

elliptical fibre. Such a waveguide has an unlimited capacity for

guiding waves; the shape-function, g, does **not** vanish as $R \to \infty$.

The Gaussian approximation is extensively used in chapter 3, where

its accuracy for step, elliptical fibres is assessed.

§1.3.E Example: Infinite linear profile

As a simple example of the application of the Gaussian

approximation, it is used to describe the fundamental mode of the

infinite linear profile (5). Assuming, as an approximate modal field of

the fundamental mode,

$$\psi \approx \exp\left(-\frac{1}{2}\left(\frac{X^2}{A_X^2} + \frac{Y^2}{A_Y^2}\right)\right) ,$$

The spot-sizes are (Snyder & Love, §17-2)

$$A_X^2 = \frac{\pi^{1/3}}{V^{4/3}} \, \varepsilon^{7/6}$$

and

$$A_Y^2 = \frac{\pi^{1/3}}{V^{4/3}} \, \varepsilon^{-7/6} ,$$

and the normalized propagation constant is

$$U_{00} \approx \frac{\sqrt{3}}{\sqrt{2} \, \pi^{1/6}} \left(\varepsilon^{1/3} + \varepsilon^{-1/3} \right)^{1/2} V^{2/3} .$$

Compared with (4), this has the **same** explicit dependence on ε and V, and the numerical factor differs by a mere 0.6%. Because of the identical dependence on V, this relative error translates directly to this dispersion, D. This profile is an example where differentiating an approximation for U does not introduce large errors in D. In general, such a procedure is fraught with danger (Sammut, 1979).

Because this profile is infinite, it is not unexpected that the exact result and the Gaussian approximation agree so well for all V.

§1.4   Perturbation methods

For refractive index profiles which vary slightly from axisymmetry, it is simplest to treat the variation as a perturbation of the circular profile, and derive an approximate solution of (1). This method is explained in detail in Snyder & Love (1983, ch.18). The derivation of the formula is shown in §1.A where the formula for a perturbation estimate of cut-off is obtained. An application of this method to a specific profile is given in §5.6.

Of course the accuracy of the perturbation result decreases as the variation from circularity increases. It is important to obtain an estimate on this accuracy. For example, in §5.6, it is seen to be very useful for the butterfly profile whereas results for the ellipse, §3.3 – §3.5, show it is the limit of very small eccentricities. Even when of limited accuracy, the perturbation method does provide an exact limiting form of the way parameters vary with the non-axisymmetry of the profile. In chapter 3 it is shown how this can be exploited to provide very good approximation formulae.

Sometimes, e.g. §3.A.2, it is possible to treat a non-axisymmetric waveguide as a slight variation of a planar waveguide. In general this is awkward because a slab has three unconnected regions, a fibre only two. Within a plane, such figures are topologically distinct.

§1.5   Other approximation methods

The variational and perturbation methods not only estimate propagation constants and other parameters, but also define an approximate form of ψ. There are other approximation methods which concentrate on propagation constants.

The moment method (Hussey & Pask, 1981 & 1982; Sammut, 1982a; Black & Pask, 1984) prescribes an equivalence between waveguides of different shape or different form of refractive index. It is an efficient method of estimating propagation constants to within a few percent, and its accuracy is extensively examined in chapters 3 and 4 of this thesis.

The effective index method (eg. Adams, 1981, ch.6) replaces a two dimensional cross-section with a superposition of two one-dimensional planar waveguides, whose refractive index profiles are derived from the original fibre.

1.6   Numerical Methods

Because of the difficulty involved in extracting exact, or even approximate, analytic results for non-axisymmetric waveguides from (1), much use is made of numerical methods. Notable here is the finite element method which, for fibres, is exploited successfully by many authors. Although it has proved a very powerful technique, the finite element method does have shortcomings. For general application, a large amount of computer memory is required. In a waveguide this problem

exacerbated as the mode approaches cut-off, i.e. ψ spreads further into the cladding. As this occurs, more and more points are required to achieve a given accuracy. In this thesis, the chosen method is **more** accurate as the mode approaches cut-off.

For an axisymmetric waveguide, (1) reduces to an equation in one variable. Sammut & Pask (1982) developed a simple shooting method to integrate directly this equation when the refractive index has a uniform cladding. Attempts to extend this to two-dimensions were unsuccessful. Not only were there unresolved numerical instabilities, but the implementation was more cumbersome than the series expansion technique of §1.2.

§1.A   Appendix: Perturbation method for cut-off frequencies

Snyder & Love (1983, ch.18) explain how to obtain an estimate of the propagation characteristics of one waveguide in terms of those of another, whose refractive index distribution is similar. This argument can be extended to provide an estimate of the scalar cut-off frequency of the first waveguide in terms of the second.

At cut-off, the normalized propagation constants have the values $U=V_c$ and $W=0$, where V_c is the normalized cut-off frequency. Thus (1) becomes

$$L[\psi] = 0 \tag{15}$$

where the differential operator L is

$$L = \nabla^2 + V_c^2\, g \,, \tag{16}$$

and g, defined in (P.1), is the shape-function of the waveguide and vanishes as $R \to \infty$. For another waveguide, characterized by $\bar{g}$ and for which all symbols are barred,

$$\bar{L} = \nabla^2 + \bar{V}_c^2 \, \bar{g} \, , \tag{17}$$

and the companion to (15) is obvious.

Proceeding analogously to Snyder & Love, the combination of (15) to (17) gives

$$V_c^2 - \bar{V}_c^2 = \frac{\bar{V}_c^2 \int_{\mathcal{S}_\infty} \psi \, \bar{\psi} \, (\bar{g} - g) \, dS}{\int_{\mathcal{S}_\infty} \psi \, \bar{\psi} \, g \, dS} \, , \tag{18}$$

where $\int_{\mathcal{S}_\infty}$ indicates the integrals are evaluated over the infinite cross-section.

If the second profile differs only slightly from the first, i.e.,

$$\bar{g} - g = \varepsilon f \tag{19}$$

where $\varepsilon < 1$, then

$$\psi = \bar{\psi} + \varepsilon \phi \tag{20}$$

and substituting (19) and (20) into (18) shows

$$V_c^2 \approx \bar{V}_c^2 \left(1 + \varepsilon \frac{\int_{\mathcal{S}_\infty} \bar{\psi}^2 \, f \, dS}{\int_{\mathcal{S}_\infty} g \, \bar{\psi}^2 \, dS} \right) .$$

Thus the scalar cut-off frequencies of one profile are estimated from the scalar cut-off frequencies of another profile.

CHAPTER TWO

General Solution for Step-Profile Waveguides

"Rabbit's clever," said Pooh thoughtfully.
"Yes," said Piglet, "Rabbit's clever."
"And he has Brain."
"Yes," said Piglet, "Rabbit has Brain."
There was a long silence.
"I suppose," said Pooh, "that that's why he
never understands anything."

A.A. Milne, "The House at Pooh Corner"

In this chapter a new, exact method for solving the scalar problem for a step waveguide with a non-circular core is developed. It is based upon the expansion of the modal field, ψ, in terms of circular harmonic functions, but differs from the methods of both Goell (1969) and Eyges et al (1979) in the manner in which the continuity requirements are applied. Both ψ and $\partial\psi/\partial R$ are decomposed into Fourier series which are matched across the core-cladding interface. Ultimately, the propagation constants appear as the roots of a matrix' determinant, and need to be calculated numerically. The coefficients for the expansion of ψ are obtained from the null space of this singular matrix. Also discussed are techniques to avoid potential difficulties during the inevitable numerical calculations. Using these scalar field expansions, an expression is derived for birefringence, and features of the shape of the intensity of the scalar mode are examined. Finally, it is shown how an analogous method can be used to find the modal cut-off frequencies.

§2.1   Context

Once the trivial problem, posed by a circular step waveguide, was solved, scientists referred their attention to other geometrical shapes. However, departure from the axisymmetric structure destroys any opportunity for a simple solution, except in certain special cases, e.g. the planar waveguide.

Solutions for cross-sections with small variation from circularity have been obtained using perturbation theory (e.g. Eyges, 1978; Love et al, 1979). However, this method is obviously of limited usefulness, being helpful in analysing the consequences of small fluctuations from an intended circular cross-section, but not accurate for gross departures from circular symmetry.

Recent optical fibres, designed for special purposes such as the maintenance of polarization, and developments in integrated optics make extensive use of profiles which are nowhere near axisymmetric. Consequently, a method of solution which is valid for the general cross-section is necessary.

Such a method was expounded by Eyges et al (1978), who, using a Green function, inverted the scalar wave differential equation into an integral equation which was solved using an eigenfunction expansion. This method proved satisfactory for a wide variety of geometries. However, while the Green function for a step profile is readily evaluated, those for other profiles are not. The method presented below is easily generalized to graded non-axisymmetric profiles, an example being provided in chapter 5.

Direct numerical solution of the step profile was performed, using the finite element method, by Yeh et al (1979). The problem with the finite element method is that, as a mode approaches cut-off and the field spreads further into the cladding, many more points are required to obtain a given accuracy. Using the eigenfunction expansion below, the number of components in the expansion needed for a given accuracy decreases as the cut-off of the mode is approached, because, while the field is spreading out, it becomes more circular in appearance at large distances from the fibre's axis.

Both direct numerical computation and approximation methods suffer
from an inability to retain accuracy when singularities of various types
are approached, notably as the mode comes close to cut-off. Derivation
of an analytic method allows asymptotic forms to be used and accuracy
maintained.

Of the general approximation methods mentioned in chapter 1, the
Gaussian approximation - §1.3 - is not expected to be especially good
as a mode approaches cut-off. In general, the effective dielectric
constant method is probably better. The most appealing method for
approximating a step fibre is the profile volume approach, which matches
step waveguides whose core's have equal areas.

For specific profile shapes, methods for exact or approximate
solutions have been derived. Those for elliptical and rectangular
cross-sections will be discussed in chapters 3 and 4, respectively.

§2.2   Series solution for propagating modes

Within the weak guidance formalism, the modal fields are described
by solutions of the scalar wave equation (P.3)

$$\left[\nabla^2 - W^2 + V^2 g(R, \theta) \right] \psi = 0 \tag{1}$$

where ∇^2 is the two-dimensional Laplacean operator and g defines the
refractive index profile's shape. V is the normalized frequency, (P.4),
defined by

$$V^2 = k^2 n_{c\ell}^2 \rho^2 2\Delta$$

where ρ is some chosen length scale. W is the corresponding
dimensionless propagation constant, (P.5a).

For the case of a step fibre with a core whose cross-section's boundary is defined by

$$R = R_B(\theta) \, ,$$

where (R, θ) are plane polar co-ordinates, the shape-function is

$$g = \begin{cases} 1 & , \quad R < R_B(\theta) \\ 0 & , \quad R > R_B(\theta) \end{cases}$$

$$= 1 - H\left(R - R_B(\theta)\right) \, , \tag{2}$$

H being the Heaviside step-function. This yields a simple form for (1):

$$\left(\nabla^2 + U^2\right) \psi = 0 \quad , \quad R < R_B(\theta) \tag{3a}$$

$$\left(\nabla^2 - W^2\right) \psi = 0 \quad , \quad R > R_B(\theta) \tag{3b}$$

where U is given by (P.5b).

For ψ to be a physically meaningful modal field, it must satisfy certain boundary and continuity conditions. It is required that ψ vanishes exponentially as $R \to \infty$, and that ψ and $\partial\psi/\partial R$ are continuous everywhere, including $R=0$ and $R=R_B(\theta)$.

§2.2.1 Outline of method of solution

The scalar wave equation (3) has an infinite number of solutions, not all of which are physically meaningful. For those which are, a particularly simple basis of circular harmonic functions – a trigonometric function multiplied by a Bessel function – exists. ψ can be expanded in terms of this basis, and this is done below, (4) & (6). However, only particular sums are valid modes, those sums which exhibit the continuity conditions outlined above. These modes themselves will provide a basis for the solution space of (3).

The idea of expanding the field of a step profile in terms of trigonometric and Bessel functions is not new. Eyges et al (1979) used such an expansion to obtain the solution to their integral equation. Goell (1969), in solving for a rectangular cross-section, developed what has become known as the point matching method. After expanding ψ in a series like (7), he equated ψ and $\partial\psi/\partial R$ at a finite number of points on the boundary, and thus obtained two simultaneous matrix equations.

However, in the point matching method there is no optimal choice for the points. Goell spaced them at an equal angular separation around the boundary of the rectangle, an approximation which will converge as the number of such points becomes large. Metaphorically, this is a piecewise linear approximation to a smooth function.

In the method presented in this chapter, continuity is obtained .by expanding the inner and outer field and derivatives in terms of Fourier series, and matching the coefficients. In principle, this method is. more elegant, being analytic. For any Fourier expansion, after a certain number of terms, the contribution of the remainder is insignificant. Thus, once this number is obtained, convergence ought to be rapid.

The continuity requirements on ψ and $\partial\psi/\partial R$ reduce to two infinite matrix equations. However, as explained, these can be truncated at a particular size, and an accurate solution retained. Combining these two equations, an even larger matrix appears, and the propagation constants U and W(U) are obtained as the values at which this matrix' determinant vanishes. Numerical routines are needed to find this root, and consequently approximation methods can be exploited usefully to provide either an initial guess for U or bounds between which U must be located.
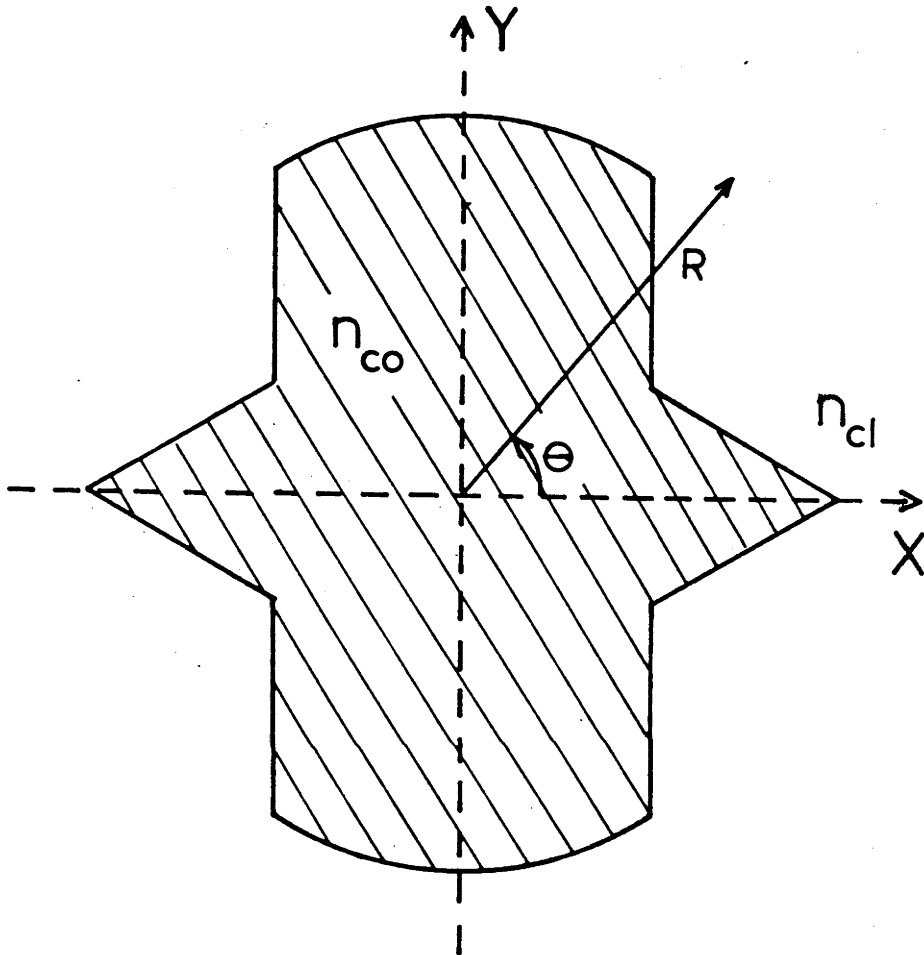
Figure 2.1

A cross-section with two axes of symmetry, along which the Cartesian axes are aligned.

§2.2.2 Expansion of the Field

Firstly, consider the modal field within the core. From (3a), one finds the simplest basis for solutions, which are finite at R=0, to be

$$\psi_{I\ell} = J_\ell(UR)(a_\ell \cos \ell\theta + b_\ell \sin \ell\theta) \tag{4}$$

where a_ℓ and b_ℓ are arbitrary real constants, and J_ℓ is the Bessel function of the first kind. Because $\{\psi_{I\ell}\}$ is a complete, orthogonal set within the permitted solution space for ψ, one can expand the interior modal field in terms of this basis.

$$\psi_I = \sum_{n=0}^{\infty} J_n(UR) (a_n \cos n\theta + b_n \sin n\theta) \ . \tag{5}$$

Similarly, the solution of (3b) produces, as an expansion of the exterior modal field,

$$\psi_E = \sum_{n=0}^{\infty} K_n(WR) (c_n \cos n\theta + d_n \sin n\theta) \tag{6}$$

where K_n is the modified Bessel function of the third kind, and c_n and d_n are constants.

If one recalls that for waveguides which are symmetric about two orthogonal axes there are two orthogonal optical axes, about which the scalar modal field, ψ, is either symmetric or antisymmetric, one can appreciate the origin of the a_n, b_n, c_n and d_n in the expansions.

Suppose the Cartesian axes are aligned with these optical axes. For modes which are symmetric about the X-axis, $\forall n \geqslant 0$, $b_n=0$ and $d_n=0$, and, for those which are antisymmetric, all a_n and c_n vanish . In addition, the symmetry property about the Y-axis ensures that half the remaining constants vanish; symmetric behaviour means only even cosine or odd sine harmonics are present, and an antisymmetric pattern produces

odd cosine or even sine functions. Because the fundamental mode is
symmetric about both axes, for the remainder of this analysis, modal
fields of the form

$$
\psi^{(ee)} = \begin{cases} \displaystyle\sum_{n=0}^{\infty} \alpha_n J_{2n}(UR) \cos 2n\theta \quad , \quad R < R_B(\theta) & \text{(7a)} \\[4ex] \displaystyle\sum_{n=0}^{\infty} \beta_n K_{2n}(WR) \cos 2n\theta \quad , \quad R > R_B(\theta) & \text{(7b)} \end{cases}
$$

are examined. The series defined by (7a) gives a real, though
physically meaningless, function for $R > R_B(\theta)$, and similarly for (7b).

§2.2.3 Fourier analysis and continuity

Expansion (7) is a general solution of the equation given in (3),
but for ψ to be a modal field, it must also satisfy continuity
conditions: ψ and its first partial derivatives are continuous
everywhere, and in particular, across the boundary. Specifically this
means

$$
\psi_I\big(R_B(\theta),\theta\big) = \psi_E\big(R_B(\theta),\theta\big) \tag{8}
$$

and

$$
\frac{\partial\psi_I}{\partial R}\big(R_B(\theta),\theta\big) = \frac{\partial\psi_E}{\partial R}\big(R_B(\theta),\theta\big) \; . \tag{9}
$$

The boundary function, $R_B(\theta)$, is obviously 2π-periodic.
Consequently, functions of $R_B(\theta)$ are also 2π-periodic in θ. Using
Fourier theory, these functions can be expanded as a series of sine and
cosine harmonics.

If one employs this result in (7), (8) and (9), then

$$\sum_{n,m=0}^{\infty} G_n \alpha_{nm} \left(\cos 2(n+m)\theta + \cos 2|n-m|\theta \right)$$

$$= \sum_{n,m=0}^{\infty} \beta_n H_n b_{nm} \left(\cos 2(n+m)\theta + \cos 2|n-m|\theta \right) \qquad (10)$$

and

$$\sum_{n,m=0}^{\infty} G_n \alpha_n c_{nm} \left(\cos 2(n+m)\theta + \cos 2|n-m|\theta \right)$$

$$= \sum_{n,m=0}^{\infty} H_n \beta_n d_{nm} \left(\cos 2(n+m)\theta + \cos 2|n-m|\theta \right) \quad , \qquad (11)$$

where

$$\frac{J_{2n}\left(UR_B(\theta)\right)}{G_n} = \sum_{m=0}^{\infty} a_{nm} \cos 2m\theta \quad , \qquad (12a)$$

$$\frac{UJ'_{2n}\left(UR_B(\theta)\right)}{G_n} = \sum_{m=0}^{\infty} c_{nm} \cos 2m\theta \quad , \qquad (12b)$$

$$\frac{K_{2n}\left(WR_B(\theta)\right)}{H_n} = \sum_{m=0}^{\infty} b_{nm} \cos 2m\theta \quad , \qquad (12c)$$

and

$$\frac{WK'_{2n}\left(WR_B(\theta)\right)}{H_n} = \sum_{m=0}^{\infty} d_{nm} \cos 2m\theta \quad , \qquad (12d)$$

where the primes denote differentiation with respect to argument and the constants G_n and H_n are introduced so that the matrix defined in (15) will be well conditioned. Their values depend on U,W and the form of $R_B(\theta)$.

§2.2.4 Solution of the system of matrices

If the coefficients of identical harmonics in the left-hand expressions and right-hand expressions of (10) and (11) are matched, there is the resulting system of matrix equations

$$A \; \alpha = B \; \beta \qquad\qquad (13\,a)$$

$$C \; \alpha = D \; \beta \; . \qquad\qquad (13\,b)$$

Here, the matrix elements are

$$X_{ij} = \begin{cases} x_{j \; j-i}(1-\delta_{i0}) + x_{j \; j+i} \;, & i < j \\[2mm] x_{j0}(2-\delta_{i0}) + x_{j \; j+i} \;, & i = j \\[2mm] x_{j \; i-j} + x_{j \; j+i} \;, & i > j \end{cases} \qquad (14)$$

with X and x representing A,B,C or D, and a,b,c or d, respectively. The vector elements are $(\alpha_n G_n)$ and $(\beta_n H_n)$ in the obvious way.

The matrices of (13) are infinite in size. Thus, one needs to examine their convergence, if one hopes to use them in meaningful computation. This is done operationally, ie. by increasing the order of the truncation and observing the results.

For a non-trivial solution of (13), either α or β could be eliminated to give, for example,

$$(CA^{-1}B - D) \; \beta = 0 \quad ,$$

and the determinant of the new matrix must vanish. However, this involves a matrix inversion operation, and a more satisfactory method is to form the direct sum of the solution spaces for α and β. Upon this, define the operator M, corresponding to the augmented matrix

$$M = \begin{vmatrix} A & -B \\ \hline -C & D \end{vmatrix} \quad . \tag{15}$$

Non-trivial solutions of (13) occur when det(M) vanishes. This occurs for only discrete values of U, which are the propagation constants of the modes. Thus, an analytic expression to determine the propagation constants has been obtained. It is stressed that this is valid for an arbitrary cross-section, but the above representation is simplest when the optical axes are apparent from symmetry.

Having found the values of U and W, solving for the element of the null space of M yields the coefficients in the field expansion (7).

$$M \begin{pmatrix} \alpha \\ \beta \end{pmatrix} = M\gamma = 0 \quad . \tag{16}$$

§2.2.5 Example: Circular cross-section

As an indication of how this method proceeds, it will be shown how the familiar soution of the waveguide with a circular, step profile is recovered. In this case, the boundary function is

$$R = R_B(\theta) = 1 \quad .$$

and lengths are scaled by the radius of the core.

Thus, in the Fourier series (12), the only non-vanishing coefficient is the constant term:

$$a_{n0} = \frac{J_{2n}(U)}{G_n} \quad ,$$

$$c_{n0} = \frac{UJ'_{2n}(U)}{G_n} \quad ,$$

$$b_{n0} = \frac{K_{2n}(W)}{H_n} \quad ,$$

$$d_{n0} = \frac{WK'_{2n}(W)}{H_n} \quad ,$$

and all the higher values of m are zero. From (14), these give matrices which are diagonal:

$$X_{ij} = \delta_{ij} 2x_{j0}$$

Finally, the augmented matrix (15) has the determinant

$$\det(M) = \prod_{j=0}^{\infty} \frac{J_{2j}(U)WK'_{2j}(W) - UJ'_{2j}(U)K_{2j}(W)}{G_j H_j} \quad , \tag{17}$$

and, since $G_j H_j \neq 0$, this vanishes if

$$\frac{UJ'_{2n}(U)}{J_{2n}(V)} = \frac{WK'_{2n}(W)}{K_{2n}(W)} \quad ,$$

the familiar eigenvalue equation for the modes which are symmetric about both axes of a circular step-profile.

If a different form of symmetry had been assumed in (7), then the $(2n+1)^{th}$ order eigenvalue equation would be recovered.

Because A,B,C and D are diagonal, the vector $\binom{\alpha}{\beta}$ of (16) will be given by

$$\alpha_j = \frac{P\delta_{jn}}{G_j} \quad ; \quad \beta_j = \frac{\delta_{jn} PJ_{2n}(U)H_n}{H_j G_n K_{2n}(W)}$$

where n is the chosen factor from (17). This produces the customary modal fields

$$\psi = \begin{cases} \dfrac{J_{2n}(UR)}{J_{2n}(U)} & , \quad R < 1 \\[2em] \dfrac{K_{2n}(WR)}{K_{2n}(W)} & \quad R \geqslant 1 \end{cases}$$

if

$$P = G_n / J_{2n}(U) \ .$$

Using the asymptotic forms for Bessel functions of large orders (e.g. Watson, 1966, ch.8), it is easy to show the higher-order factors in (17) vanish, regardless of the choice of normalization, as mentioned in §2.2.6. This induces confidence that the matrices obtained from the non-circular cross-sections will also converge.

§2.2.6 Computational details

Because A,B,C and D are all infinite themselves, rather than the form of M shown in (15), it is better to permute rows and columns to give, explicitly, for i,j ε N,

$$M_{ij} = \begin{cases} A_{[i/2][j/2]} & , \quad i,j \ \varepsilon \ 2Z \\ -B_{[i/2][j/2]} & , \quad i \ \varepsilon \ 2Z \ , \ j \notin 2Z \\ -C_{[i/2][j/2]} & , \quad i \notin 2Z \ , \ j \ \varepsilon \ 2Z \\ D_{[i/2][j/2]} & , \quad i,j \notin 2Z \end{cases}$$

where [x] indicates the integer part of x. The corresponding description for γ is, $\forall$ i ε N,

$$\gamma_i = \begin{cases} G_i \alpha_i & , \quad i \ \varepsilon \ 2Z \\ H_i \beta_i & , \quad i \notin 2Z \ . \end{cases}$$

A standard numerical algorithm can be used to find the determinant of M.

Consideration of (12) shows how an analytic formulation can enhance numerical evaluation. One problem in solving modal propagation arises near cut-off. This corresponds to $W \to 0$ and thus $K_{2n}(W)$ becomes unbounded. Under this condition, setting $H_n = K_{2n}(WS)$, where S is the maximum value of $R_B(\theta)$, leads to the following Fourier decomposition of the asymptotic form (refer A&S, 9.6.8 & 9.6.9):

$$\sum_{m=0}^{\infty} b_{0m} \cos(2m\theta) \sim 1 + \frac{\ln\left(R_B(\theta)/S\right)}{\ln S + \ln W} \sim 1,$$

$$\sum_{m=0}^{\infty} b_{nm} \cos(2m\theta) \sim \left(\frac{S}{R_B(\theta)}\right)^n, \quad n \geq 1,$$

$$\sum_{m=0}^{\infty} d_{0m} \cos(2m\theta) \sim \frac{1}{R_B(\theta)(\ln S + \ln W)} \sim 0,$$

and

$$\sum_{m=0}^{\infty} d_{nm} \cos(2m\theta) \sim \frac{-n}{R_B(\theta)} \left(\frac{S}{R_B(\theta)}\right)^n, \quad n \geq 1.$$

If W is large, $H_n = 1$.

For the fundamental mode, further complications occur as $V \to 0$. On all fibres, bound modes satisfy $U < V$, so that $U \to 0$, as $V \to 0$. For $n \geq 1$, $J_n(z) \to 0$ as $z \to 0$. Under these circumstances, the choice of G_n as $J_{2n}(US)$ facilitates the numerical work. Again, asymptotic results are employed (A&S, 9.1.10).

$$\sum_{m=0}^{\infty} a_{nm} \cos 2m\theta \sim \left(\frac{R_B}{S}\right)^{2n} \left(1 + \frac{U^2}{4(2n+1)} (S^2 - R_B^2)\right), \quad n \geq 1$$

and

$$\sum_{m=0}^{\infty} c_{nm} \cos 2m\theta \sim \frac{2n}{R_B} \left(\frac{R_B}{S}\right)^{2n} \left(1 - \frac{U^2}{4(2n+1)} \left(\left(\frac{n+1}{n}\right)R_B^2 - S^2\right)\right), \quad n \geq 1.$$

Of course, as $J_0(0)=1$, it suffices that $G_0=1$, even when $U\to0$. If U is sufficiently large, $G_n=1$ for larger values of n.

This use of G_n and H_n avoids the evaluation of a matrix which has over 40 orders of magnitude difference between the greatest and smallest elements of its major diagonal. No machine can ensure satisfactory accuracy under those circumstances.

§2.2.7 Estimate on propagation the constant

In finding the solution of det(M)=0, a suitable numerical, root finding routine is needed. The best of these, given that derivatives of matrix determinants ought to be avoided, require estimates of the root, preferably a lower and upper bound on the value.

To find these, it is useful to consider the equation (e.g. see · Snyder & Love, p.376)

$$\beta^2 - \beta_0^2 = \frac{k^2}{\langle \psi, \psi_0 \rangle} \int_{S_\infty} \psi_0\psi(n^2 - n_0^2)\, dS \tag{18}$$

where the propagation constants of two profiles, n and n_0, are related. The integrals are over the infinite cross-section, and the subscript zeroes distinguish between the quantities related to the two different fibres. The notation $\langle f,h \rangle$ is defined in (P.9b).

If n_0 is the profile of a circular step fibre, and n is the profile of an arbitrary step fibre with identical values of n_{co} and $n_{c\ell}$, the core and cladding indices, respectively, then (18) can be rewritten as (recalling (P.5b))

$$U_0^2 - U^2 = \frac{V^2}{\langle \psi, \psi_0 \rangle} \int_{S_\infty} \psi_0\psi\,(g_0 - g)\, dS, \tag{19}$$

where a length scale, ρ, was introduced to non-dimensionalize quantities and

$$n_j^2 = n_{c\ell}^2 (1 + 2\Delta g_j).$$

If the circle is contained fully within the other shape, Black & Pask (1984) observed that the integrand in (19) is positive, whereas, if the circle fully encloses the other figure, the integrand in (19) is everywhere non-positive. This follows since ψ and ψ_0 are everywhere positive for the fundamental mode. In the former case

$$U_0^2 > U^2,$$

and in the latter,

$$U_0^2 < U^2.$$

Thus, for some circle, it follows that

$$U^2 = U_0^2.$$

This is the ideal equivalent circular guide.

Sammut (1982) suggested the easiest equivalent fibre possessed an area equal to that of the arbitrary shape. However, in this case $U^2 \neq U_0^2$. In fact, observation of results indicates that the circular waveguide with equal cross-sectional area provides a lower bound:

$$U_0^2 < U^2. \tag{20}$$

Obviously this is closer to U^2 than the previous estimate of a lower bound. It is suggested that the inequality (20) is valid for any convex cross-section.

To understand the intuitive motivation for this, consider figure 2.2. The centre of the circle is such that the area of $\mathcal{S}_1$ is a
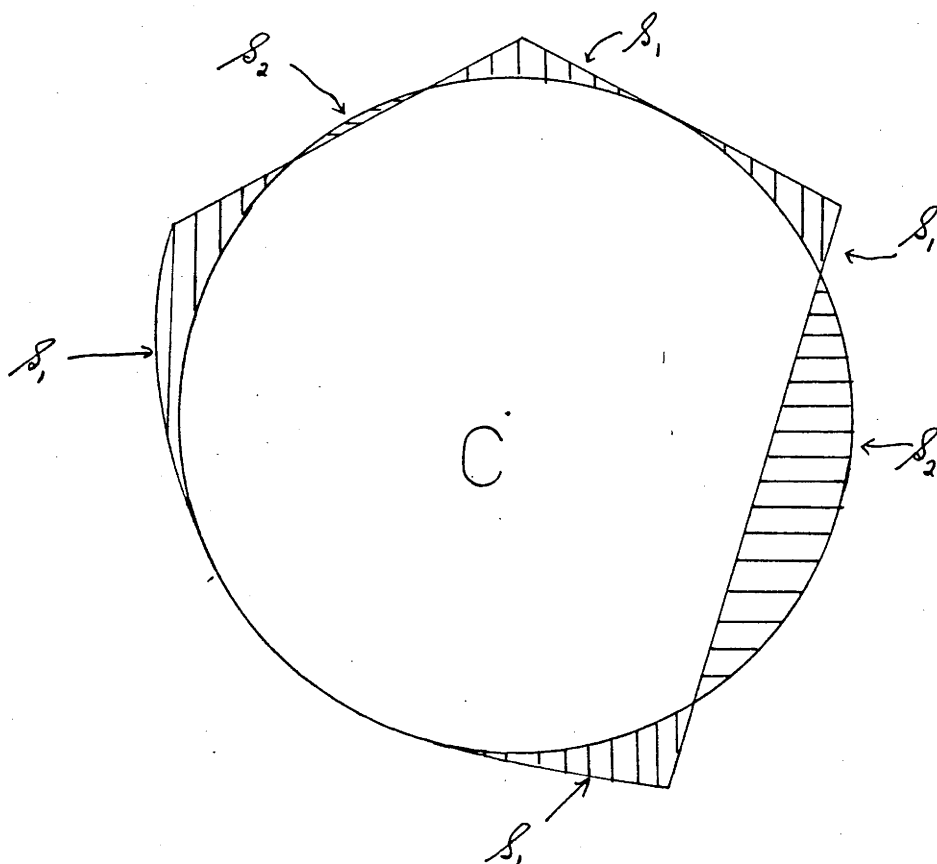
Figure 2.2

A general convex cross-section and the equal area circle, which is centred such that the area of $\mathcal{S}_1$ is a minimum. In $\mathcal{S}_1$, $(g_0-g)=-1$; in $\mathcal{S}_2$, $(g_0-g)=1$.

minimum. In the regions $\mathscr{S}_1$, $(g_0-g)= -1$; in the regions $\mathscr{S}_2$, $(g_0-g)= 1$; elsewhere g_0-g vanishes. Hence, from (19),

$$U^2 - U_0^2 = \frac{V^2}{\langle\psi,\psi_0\rangle} \left[\int\!\!\int_{\mathscr{S}_2}\psi_0\psi \, dS - \int\!\!\int_{\mathscr{S}_1}\psi_0\psi \, dS \right]. \tag{21}$$

The factor outside the square brackets is positive. Since the areas of $\mathscr{S}_1$ and $\mathscr{S}_2$ are equal,

$$\int_{\mathscr{S}_1} dS - \int_{\mathscr{S}_2} dS = 0.$$

The fundamental modal field of a circular fibre, ψ_0, is smaller in $\mathscr{S}_1$ than in $\mathscr{S}_2$. Further, ψ decreases exponentially away from R=0, and, in general, the total weighting function, $\psi_0\psi$, will satisfy

$$\int_{\mathscr{S}_2} \psi_0\psi dS > \int_{\mathscr{S}_1} \psi_0\psi \, dS.$$

For a general convex cross-section, ψ ought to be sufficiently well behaved, and (20) then follows from (21).

For some profiles, the Gaussian approximation provides a simple method for calculating an estimate of U. In these cases, examination of (19) shows

$$U_0^2 > U^2$$

because the approximation corresponds to the the infinite parabolic profile. However, most step cross-sections do not lead to explicit solutions within the Gaussian approximation, and thus not always a simple upper bound on U.

§2.3   Shape of the modal field

Having obtained the modal propagation constant, the modal field can be determined. Several facets can be investigated for a general profile. Notably the series (7) allow an examination of ψ in limiting cases.

Firstly, for large z, the asymptotic form of $K_n(z)$ (see A&S, 9.7.2) is independent of n, at a large distance from the guide's axis, and thus ψ separates in R and θ. Explicitly

$$\psi(R,\theta) \sim e^{-WR} \sqrt{\frac{\pi}{2WR}} \sum_{n=0}^{\infty} \beta_n \cos 2n\theta.$$

In general, this remains a transcendental function for the intensity contours of the modal field. However, for convex profiles, Black (1984) showed that the contours do become close to circles in this limit.

For small R, the situation is simpler. Using the series expansion for $J_n(z)$ (A&S, 9.1.10), it follows that

$$\psi(R,\theta) \sim \alpha_0 + \frac{U^2 R^2}{4} \left(\frac{\alpha_1}{2} \cos(2\theta) - \alpha_0\right) + O(R^4). \tag{22}$$

Thus, to this order of approximation, the intensity contours

$$\psi^2 = C,$$

where $C < \alpha_0^2$, correspond to ellipses with an inverse aspect ratio, ε, and semiminor axis, b, given by

$$\varepsilon^2 = 1 - \frac{2\alpha_1}{2\alpha_0 + \alpha_1} \tag{23}$$

and

$$b^2 = \frac{4(\alpha_0^2 - C)}{U^2 \alpha_0(2\alpha_0 + \alpha_1)} ,$$

respectively. Implicit in this analysis is the assumption

that $0 < \alpha_1 < 2\alpha_0$. In §3.5.1 and §4.4 this is shown to be true for

elliptical and rectangular cross-sections. An appropriate choice of

normalization ensures that $\alpha_0 > 0$. From (30), it follows that, if $\alpha_1 > 0$,

the major axis of the intensity contour is aligned with the X-axis. If

$\alpha_1 < 0$, the major axis is along the Y-axis. It is also interesting

that ε, in (23), is independent of C. Thus, at least near the axis, the

modal field is a family of concentric ellipses.

With interest concentrated on the fundamental mode, it is natural

to investigate the situation as $V \to 0$. Assuming that as $V \to 0$, the α_n

remain bounded, the expansion (22) is again valid, except that the

remainder is now $O(V^4)$. Hence, for an arbitrary cross-section, the

step-profile produces elliptical field patterns for small V. This is

expected, since as $V \to 0$, the field senses the shape of the core's

boundary less and less, becoming more nearly axi-symmetric. From (23),

as $\alpha_1 / \alpha_0 \to 0$, $\varepsilon \to 1$.

For large values of V, the field is, of course, confined to the

core, so that as $V \to \infty$, $\beta_n \to 0$. In this limit the shape of the field is

very sensitive to the shape of the core. In general, nothing can be

deduced about the α_n. Of course, as $V \to \infty$, the approximation of geometric

optics is applicable.

§2.4   Birefringence

In §P.3.1 it was explained how birefringence arises on a non-

circular step-fibre. Recalling (P.10), the formula for the normalized

birefringence of a step-profiled fibre is

$$B_p = \frac{1}{V^2 + \|\psi\|^2} \int_C d\ell \; D[\psi^2] \tag{24a}$$

where $\|\psi\|^2$ is defined in (P.9b), C is the boundary defined by $R_B(\theta)$, and the differential operator $\mathbb{D}$ is

$$D = n_x \frac{\partial}{\partial Y} - n_y \frac{\partial}{\partial X} . \qquad (24b)$$

(n_x, n_y) are the components of $\hat{n}$, the unit outward normal to C. (While the subsequent analysis is not new, it is inserted because it is not available elsewhere and is not trivially straightforward.)

Define a normalized radius, $F(R, \theta)$, by

$$F(R, \theta) = R/R_B(\theta).$$

F=1 on the core-cladding interface, but more importantly it produces a simple, useful expression for $\hat{n}$:

$$\hat{n} = \frac{\mathbf{N}}{\|\mathbf{N}\|} ,$$

where

$$\mathbf{N} = \nabla F$$

$$= \frac{\hat{r}}{R_B} - \frac{R_B'}{R_B^2} \hat{\theta} ,$$

giving

$$\hat{n} = \frac{R_B \hat{r} - R_B' \hat{\theta}}{\left(R_B^2 + R_B'^2\right)^{1/2}} \qquad (25a)$$

$$= n_r \hat{r} + n_\theta \hat{\theta} , \qquad (25b)$$

where the components (n_r, n_θ) are defined in the obvious way.

Transformation from Cartesian to plane polar co-ordinates is a standard result. From (24b), this gives a new form for $\mathbf{D}$:

$$\mathbb{D} = (n_r \cos 2\theta - n_\theta \sin 2\theta) \frac{\partial}{\partial R} - \frac{(n_r \sin 2\theta + n_\theta \cos 2\theta)}{R} \frac{\partial}{\partial \theta} . \qquad (26)$$
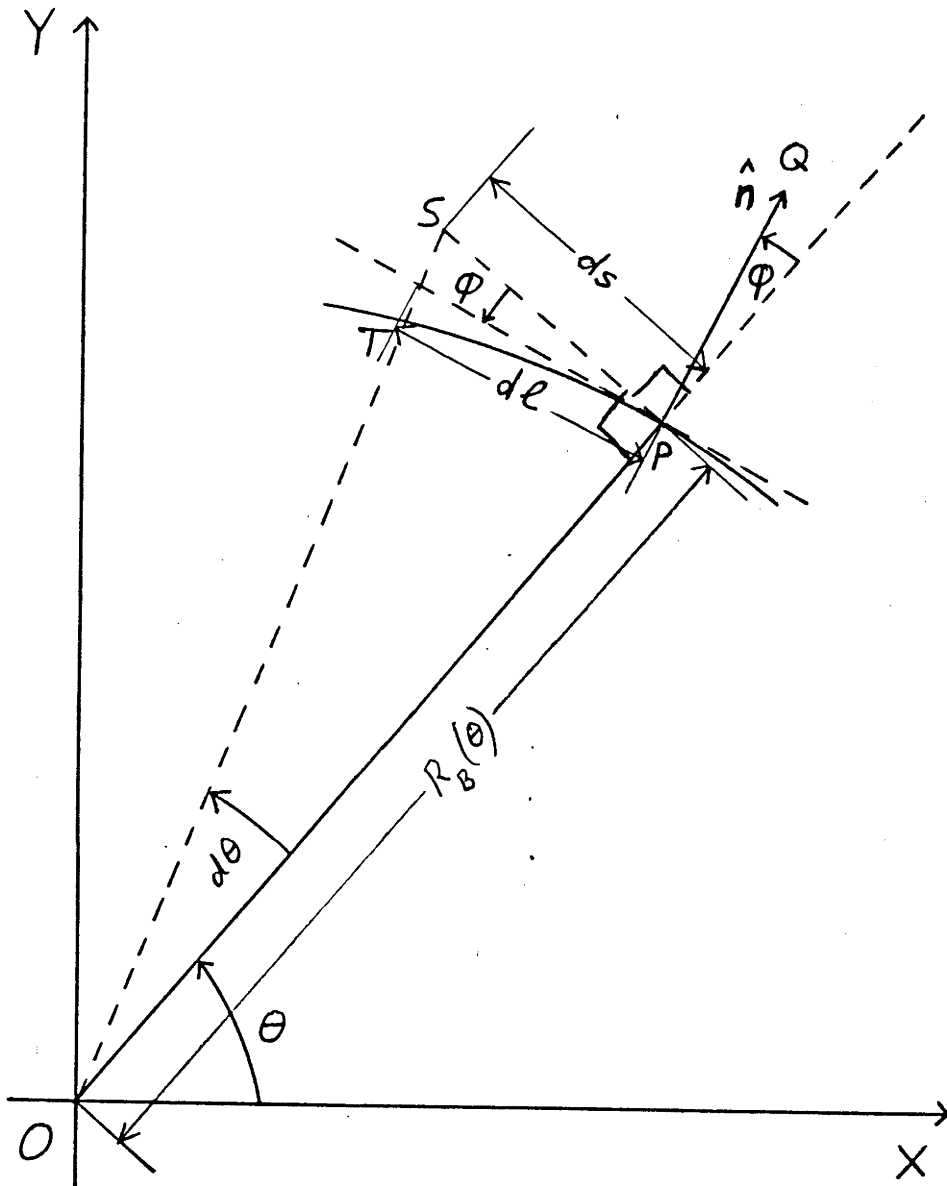
Figure   2.3

An arc of the boundary function, $R_B(\theta)$, defining the core-cladding interface in the XY-plane. $\hat{n}$ is the unit, outward normal vector to this curve.

To find an expression for $d\ell$, defined above (P.10), consider figure 2.3, in which TP is an arc of the contour C with arclength $d\ell$, and subtends angle $d\theta$ at the origin. Because $\hat{n}$ is normal to this curve, angle TPQ is $\pi/2$. Also, by the construction, angle OPS is $\pi/2$, and consequently angle ϕ appears in the two places indicated. Using the formula of trigonometry,

$$d\ell = ds/\cos\phi$$

and

$$ds = R_B(\theta)\tan(d\theta)$$
$$\sim R_B(\theta)\,d\theta,$$

since $d\theta \ll 1$, it is immediate that

$$n_r = \hat{n}\cdot\hat{r} = \cos\phi.$$

Combining these results yields

$$d\ell \sim \frac{R_B(\theta)\,d\theta}{n_r}. \tag{27}$$

Replacing (24b) and (27) in (24a) produces, after simpification

$$B_p = \frac{1}{V^2\|\psi\|^2} \int_0^{2\pi} d\theta \left\{ \left(R_B\cos 2\theta + R_B'\sin 2\theta\right)\psi_R^2 \right.$$
$$\left. - \left(\sin 2\theta - \frac{R_B'}{R_B}\cos 2\theta\right)\psi_\theta^2\right\} \tag{28}$$

where (25a) and the definition of C have also been used.

Since $R^B(\theta)$ is 2π-periodic and, at worst, R_B' is discontinuous at a discrete set of points, $\{\theta_j\}$ (This is not true of fractals, but these

are unphysical "shapes" for fibres.), the result (ii) of §2.A can be

applied. This gives

$$-\int_0^{2\pi} d\theta \left(\sin 2\theta - \frac{R_B'}{R_B} \cos 2\theta\right) \psi_\theta^2(R_B(\theta),\theta)$$

$$= \int_0^{2\pi} d\theta\ \psi^2 \left\{ \frac{2R_B'}{R_B} \sin 2\theta + \left(2 - \frac{R_B''}{R_B} + \frac{R_B'^2}{R_B^2}\right) \cos 2\theta \right\}$$

$$+ \int_0^{2\pi} d\theta\ \psi_R^2 \left\{ R_B' \left(\sin 2\theta - \frac{R_B'}{R_B} \cos 2\theta\right) \right\}$$

$$+ \sum_{j=1}^{N-1} \psi^2(R_B(\theta_j),\theta_j)\ H(\theta_j)\ .$$

where $H(\theta_j)$ follows from the details in §2.A. When substituted into

(28), this yields

$$B_p = \frac{1}{V^2 \|\psi\|^2} \left(\int_0^{2\pi} d\theta\ \psi^2(R_B(\theta),\theta) \left(\left(2 - \frac{R_B''}{R_B} + \frac{R_B'^2}{R_B^2}\right) \cos 2\theta + \frac{2R_B'}{R_B} \sin 2\theta \right) \right.$$

$$+ \int_0^{2\pi} d\theta\ \psi_R^2(R_B(\theta),\theta) \left(2R_B' \sin 2\theta + \left(R_B - \frac{R_B'^2}{R_B}\right) \cos 2\theta \right)$$

$$+ \sum_{j=1}^{N-1} \psi^2(R_B(\theta_j),\theta_j)\ H(\theta_j)\ . \tag{29}$$

This result is valid for **all** step-profile fibres, regardless of the

shape of the cross-section. However, as it stands, it is not

particularly useful.

Suppose further constraints are imposed on the waveguide, as in

previous work, such as requiring that the shape of the cross-section is

symmetric about two orthogonal axes, which are aligned with the

Cartesian axes. In this case, if the required symmetry conditions are

satisfied the summation over j in (29) can be removed, using (iv) of

§2.A. Further, both ψ^2 and ψ_R^2, as well as each of the terms inside the

square brackets have the required periodicity property to allow the

evaluation of the integrals over $[0,\frac{\pi}{2}]$.

If expansion (7a), is used for the field on the interface, then

substitution of this in (29), and then massive simplification, produces

$$B_p =$$

$$\frac{4}{V^2 \|\psi\|^2} \sum_{n=0}^{\infty} \sum_{m=0}^{n} (2-\delta_{nm})\alpha_n \alpha_m \int_0^{\pi/2} d\theta \cos 2n\theta \cos 2m\theta \, J_{2n}(UR_B)J_{2m}(UR_B)E_{nm}(\theta) \tag{30a}$$

where

$$E_{nm}(\theta) = \left(2 - \frac{R_B''}{R_B} + \frac{R_B'^2}{R_B^2}\right)\cos 2\theta + \frac{2R_B'}{R_B}\sin 2\theta + \tag{30b}$$

$$U\left(\frac{J_{2n}'(UR_B)}{J_{2n}(UR_B)} + \frac{J_{2m}'(UR_B)}{J_{2m}(UR_B)}\right)\left(2R_B'\sin 2\theta + (R_B - \frac{R_B'^2}{R_B})\cos 2\theta\right)$$

In general, the integral in (30) needs numerical evaluation. No

suitable shape for an analytic result has been found.

§2.5   Series solution for modal cut-off

To obtain a solution for the values of modal cut-offs, one can

proceed in an analogous fashion to §2.2, remembering that for cut-off,

W=0. In this case it is necessary to solve

$$[\nabla^2 + V_{co}^2 g]\psi_c = 0 \tag{31}$$

where V_{co}^2 is the eigenvalue to be determined. The countable family of

these values corresponds to the countable family of cut-off frequencies

for the waveguide.

Once again, using (2), (31) can be written in distinct form for the core and the cladding.

$$\left(\nabla^2 + V_{co}^2\right) \psi_c = 0 \quad , \quad R \lessgtr R_B(\theta) \tag{32a}$$

$$\nabla^2 \psi_c = 0 \quad , \quad R > R_B(\theta) \ . \tag{32b}$$

The former equation is identical in form to (3a), for which the eigenfunctions have been obtained and listed in (4). In this case, U is replaced by V_{co}. The latter is the Laplace equation, and in plane polar co-ordinates its solutions are

$$\psi_\ell = \frac{1}{R^\ell} \left(a_\ell \cos \ell\theta + b_\ell \sin \ell\theta\right) \quad , \quad \ell \in Z^+ \tag{33a}$$

and

$$\psi_0 = \text{constant} \ . \tag{33b}$$

Thus, the modal field can again be expanded in terms of basis functions, and then Fourier decomposition of the continuity condition will provide a matrix whose determinant will vanish at the required values, V_{co}.

§2.5.1 Cut-off and symmetry

As explained in §2.2.2, the waveguide, is symmetric about two orthogonal axes, which leads to four different symmetry patterns for ψ, corresponding to four different series expansions for ψ. In seeking the hierarchy of modal cut-offs, it is necessary to examine the solutions obtained from **all four** series. This is particularly important in determining the range of single mode operation of a waveguide.

In §P.2.4 and §P.2.5 it was explained how the first higher-modal cut-off frequency of a circular fibre corresponds to the modal cut-off

of two distinct modes -- the LP_{02}^E- and LP_{02}^O- modes -- on a non-circular fibre. Since, subsequently, interest is with the first higher-order mode's cut-off (On a simple step waveguide the fundamental mode is not cut-off.) and the waveguides are symmetric about two, orthogonal axes, the modal field expansions applicable to this analysis is provided. For these modes,

$$
\psi_c = \begin{cases} \displaystyle\sum_{n=0}^{\infty} \alpha_n J_{2n+1}\left(V_{co}R\right)\left\{\begin{matrix}\cos\\\sin\end{matrix}\right\}(2n+1)\theta & , \quad R<R_B(\theta) \quad (34a) \\[3ex] \displaystyle\sum_{n=0}^{\infty} \frac{\beta_n}{R^{2n+1}}\left\{\begin{matrix}\cos\\\sin\end{matrix}\right\}(2n+1)\theta & , \quad R>R_B(\theta), \quad (34b) \end{cases}
$$

where cosine and sine refer to the LP_{11}^E- and LP_{11}^O- modes, respectively.

§2.5.2 Matrix equations

At cut-off, the continuity of ψ_c and $\partial\psi_c/\partial R$ needs to be maintained. Thus,

$$
\sum_{n=0}^{\infty} \alpha_n J_{2n+1}\left(V_{co}R_B(\theta)\right)\left\{\begin{matrix}\cos\\\sin\end{matrix}\right\}(2n+1)\theta
$$

$$
= \sum_{n=0}^{\infty} \frac{\beta_n}{R_B(\theta)^{2n+1}}\left\{\begin{matrix}\cos\\\sin\end{matrix}\right\}(2n+1)\theta
$$

$$
\sum_{n=0}^{\infty} \alpha_n V_{co} J'_{2n+1}\left(V_{co}R_B(\theta)\right)\left\{\begin{matrix}\cos\\\sin\end{matrix}\right\}(2n+1)\theta
$$

$$
= -\sum_{n=0}^{\infty} \frac{(2n+1)\,\beta_n}{R_B^{2n+2}(\theta)}\left\{\begin{matrix}\cos\\\sin\end{matrix}\right\}(2n+1)\theta \;.
$$

These functions of $R_B(\theta)$ are expanded as Fourier series, which, within the symmetry assumptions, will have only even cosine harmonics. Matching of the coefficients of $\left\{\begin{matrix}\cos\\\sin\end{matrix}\right\}(2k+1)\theta$ again produces two simultaneous matrix equations, which can be solved using the direct sum, as explained in §2.2.4.

§2.6   Comment

Presented above is a method of solution for the general step profile fibre. It is analytic, in the sense that matrices, albeit infinite, are obtained and these describe the solution of the scalar wave equation. The analytic nature of the method permits special steps being taken to simplify numerical evaluation, notably when singularities occur.

Using these eigenfunctions reveals features of the modal field in a straightforward manner, the plane polar co-ordinates being natural co-ordinates for the system.

Finally, it is worth noting the little appreciated fact that for the step-profile fibre, any analytic solution of the scalar wave equation also provides an analytic solution of the full Maxwell equations. Then, the equation for the longitudinal component of both the electric and magnetic field vector, E_z and H_z, are given as the solutions of a partial differential equation, identical to the scalar wave equation, although the boundary conditions differ. From E_z and H_z, complete electric and magnetic fields can be derived.

§2.A   Appendix: Partial derivatives integrated by parts

LEMMA:

Suppose $I, \Omega \subset R$; $x,y : I \to \Omega$; $x,y \in C^1(I)$; $f : \Omega \to R$; $f \in C^1(\Omega)$; $g \in \Omega^2 \to R$; $g \in C^1(\Omega^2)$; and all the integrals exist, then

$$\int_I ds \ f\big(y(s)\big) \frac{\partial g}{\partial y}\big(x(s),y(s)\big)$$

$$= \frac{f\big(y(s)\big) \ g\big(x(s),y(s)\big)}{dy/ds} \bigg|_I - \int_I ds \ g\big(x(s),y(s)\big) \frac{df}{dy}\big(y(s)\big)$$

$$- \int_I ds \ \frac{f\big(y(s)\big)}{dy/ds} \frac{dx}{ds} \frac{\partial g}{\partial x}\big(x(s),y(s)\big) \ . \tag{35}$$

PROOF:

$$\frac{dg}{ds} = \frac{dy}{ds}\,\frac{\partial g}{\partial y} + \frac{dx}{ds}\,\frac{\partial g}{\partial x}$$

$$<=> \frac{\partial g}{\partial y} = \frac{1}{dy/ds}\,\frac{dg}{ds} - \frac{1}{dy/ds}\,\frac{dx}{ds}\,\frac{\partial g}{\partial x} \; ,$$

Substitute this result in the left-hand espression of (35), integrate by parts, and the lemma follows.

NOTES (i) If $x \notin C'(I)$, but $x \in C^0(I)$ and x is only piecewise continuously differentiable, then, if I is decomposed into segments J_j such that $x \in C^1(J_j)$, the lemma can be used on each J_j and the results added to recover (35), since integrals are unaffected if an integrand is discontinuous at only a finite number of points.

(ii) What happens if f misbehaves? In particular, suppose $f \notin C^0(I)$. Again, decompose I into segments K_j such that $f \in C'(K_j)$. Now apply the lemma to each segment.

$$\int_I ds\; f\big(y(s)\big)\,\frac{\partial g}{\partial y}\big(x(s),y(s)\big)$$

$$= \sum_{j=1}^{N}\int_{K_j} ds\; f\big(y(s)\big)\,\frac{\partial g}{\partial y}\big(x(s),y(s)\big)$$

$$= \sum_{j=1}^{N}\frac{f\big(y(s)\big)\,g\big(x(s),y(s)\big)}{dy/ds}\bigg|_{K_j} - \sum_{j=1}^{N}\int_{K_j} ds\;\big(g(s),y(s)\big)\,\frac{df}{dy}\big(y(s)\big)$$

$$- \sum_{j=1}^{N}\int_{K_j} ds\;\frac{f\big(y(s)\big)}{dy/ds}\,\frac{dx}{ds}\,\frac{\partial g}{\partial x}\big(x(s),y(s)\big)$$

$$= \frac{f\big(y(s)\big)\,g\big(x(s),y(s)\big)}{dy/ds}\bigg|_I - \int_I ds\; g\big(x(s),y(s)\big)\,\frac{df}{dy}\big(y(s)\big)$$

$$- \int_I ds\;\frac{f\big(y(s)\big)}{dy/ds}\,\frac{dx}{ds}\,\frac{\partial g}{\partial x}\big(x(s),y(s)\big)$$

$$- \sum_{j=1}^{N-1}\frac{g\big(x(s),y(s)\big)}{dy/ds}\,H(\alpha_j) \tag{36}$$

where $T=\{\alpha_1,\ldots\alpha_{N-1}\}$ divides I into the K_j's and

$$H(\alpha_j) = \lim_{h \to 0} [f'(y(\alpha_j + h)) - f(y(\alpha_j - h))]. \qquad (37)$$

(iii) If $y \equiv s$ and $I=\Omega$, then expressions (35) - (37) become much neater.

(iv) Suppose now that $I = [0,2\pi]$ and $f(s)$ and $g(x(s),s)$ are 2π-periodic functions. Also, suppose

$$f(s) = f(\pi - s) = f(\pi + s) = f(2\pi - s) \qquad (38)$$

everywhere, thus showing that

$$\alpha_j, \quad \pi - \alpha_j, \quad \pi + \alpha_j, \quad 2\pi - \alpha_j$$

are all in T. Symmetry condition (38) shows

$$H(\alpha_j) = -H(\pi - \alpha_j) = H(\pi + \alpha_j) = -H(2\pi - \alpha_j).$$

Thus, in this case, the symmetry simplifies (36) to

$$\int_0^{2\pi} ds \, f(s) \, \frac{\partial g}{\partial s}(x(s),s) = -\int_0^{2\pi} ds \, [f'(s) \, g(x(s),s) + f(s) \, x'(s) \, \frac{\partial g}{\partial s}(x(s),s)] \, .$$

THE THIRD CHAPTER

Step Elliptical Waveguides

At first Pooh and Rabbit and Piglet walked
together, and Tigger ran round them in circles,
and then, when the path got narrower, Rabbit,
Piglet and Pooh walked one after another, and
Tigger ran round them in oblongs, and by-and-by,
when the gorse got very prickly on each side of
the path, Tigger ran up and down in front of
them, and sometimes he bounced into Rabbit and
sometimes he didn't.

A.A. Milne, "The House at Pooh Corner"

In this chapter, exact results for an elliptical, step waveguide are

obtained, the accuracy of various known approximation methods is

examined, and other approximations are developed. Combining both the

limiting cases of the circular and the planar waveguides, a new

approximation method is exploited to provide very good estimates of

several quantities of interest.

§3.1 Background

The elliptical waveguide is a simple departure from a circular

fibre. Being one of the easiest non-axisymmetric waveguides to analyse,

it offers a good opportunity to understand such structures.

Classically the eccentricity, e, is used to describe the shape of

an ellipse. Considering figure 3.1(a), this is defined

$$e^2 = 1 - \rho_y^2 / \rho_x^2,$$

where ρ_x and ρ_y are the semimajor and semiminor axes, respectively. As

well as the eccentricity, the shape of an ellipse can be described by

the inverse aspect ratio, ε. This is

$$\varepsilon = \rho_y / \rho_x,$$

the ratio of the minor axis' length to that of the major axis. Clearly,

$$e^2 + \varepsilon^2 = 1.$$

Originally the elliptical dielectric waveguide was examined by Yeh (1962) who, utilizing elliptical co-ordinates, presented a full solution of the Maxwell equations. Subsequently (Yeh-Citerne, 1976) this was simplified to a solution of the weak guidance problem, and then further simplified to the solution for small eccentricities. Although elliptical co-ordinates define the core-cladding interface in terms of one co-ordinate, the description of the modes requires an infinite sum of the basis functions and the eigenvalues are obtained from the determinant of an infinite matrix. Consequently no obvious advantage is gained over the expansion in §2.2. On the other hand, the physical interpretation of elliptical co-ordinates is not as easy as the (R, θ) combination of the plane polar description.

Exact results for the propagation constants of an elliptical cross-section were obtained by Eyges et al (1978).

Perhaps the most appealing way to investigate the elliptical cross-section is to perturb the corresponding circularly cross-sectioned fibre (eg. see Adams, 1981, §7.2.5; Snyder & Love, 1983, §18.10). For slight ellipticity, $e < 1$ a series expansion in e can be constructed. Sammut et al (1981) derived such an expansion to order e^4 in examining birefringence, and later Sammut (1982b) calculated terms to order e^6 in assessing modal cut-off frequencies. With the advent of good computer algebra systems, this expansion technique, which, in principle, can be extended to an arbitrary order of accuracy, will become more versatile in investigating elliptical fibres.

For the elliptical waveguide, the Gaussian approximation for arbitrary eccentricity was obtained by Snyder & Love (§17.4).

Figure 3.1

(a) An elliptical cross section, showing the semimajor, ρ_x, and semiminor, ρ_y, axes.
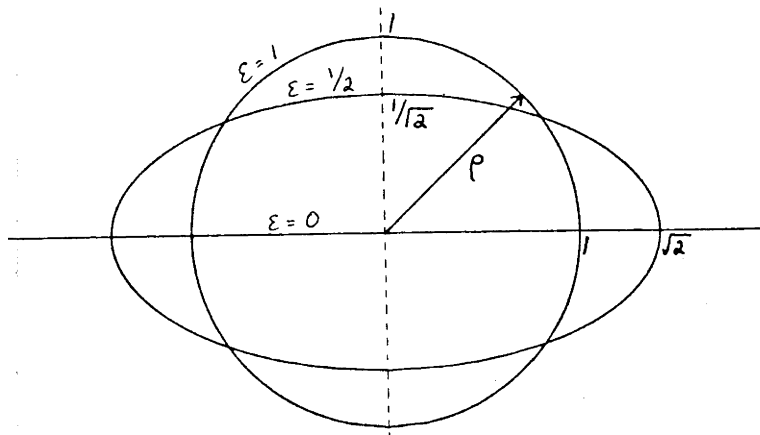
(b) The family of ellipses with an identical area. Lengths are scaled by the circle's radius, $\bar{\rho}$.
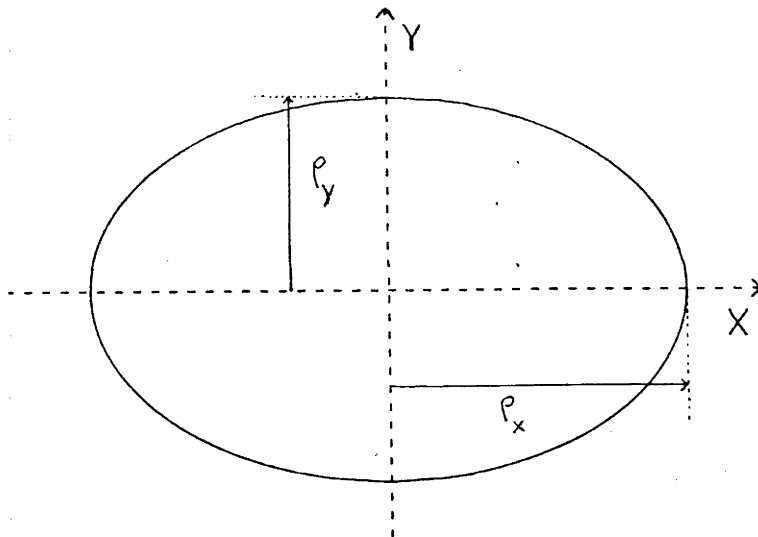
(c) The family of ellipses with an identical semiminor axis. Lengths are scaled with ρ_y.
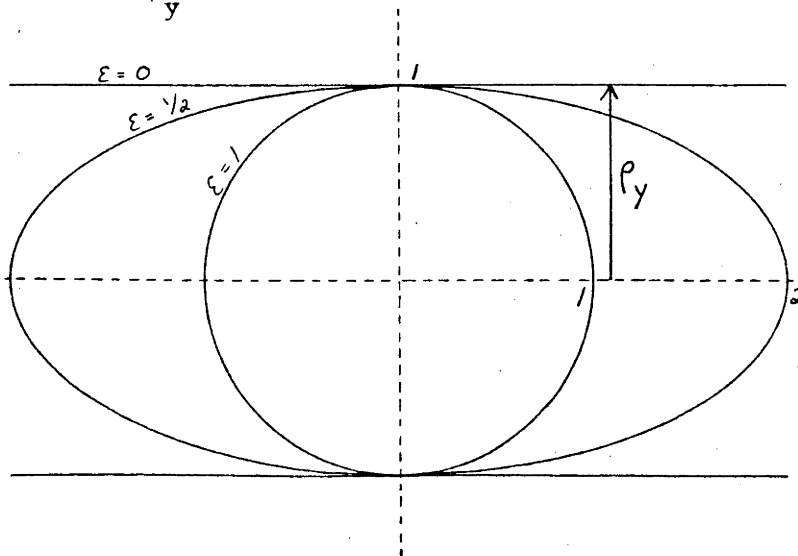
Kumar & Varshney (1984) defined an equivalent pseudo-rectangular waveguide which was perturbed to estimate the parameters of the elliptically cross-sectioned fibre.

§3.2 Families of ellipses

Naturally, there is considerable interest in how certain quantities vary as the aspect ratio of an ellipse varies. Thus, it is necessary to characterize families of ellipses. Alas, there is no standardization on how this is best achieved, and, as a result, some confusion has appeared in the literature.

Basically there are two families of ellipses, as illustrated in figure 3.1. In the first, all have the same area. As ε decreases from 1, the shape changes form circular to an infinitely close pair of parallel lines. These cross-sections describe fibres with identical profile volume or canonical frequency, $\bar{V}$, (P.4), where

$$\bar{V}^2 = k^2 n_{c\ell}^2 \, 2\Delta \, \rho_x \rho_y.$$

From (P.6) it follows that the canonical length is $\bar{\rho} = \sqrt{\rho_x \rho_y}$. Hence, the canonical propagation constant, $\bar{U}$, is defined by

$$\bar{U}^2 = \rho_x \rho_y \left(k^2 n_{co}^2 - \beta^2 \right)$$

where β is the customary modal propagation constant.

In the other family of ellipses, all possess the same semiminor axis, ρ_y. Here, as ε varies from 1 to 0, the cross-section changes from circular to a slab of finite thickness, $2\rho_y$. These waveguides are characterized by a constant value of V_y, defined by

$$V_y^2 = k^2 n_{c\ell}^2 \, \rho_y^2 \, 2\Delta,$$

a different prescription for normalized frequency. The normalized propagation constant is

$$U_y^2 = \rho_y^2 (k^2 n_{co}^2 - \beta^2).$$

As an example of this confusion between families, Sammut et al (1981) in their perturbation analysis, used the sequence of waveguides defined by V_y, whereas Snyder et al (1982), using a different perturbation method, examined the family defined by $\bar{V}$.

Most authors have employed the V_y description of ellipses. However, in this chapter, the family defined by the canonical frequency, $\bar{V}$, is examined. This is because these profiles of equal volume are expected to have guidance properties which are approximately equivalent (e.g. Hussey & Pask, 1981).

§3.3 Details of solution

The solution of the scalar wave equation, (P.3), for the elliptical step profile proceeds as outlined in §2.2. For such a cross-section, the boundary function is

$$R_B(\theta) = \frac{\rho_y}{\rho} \left(1 - e^2 \cos^2 \theta\right)^{-1/2} \tag{1}$$

where ρ is the length scale. In the numerical computations reported below, ρ_y was employed. In examining the results, the equal area family was assessed and, hence, $\bar{\rho}$ was utilized.

Estimated bounds on U were evaluated from the equal area circle (§2.7) and Gaussian approximation.

§3.3.1 Fourier coefficients

The decompositions required in (2.12) can be obtained analytically, by using Barnes' integral representatin for $K_n(z)$ (Watson, §6.5) and the series expansion in z for $J_n(z)$ (A & S, 9.1.10). These results require the evaluation of infinite series. For example, in (2.12c),

$$K_{2n}\left(WR_B(\theta)\right) = \sum_{m=0}^{\infty} \cos(2m\theta) \; b_{nm}$$

means

$$b_{mn} = \frac{2}{1+\delta_{m0}} \left(\frac{e^2}{2(2-e^2)}\right)^m \sum_{p=0}^{\infty} \left(\frac{e^2}{2(2-e^2)}\right)^{2p} \frac{(2p+m)!(n+2p+m-1)!}{p!(p+m)!}$$

$$\times \sum_{s=0}^{2p+m} \left(\frac{-Y}{2}\right)^s \frac{K_{2n+s}(Y)}{s!(n+s-1)!(2p+m-s)!}$$

where

$$Y^2 = \frac{2\,W^2}{1+\varepsilon^2}.$$

Consideration of this expression indicates that the determination of the Fourier decomposition using explicit formulae for the coefficients will, in general, be no more accurate than implementing the well refined, numerical, fast Fourier routines available on most computers. This latter method was utilized in obtaining subsequent results.

It was found that these numerical calculations introduced a relative error in the results of less than 10^{-6} and this was insignificant when compared with the error introduced by terminating the infinite determinant of M, defined by (2.15).

§3.3.2 Convergence and errors

To see details of this dominant form of error, table 3.1 shows the results obtained by truncating this matrix to various orders. As expected, the more axi-asymmetric the cross-section, the more components are required to achieve a nominated standard of accuracy. Calculations stopped at 20x20 because of the limitations of the available Bessel function routines.

Also, it is interesting that convergence improved for lower values of $\bar{V}$. This is to be expected, for as $\bar{V}$ becomes smaller, the field becomes more nearly circular and fewer components in the expansion (2.7) are needed to achieve the same level of accuracy. This improved behaviour at these low $\bar{V}$ differs from previous approximation and numerical techniques which have greater difficulty coping with a field that spreads further into the cladding, but is consistent with other exact expansions of ψ (Yeh, 1962; Eyges et al, 1979).

It is interesting to compare the rates of convergence, shown in table 3.1, with such indications as other authors provide of their success with truncated matrices. Table 1's in both Yeh (1962) and Rengarajan & Lewis (1980), who sought higher modal cut-offs rather than U, show the same trends as outlined above. However, both used a Mathieu function analysis. At $\epsilon=0.87$ and $\bar{V}=1.282$ (2.477), the former found 0.7% (0.8%) variation in $\bar{U}$ as the matrix' dimension increased from four to six. In a similar increase in the size of the determinant, the method of chapter 2 produced a variation in $\bar{U}$ of less than 0.1%. At $\epsilon=0.20$, a further increase by Yeh of the matrix to eight dimensional caused a 0.50% variation in $\bar{U}$ at $\bar{V}=0.822$. This stability might reflect the exceptionally low $\bar{V}$, or be a manifestation of the same trend as is

Table 3.1

Demonstration of the convergence of the propagation constants of the step elliptical waveguide as the order of the truncated matrix is increased.

$\bar{V}$	ε	dimension of matrix							
		6	8	10	12	14	16	18	20
2.8	0.90	1.7358	1.7358		1.7358	1.7358			
	0.80	1.7415	1.7416		1.7416	1.7416			
	0.70	1.7527	1.7528		1.7529	1.7529			
	0.60	1.7707	1.7717		1.7720	1.7720	1.7720		
	0.50		1.7990	1.8011	1.8020	1.8024	1.8025	1.8026	1.8026
	0.40		1.8129	1.7925	FAIL	1.8532	1.8506	1.8502	1.8501
	0.30			FAIL		1.9251	1.9157	1.9460	1.9286
	0.20			2.0209		FAIL	2.0758	2.0660	2.0602
2.4	0.90	1.6466	1.6466		1.6466				
	0.80	1.6511	1.6511		1.6511				
	0.70	1.6598	1.6599		1.6599	1.6599			
	0.60		1.6746		1.6749	1.6749	1.6749		
	0.50		1.6957	1.6975	1.6983	1.6986	1.6987	1.6987	1.6988
	0.40		1.7041	1.6896	FAIL	1.7391	1.7364	1.7359	1.7358
	0.30			FAIL		1.7948	1.7858	FAIL	1.7972
	0.20			1.8713		FAIL	1.9158	1.9064	1.9006
2.0	0.90		1.5291		1.5291				
	0.80		1.5322		1.5322				
	0.70		1.5384		1.5384	1.5384			
	0.60		1.5486		1.5489	1.5489	1.5489		
	0.50		1.5629	1.5869	1.5650	1.5652	1.5653	1.5654	1.5654
	0.40		1.5657	1.6158	FAIL	1.5945	1.5918	1.5911	1.5910
	0.30			FAIL		1.6328	1.6245	1.6591	1.6346
	0.20			1.6891		FAIL	1.7211	1.7127	1.7075
1.6	0.90		1.3675		1.3675				
	0.80		1.3692		1.3692				
	0.70		1.3727		1.3727	1.3727			
	0.60		1.3783		1.3785	1.3785	1.3785		
	0.50		1.3858	1.3868	1.3872	1.3875	1.3875	1.3875	1.3876
	0.40		1.3838	1.3761	1.4327	1.4049	1.4024	1.4018	1.4017
	0.30			1.4528	1.4341	1.4259	1.4191	1.4518	1.4276
	0.20			1.4669	FAIL	FAIL	1.4795	1.4731	1.4691

apparent in the work of Rengarajan & Lewis, where for $\varepsilon > 2/3$, the cut-off values are stable to three decimal places as the truncation moves from five to seven components.

The advantage of the Mathieu function analysis is, unquestionably, that the degree of ellipticity is absorbed into the Mathieu functions themselves, rather than requiring more terms in a series or, equivalently, bigger matrices. It is a question of whether the added complexity of computing Mathieu functions counteracts the increased computing resources needed to process the larger matrices. Ultimately, this choice depends upon the machine used.

There is no general analysis of the error introduced by truncating an infinite determinant. One must proceed operationally, by increasing the dimension, to find convergence.

§3.4   Fundamental mode propagation constants

The canonical propagation constant is plotted in figures 3.2 and 3.3.

The limiting value of $\bar{U}$, as $\varepsilon \to 0$, is evaluated readily. Given $\bar{V}$, the associated value

$$V_y = \bar{V}\sqrt{\varepsilon}$$

becomes small as $\varepsilon \to 0$. The cross-section approaches a planar waveguide of width $2\rho_y$ with normalized propagation constant U_y. For an infinitely thin slab, as $V_y \to 0$, $U_y \to V_y$. The identity

$$\bar{U} = U_y/\sqrt{\varepsilon} \;\to\; V_y/\sqrt{\varepsilon} = \bar{V}$$

summarizes the argument.

Figure 3.2

For the elliptical, step fibre, the fundamental mode's canonical propagation constant, $\bar{U}$, as a function of canonical frequency, $\bar{V}$. Crosses indicate results taken from Kumar & Varshney (1984).
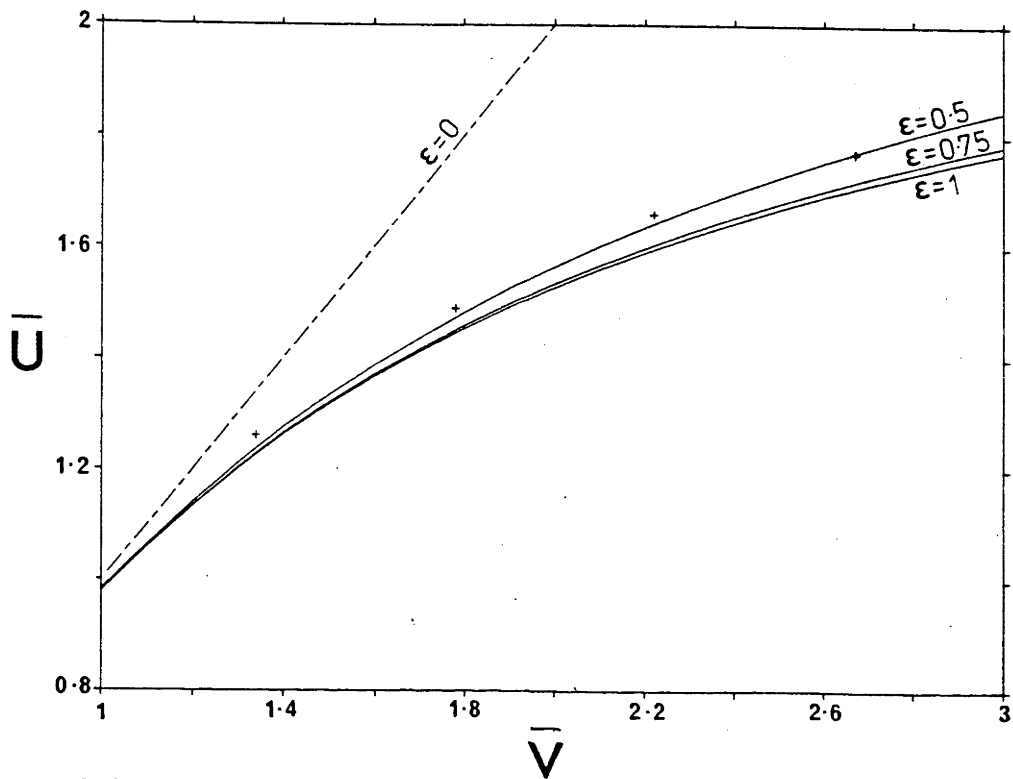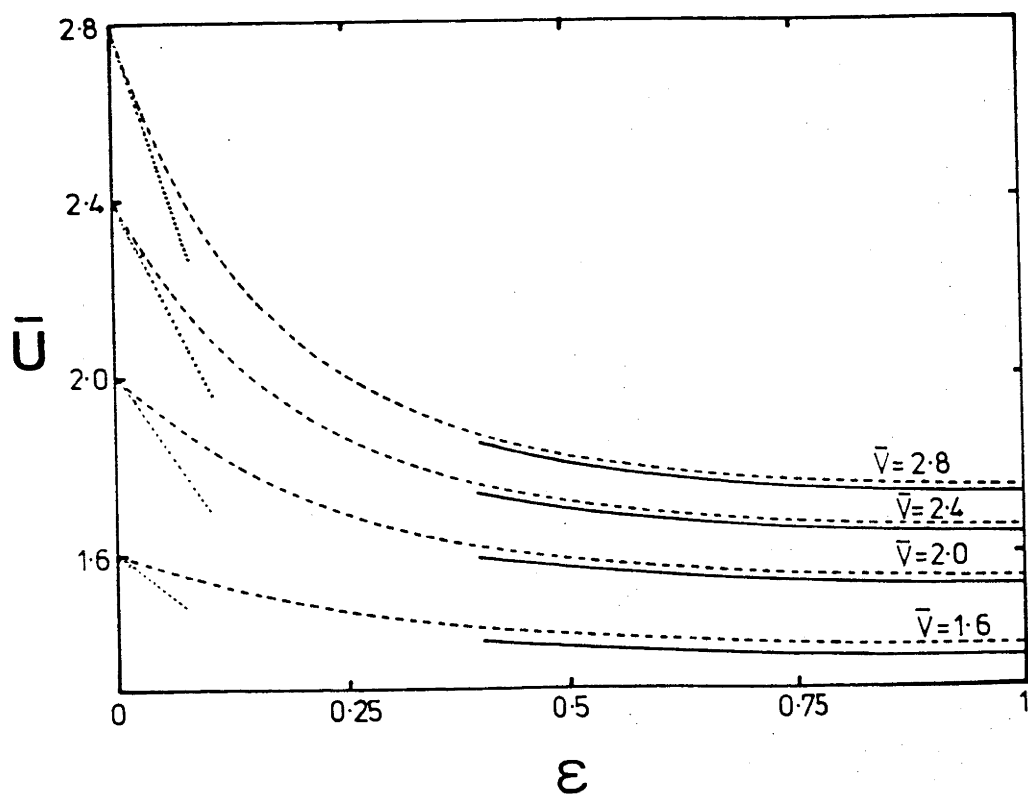

Figure 3.3

For the elliptical, step fibre, the fundamental mode's canonical propagation constant, $\bar{U}$, as a function of the inverse aspect ratio, ε, are shown as solid curves. The broken curves are the Gaussian approximation. The dotted curves are the linear form (2).

To obtain the variation of $\bar{U}$ with ε, as $\varepsilon \to 0$ and $\bar{V}$ is fixed, the
infinitely thin slab is perturbed (refer §3.A.2). The result is

$$\bar{U} \sim \bar{V} - \varepsilon \bar{V}^3 \left(\frac{\pi-2}{4}\right), \qquad (2)$$

which is linear in ε. This is shown as the dotted portions in figure
3.3.

§3.4.1 Comments on approximations

Figure 3.3 shows how slowly $\bar{U}$ varies as ε decreases from 1.
For $\bar{V}=2.8$, ε decreases to 0.7 before $\bar{U}$ has increased by 1% ;
for $\bar{V}=1.6$, ε decreases to 0.6 before the same increase in $\bar{U}$ occurs.
That the circular profile with equal area is an accurate approximation
in this region is not surprising. Sammut et al (1981) showed that the
first order correction to $\bar{U}$, which is of order e^2, vanishes.

An indication of the utility of the Gaussian approxiation is also
provided by figure 3.3. A detailed analysis of the error is tabulated
in table 3.2(a). The trend of decreasing accuracy with decreasing $\bar{V}$ is
as anticipated in §1.3. A significant disadvantage with the Gaussian
approximation is its inability to reproduce the correct value
at $\varepsilon=1$, the circular limit. Another problem is that it does not provide
a simple, explicit formula for $\bar{U}(\bar{V}, \varepsilon)$.

Results obtained by Kumar & Varshney (1984), who utilized an
equivalent pseudo-rectangular mode, are shown in figure 3.2. This
approximation is seen to be accurate at larger values of $\bar{V}$.

§3.4.2 New approximation

In this section, a new, semi-empirical, explicit approximate
formula for $\bar{U}(\bar{V}, \varepsilon)$ is developed. This is found to be exceptionally

Figure 3.4

An indication of the accuracy of the approximation developed in §3.4.2. The circles are exact results; the solid curve is the hyperbolic approximation (3) and (4) with the best value of σ; the dotted curves are the limiting forms (6) and (7); the broken curve is the Gaussian approximation.
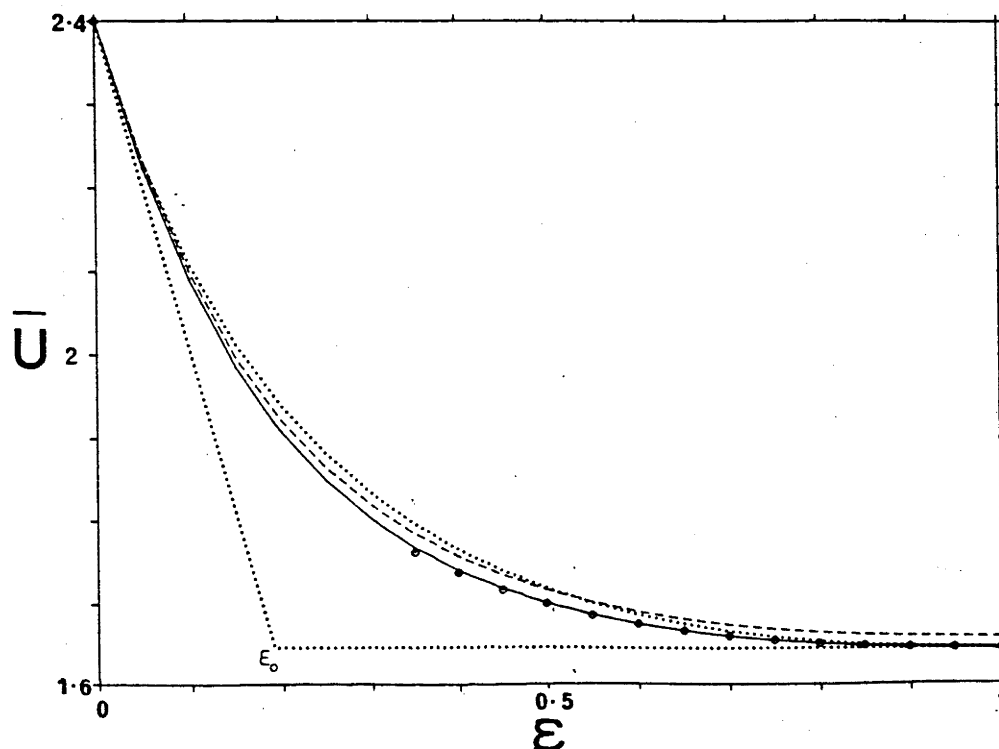
Table 3.2

(a) The percentage relative error of the Gaussian approximation for canonical propagation constants.

(b) The percentage relative error of the hyperbolic approximation, (3) and (4), for the canonical propagation constants.

(a)

$\bar{v}$ \ ε	1.00	0.75	0.50	0.35
1.6	1.9%	1.9%	2.1%	2.4%
2.0	1.1%	1.1%	1.4%	1.7%
2.4	0.8%	0.8%	1.0%	1.3%
2.8	0.9%	0.9%	0.9%	1.0%

(b)

$\bar{v}$ \ ε	0.75	0.50	0.35
1.6	-0.015%	-0.09%	-0.07%
2.0	0.007%	0.006%	0.37%
2.4	0.000%	0.06%	0.3%
2.8	-0.03%	-0.09%	0.11%

accurate over practical values of $\bar{V}$ and all values of ε. The form of

the curves in figure 3.3 motivates the approximation. For a

fixed $\bar{V}$, each curve has two nearly linear sections near $\varepsilon=0$ and $\varepsilon=1$,

connected by a tightly curved arc. This behaviour is reminiscent of a

hyperbola. In general such a curve is defined by five constants and has

the general Cartesian form

$$ax^2 - by^2 + 2cxy + dx + ey + 1 = 0,$$

where $a>0$ and $b<0$, or, equivalently.

$$y = px + q \pm \sqrt{rx^2 + sx + t}\ .$$

Thus, it is proposed that $\bar{U}(\varepsilon)$, defined on $[0,1]$, is of this form, and

the constants need to be determined.

Firstly, at the end $\varepsilon=1$, the waveguide's cross-section is circular

which provides an easily calculated value:

$$\bar{U}(1) = U_0,$$

where U_0 is the propagation constant, well approximated by the Rudolph-

Neumann formula or available from tables (e.g., Snyder & Love, p.317 or

table 14-4 respectively). Further, as $\varepsilon\to1$ (i.e. $e\to0$), the correction of

order $(\varepsilon-1)$ (i.e. e^2) to $\bar{U}$, vanishes. Thus,

$$\bar{U}'(1) = 0.$$

At the other end of $[0,1]$, the limit is given in (2):

$$\bar{U}(0) = \bar{V}$$

and

$$\bar{U}'(0) = -\bar{V}^3(\pi-2)/4 \equiv G,$$

defining G.

Combining these four conditions, only one constant remains unfixed in the suggested hyperbolic approximation. Writing the undetermined constant as σ, the prescription for $\bar{U}$ is

$$\bar{U} = q - p\varepsilon + \left(r + s\varepsilon + t\varepsilon^2\right)^{1/2}, \tag{3}$$

where

$$q = U_0 - \frac{G}{2\varepsilon}(\sigma - \varepsilon_0^2), \tag{4a}$$

$$p = \frac{G}{2\tau}(\sigma + \tau), \tag{4b}$$

$$r = \frac{G^2}{4\varepsilon_0^2}(\sigma + \varepsilon_0^2)^2, \tag{4c}$$

$$s = \frac{G^2}{4\varepsilon_0\tau}(\sigma + \varepsilon_0^2)(\sigma - \tau), \tag{4d}$$

$$t = \frac{G^2}{4\tau^2}(\sigma + \tau)\left(\sigma + \frac{\tau^2}{\varepsilon_0^2}\right), \tag{4e}$$

$$\tau = \varepsilon_0^2/(1 - 2\varepsilon_0) \tag{4f}$$

and

$$\varepsilon_0 = \frac{\bar{V} - U_0}{G}. \tag{5}$$

The value of ε_0 is significant, being the transition point in the piecewise linear approximation, as shown in figure 3.4.

So long as σ is positive, it remains arbitrary, and the above system (3) and (4) defines a family of hyperbolae. If $\sigma=0$,

$$\bar{U} = \begin{cases} \bar{V} - G\varepsilon, & \varepsilon \leqslant \varepsilon_0 \\ U_0, & \varepsilon \geqslant \varepsilon_0, \end{cases} \tag{6}$$

which is the piecewise linear curve; the limit $\sigma \to \infty$,

$$\overline{U} = U_0 + \frac{(\overline{V} - U_0)(1 - \varepsilon)^2 \tau}{\tau + \varepsilon\varepsilon_0} \,. \tag{7}$$

These two cases are shown by the dotted curves in figure 3.4, and provide bounds on the true values of $\overline{U}$.

If the value

$$\sigma = (0.3754) \exp\left(-(0.6855)\overline{V}\right)$$

is assumed, the relative error in using the hyperbolic approximation is less than 0.5% over the range of practical values of ε and $\overline{V}$. A selection of the errors is shown in table 3.2(b). In figure 3.4, the exact results are shown as circles, superimposed on the hyperbolic approximation, the solid curve.

It is apparent that this hyperbolic approximation is excellent, and overcomes the shortfalls of the Gaussian approximation. In particular, it provides a **simple explicit expression** for $\overline{U}$ in terms of $\overline{V}$, ε and U_0, the normalized propagation constant of the equivalent circular waveguide.

§3.5 Behaviour of field

The co-efficients α_n and β_n from expansion (2.7) were examined for $e \ll 1$ or, equivalently, $(1-\varepsilon) < 1$, and agreed with the field expansion obtained using a perturbation method (e.g., Snyder et al, 1982).

Another known limit for the modal field of an elliptical waveguide is that as $\overline{V} \to \infty$. Here the solution of the metallic waveguide (Chu, 1938) is recovered. A calculation of α_n and β_n under this condition is awkward.

§3.5.1 Slab limit

From expansion (2.7a), it is interesting to obtain the field of a planar waveguide's core. If the series representation of $J_{2n}(z)$ (A&S, 9.1.10) is substituted, then, after re-ordering the sum,

$$\psi = \sum_{p=0}^{\infty} \left(\frac{-U^2 R^2}{4}\right)^p \sum_{n=0}^{p} \frac{(-1)^n \alpha_n}{(p+n)!(p-n)!} \cos 2n\theta.$$

In particular, for $\theta=0$ or $\theta=\pi$ — along the X-axis —

$$\psi = \sum_{p=0}^{\infty} \left(\frac{-U^2 R^2}{4}\right)^p \sum_{n=0}^{\infty} \frac{(-1)^n \alpha_n}{(p+n)!(p-n)!} . \tag{8}$$

As the elliptical cross-section becomes increasingly eccentric, the variation of ψ along the X-axis becomes negligible. Thus, from (8), the coefficient of each higher power of R must vanish independently. This condition produces recurrence relations for the set $\{\alpha_n\}$, and, using induction, an explicit solution for α_n/α_0 can be found. Notably, $\forall\, p \geqslant 1$,

$$\frac{\alpha_p}{\alpha_0} = (2p)!(-1)^{p+1} \sum_{n=0}^{p-1} \frac{(-1)^n (\alpha_n/\alpha_0)}{(p-n)!(p+n)!} ,$$

which yields the solution

$$\alpha_p = 2\alpha_0. \tag{9}$$

Returning this to (2.7a), the field of the limiting slab is,

$$\psi = \alpha_0 \sum_{n=0}^{\infty} \left(2-\delta_{n0}\right) J_{2n}(UR) \cos(2n\theta)$$

$$= \alpha_0 \sum_{n=0}^{\infty} \left(2-\delta_{n0}\right)(-1)^n J_{2n}(UR) \cos 2n\left(\frac{\pi}{2}\right)$$

$$= \alpha_0 \cos(UY),$$

as one intuitively expects. In obtaining this form, use was made of a generating function for $J_n(z)$ (A&S, 9.1.44) and polar co-ordinates changed to Cartesians. This formalism is not restricted to the fundamental mode, but applies to any mode with the same symmetry property for ψ.

Thus, the modal field pattern of a slab waveguide in its core is obtained as the limiting form of the field within the core of a highly eccentric elliptical guide. Unfortunately, a corresponding result in the cladding is not possible. As $R \to \infty$, even a thin ellipse is seen as a finite cross-section and hence the field cannot match that of a slab. However, close to the core-cladding interface in the middle of the long sides, ψ ought to be like the field of a planar waveguide.

For modes exhibiting different symmetry, ie. described by a different circular harmonic expansion, other generating functions and assumed forms of ψ along the X-axis of the cross-section, produce different limiting forms of ψ in the core. These always correspond to a definite modal pattern of the core of a planar waveguide.

§3.5.2 Numerical bounds

The true utility of this analysis is in (9). If it is assumed that, $\forall\, p \geqslant 1$,

$$0 \leqslant \alpha_p \leqslant 2\alpha_0,$$

then bounds exist on the coefficients. A **qualitative** indication of the behaviour of α_n as $\varepsilon \to 0$ is shown in figure 3.5. Why these bounds are useful is seen from the manner in which $\{\alpha_n\}$ is obtained. In §2.2.4, these are the components of an eigenvector of an infinite matrix. Truncation of this matrix, together with the inevitable numerical errors
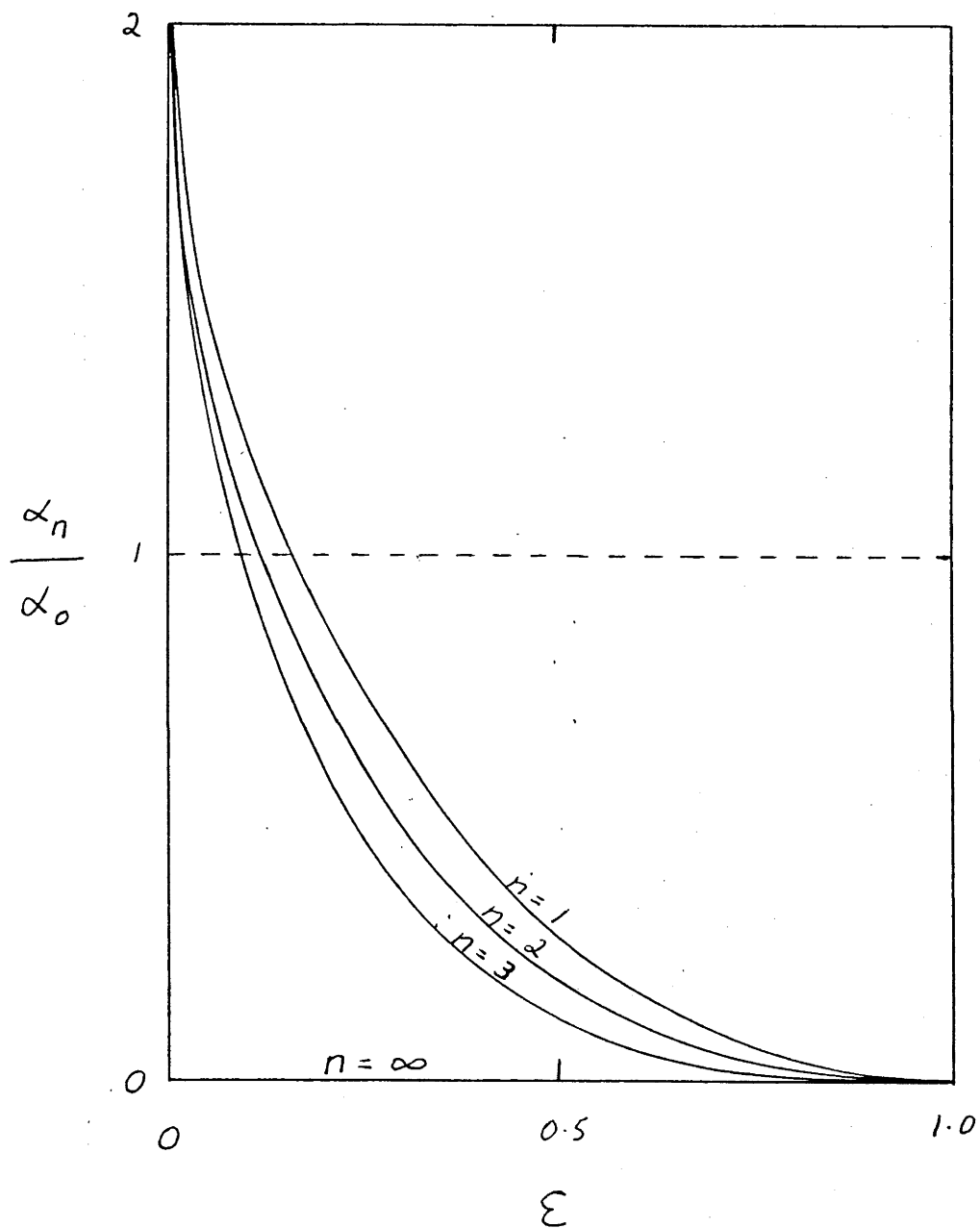
Figure 3.5

A qualitative indication of the behaviour of the field expansion coefficients, α_n, as the aspect ratio of the elliptical cross-section changes.

introduced by computer solution of matrix equations, means that the higher-order components of α_n will be inaccurate. By assuming

$$2\alpha_0 \geqslant \alpha_1 \geqslant \alpha_2 \geqslant \alpha_3 \geqslant \ldots ,$$

a test exists for which components can be retained as reliable. Typically, the sequence becomes monotonic, increasing half way to the truncation dimension of the matrix.

§3.6   Petermann spot-size

To obtain an estimate on the way in which a field behaves, various definitions of spot-size are available. The simplest is to fit a Gaussian function. This is particularly useful in determining jointing – off-set and tilting – losses. Sarkar et al (1984) used the Gaussian field defined by Snyder (1981) to derive such losses for an elliptical, step profile.

An alternative approach to field behaviour is to assess the way in which it spreads out. This, in particular, influences the losses caused by bending. Petermann (1976, 1977) related a root-mean-square (RMS) evaluation of ψ to the microbending loss. Intuitively, an RMS evaluation of the field ought to provide a good indication of the way power is distributed.

For any axi-asymmetric profile, an obvious generalization of the spot-size for circular fibres, is to define the angularly dependent $R_s(\theta)$:

$$\rho^2 R_s^2(\theta) = \rho^2 \frac{\int_0^\infty \psi^2(R,\theta) R^3 dR}{\int_0^\infty \psi^2(R,\theta) R dR} , \tag{10}$$

where ρ is the chosen length scale, making R_s dimensionless. Retaining

the angular dependence, $R_s(\theta)$ provides an indication of both how the

field is distributed for a given angle, and how this varies with θ. For

example, if ψ is defined by a Gaussian function

$$\psi_G = \exp\left(\frac{-1}{2}\left(\frac{X^2}{A_X^2} + \frac{Y^2}{A_Y^2}\right)\right),$$

then

$$R_s^2(\theta) = \frac{2\,A_X^2\,A_Y^2}{(A_Y^2+A_X^2)\left(1 - \left(\frac{A_X^2-A_Y^2}{A_X^2+A_Y^2}\right)\cos 2\theta\right)}.$$

This elliptical contour represents the position at which the modal

intensity, ψ^2, is $1/e$ of its maximum value, which occurs at $R=0$.

In general, if the contours of constant ψ form a pattern of

concentric ellipses, then $R_s(\theta)$ is an ellipse. For a step fibre, these

contours were shown in §2.3 to vary from elliptical near the core, to

circular as $R \to \infty$. Nevertheless, for an elliptical cross-section, it is

suggested that $R_s(\theta)$ defines an ellipse:

$$R_s^2(\theta) = \frac{2L^2}{(1+\varepsilon_s^2) - (1-\varepsilon_s^2)\cos 2\theta} \tag{11}$$

where L is the scaled, semiminor-axis and ε_s the inverse aspect ratio of

this ellipse.

§3.6.1 Spot-size for elliptical step fibre

Using direct substitution of the modal fields into (10),

computation of spot-sizes for an elliptical step fibre shows that $R_s(\theta)$

is, indeed, nearly elliptical. At worst there is a 2% variation from an

elliptical shape, and this occurs for combinations of $\bar{V}$ and ε for which ψ spreads significantly into the cladding.

The behaviour of the spot-size is represented pictorially in figure 3.6. As either $\bar{V}$ decreases or ε decreases, power moves into the cladding. The interesting feature is the insensitivity to the core's shape; when the core's inverse aspect ratio is 0.5, the field's is 0.85. As $\bar{V}$ decreases, the field not only spreads out, but becomes more circular. As $\bar{V} \to \infty$, the spot will conform more to the shape of the core. This slow variation is better seen in figure 3.8, where the ratio of $R_s(\pi/2)$ to $R_s(0)$ is plotted. $R_s(\pi/2)$ is shown in figure 3.7.

§3.6.2 Approximation for the spot-size

Direct calculation of spot-sizes is cumbersome. It is preferable to have a reasonably accurate expression which gives a usable spot-size as a simple function of characteristic parameters of the fibre. The elliptical profile is characterized by $\bar{V}$ and ε. Thus, approximate, explicit functions $L^2(\bar{V}, \varepsilon)$ and $\varepsilon_s(\bar{V}, \varepsilon)$ are sought, since L and ε_s give R_s via (11).

To determine these functions, there are several pieces of information available. Firstly, for the circular, step fibre, the Petermann spot-size (Gambling & Matsumura, 1977) is

$$R_0^2(\bar{V}) = \frac{2}{3} \left(\frac{1}{\chi} + \frac{1}{2} + \frac{1}{W_0^2} - \frac{1}{U_0^2} \right)$$

where

$$\chi = \frac{U_0 J_1(U_0)}{J_0(U_0)}$$

and U_0 and W_0 are the propagation constants of the circular waveguide with normalized frequency $\bar{V}$. Thus,

Figure 3.6
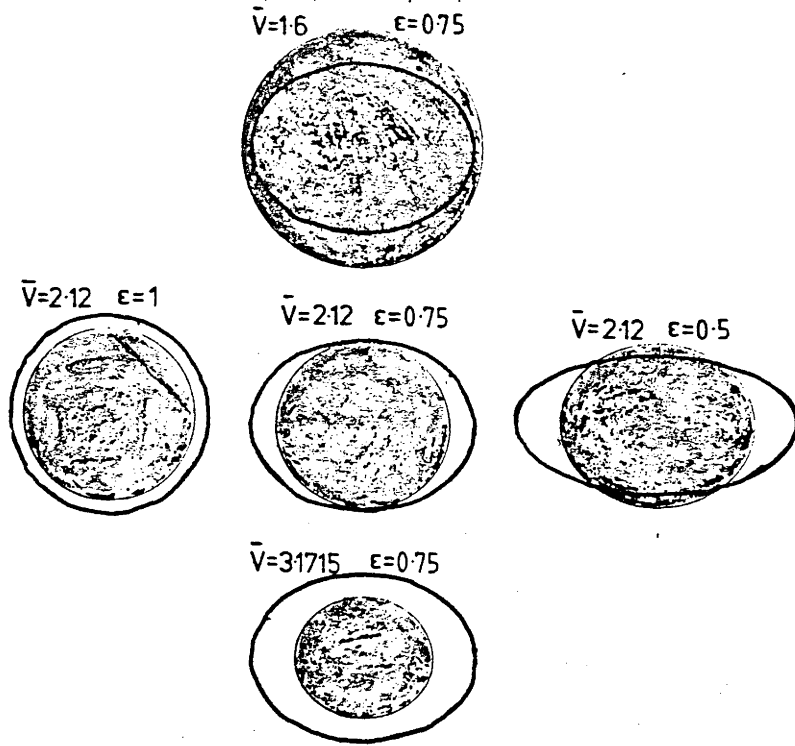
The extent of the fundamental modal field intensity, ψ^2, as indicated by the Petermann spot-size, (10).
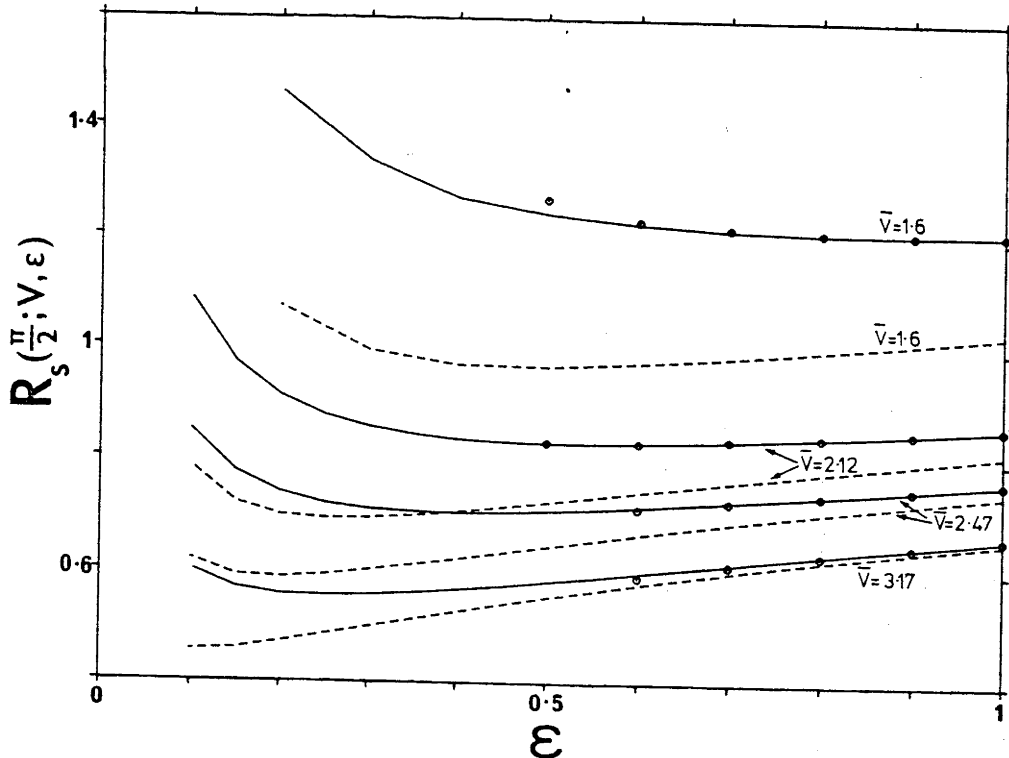
Figure 3.7

The variation in the extent of the spot-size along the Y-axis as the inverse aspect ratio changes. The circles indicate exact results; solid curves correspond to the approximation (21); broken curves are obtained from the Gaussian approximation.

Figure 3.8

The shape of the Petermann spot as measured by an inverse aspect ratio. Exact results are shown ━━━━ ; the Gaussian approximation is shown ‒ ‒ ‒ ‒ ; the approximation developed in §3.6.2 is shown ━ ‒ ━ ‒ .
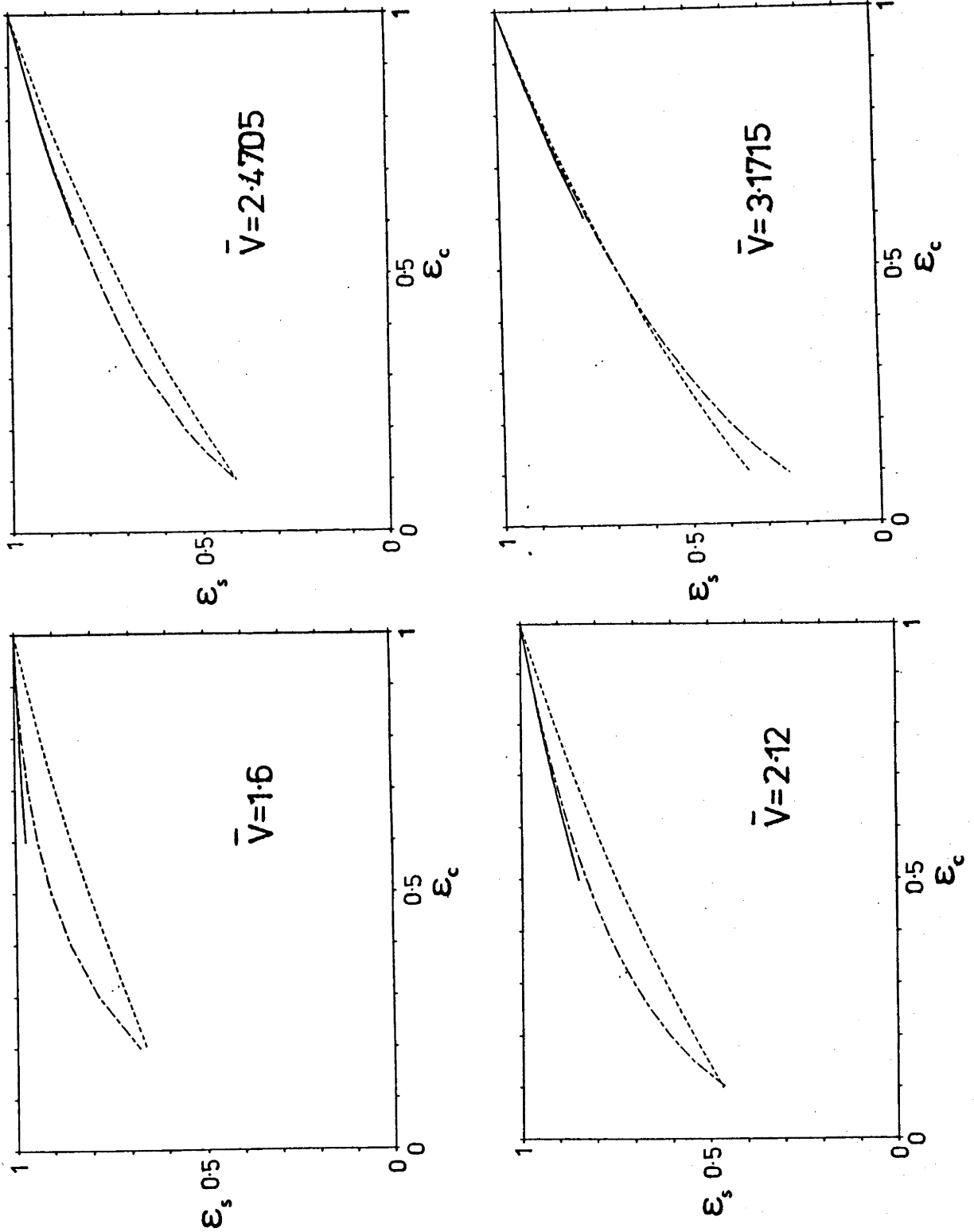
$$L^2(\bar{V},1) = R_0^2(\bar{V}) \tag{12}$$

and

$$\varepsilon_s(\bar{V},1) = 1. \tag{13}$$

Also, as $\varepsilon \to 0$, the waveguide becomes increasingly like a planar guide. In this case (refer §3.A.3)

$$R_s^2(\theta,\bar{V},\varepsilon) \sim \frac{3}{2\varepsilon\bar{V}^4 \sin^2\theta} \, ,$$

which indicates that

$$\varepsilon_s(\bar{V},0) = 0, \tag{14}$$

the result intuitively expected, and

$$L^2(\bar{V},\varepsilon) \sim 3/(2\varepsilon\bar{V}^4). \tag{15}$$

This means that the strongest singularity of L^2 is a simple pole at $\varepsilon=0$.

Since ε is always in $[0,1]$, and has no other points of singularity, it is appealing to seek L^2 of the form

$$L^2(\bar{V},\varepsilon) = \frac{C(\bar{V})}{\varepsilon} + \sum_{j=0}^{\infty} A_j(\bar{V}) \, \varepsilon^j. \tag{16}$$

Consideration of (15) immediately shows

$$C(\bar{V}) = 3/(2\bar{V}^4). \tag{17}$$

Similarly, (12) produces

$$\sum_{j=0}^{\infty} A_j(\bar{V}) = R_0^2(\bar{V}) - C(\bar{V}). \tag{18}$$

This is one condition to determine an infinite number of quantities, the functions $A_j(\bar{V})$. Because ε is restricted to $[0,1]$, the series can be truncated without too much error being produced. The dominant dependence in this interval is on the $1/\varepsilon$ and constant terms.

If only A_0 and A_1 are retained, another condition must be determined. Snyder et al (1982) gave ψ for a slightly elliptical step fibre. Hence, both the conditions used to fix A_0 and A_1 can be calculated from the behaviour near $\varepsilon=1$, the end of the interval where trouble with the series in (16) is more likely to occur. Using ψ and redefining the shape dependence to be the small parameter

$$\zeta = 1 - \varepsilon,$$

produces

$$R_s^2(\theta,\bar{V},1-\zeta) = R_0^2(\bar{V})\left(1 + \zeta 2G(\bar{V})\cos 2\theta\right) \tag{19a}$$

where

$$G(\bar{V}) = \frac{U_0^2 W_0^2}{6\chi R_0^2}\left[\frac{8}{U^2 W^2} + \frac{3}{\chi}\left(\frac{1}{U_0^2} - \frac{1}{W_0^2}\right) - \frac{2}{\chi^2}\left(\frac{1}{U_0^2} - \frac{1}{W_0^2} + \frac{1 - \frac{2}{U_0^2} + \frac{2}{W_0^2}}{\bar{V}^2 J_0^2(U_0)}\right)\right.$$

$$+ \frac{1}{\chi^3}\left(3 - \frac{2}{U_0^2} + \frac{2}{W_0^2} - \frac{6 + W_0^2 - 2\frac{W_0^2}{U_0^2}}{\bar{V}^2 J_0^2(U_0)}\right)$$

$$\left.+ \frac{2}{\chi^4}\left(1 - \frac{W_0^2}{\bar{V}^2 J_0^2(U_0)}\right)\right] \tag{19b}$$

where U_0 and W_0 are the propagation constants of the circular fibre. Examination of (11) indicates

$$L^2(\bar{V},\varepsilon) = R_s^2(\frac{\pi}{2},\bar{V},\varepsilon). \tag{20}$$

Suppose ζ, rather than ε, is used in (16), and only A_0 and A_1 are retained. Recalling (19) and (20), (14) is satisfied, and

$$-A_1 = -C - 2GR_0^2,$$

which is a second equation for A_0 and A_1. Thus, an approximation for L is

$$L^2 = \frac{3}{2\bar{V}^4 \varepsilon} + \left(R_0^2 - \frac{3}{\bar{V}^4} - 2GR_0^2\right) + \left(\frac{3}{2\bar{V}^4} + 2GR_0^2\right)\varepsilon. \qquad (21)$$

Using this as an approximation in (20) produces the curves shown in figure 3.7.

To find an expression for $\varepsilon_s(\bar{V}, \varepsilon)$, observe that an ellipse satisfies

$$\varepsilon_s^2 = \frac{2R_s^2(\pi/2)}{R_s^2(\pi/4)} - 1,$$

where $R_s^2(\pi/2)$ has been approximated already. An analogous method gives $R_s^2(\pi/4)$ and

$$\varepsilon_s^2(\bar{V}, \varepsilon) = \frac{\varepsilon R_0^2(\bar{V})\left(1 - G(\bar{V})(1-\varepsilon)\right)}{R_0^2(\bar{V})\varepsilon + 2C(1-\varepsilon)}.$$

For this definition to be meaningful, it is necessary that

$$/ > 4G(\bar{V})(1-\varepsilon),$$

which has not been proven, but extensively tested numerically. This approximation for ε_s is plotted in figure 3.8.

§3.6.3 Accuracy of approximation

Figures 3.7 and 3.8 indicate the accuracy of the above approximations. The dotted curves correspond to the Gaussian approximation.

For an improved approximation, more terms could be retained from (16). If the perturbation of the circular fibre proceeded to another term, there would be a further term in (19), corresponding to the retention of A_2. The form for L would see the point at which the "rising" occurs, move closer to $\varepsilon=0$. The $\varepsilon=1$ end requires higher-order terms to retain relative accuracy; the singularity at $\varepsilon=0$ dramatically swamps other effects.

This method of expressing parametric variation in ε by simple functions could be extended to other quantities of interest. It is stressed that (21) is not a Taylor series, the coefficients of the orders of ε are found from **both** ends of the interval, not just one. The ease with which slab limits are evaluated for constant $\bar{V}$ shows, once again, the value of the equal area families.

§3.7 Birefringence

§3.7.1 Exact results

Using the condition on the components of the field explained in §3.5.2, the birefringence of the elliptical, step fibre was calculated. Using the boundary function (1) in (2.31), it follows that, for the ellipse,

$$E_{nm}(\theta) = 2(\cos 2\theta - \eta) + UR_B \left(\frac{J_{2m}'(UR_B)}{J_{2m}(UR_B)} + \frac{J_{2n}'(UR_B)}{J_{2n}(UR_B)} \right)((1+\eta)\cos 2\theta - 2\eta)^2,$$

$$(22a)$$

where

$$\eta = \frac{e^2}{2 - \epsilon^2} = \frac{1 - \epsilon^2}{1 + \epsilon^2} \, ,$$

giving

$$B_p = \frac{4}{V \, \| \psi \|^2} \sum_{n=0}^{\infty} \sum_{m=0}^{n} (2 - \delta_{nm}) \alpha_n \alpha_m \int_0^{\pi/2} d\theta \frac{\cos(2n\theta)\cos(2m\theta)}{(1 - \eta \cos 2\theta)^2} J_{2n}(UR_B) J_{2m}(UR_B) E_{nm}(\theta).$$

$$(22b)$$

Computing B_p produced the solid curves shown in figure 3.9.

As ϵ decreases, the peak value of B_p increases and the value of $\bar{V}$ for

which this is attained increases.

Also shown in figure 3.9 are values taken from the curves of Dyott

et al (1979). It is curious that these agree with the computed values

for moderate eccentricity, but as the aspect ratio declines - notably

at $\epsilon = 0.5$ - the sets of values diverge. The source of this discrepency

could be in one of two places. The field truncation mentioned above may

retain too few components. Typically, for analysis involving matrices

which were 10x10, up to α_3 or α_4 were used. It can be seen from figure

3.9 that no dramatic change in the form of the curves exists to indicate

the shift form 4 to 5 field components.

The other possibility is an error in the calcultions of Dyott et

al. They claimed to employ the full vector solution of the Maxwell

equations (Yeh, 1962). This means that the propagation constants for

the two polarizaion states were independently obtained. The analysis of

§2.4 assumes the weak guidance formalism. However, it is surprising if

the two methods give such significantly different answers. When Cozens

& Dyott (- Citerne) (1979) evaluated the higher modal cut-off

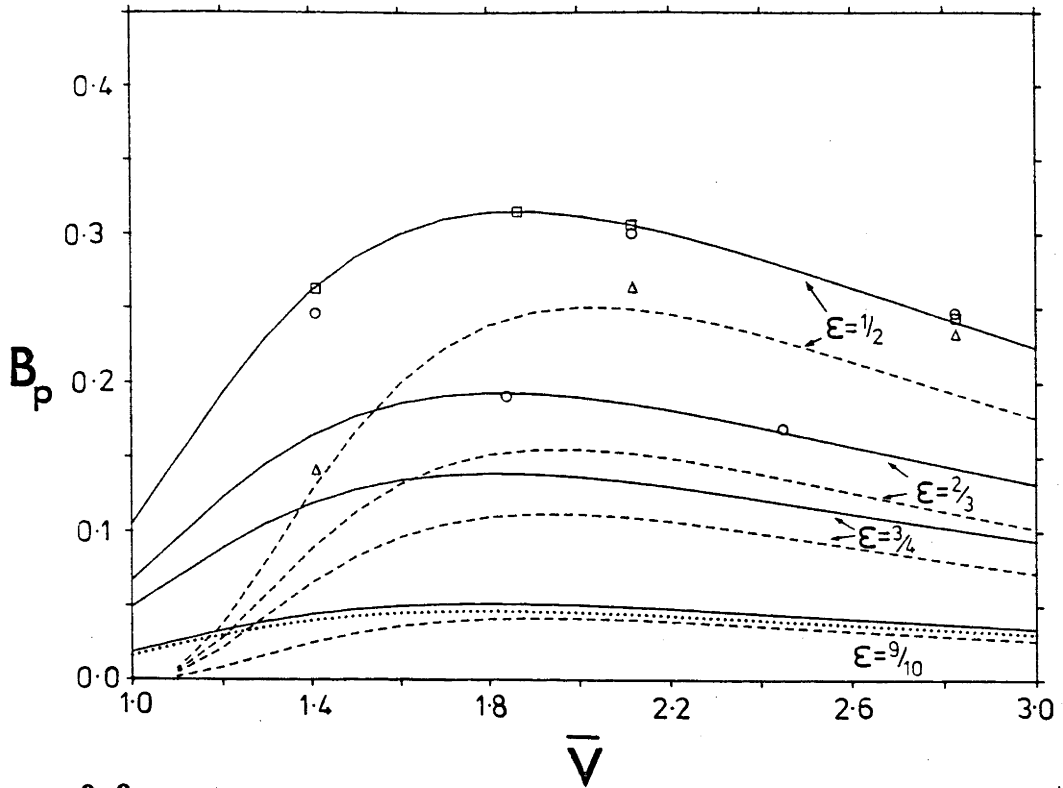frequencies, they erred in employing the assumptions of Yeh (- Citerne)

Figure 3.9

For the elliptical step fibre, normalized birefringence, B_p, as a function of canonical frequency, $\bar{V}$. The solid curves are exact results; the broken curves are Gaussian approximations; the dotted curve is obtained from the e^2 perturbation (Snyder & Love, 1983, (18-25)). o are taken from Dyott et al (1979); are taken from Kumar & Varshney (1984); Δ are obtained from a series correct to e^4 (Sammut et al, 1981).
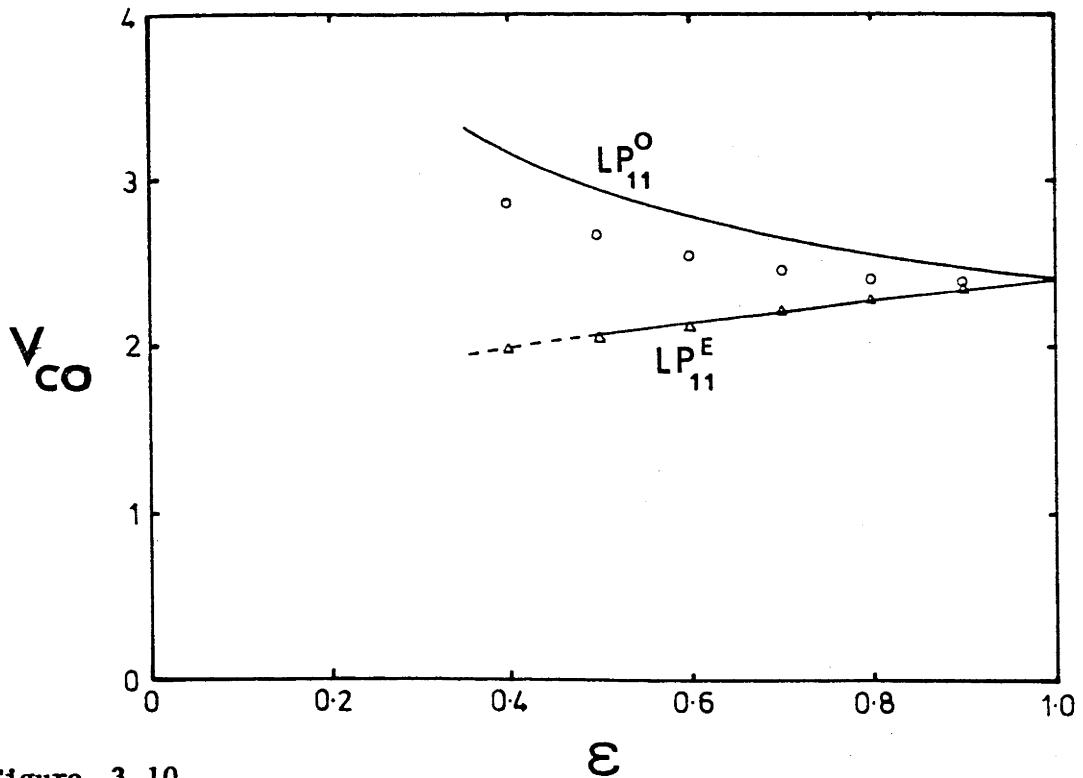

Figure 3.10

Values of higher-mode cut-off on an elliptical step fibre. The solid curves are exact; Δ are values from Rengarajan & Lewis (1980); o are values from Cozens & Dyott (-Citerne) (1979).

(1976) whose results Citerne showed to be relevant only to small eccentricities. This will be explained in §3.8. If Dyott et al employed the same assumptions in calculating B_p, then the disagreement for $\varepsilon=0.5$ is resolved.

§3.7.2 Approximate results

The broken curves shown in figure 3.9 are the birefringence values calculated using the exact Gaussian approximation for the elliptical fibre (defined by Snyder & Love, eq.(17-20)). These curves are seen to reproduce the correct qualitative form. However, their value as an estimate is doubtful. They remain approximately 20% below the true values with $\bar{V}>2$, but below this point, they decrease rapidly, to vanish much too soon at $\bar{V}=1$. The true curves peak at a lower value of $\bar{V}$ than the Gaussian approximation does.

Selected values from Kumar et al (1984) are shown. It is apparent that their pseudo-rectangular approximations agree much better with the results obtained here, than with the results of Dyott et al (1979). Thus, as a simple approximation, the pseudo-rectangular profile is more useful than the Gaussian, at least for higher eccentricities.

For only slightly eccentric cross-sections, the series solution in e^2 is the most reliable approximation. At this point it is interesting to mention yet another birefringence parameter used in the literature. For a small e^2 series, it is customary (eg. Adams et al, 1979; Love et al, 1979; Sammut, 1980a & 1980b) to divide by e^2, defining

$$\hat{B}_p = V_y B_p / e^2 .$$

A further numerical factor may involve a power of two. The series solution in e^2 (Love et al) was employed to produce an approximate

solution at $\varepsilon=0.9$, a curve which follows the exact result very well. After much tedium, the e^2 result can also be obtained from (2.29).

For $\varepsilon=0.5$, results from Sammut (1982a) indicate that the series in e^4 does require extension to higher-order terms before its accuracy improves sufficiently to be useful. However, with the aid of computer algebra packages, this should be possible. As Sammut mentioned, birefringence is a small quantity and, rather than subtract two numbers which are almost identical and thus introduce an error of comprable order to the difference, it is preferable to obtain a series in e^2 which, in principle, can be derived to arbitrary accuracy.

$3.8   Cut-off frequencies

Figure 3.10 shows the scalar cut-off frequencies, V_{co}, for the first two higher-order modes, the LP_{11}^E- and LP_{11}^O-modes. These were calculated by the method explained in §2.5, using the boundary function (1). It is clear that the LP_{11}^E-modes, corresponding to a cosine expansion in §2.5, delineates the limit of single-mode operation. For this mode, the results agree with those of Rengarajan & Lewis (1980). Subsequently Sammut (1982b), employing a series correct to order e^6, and Kumar & Varshney (1984), utilizing an equivalent pseudo-rectangular profile, matched the same results.

Cozens & Dyott (-Citerne) (1979) claimed to evaluate the first higher-modal cut-of frequency. However, their results do not agree with others. Black (1984) suggested their solution corresponded to the LP_{11}^O-mode, not the LP_{11}^E-mode, but this is not the case, as figure 3.10 shows. Rather, the explanation of the Cozens & Dyott results was provided by Citerne. Cozens & Dyott employed the analysis of Yeh (-Citerne) (1976). This is only valid as $\varepsilon \rightarrow 1$. An approximation was used, but its limitations were unrecognized.

Approaching the planar structure, ie. $\varepsilon \rightarrow 0$, more and more modes

approach the cut-off value $\bar{V}_{co}=0$. Thus it becomes difficult to resolve

the first higher-order mode from the second. Black (1984, ch.6) provided

a qualitiative discussion of this behaviour. This degeneracy of higher-

order modes is similar to that discussed in §1.1.E for the infinite

linear profile.

§3.9   Summary

Within the weak guidance approximation, the method for solving step

profiles, as explained in chapter 2, was employed to obtain exact values

of some parameters for the waveguide with an elliptical cross-section.

In particular, the propagation constant of the fundamental mode, the

normalized birefringence, the cut-off frequency of the first higher-

order modes of two different symmetry patterns, and, after generalizing

the Petermann spot-size to a non-axisymmetric fibre, an angularly

dependent spot-size.

Since the exact solution is cumbersome, examination was made of

various approximation methods - both new and existing. Special emphasis

was placed on the variation of parameters as the aspect ratio of the

cross-section changes.

In such examinations, it was found the the family of ellipses with

constant area was the most useful characterization. While the slab is

the limiting form of the elliptical cross-section, for this family the

planar guide has zero thickness. It is possible to obtain simple,

analytical expressions for the limiting values of the parameters.

Combined with the known simple expressions for the circular cross-

section, these provide conditions at $\varepsilon=0$ and $\varepsilon=1$ for simple functions

of ε which well approximate the waveguide parameters. Good
approximating functions of ε and $\bar{V}$ were given for the fundamental mode's
propagation constant and for the angularly dependent spot-size.

§3.A.1 Appendix: Properties of ellipses

One of the familiar descriptions of an ellipse is in terms of
Cartesian co-ordinates

$$\frac{x^2}{\rho_x^2} + \frac{y^2}{\rho_y^2} = 1,$$

where ρ_x and ρ_y, shown in figure 3.1(a) are the semimajor- and
semiminor-axes, respectively. The eccentricity, e, and inverse aspect
ratio, ε, are given by

$$e^2 = 1 - \rho_y^2/\rho_x^2$$

and

$$\varepsilon = \rho_y/\rho_x.$$

ε is more sensitive to changes in the shape of the ellipse. For
example, if $\rho_x = 2\rho_y$, but e=0.866. Thus the eccentricity is close to 1,
even for considerably elliptical shapes.

An alternative description of the ellipse can be obtained in terms
of polar co-ordinates:

$$\rho^2 R^2 = r^2 = \rho_y^2 \left(1 - e^2 \cos^2(\theta)\right) \tag{23}$$

where ρ is a normalizing length scale. Rearranging (23) gives

$$R_B(\theta) = \frac{\rho_y}{\rho} \left(1 - e^2 \cos^2(\theta)\right)^{-1/2}, \tag{24}$$

which defines the boundary, i.e. normalized distance from the origin, as a function of polar angle.

As $e \to 0$, perturbation methods applied to elliptical waveguides, give series expansions for various parameters in powers of e^2. To see that this should be so, expand (24) into a Fourier series. The process proceeds tediously, but exactly:

$$R_B(\theta) = (\frac{\rho_y}{\rho}) \frac{2^{3/2}}{\sqrt{\pi}\,(2-e^2)^{1/2}} \sum_{r=0}^{\infty} \frac{\cos(2r\theta)}{1+\delta_{r0}} (\frac{e^2}{2(2-e^2)})^r Q_r$$

where

$$Q_r = \sum_{p=0}^{\infty} (\frac{e^2}{2(2-e^2)})^{2p} \frac{\Gamma(2p+r+1/2)}{p!\,(p+r)!} .$$

Thus, the series is in e^2, which is equivalent, for perturbation purposes, to a series in $(1-\varepsilon)$.

§3.A.2 Appendix: Slab limit of propagation constant

Consider the exact expression (Snyder & Love, (18-4))

$$U_e^2 - U_s^2 = \frac{V_y^2}{\langle \psi_e, \psi_s \rangle} \oint\limits_{\infty} dS \, (g_s - g_e) \, \psi_e \psi_s, \tag{25}$$

which compares the propagation constant of an elliptical waveguide with that of a slab with the same value of V_y. U_e, g_e, ψ_e refer to the elliptical guide and U_s, g_s, ψ_s to the slab.

By symmetry, the integrals, evaluated over the infinite cross-section, can be restricted to the first quadrant. Here,

$$\psi_s = \begin{cases} \dfrac{\cos U_s Y}{\cos U_s} & , \quad Y<1 \\[2em] \dfrac{e^{-W_s Y}}{e^{-W_s}} & , \quad Y>1. \end{cases} \tag{26}$$

The modal field of an elliptical waveguide decays away from the axis, and at a sufficiently large distance is effectively zero. For a highly eccentric ellipse, the modal field near the centre of the cross-section is almost identical to that of a slab. For a particularly narrow slab, the difference should be even less significant. Also, beyond the ends of the elliptical cross-section, the field will be negligible (§3.6.1), since $\varepsilon \to 0$. Thus, for very small ε,

$$\psi_e = \begin{cases} \psi_s + O(\varepsilon) & , \quad X<1/\varepsilon \\[1em] O(\varepsilon) & ., \quad X>0 . \end{cases}$$

Using this expression, the integrals in (25) simplify to

$$U_e^2 - U_s^2 \approx V_y^2 \, \frac{\displaystyle\int_0^{1/\varepsilon} dX \int_0^{\frac{1}{\sqrt{1-\varepsilon^2 X^2}}} dY \, \psi_s^2}{\displaystyle\int_0^{1/\varepsilon} dX \int_0^1 dY \, \psi_s^2} \,, \tag{27}$$

since away from the indicated domain of integration either $g_e = g_s$ or $\psi_e = 0$ to dominant order. For a finite value of $\bar{V}$, V_y is exceptionally small:

$$V_y = \sqrt{\varepsilon} \, \bar{V} \,.$$

For the slab, this means

$$U^2 \to V_y^2 - V_y^4 \; ; \; W_s^2 \to U_s^2 \,, \tag{28}$$

which is small, and, from (26),

$$\psi_S \sim \begin{cases} 1 + \dfrac{U_s^2}{2} - \dfrac{U_s^2 Y^2}{2} & , \quad Y<1 \\[2em] e^{W_s(1-Y)} & , \quad Y>1 \ . \end{cases}$$

Thus, evaluating the integrals in (27) and using these limiting forms, produces

$$U_e^2 \sim V_y^2 - V_y^4 \epsilon \frac{(\pi-2)}{2}$$

$$\Rightarrow \bar{U} \sim \bar{V} - \epsilon \bar{V}^3 \left(\frac{\pi-2}{4}\right) \ ,$$

recalling the transformation from $\bar{V}$ to V_y, etc.

§3.A.3 Appendix: Petermann spot-size of slab

The field of a planar wavegide is expressed in (26). If this is substituted into (10), the angular spot-size is obtained:

$$\bar{R}_S^2(\theta) =$$

$$\frac{1}{2U^4W^2\sin^2\theta} \frac{\left(U^6\left((W+1)^4 + 2(W+1)\right) + U^4W^4(W+1)(W+3) - 3U^2W^5(W+2) + 3W^6\right)}{\left(U^4(1+W)^2 + U^2W^3(2+W) - W^4\right)}. \quad (29)$$

Here the normalizing length scale is the slab's half-width, ρ_y. This, as expected, gives contours which are parallel to the sides of the planar guide. These can be considered as ellipses with eccentricity e=1. Of particular interest is the case when $\theta = \pm\pi/2$.

As explained in §3.A.2, when the slab is considered to be the limiting case of a family of ellipses characterized by $\overline{V}$, then

$$U^2 \to \overline{V}^2\varepsilon - \overline{V}^4\varepsilon^2 \; ; \; W \to U^2.$$

Using these asymptotic expressions in (29), with $\theta = \pm\pi/2$, gives the result

$$\varepsilon\overline{R}_s^2\left(\pm\frac{\pi}{2}\right) \sim \frac{3}{2\overline{V}^4\varepsilon} \; , \qquad (30)$$

and the difference in length scale - ρ_y in (29) and $\overline{\rho}$ in (15) - explains the factor of ε in the left-hand-expression of (30). The conversion between notations is

$$\varepsilon\overline{R}_s^2 = R_s^2.$$

CHAPTER FOUR

Step Rectangular Waveguides

You remember how Pooh discovered the North
Pole; well, he was so proud of this that he
asked Christopher Robin if there were any other
poles such as a Bear of Little Brain might
discover.

"There's a South Pole", said Christopher
Robin, "and I expect there's an East Pole and a
West Pole, although people don't like talking
about them."

Pooh was very excited when he heard this,
and suggested that they should have an
Expotition to discover the East Pole.

A.A. Milne, "Winnie-the-Pooh"

In this chapter, the method outlined in chapter 2 is used to calculate

the scalar propagation constants, birefringence, and cut-off frequencies

of a dielectric waveguide with a rectangular cross-section. These are

then compared with various approximations. In particular, the equal-

area elliptical waveguide is shown to be a useful first approximation.

The variation of guidance parameters for a sequence of equal-area

rectangular cross-sections is examined.

§4.1   Background

As well as the elliptical cross-section, waveguides with a

rectangular cross-section have attracted considerable interest.

Although the rectangle is a simple shape, the fascination has a genuine

application in view: the rectangular cross-section appears in

integrated optical structures and in the guidance mechanisms of some

solid state, lasing devices.

Alas, no analytic solution, comparable with Yeh's (1962) early

result for the ellipse, exists. Even within the weak guidance

approximation, separated solutions of the scalar wave equation do not

readily satisfy the required continuity conditions, even though the boundary of a rectangular profile separates in Cartesian co-ordinates. However, this apparent intractability caused a proliferation of approximation methods.

Marcatili (1969a) suggested that a rectangular cross-section can be approximated by the intersection of two planar waveguides. For a well guided mode, the field intensity is concentrated in the core, and consequently the corners of the approximating shape have little influence on the mode's propagation. Of course, a well guided mode is one that is far from its cut-off value.

This requirement unfortunately applies to most approximation techniques. The effective index method (e.g. see Adams, 1981, ch.6) has been applied to rectangular guides as an improvement on Marcatili's method. This provides better estimates of the propagation constant close to cut-off (Hocker & Burns, 1979). Payne (1982) examined the effective index method, after transforming quantities to a Fourier domain. Recently the idea of two intersecting slabs was further improved by Kumar et al (1983).

As shall be shown below, an approximation which works better as cut-off is approached is use of the equivalent elliptical cross-section (Sammut, 1982a; Black & Pask, 1984). Intuitively this is because, as a mode approaches cut-off, the field spreads further into the cladding and is less sensitive to the exact shape of the core. This, of course, necessitates the evaluation of parameters for an elliptical profile.

Using the Gaussian variational method, Sammut (1983) produced approximate values of the propagation constant of a step rectangular fibre. Eyges et al (1979) included results for rectangular waveguides using their Green function expansion technique.

Purely numerical solution of the rectangular waveguide began with

Goell's (1969) point matching at the boundary of expansions in circular

harmonic functions. Inevitably, finite element analysis was recently

employed (Yeh et al, 1979).

§4.2 Two families of rectangles

As for elliptical waveguides, it is instructive to examine the

variation of the guidance properties of a rectangular waveguide with the

inverse aspect ratio,

$$\varepsilon = \rho_y / \rho_x ,$$

where ρ_x and ρ_y are half the longer and shorter sides, respectively

(refer figure 4.1).

Also, as with ellipses, there are two famlies of rectangular cross-

sections characterized by the same value of ε. The first has a

fixed ρ_y, but an area, A, which increases as ε declines:

$$A = 4\rho_y^2 / \varepsilon .$$

The other has a fixed area, but variable side lengths and becomes longer

and thinner as ε decreases:

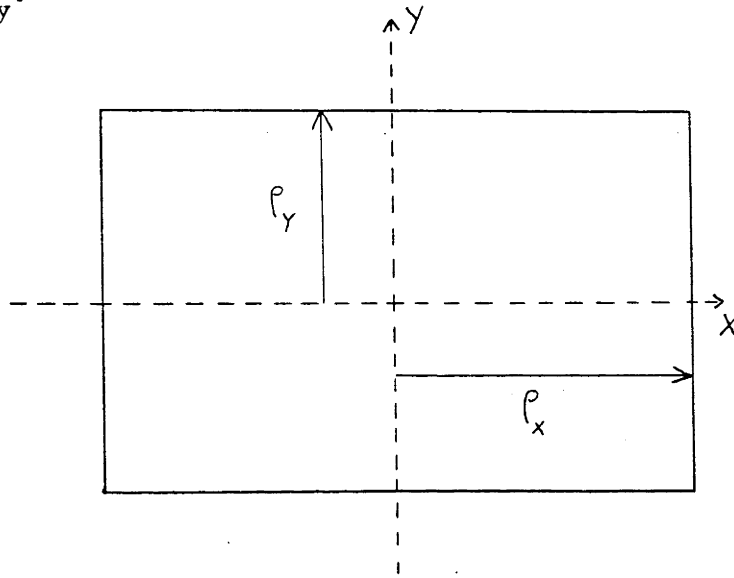$$\rho_x^2 = A/4\varepsilon \; ; \; \rho_y^2 = \varepsilon A/4 .$$

These two sequences are illustrated in figure 4.1. Any rectangular

cross-section is uniquely specified by pairing either an area or a side

length with an inverse aspect ratio.

Following the definition in §P.2.3 , the canonical length scale is
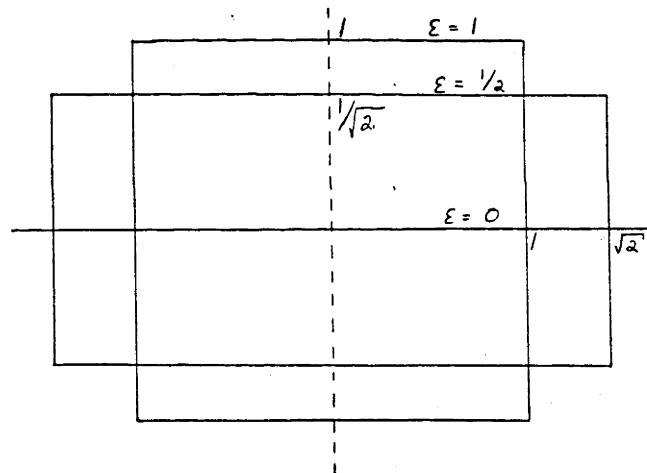
$$\bar{\rho} = 2\sqrt{\rho_x \rho_y / \pi}$$

Figure 4.1
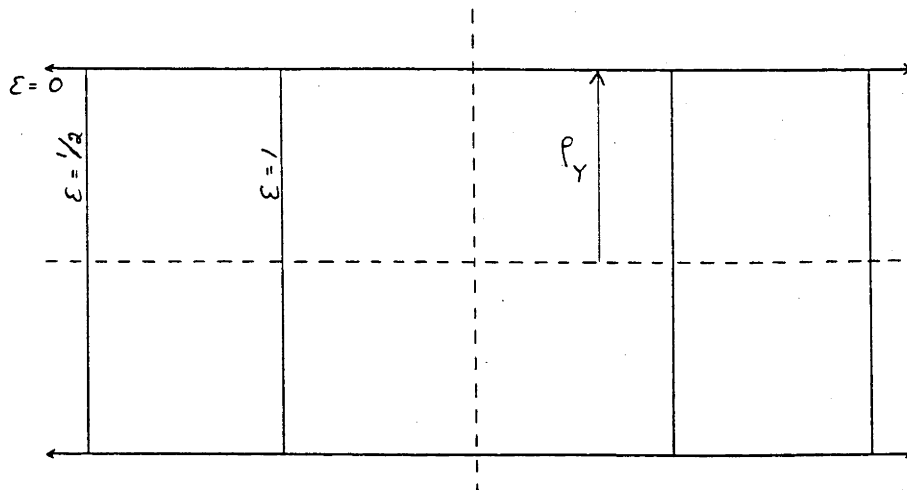
(a) The rectangular cross-section, showing the lengths of the sides, $2\rho_x$ and $2\rho_y$.

(b) The family of rectangles which have identical areas.

(c) The family of rectangles which have the same shorter sides, parallel to the Y-axis.

and the canonical frequency, $\bar{V}$, follows as

$$\bar{V}^2 = k^2 n_{c\ell}^2 \frac{4 \rho_x \rho_y}{\pi} 2\Delta.$$

This contrasts with the more familiar definitions

$$V_y^2 = k^2 n_{c\ell}^2 \rho_y^2 2\Delta$$

$$= \frac{\pi}{4\varepsilon} \bar{V}^2$$

and

$$V_a^2 = k^2 n_{c\ell}^2 \rho_x \rho_y 2\Delta$$

$$= \frac{\pi}{4} \bar{V}^2.$$

For each quantity the variation with ε will be investigated for fixed area rectangles, i.e. when $\bar{V}$ is constant.

§4.2.1 Optical axes

In general, a rectangular cross-section is significantly axi-asymmetric and the LP-modes correspond to the true modes. The optical axes are obvious from symmetry. However, the symmetry of a square cross section is such that the obvious choice of axes is ambiguous. Should they be as for a rectangle or aligned with the diagonals? The vector perturbation method of Snyder & Young (1978) does not fix any preferred pair of axes, so any orthogonal pair can be used.

§4.3 Fundamental mode propagation constant

Using the general analysis of chapter 2, the solution of the step-profile rectangular waveguide is easily obtained. The boundary function is

$$
R_B(\theta) = \begin{cases} (\rho_x/\rho)/\cos\theta \ , & 0 \leqslant \theta \leqslant \theta_0 \\[2ex] (\rho_y/\rho)/\sin\theta \ , & \frac{\pi}{2} \geqslant \theta \geqslant \theta_0 \end{cases} \tag{2}
$$

in the first quadrant. Extending to $\theta \epsilon (0, 2\pi)$ follows from symmetry. Here ρ is the chosen length scale and

$$\theta_0 = \arctan(\epsilon),$$

depending only on the inverse aspect ratio, defines the shape of the rectangle.

§4.3.1 Fourier coefficients

To obtain the Fourier co-efficients required in §2.2.3 is straightforward. For example, if even-even modes are examined,

$$
a_{nm} = \int_0^{2\pi} J_{2n}(UR_B)\frac{\cos 2m\theta}{\pi(1+\delta_{m0})}\, d\theta \ . \tag{3}
$$

Again, interest is primarily with the fundamental mode, which is of this type. Using the series expansion for the Bessel function (A&S, 9.1.10) in (3),

$$
a_{nm} = \frac{U^{2n}}{\pi(1+\delta_{m0})4^{n-1}} \sum_{k=0}^{\infty} \left(\frac{-U^2}{4}\right)^k \frac{1}{k!(2n+k)!} \mathrm{Re}\left(\int_0^{\pi/2} d\theta\, R_B^{2n+2k}(\theta)e^{i2m\theta}\, d\theta\right).
$$

The integral naturally decomposes into two parts.

$$\int_0^{\pi/2} d\theta \, R_B^{2n+2k}(\theta) \, e^{2im\theta}$$

$$= \left(\frac{\rho_x}{\rho}\right)^{2n+2k} I^{(k)}(\theta_0) + \left(\frac{\rho_y}{\rho}\right)^{2n+2k} (-1)^{m+1} I^{(k)}(\theta_0 - \pi/2)$$

where

$$I^{(k)}(\phi) = \int_0^\phi \frac{e^{i2m\theta} \, d\theta}{\cos^{2n+k}\theta}$$

$$= \sum_{\ell=0}^\infty \sum_{r=0}^{2\ell} \frac{(n+k+\ell-1)!(2\ell)!(-1)^{\ell+r}}{\ell! \, r! \, (2\ell-r)!(n+k-1)! \, 4^\ell} \left[\frac{e^{i2\phi(m+\ell-r)} - 1}{2i(m+\ell-r)}\right] ,$$

and a limiting form for the factor in the square brackets is required whenever $m+\ell=r$. No simpler form for a_{nm} was found. Thus, once again, it is as suitable to use the numerical fast Fourier transform to evaluate the boundary decomposition coeffiecients $\{a_{nm}\}$, $\{b_{nm}\}$, $\{c_{nm}\}$ and $\{d_{nm}\}$, as to employ their analytic representations, and considerably faster.

§4.3.2 Results

Figure 4.2 shows the canonical propagation constant, defined by

$$\bar{U}^2 = \frac{4\rho_x\rho_y}{\pi}\left(k^2 n_{co}^2 - \beta^2\right). \tag{4}$$

The curve denoted by $\varepsilon=0$ corresponds to a planar waveguide of finite area and, hence, zero thickness. For a slab approaching this limit, $U_y \to V_y$ and, thus, $\bar{U} \to \bar{V}$.
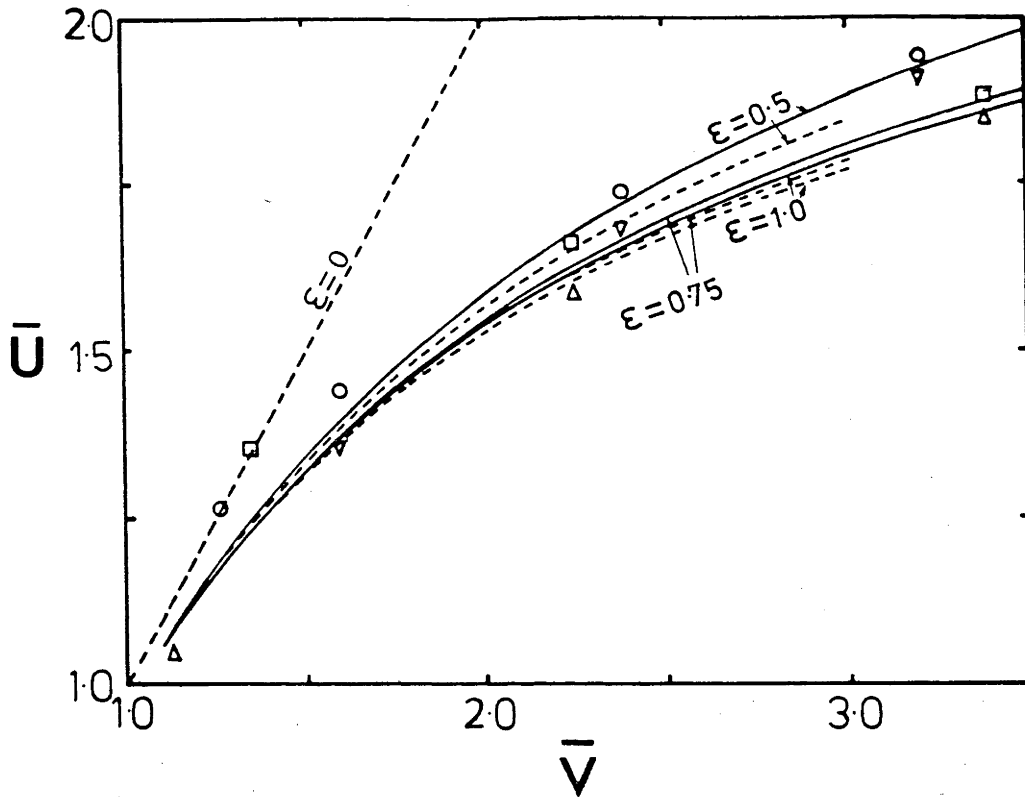
Figure 4.2

For the rectangular step waveguide, the fundamental mode canonical propagation constant, $\bar{U}$, as a function of the canonical frequency, $\bar{V}$, is shown as solid curves. The broken curves are obtained from the equivalent elliptical waveguide. $\triangle$ and $\triangledown$ indicate Marcatili's approximation for $\varepsilon=1$ and $\varepsilon=0.5$, respectively; $\square$ and o were calculated by the effective index method for $\varepsilon=1$ and $\varepsilon=0.5$, respectively.
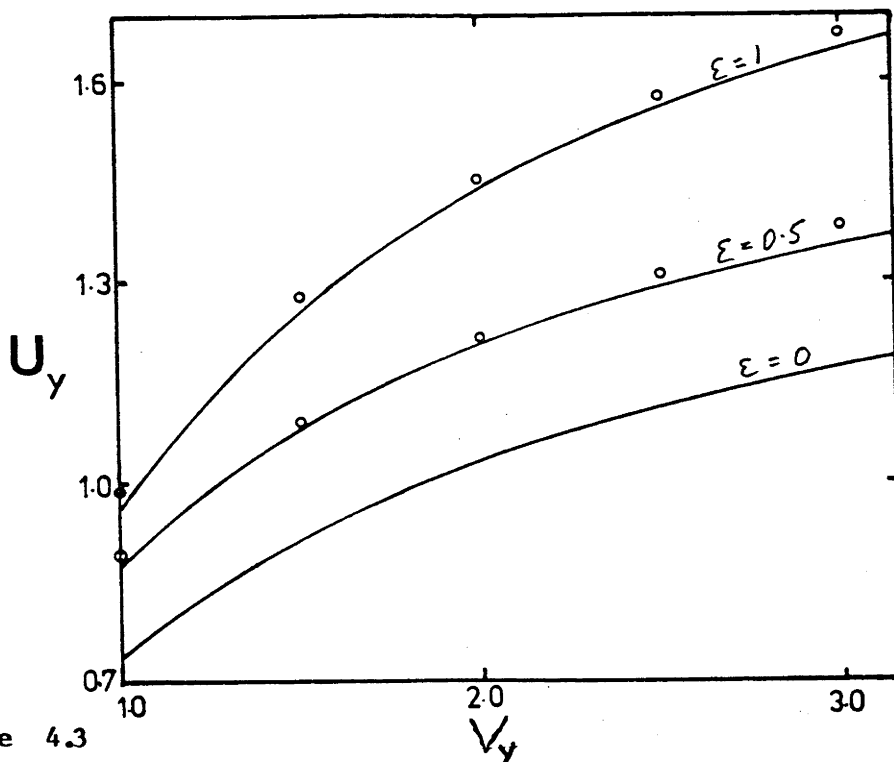

Figure 4.3

For the rectangular step wavegide, the variation of the normalized propagation constant, U_y as a function of the normalized frequency, V_y. Circles indicate the Gaussian approximation.

More familiar combinations than $(\bar{V},\bar{U})$ are (V_a,U_a) and (V_y,U_y) with V_a and V_y defined in §4.2 and

$$U_a^2 = \frac{\pi}{4} \bar{U}^2$$

and

$$U_y^2 = \frac{\pi}{4} \varepsilon \bar{U}^2.$$

The form of a sequence of (V_a,U_a) curves is the same as for $(\bar{V},\bar{U})$. However, the (V_y,U_y) curves differ. These are shown in figure 4.3 where the planar limit occurs in its more customary fashion.

Variation of $\bar{U}$ with ε is shown explicitly in figure 4.4. For cross-sections which vary only slightly from square, it is clear that $\bar{U}$ varies only slightly from its value for a square, $\varepsilon{=}1$, waveguide. As explained above and in §3.A.2, the limiting form as $\varepsilon{\to}0$ is known.

In calculating these results, convergence was slower than for the elliptical cross-section, but comparable with that found by other authors (Goell, 1969; Eyges et al, 1979) using expansions for ψ. The gap in the curves of figure 4.4 could be filled if computations of very high precision were possible. As mentioned in §3.3.2 the constraint is limitations of the numerical routines for evaluating the higher-order Bessel functions.

§4.3.3 Comments on approximations

Black & Pask (1984) defined the elliptical waveguide equivalent to the rectangular waveguide, to be the one with identical aspect ratio and canonical frequency, i.e. $\bar{V}$ and ε are the same. In figure 4.2, the estimated values of $\bar{U}$, based on this equivalent elliptical cross-section, are shown beside the exact results. The accuracy of this

Figure 4.4

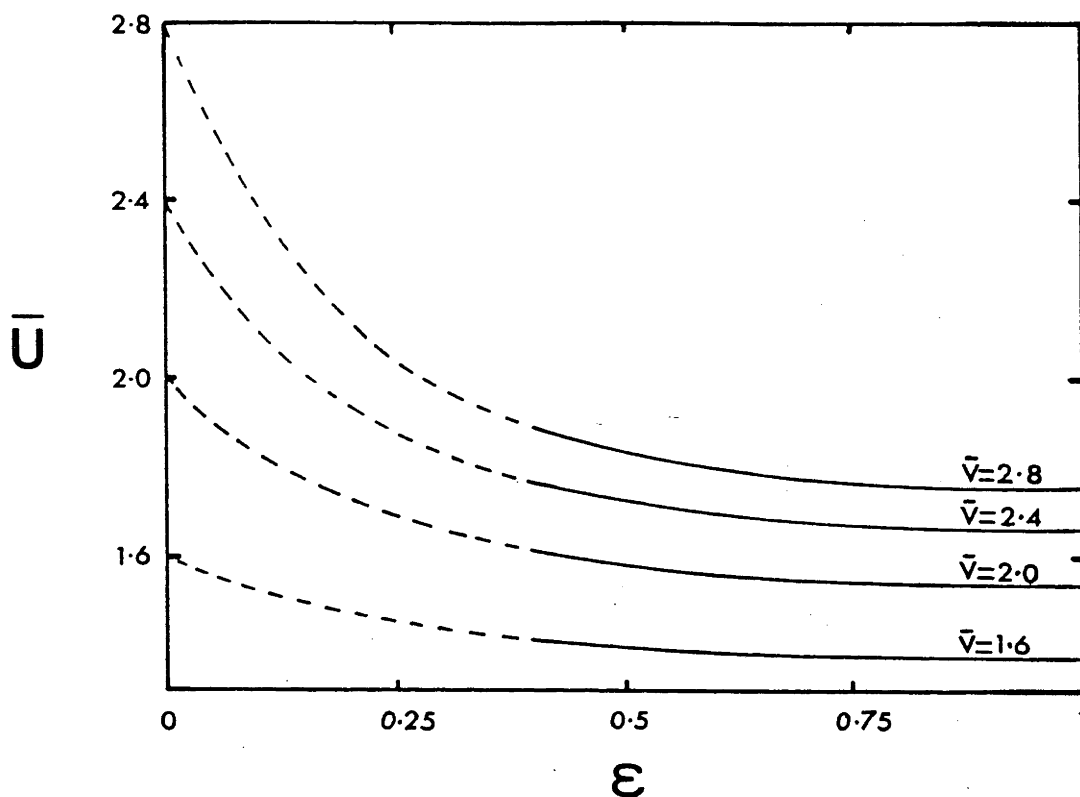For the rectangular step waveguide, variation of the canonical propagation constant with inverse aspect ratio.

Table 4.1

The percentage relative error in the canonical propagation constant, $\bar{U}$, estimated from the equivalent elliptical waveguide.

ε \ $\bar{V}$	1.5	2.5	3.0
1	-0.3%	-1.0%	-1.3%
0.75	-0.3%	-1.1%	-1.4%
0.5	-0.8%	-1.6%	-1.9%

underestimation is indicated in table 4.1. The improving accuracy as $\bar{V}$ decreases is expected. In this limit, the field spreads into the cladding and is less sensitive to the exact shape of the cross-section; as $\bar{V} \to \infty$ - the ray optics limit - ψ is restricted to the core whose shape is important.

While the equivalent elliptical waveguide is a good approximation, the computation of the exact propagation constant for an elliptical waveguide is as complex as for the rectangular cross-section itself. However, the exceptionally accurate, simple formula of §3.4.2 could be used to give a simple, very accurate estimate of $\bar{U}$ for a step rectangular fibre.

In figure 4.3, Sammut's (1983) results from the Gaussian approximation are shown. As expected, the accuracy of this overestimate decreases as $\bar{V} \to 0$.

Figure 4.2 also includes estimates obtained from the method of Marcatili and the effective index method. These are taken from figures 6.4 and 6.6, respectively, of Adams (1981). As expected, these approximations, which employ unphysical profiles that do not match the step profile, become worse as $\bar{V} \to 0$, i.e. as cut-off is approached.

A more detailed comparison of these two approximation techniques with that using the pseudo-rectangular profile is illustrated in figures 1 and 2 of Kumar et al (1984), where the numerical results of Goell (1969) are also included as reference values.

§4.4   Behaviour of the modal field

In §2.3 it was shown that, close to the centre of the cross-section, the modal field is approximately elliptical. To describe the evolution of this form to its shape further away from the fibre's axis
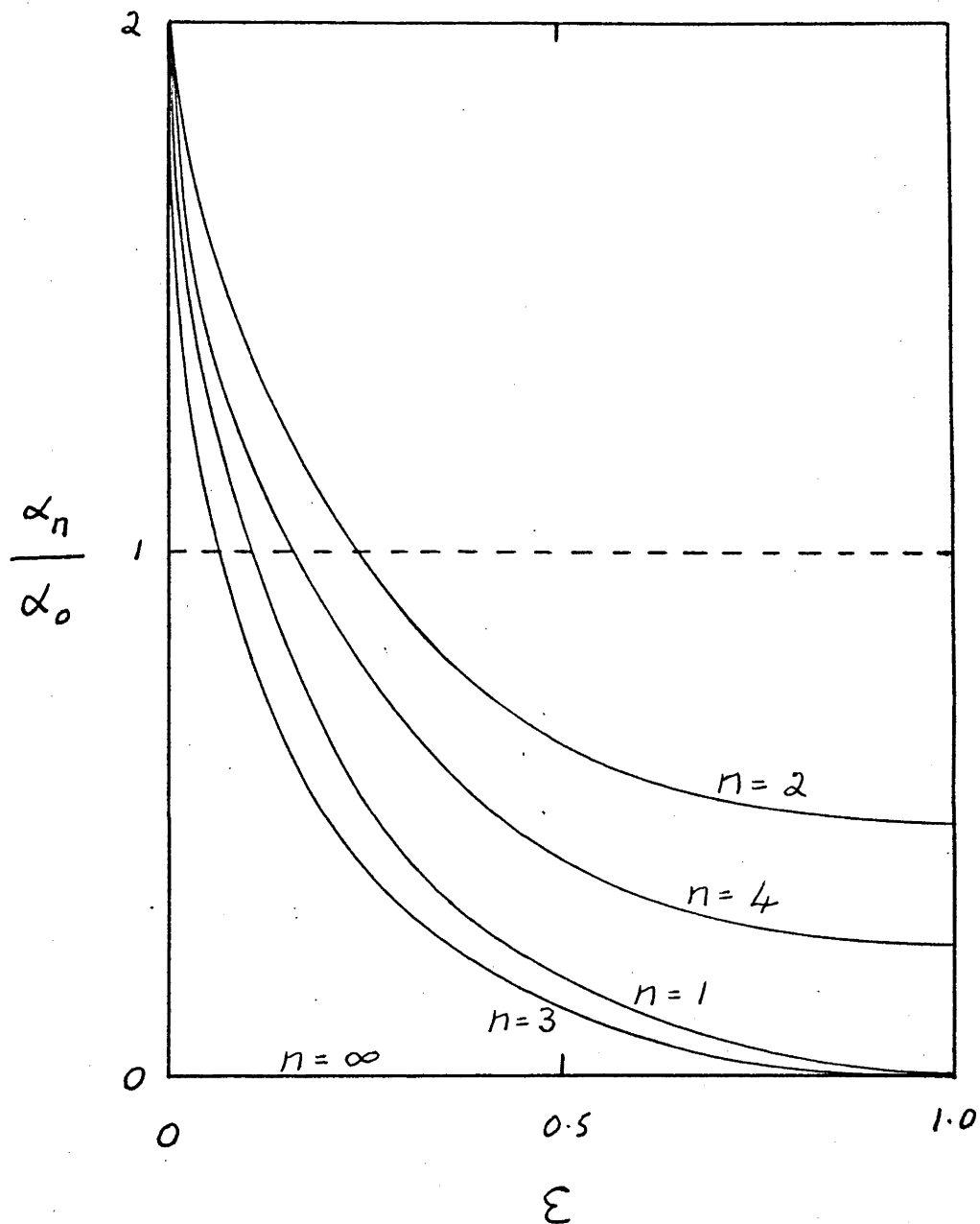
Figure 4.5

A qualitative indication of the behaviour of the field expansion coefficients, α_n, as the aspect ratio of the rectangular cross-section changes.

is no easier for the rectangular case than for the elliptical one. Similarly, for a small value of $\bar{V}$, the modal field becomes elliptical in form.

As in §3.5.1, the behaviour of the co-efficients in the limiting case of $\varepsilon=0$ can be examined, with an identical result obtained. Once again, the slab limit is found and, $\forall\, n \geqslant 1$, the coefficients of expansion (2.7) become

$$\alpha_n = 2\alpha_0.$$

The case of the square cross-section does not provide an obvious, simple limiting form. That is, except for the symmetry which shows, $\forall\, n \geqslant 0$,

$$\alpha_{2n+1} = 0.$$

Combining these features, figure 4.5 provides a qualitative insight into the behaviour of the coefficients $\{\alpha_n\}$. This pattern is independent of $\bar{V}$, although, as $\bar{V} \to 0$, ψ becomes more circular and $\alpha_n \to 0$, $\forall\, n \geqslant 1$.

Whether the curves shown in figure 4.5 intersect is not known, but the trends indicated again permit a test on the accuracy of the field components of the numerical computations. In the subsequent work, components are retained up to a value N such that

$$\alpha_N > \alpha_{N-2}.$$

§4.5   Birefringence

The first theoretical analysis of birefringence (Ramaswamy et al, 1970) employed Marcatili's (1969a) results for the rectangular cross-section. Surprisingly, subsequent examination of birefringence has been restricted almost exclusively to the elliptical cross-section.

Results for the normalized birefingence, B_p, of the rectangular cross-section, were obtained employing the method outlined in §2.4. In the case of this shape, the boundary function (2) is discontinuous at $\theta = \theta_0$. However, the results of §2.4 remain valid, although the derivation is complicated by considering the four pathological corner points. The results give

$$2R_B' \sin 2\theta + R_B\left(1 - \frac{R_B'^2}{R_B^2}\right) \cos 2\theta = \begin{cases} R_B/\cos^2\theta \ , & \theta < \theta_0 \\ \\ -R_B/\sin^2\theta \ , & \theta > \theta_0. \end{cases} \tag{5}$$

and

$$\frac{2R_B'}{R_B} \sin 2\theta + \left(2 - \frac{R_B''}{R_B} + \frac{R_B'^2}{R_B^2}\right) \cos 2\theta = \begin{cases} 1/\cos^2\theta \ , & \theta < \theta_0 \\ \\ -1/\sin^2\theta \ , & \theta > \theta_0. \end{cases} \tag{6}$$

Substituting (5) and (6) in (2.30) shows

$$B_p = \frac{4}{V^2 \|\psi\|^2} \sum_{n=0}^{\infty} \sum_{m=0}^{n} (2 - \delta_{nm}) \, \alpha_n \, \alpha_m$$

$$\times \left[\int_0^{\theta_0} d\theta \, \frac{\cos 2n\theta \cos 2m\theta}{\cos^2\theta} \, J_{2n}\left(\frac{U_y}{\varepsilon \cos\theta}\right) J_{2m}\left(\frac{U_y}{\varepsilon \cos\theta}\right) E_{nm}^{(1)}(\theta) \right.$$

$$\left. - \int_{\theta_0}^{\pi/2} d\theta \, \frac{\cos 2n\theta \cos 2m\theta}{\sin^2\theta} \, J_{2n}\left(\frac{U_y}{\sin\theta}\right) J_{2m}\left(\frac{U_y}{\sin\theta}\right) E_{nm}^{(2)}(\theta) \right]$$

where

$$E_{nm}^{(1)} = 1 + \frac{U_y}{\varepsilon \cos\theta} \left(\frac{J_{2m}'\left(\frac{U_y}{\varepsilon \cos\theta}\right)}{J_{2m}\left(\frac{U_y}{\varepsilon \cos\theta}\right)} + \frac{J_{2n}'\left(\frac{U_y}{\varepsilon \cos\theta}\right)}{J_{2n}\left(\frac{U_y}{\varepsilon \cos\theta}\right)} \right)$$

and

$$E_{nm}^{(2)} = 1 + \frac{U_y}{\sin \theta} \left(\frac{J_{2m}' \left(\frac{U_y}{\sin \theta}\right)}{J_{2m} \left(\frac{U_y}{\sin \theta}\right)} + \frac{J_{2n}' \left(\frac{U_y}{\sin \theta}\right)}{J_{2n} \left(\frac{U_y}{\sin \theta}\right)} \right) .$$

The results obtained using these expressions are shown in figure 4.6. It is apparent that, as expected, the qualitative behaviour of the rectangular and elliptical geometry is similar.

Also shown is the approximate birefringence obtained by Black & Pask (1984). Their equivalence is outlined in §4.3.3. It shows that

$$3 \Delta_r = \pi \Delta_e ,$$

which implies from the definition of B_p in (P.7),

$$B_{pr} = \frac{9}{\pi^2} B_{pe}$$
(7)

where subscripts r and e refer to the rectangular and elliptical waveguides, respetively. The identification (7) corresponds to the broken curve in figure 4.6.

It is interesting that the peak value of birefingence occurs at a higher value of $\bar{V}$ than on the equivalent elliptical waveguide. Also, the peak value of birefringence is lower, especially when one remembers the factor of $9/\pi^2$ in (7).

Kumar et al (1984) identified their pseudo-rectangular profile with an elliptical profile, defined by the same criteria as Black & Pask employed. Thus, the approximate birefringence they ascribe to the elliptical cross-section can be ascribed to the equivalent rectangular cross-section with equal validity.

Figure 4.6

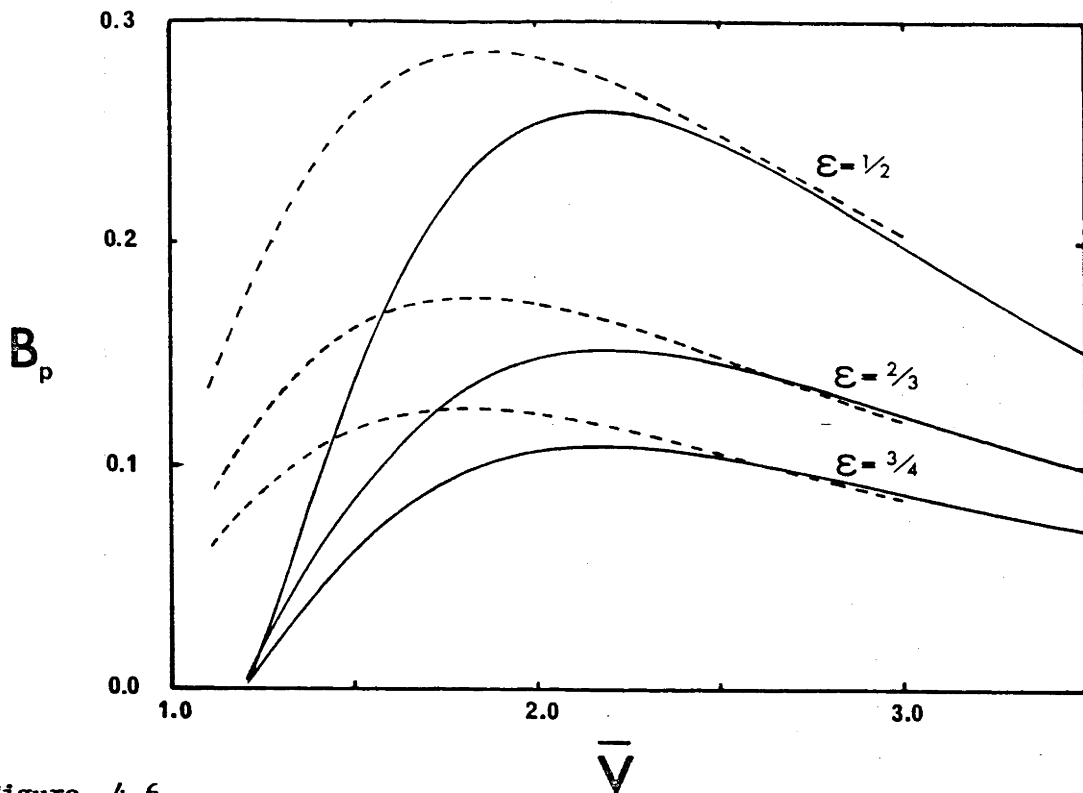For the rectangular step waveguide, normalized birefringence, B_p, as a function of canonical frequency, $\overline{V}$. The solid curves are exact results; the broken curves come from the equivalent elliptical waveguide.
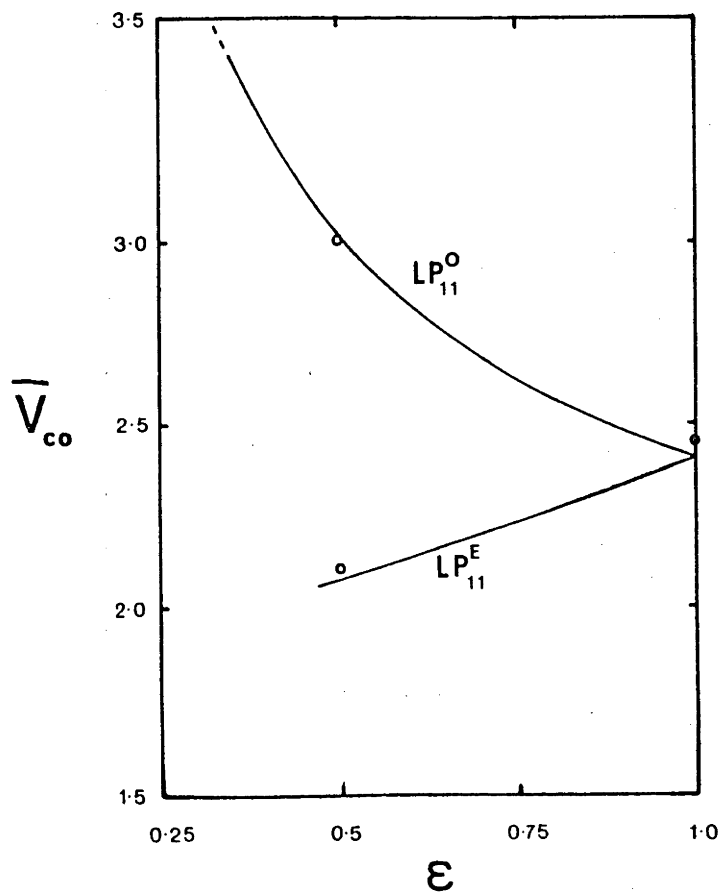

Figure 4.7

For the rectangular step waveguide, canonical cut-off frequencies, $\widetilde{V}_{co}$, for the first higher-order modes. The circles come from the literature.

It is worth commenting that, from symmetry, it is apparent that there is no birefringence in a square cross-sectional waveguide. Of necessity, $\beta_x = \beta_y$.

§4.6 Cut-off frequencies

In figure 4.7 are presented the canonical cut-off frequencies of waveguides with rectangular cross-sections. The *circles* indicate the only values in the literature: for $\varepsilon = 1$, Goell (1969) obtained 2.45; for $\varepsilon = 0.5$, Eyges et al (1979) calculated the pair 2.11 and 3.01 for the two types of modes. These agree well with the evaluated curves.

For the determination of single-mode operation, the cut-off of the LP_{11}^E-mode is the determining limit. This is the lower curve in figure 4.7. Sammut (1982a) suggested that, for a nominated value of ε, the canonical cut-off parameter of an elliptical waveguide equals that of a rectangular guide. Black & Pask (1984) suggested a different equivalence. If $\varepsilon_r = 0.7746 \, \varepsilon_e$, then $\bar{V}_{co}^{(r)} = 1.054 \, \bar{V}_{co}^{(r)}$. The results of figure 4.7 are not sufficiently accurate to make a definitive statement about the relative utility of these two approximations. Black & Pask also showed how an approximation for the curves of figure 4.7 can be obtained from the cut-off frequency of the square – $\varepsilon = 1$ – cross-section.

§4.7 Discussion

As one might expect, the behaviour of the rectangular cross-section is similar to that of an elliptical cross-section, and similar techniques – both exact and approximate – can be used to describe both.

The description outlined in §4.3.3 appears to model well the similarity in guidance properties between the two shapes. However, there is still a small, systematic difference between the two. The

rectangular cross-section appears consistently to be not quite as effective a waveguide as an elliptically cross-sectional fibre with the same area and aspect ratio. For example, the normalized birefringence, B_p, is lower; the propagation constant, U, is higher; the cut-off parameters are lower. This lessening of effectiveness can be intuitively appreciated by considering the corners of the rectangle and an analogy.

If an ice-skating rink has an elliptical boundary, the skaters enjoy a greater area, in which to move, than if the boundary is rectangular and the enclosed area the same. Due to the turning circle required for a skater to change his direction, the very corner regions of a rectangular rink are inaccessible. Similarly, a discontinuity in the derivative of the bondary function, $R_B(\theta)$, describing the core-cladding interface, weakens the ability of a waveguide to confine the modal field whose derivatives are always everywhere continuous.

CHAPTER FIVE

Modelling Single Polarization Fibres

Piglet said, "I thought your Idea was a
very good Idea."

Pooh began to feel a little more
comfortable, because when you are a Bear of Very
Little Brain, and you Think of Things, you find
sometimes that a Thing which seemed very
Thingish inside you is quite different when it
gets out into the open and has other people
looking at it.

A.A.Milne, "The House at Pooh Corner"

In this chapter, a model profile - the butterfly profile - which

exhibits the key features of practical single polarization fibres is

developed. The refractive index incorporates both a depressed inner

cladding and non-axisymmetric contours of constant refractive index. It

is shown how material anisotropy can be included to improve the

predictive power of the model. Within the weak guidance formalism, the

exact solution of the butterfly profile is obtained analytically, using

an analogous method to that described in chapter 2. This enables the

evaluation of the geometric birefringence and the cut-off frequencies of

the two polarization states of the first three modes, including the

fundamental mode. Also, by perturbing an axisymmetric profile, a

remarkably accurate approximate solution is obtained.

§5.1 Motivation

Recently, considerable interest has been shown in single-moded,

single-polarization (SMSP) fibres. These have important applications in

instrumentation based on fibre optics, as well as improving

communication networks. With only one guided mode present on a fibre,

it is desired that light launched with a specific state of polarization

is not scatterred into another state of polarization.

§5.1.1 Single polarization operation

To achieve the sought characteristic of only propagating one state of polarization, various mechanisms can be employed, and most fibre designs feature more than one of these.

Of major concern is the maximization of the birefringence of the two polarization states of the fundamental modes. As explained in §P.3, this is caused by geometric and/or anisotropic effects. The stress birefringence normally dominates the shape birefringence (Kaminow & Ramaswamy, 1979), so designs seek to impose maximum asymmetric stress on the core, to cause maximum anisotropy. In such configurations, regions of doping are placed about the core in a non-axisymmetric arrangment. For example, there are the panda fibres of Kitayama et al (1981), the designs of Okoshi (1981) and Sasaki et al (1982), and the bow-tie fibre of Varnham et al (1983b). In all of these, the regions producing stress have a refractive index below that of the remainder of the cladding. This is a property of the dopants used to obtain the necessary variation in thermoelastic properties for a residual stress within the fibre.

These refractive index depressions within the inner regions of the cladding also produce another effect which enables single-polarization operation of the waveguide. On a W-fibre (Kawakami et al, 1976), the fundamental mode may have a finite cut-off frequency. In an anisotropic W-fibre, the two polarization states of this mode, and, of course, subsequent modes, can have significantly different cut-off frequencies (Simpson et al, 1983).

Without the anisotropy, the same phenomena are induced by the geometric configuration alone, albeit at a smaller order of magnitude. In an effort to better understand the operation of practical SMSP fibres, a simple model is constructed.

§5.1.2 Model: the butterfly profile

As usual, the refractive index profile examined is assumed to have a cladding which is infinite in extent, an unphysical, but accurate, approximation. Also, as in an ideal waveguide, it does not vary along the fibre.

From the scalar wave equation (P.3), it is seen that, if the R-dependence of g is of an inverse-square form, the equation is separable. Thus, for the simplest non-axisymmetry, the model selected has the refractive index variation

$$n^2(R,\theta) = \begin{cases} n_{co}^2 & , R<1 \\ n_{c\ell}^2 - \dfrac{A\,(2\Delta n_{c\ell}^2)\cos^2\theta}{R^2} & , R>1 \end{cases} \tag{1}$$

where lengths have been non-dimensionalized by the core's radius, ρ. This gives a shape-function

$$g(R,\theta) = \begin{cases} 1 & , R<1 \\ -A\,\dfrac{\cos^2\theta}{R^2} & , R>1 \ . \end{cases} \tag{2}$$

The core-depth parameter A fully describes this profile; it is the ratio of the height of the core to the maximum depth of the inner cladding region.

This profile, termed the **butterfly** profile, is illustrated in figure 5.1. The contours of constant refractive index in the cladding form a pattern of circles of Apollonius. It is apparent that this profile exhibits the necessary features for a SMSP fibre: the two regions where the refractive index is depressed; the uniformity of the

Figure 5.1

The butterfly profile, defined by (1)
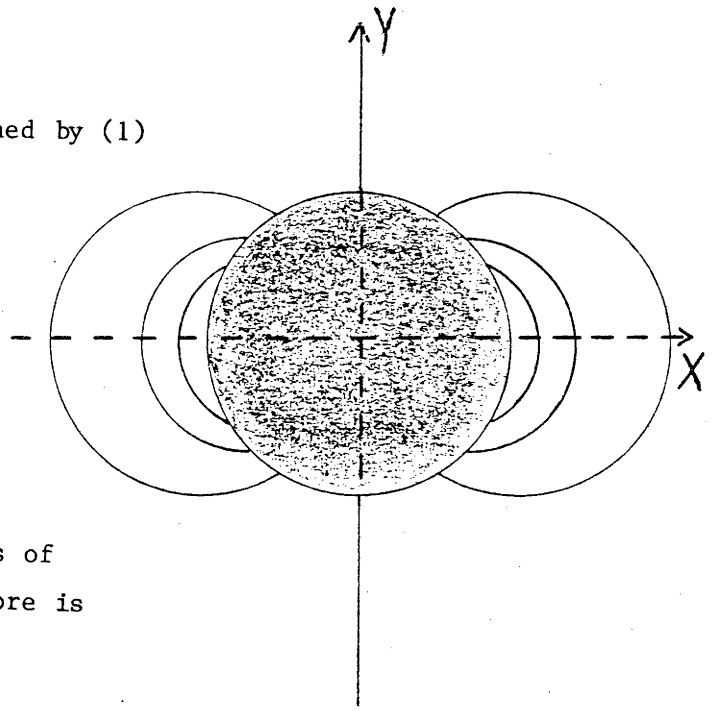
(a) In the cladding, the
contours of constant
refractive index are arcs of
circles. The circular core is
shaded.

(b) Along the X-axis, the
butterfly-profile is like an
inverse-square W-profile.

(c) Along the Y-axis, the
butterfly-profile is like a
step-profile.

$2\Delta n^2_{cl}$

$A2\Delta n^2_{cl}$

n^2_{co}

$2\Delta n^2_{cl}$

n^2_{cl}

n^2_d
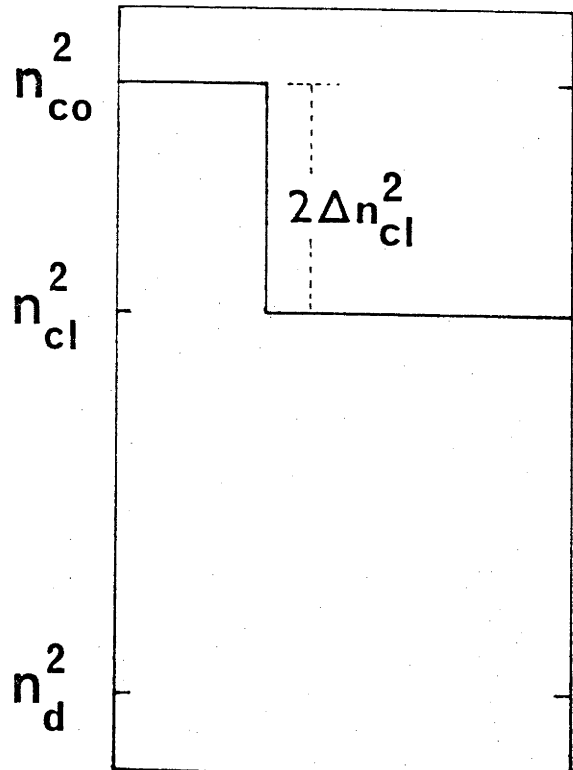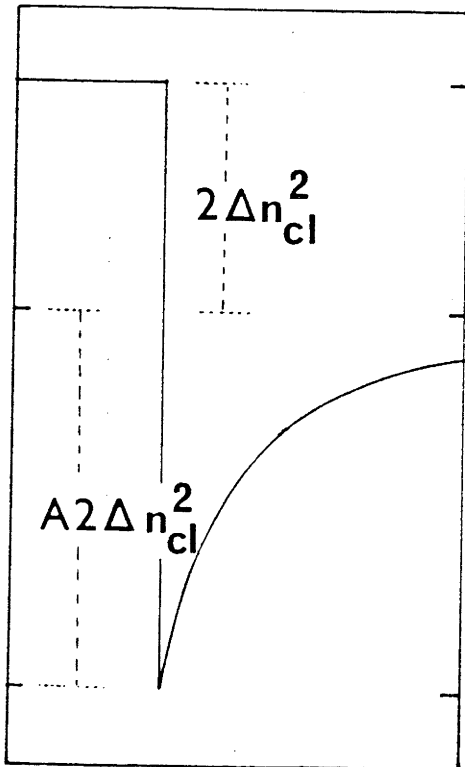
cladding at a great distance from the core; the lack of axisymmetry.
This best matches the isotropic average of the bow-tie fibre (Birch et
al, 1982). In §5.7 it is shown how anisotropy can be included.

§5.2   Solution for the butterfly fibre

Employing the weak guidance formalism of §P.2, the replacement of
(2) in (P.3) gives, in the two regions

$$(\nabla^2 + U^2)\psi = 0 \qquad , \quad R<1 \tag{3a}$$

and

$$\left(\nabla^2 - W^2 - \frac{AV^2(1 + \cos2\theta)}{2R^2}\right)\psi = 0 \qquad , \quad R>1 \tag{3b}$$

where U and W are the normalized propagation constants. Again, for a
physically meaningful solution for the modal pattern, ψ, it is necessary
that ψ and $\partial\psi/\partial R$ are continuous at the interface R=1, and that ψ is
finite at R=0 and vanishes as $R\rightarrow\infty$.

To solve, one proceeds as in chapter 2, expanding ψ in terms of the
natural basis defined by (3), then using Fourier series to ensure the
continuity requirements, and ultimately deriving a matrix whose
determinant will vanish if U is a propagation constant of the waveguide.

§5.2.1 Series expansion of the field

Equation (3a) has an uncountable set of solutions, which satisfy
the above conditions and are 2π-periodic. A convenient basis for these
functions is $\{J_n(UR) \cos(n\theta), J_n(UR) \sin(n\theta)\}$, where J_n is the Bessel
function of the first kind. As explained in §2.2.2, different modes
display different symmetry patterns, and different sub-bases fully

describe different symmetry patterns. Because g, defined in (2), is
symmetric about both the X- and Y-axes, the fundamental mode also has
this symmetry. Thus the interior portion of ψ can be expanded as

$$\psi_I = \sum_{n=0}^{\infty} \alpha_n \frac{J_{2n}(UR)}{J_{2n}(U)} \cos(2n\theta) \quad , \tag{4}$$

where $\{\alpha_n\}$ are real constants to be evaluated.

Similarly, (3b) produces a convenient, separated basis, complete in
the permitted solution space. The same symmetry argument as mentioned
above shows that the relevent functions are

$$K_{\lambda_n}(WR) \; ce_{2n}(\theta,q)$$

where ce_{2n} is a periodic, even Mathieu function (A&S, 20.2.27) with

$$q = AV^2/4 \tag{5}$$

and associated characteristic value $a_{2n}(q)$, and K_ν is a fractional
order, modified Bessel function of the third kind (A&S, 9.6.24) with

$$\lambda_n^2 = 2q + a_{2n} \; . \tag{6}$$

For all $n \gtrless 0$ and real q, $a_{2n} > (-2q)$. Hence, the order of K_{λ_n}, while
fractional, remains real. (For further details of Mathieu functions,
see §5.A.1.) Finally, the portion of ψ external to the core can be
expanded as

$$\psi_E = \sum_{n=0}^{\infty} \beta_n \frac{K_{\lambda_n}(WR)}{K_{\lambda_n}(W)} \; ce_{2n}(\theta,q) \; . \tag{7}$$

where the $\{\beta_n\}$ are real constants which need to be determined.

§5.2.2 System of equations from continiuity

In (44) it is shown explicitly how $ce_{2n}(\theta, q)$ can be decomposed into a Fourier series. Substituting this in (7) yields

$$\psi_E = \sum_{p,n=0}^{\infty} \beta_n A_{2p}^{(2n)} \frac{K_{\lambda_n}(WR)}{K_{\lambda_n}(W)} \cos(2p\theta) \ .$$

In combination with (4), this is more useful than (7) in imposing continuity conditions on ψ and $\partial\psi/\partial R$. After matching harmonics, these give, $\forall n \geqslant 0$,

$$\alpha_n = \sum_{p=0}^{\infty} A_{2n}^{(2p)} \beta_p \tag{8}$$

and

$$\alpha_n U \frac{J'_{2n}(U)}{J_{2n}(U)} = \sum_{p=0}^{\infty} \beta_p W \frac{K'_{\lambda_p}(W)}{K_{\lambda_p}(W)} A_{2n}^{(2p)} \ , \tag{9}$$

respectively.

Because the boundary corresponds to a level curve of R, the circular harmonic functions give the left-hand expressions in (8) and (9), which do not involve summations. Thus, unlike §2.2.5, it is unnecessary to define an augmented matrix which is required to be singular. Rather, (8) and (9) can be combined directly to solve for the vector $\boldsymbol{\beta}$, whose entries are β_i.

$$\mathbf{M}\boldsymbol{\beta} = 0 \tag{10}$$

and the determinant of $\mathbf{M}$, specified by

$$M_{ij} = \left(\frac{UJ'_{2i}(U)}{J_{2i}(U)} - \frac{WK'_{\lambda_j}(W)}{K_{\lambda_j}(W)} \right) A_{2j}^{(2i)}(q) \ , \tag{11}$$

vanishes at only a finite number of real values of U. The lowest of these corresponds to the fundamental mode.

Thus, specifying a combination of V and A, which uniquely defines a butterfly profile, determines M. Roots of this matrix' determinant correspond to propagation constants of such modes as are guided and possess the symmetry outlined in §5.2.1. The field expansion coefficients are then found by solving (10) for $\{\beta_n\}$ and (8) for $\{\alpha_n\}$.

§5.2.3 Axisymmetric limit

If A is small, the departure of the profile from a step profile is negligible. However, examination of (3b) shows that there may be an ambiguity in the axisymmetric limit. The oscillation of the $\cos 2\theta$ may vanish before the inverse-square dependence on R. Below, it is shown that it does. The effect of the axisymmetry ceases before the effect of the depressed inner cladding, and the inverse-square W-fibre (see §5.A.2) results.

To see this, observe that A influences the solution of the butterfly profile only via the parameter q, given in (5). Thus, $A \to 0$ means $q \to 0$, which defines an asymptotic limit of the quantities associated with Mathieu functions. Notably (McLachlan, 1947, §3.33),

$$A_{2j}^{(2j)}(q) \sim 1 + O(q^2) , \tag{12a}$$

$$A_{2j\pm1}^{(2j)}(q) \sim O(q) , \tag{12b}$$

and higher coefficients are all at least an order smaller. Hence, correct to first order, the determinant of M, given in (11), becomes the determinant of a diagonal matrix:

$$\prod_{j=0}^{\infty} \left(\frac{U J_{2j}'(U)}{J_{2j}(U)} - \frac{W K_{\lambda_j}'(W)}{K_{\lambda_j}(W)} \right) = 0 \quad .$$

The factors of this product are eigenvalue equations (63) of the inverse-square W-fibre's modes with the corresponding symmetry.

For small q, (5) and (52) in (6) indicate

$$\lambda_n^2 = 4n^2 + AV^2/2 \quad ,$$

which is result (60) of the inverse-square W-fibre with a depression of depth A/2. Thus, the axisymmetric limit recovered is **not** a step-profile, but an inverse-square W-profile with a depth of the mean of that of the butterfly profile.

From (11) and (12), it is apparent, that, to order q, M has elements of the form

$$M_{ij} = \begin{cases} m_i + O(q^2) \ , & i=j \\ O(q) & , \ i=j\pm1 \\ O(q^2) & , \ \text{elsewhere.} \end{cases}$$

Since U and W satisfy the eigenvalue equation (63), $m_n=0$ for a unique n. Hence, to order q, β is of the form

$$\beta_j = \begin{cases} 1 + D_n q \ , & j=n \\ D_{n\pm1} q & , \ j=n\pm1 \\ 0 & , \ \text{elsewhere,} \end{cases}$$

and the constants D_j are the same as those obtained in §5.6.4 by direct application of perturbation methods.
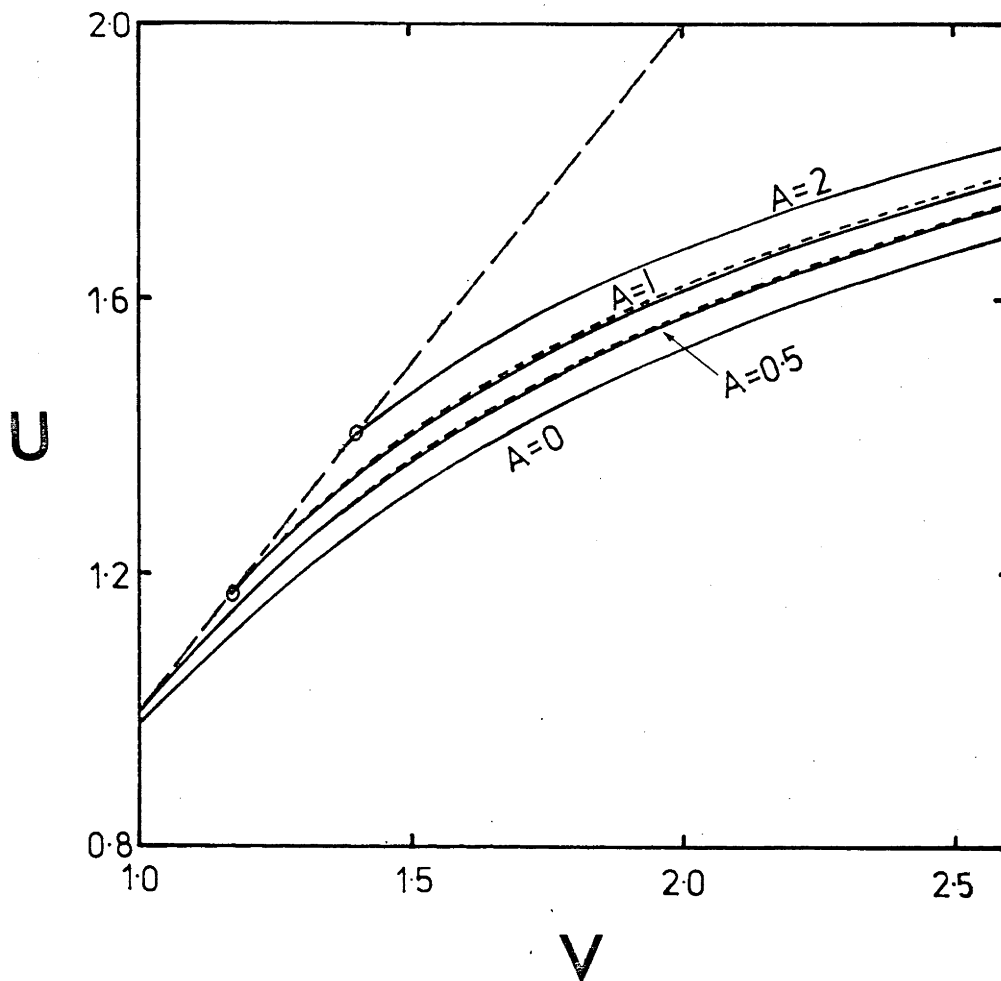
Figure 5.2

For the butterfly profile, the propagation constant, U - a function of normalized frequency, V, for various depth parameters, A - is plotted as the solid curve. The perturbation solution is indicated by a broken curve.

Table 5.1

An indication of the rate of convergence of the propagation constant, U, as the order of the truncated matrix, M, increases.

V	A	matrix size			
		4x4	5x5	6x6	7x7
1.20	0.25	1.1512	1.1512	1.1512	
1.80	0.25	1.4786	1.4787	1.4786	
2.60	0.25	1.7160	1.7160	1.7160	
1.20	0.50	1.1669	1.1669	1.1669	
1.80	0.50	1.5007	1.5009	1.5007	
2.60	0.50	1.7367	1.7367	1.7367	
1.20	1.00	1.1935		−	−
1.80	1.00	1.5399		1.5399	1.5399
2.60	1.00	1.7717		1.7717	1.7717

§5.3   Propagation constant of the fundamental mode

The normalized propagation constant for the fundamental mode is shown in figure 5.2. As expected, increasing the depth parameter increases U. Physically, an increase in A means a greater variation between the core's index and the adjacent region of the cladding.

Of course these values of U were obtained from a truncation of the infinite matrix (11). An indication of how U converges with an increasing order of truncation is provided in table 5.1. There was very good convergence — five figure accuracy — for only a few components.

§5.4   Modal cut-off frequencies

§5.4.1 Fundamental mode

It may be that the determinant of. M — (11) — does not vanish for any real values of U. This means that, for the specified pair A and V, the fundamental mode is not bound, i.e. has a non-zero cut-off frequency. The fundamental mode is cut-off if (e.g. Hussey & Pask, 1982)

$$\int_{\mathcal{A}_\infty} (n^2 - n_{c\ell}^2) \, dS < 0$$

where integration is over the infinite cross-section of the waveguide and $n_{c\ell}$ is the value of the refractive index at R=∞. For the butterfly profile, with A>0, substitution of (1) shows this integral to be always infinite and negative. Thus, all values of A characterize a fibre on which the fundamental mode has a non-trivial cut-off, V_{co}. However, if A is small, V_{co} is small.

To evaluate V_{co}, which depends only on A, setting W=0 and $U=V_{co}=V$ in (3) and proceeding as before shows that solutions are roots of the determinant of the matrix N, defined by

$$N_{ij} = \left(\frac{V_{co} J'_{2i}(V_{co})}{J_{2i}(V_{co})} + \lambda_j\right) A^{(2j)}_{2i}(q)$$

where λ_j is again given by (6). In this case an infinite set of discrete, positive solutions for V_{co} exists. The lowest of these corresponds to the fundamental mode, and the remainder to successively higher-order modes for which ψ, the modal pattern, is symmetric about both the X- and Y-axes.

For this, the LP_{01}-mode, the solution for V_{co} is shown in figure 5.3. It is seen how V_{co} rapidly increases from 0, the A=0, step limit.

§5.4.2 Higher-order modes

To calculate the cut-off values of the LP_{11}-modes, instead of (6), define

$$\lambda_n^2 = \begin{cases} 2q + a_{2n+1}(q), & LP^E_{11}\text{-mode} \\ 2q + b_{2n+1}(q), & LP^O_{11}\text{-mode} \end{cases}$$

where a_{2n+1} and b_{2n+1} are Mathieu characteristic values, and, instead of (4) and (7),

$$\psi = \begin{cases} \sum_{n=0}^{\infty} \alpha_n \dfrac{J_{2n+1}(V_{co}R)}{J_{2n+1}(V_{co})} \{^{\cos}_{\sin}\}((2n+1)\theta) , & R<1 \quad (13\,a) \\ \sum_{n=0}^{\infty} \beta_n (1/R^{\lambda_n}) \{^{ce}_{se}\}_{2n+1}(\theta,q) , & R>1 \quad (13\,b) \end{cases}$$

where upper or lower periodic fuctions apply to the LP^E_{11}- and LP^O_{11}-modes, respectively, q is defined by (5), and ce_{2n+1} and $se2n+1$ are Mathieu functions.
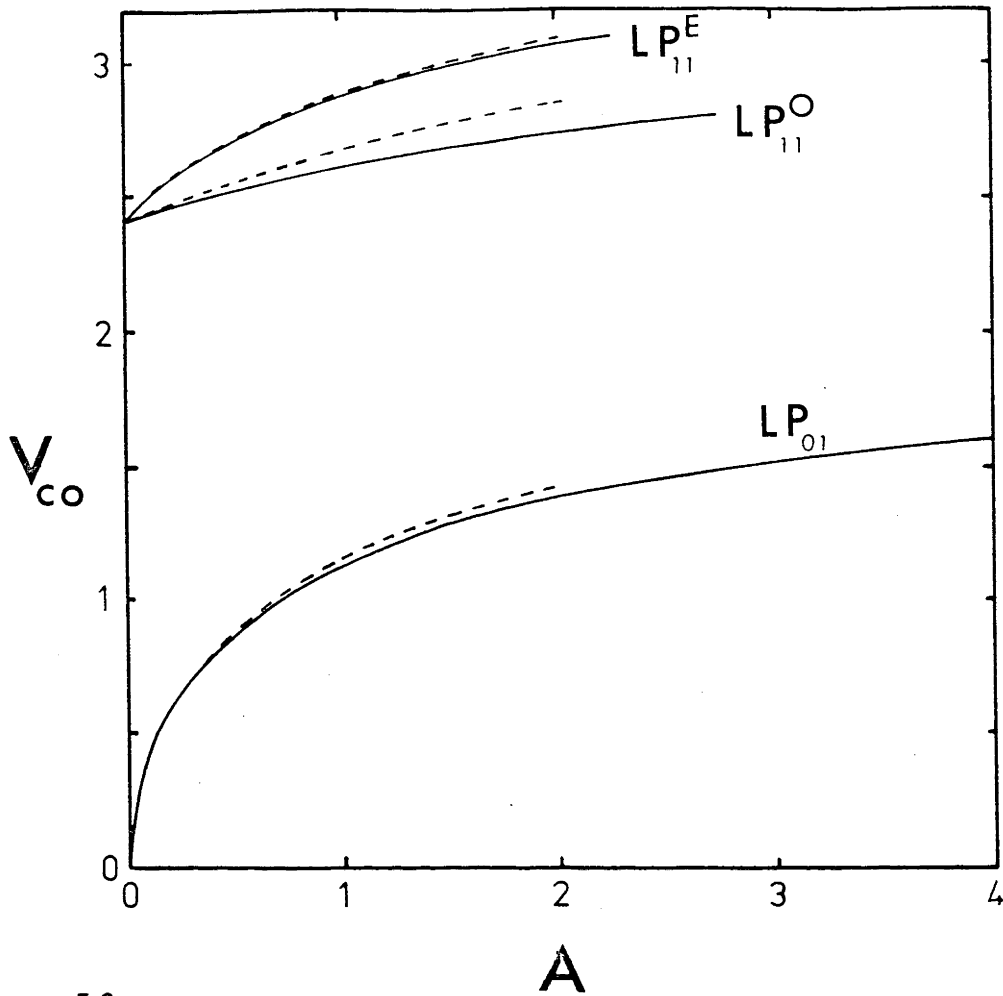
Figure 5.3

For the butterfly profile, the scalar cut-off values, V_{co} – a function of the depth parameter, A – are shown by the solid curves. The perturbation approximations are indicated by the broken curves.

Table 5.2

The polarization corrections to the scalar cut-off frequencies of the first three modes, for various depth parameters, A. $\Delta = 1/3\%$.

mode	LP_{01}		LP_{11}^{E}		LP_{11}^{O}	
A	(X) V_{co}	(Y) V_{co}	(X) V_{co}	(Y) V_{co}	(X) V_{co}	(Y) V_{co}
0.75		1.032	2.811	2.806	2.579	2.575
1.00		1.137	2.885	2.882	2.620	2.617
1.25	1.224	1.219	2.945	2.941	2.657	2.653
1.50	1.290	1.284	2.995	2.991	2.689	2.685
1.75	1.345	1.339	3.037	3.033	2.717	2.713
2.00	1.391	1.385		3.070		2.739
2.25	1.431	1.425	3.105	3.101		2.763

This time the standard continuity conditions produce the matrix

$$
N_{jk} = \begin{cases}
\left(V_{co}\, \dfrac{J'_{2j+1}(V_{co})}{J_{2j+1}(V_{co})} + \lambda_k\right) A^{(2k+1)}_{2j+1}(q) \ , & LP^E_{11}\text{-mode} \\[4ex]
\left(V_{co}\, \dfrac{J'_{2j+1}(V_{co})}{J_{2j+1}(V_{co})} + \lambda_k\right) B^{(2k+1)}_{2j+1}(q) \ , & LP^O_{11}\text{-mode} \ ,
\end{cases}
$$

where $A^{(2k+1)}_{2j+1}$ and $B^{(2k+1)}_{2j+1}$ are given in the expansions (45) and (46), and the determinant of this vanishes at cut-off.

The solutions for V_{co} are shown in figure 5.3 , where it is evident that the LP^O_{11}-mode is cut-off before the LP^E_{11}-mode. Also, away from A=0, the two values rapidly separate.

§5.4.3 **Polarization corrections**

In the preceeding sections, the cut-off values calculated are normalized scalar cut-off frequencies, i.e. the limiting values as $\Delta \to 0$. For a real waveguide, Δ is finite and there will be corrections of order Δ to the scalar cut-off values. As explained in §P.3.4, for a birefringent structure, the cut-off frequencies of different polarization states differ. Thus, for the butterfly fibre, the scalar fudamental and two higher-order cut-off frequencies become six cut-off frequencies when corrections for polarization effects are included.

From (P.12) and (2), the correction to the scalar cut-off is

$$
\delta V^{(p)}_{co} = \frac{\Delta\, N_p}{V_{co}\, D} \tag{14}
$$

where

$$
D = 2\int_0^{2\pi} d\theta \int_0^1 dR\, R\psi^2 - A\int_0^{2\pi} d\theta \int_1^\infty dR\, \frac{\psi^2}{R}(1+\cos 2\theta) \tag{15a}
$$

and

$$N_P = - \int R dR \int_0^{2\pi} d\theta \frac{\partial g}{\partial P} \frac{\partial \psi}{\partial P}^2 \quad , \qquad (15b)$$

with P, either X or Y, indicating the linear polarization state and ψ being the modal field at cut-off.

Directly substituting (13) in these formulae, with the aid of the notation p=0,1,-1 for the LP_{01}^-, $LP_{11}^E{}^-$, and $LP_{11}^O{}^-$modes, respectively, and the definitions

$$c_n = \begin{cases} a_{2n} & , \ p=0 \\ a_{2n+1} & , \ p=1 \\ b_{2n+1} & , \ p=-1 \ ; \end{cases}$$

$$\lambda_n^2 = 2q + c_n \ ;$$

and

$$C_k^\ell = \begin{cases} A_{2n}^{(2\ell)} & , \ p=0 \\ A_{2n+1}^{(2\ell+1)} & , \ p=1 \\ B_{2n+1}^{(2\ell+1)} & , \ p=-1 \ ; \end{cases}$$

gives, with the argument V_{co} omitted from J_k,

$$D = \sum_{n=0}^{\infty} (1+\delta_{n0}\delta_{p0}) \left(\alpha_n^2 (1 - \frac{J_{2n+|p|-1} \ J_{2n+|p|+1}}{J_{2n+|p|}^2}) - \frac{A\beta_n^2}{2\lambda_n} \right)$$

$$- \frac{A}{2} \sum_{k,\ell,m,n=0}^{\infty} \frac{\beta_k \beta_\ell C_\ell^k C_n^\ell}{\lambda_k + \lambda_\ell} Y_{lmn} \quad ,$$

$$N_X = \frac{A}{2}T_0 + (\frac{2+3A}{2})T_1 + AT_2 + (\frac{4+3A}{8})T_3 + (\frac{1+A}{2})T_4 + \frac{A}{8}T_5$$

$$- AT_6 - 2AT_7 - 3AT_8 \quad,$$

and

$$N_Y = \frac{A}{2}T_0 - (\frac{2+A}{2})T_1 - AT_2 + (\frac{4+A}{8})T_3 - \frac{1}{2}T_4 - \frac{A}{8}T_5$$

$$- AT_6 + 2AT_7 + 3AT_8 \quad,$$

where, with $\ell = 1,2$,

$$T_0 = \sum_{n=0}^{\infty} \alpha_n^2 (1 + \delta_{n0}\delta_{p0}) \quad,$$

$$T_\ell = \sum_{n,m=0}^{\infty} \frac{\alpha_n \alpha_m}{2} Y_{\ell nm} \quad,$$

$$T_3 = \sum_{n=0}^{\infty} \alpha_n^2 (1+\delta_{n0}\delta_{p0})\, 2V_{co} \frac{J'_{2n+|p|}}{J_{2n+|p|}} \quad,$$

$$T_{3+\ell} = \sum_{n,m=0}^{\infty} \alpha_n \alpha_m \frac{V_{co} J'_{2n+|p|}}{J_{2n+|p|}} Y_{\ell nm} \quad,$$

$$T_6 = \sum_{n=0}^{\infty} \beta_n^2 \frac{(1+\delta_{n0}\delta_{p0})}{2 + 2\lambda_n} \quad,$$

$$T_{6+\ell} = \sum_{j,k,m,n=0}^{\infty} \frac{\beta_n \beta_m}{2(\lambda_n + \lambda_m + 2)} C_j^m C_k^n Y_{\ell jk} \quad,$$

and

$$Y_{jnm} = \delta_{j\,|n-m|} + \delta_{j\,n+m+|p|}$$

with a positive sign for p=0,1 but a negative sign for p=-1.

In table 5.2 are listed the first six normalized cut-off frequencies V_{co}, those of the two polarization states of the fundamental and first two higher-order modes. In this case, Δ is chosen as $1/3\%$, a physically useful value. A higher value of Δ would produce, naturally, greater separation of the values for different polarization states corresponding to the same scalar mode.

Varnham (1984) measured the first six cut-off frequencies of a bow-tie fibre, and found a much greater separation of polarization states than predicted by this isotropic model. This is discussed in §5.7.2.

§5.5 Geometric birefringence

The asymmetry of the butterfly profile means that there will be geometric birefringence. In particular, the fundamental mode, which is examined subsequently, exhibits this phenomenon.

Using the method of §P.3.3, the normalized birefringence can be obtained from the scalar modal field and propagation constants. Firstly, because of the orthogonality of the periodic functions, the normalization integral follows simply from the expansions (4) and (7),

$$\|\psi\|^2 = \pi \sum_{n=0}^{\infty} \left(\frac{1+\delta_{n0}}{2}\right) \left(\alpha_n^2 \left(1 - \frac{4nJ_{2n+1}}{UJ_{2n}} + \frac{J_{2n+1}^2}{J_{2n}^2}\right) + \beta_n^2 \left(\frac{K_{\lambda_n+1}^2}{K_{\lambda_n}^2} - \frac{2\lambda_n K_{\lambda_n+1}}{WK_{\lambda_n}} - 1\right)\right)$$

where again the implicit arguments for J_{ℓ} and K_{ν} are U and W, respectively.

§5.5.1 Simplification of the integrals

Because the core-cladding interface corresponds to a constant function of the polar angle, θ, the θ-derivatives of ψ within the integrals of (P.10b) can be removed straightforwardly by integrating by parts. This means

$$B_p = \frac{1}{V^2 \|\psi\|^2} \int_{\infty} dS \left((2g_\theta \sin2\theta - g_{\theta\theta}\cos2\theta - 2Rg_R\cos2\theta - \frac{1}{R}g_{R\theta}\sin2\theta) \frac{\psi^2}{R^2} \right.$$

$$\left. + \left(\frac{1}{R}g_\theta \sin2\theta - g_R\cos2\theta\right) \psi_R^2 \right), \tag{16}$$

where use is made of the periodicity in θ of ψ and g. Examination of

(2) reveals g_R includes $\delta(R-1)$, the Dirac delta function. After complete substitution of (2) in (16), considering also the angular symmetry of the expansions (4) and (7), the integral in (16) gives

$$B_p = \frac{\pi}{V^2 \|\psi\|^2} \left((2+2A)T_1 + 2AT_2 + \frac{1}{4}AT_3 + (\frac{2+1}{2}A)T_4 \right.$$
$$\left. + \frac{1}{2}AT_5 - 4AT_6 - 6AT_7 \right), \qquad (17)$$

where, with $\ell=1,2$,

$$T_\ell = \frac{1}{\pi} \int_0^{2\pi} d\theta \, \psi^2(1,\theta) \cos(2\ell\theta) \qquad (18a)$$

$$= \frac{1}{2} \sum_{n=0}^{\infty} \alpha_n \left(\alpha_{n+\ell} + (1+\delta_{n\ell})\alpha_{|n-\ell|} \right);$$

$$T_3 = \frac{1}{\pi} \int_0^{2\pi} d\theta \, \psi_R^2(1,\theta) \qquad (18b)$$

$$= 2 \sum_{n=0}^{\infty} U\alpha_n^2 (1+\delta_{n0}) \frac{J'_{2n}}{J_{2n}};$$

$$T_{3+\ell} = \frac{1}{\pi} \int_0^{2\pi} d\theta \, \psi_R^2(1,\theta) \cos(2\ell\theta) \qquad (18c)$$

$$= \frac{1}{2} \sum_{n=0}^{\infty} U\alpha_n \left(\left(\frac{J'_{2n+2\ell}}{J_{2n+2\ell}} + \frac{J'_{2n}}{J_{2n}} \right) \alpha_{n+\ell} \right.$$
$$\left. + (1+\delta_{n\ell})\alpha_{|n-\ell|} \left(\frac{J'_{|2n-2\ell|}}{J_{|2n-2\ell|}} + \frac{J'_{2n}}{J_{2n}} \right) \right);$$

$$T_{5+\ell} = \frac{1}{\pi} \int_0^{2\pi} d\theta \cos(2\ell\theta) \int_1^{\infty} dR \, \frac{1}{R^3} \psi^2(R,\theta) \qquad (18d)$$

$$= \frac{1}{2} \sum_{r,s,k=0}^{\infty} \beta_r \beta_s \int_1^{\infty} dR \, R^{-3} \frac{K_{\lambda_r}(WR)K_{\lambda_s}(WR)}{K_{\lambda_r} K_{\lambda_s}} A_{2k}^{(2r)}$$
$$\times \left(A_{2k+2\ell}^{(2s)} + (1+\delta_{k\ell})A_{|2k-2\ell|}^{(2s)} \right);$$

where the implicit arguments of J_n and K_ν are U and W, respectively.
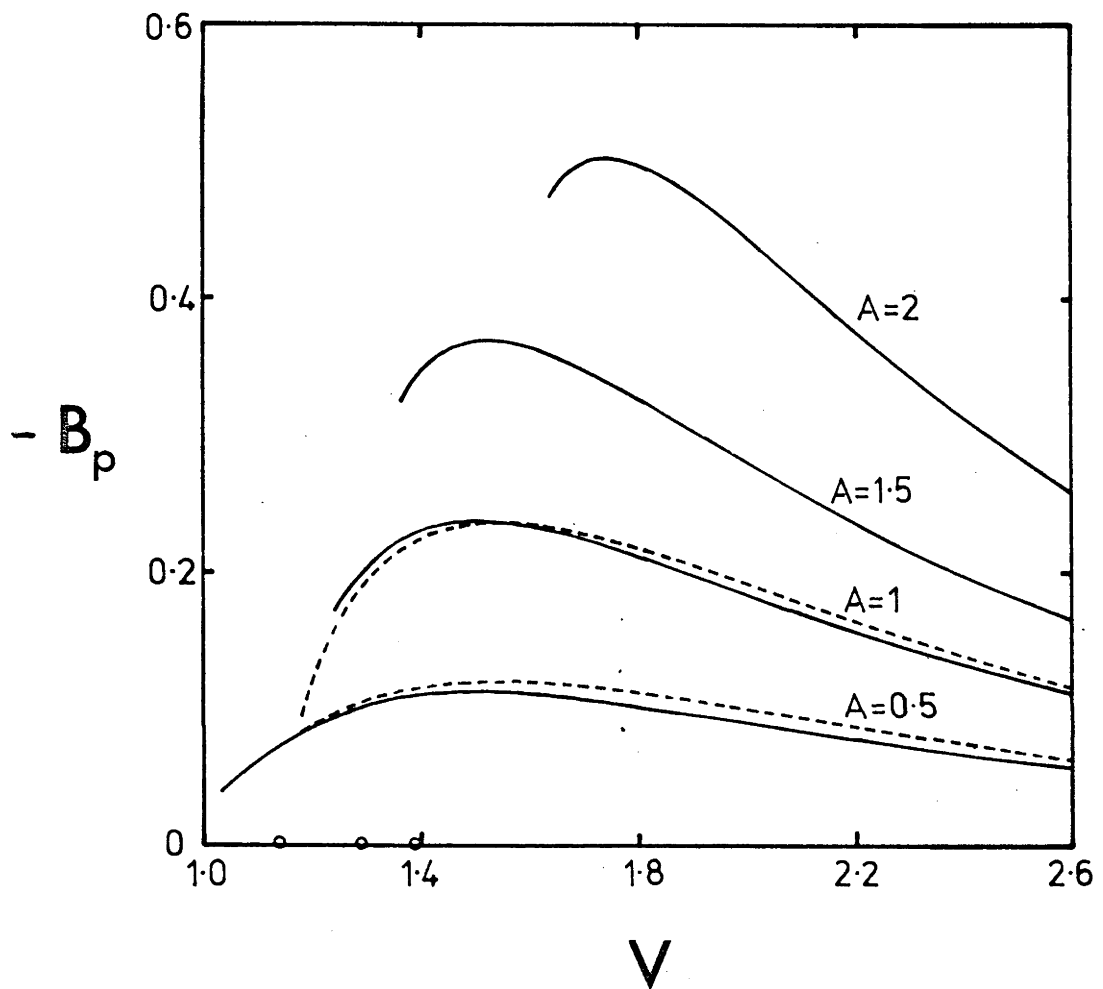
Figure 5.4

For the butterfly profile, the normalized birefringence, B_p — a function of normalized frequency, V for various values of the depth parameter, A — is shown as the solid curves. The peturbation approximation is shown by the broken curves.

§5.5.2 Results

B_p is negative, which merely indicates that the fast and slow axes are interchanged with respect to their normal definitions. In the butterfly fibre, the mode, polarized in the directions of the depressions, has a faster phase velocity.

Figure 5.4 shows the normalized birefringence for several values of the depth parameter. The same trend is apparent as in seen in figures 3.9 and 4.6, for the step elliptical and step rectangular waveguides, respectively. Increasing axi-asymmetry, measured by A, causes an increase in the maximum value of geometric birefringence and increases the value of V at which this is attained.

In a stressed SMSP fibre, the actual birefringence is dominated by the component due to anisotropy. For the bow-tie fibre (Varnham, 1984), this is approximately 60 times greater than the maximum value indicated in figure 5.4. The improvement of the model to include this effect is discussed in §5.7.

§5.6 Perturbation solution

Having solved exactly for the properties of the butterfly profile, it is useful to assess the accuracy of a standard approximation technique for this asymmetric refractive index distribution. Of interest here is the perturbation method, which starts with an axisymmetric profile.

As explained in in §5.2.3, the optimal choice of the first approximation – the circular profile – is the inverse-square W-profile, with a depth parameter of A/2.

§5.6.1 General method

Consider a butterfly profile as $A \to 0$. This permits the axi-asymmetric portion of the profile to be treated as a perturbation. The method for such treatment is expounded in Snyder & Love (1983, ch18). In essence, the refractive index is decomposed:

$$n^2(R, \theta) = n_0^2(R) + An_1^2(R, \theta) \ , \qquad (19a)$$

where n_0^2 describes an axisymmetric profile which is chosen either because it has a simple solution, or because n_1^2 displays such benefits. This decomposition implies the division of the shape-function as

$$g(R, \theta) = g_0(R) + Ag_1(R, \theta) \ , \qquad (19b)$$

where g_0 is the chosen axisymmetric profile's shape-function and

$$g_1 = \frac{n_1^2(R, \theta)}{2 \Delta n_{c\ell}^2} \ .$$

Given the decomposition (19), the propagation constants U and W can be easily reconstructed in terms of the values U_0 and W_0 of the chosen axisymmetric distribution, $g_0(R)$, which has a modal field, $\overline{\psi}_0(R)$. The true modal field, ψ, will differ from $\overline{\psi}_0$ only by a correction term of order A, giving

$$\psi = \overline{\psi}_0 + A\overline{\psi}_1 \ . \qquad (20)$$

For a perturbation correction (Snyder & Love, eq(18-4)),

$$W^2 - W_0^2 = \frac{\rho^2 k^2}{\langle \psi, \overline{\psi}_0 \rangle} \int_{\mathscr{A}_\infty} dS \, (n^2 - n_0^2) \, \overline{\psi\psi}_0$$

$$\Rightarrow \quad W^2 \approx W_0^2 + \frac{AV^2}{\|\psi_0\|^2} \int_{\mathscr{A}_\infty} dS \, g_1 \overline{\psi}_0^2 \, , \tag{21}$$

where the integrals are evaluated over the infinite cross-section, and use was made of (19) and (20). Of course, U follows immediately from

$$U^2 = V^2 - W^2 \, .$$

Thus, the propagation eigenvalues are found, correct to order A, in terms of the eigenvalues and modal field of the selected, axisymmetric profile n_0.

Once these eigenvalues are determined, the modal field, ψ, can be constructed, again to order A. This is possible since U and W are correct to order A. Solutions are sought in the form

$$\psi \approx \psi_0 + A\psi_1 \, . \tag{22}$$

It is stressed that the corresponding barred and unbarred functions in (20) and (22) are **not** the same. In (20), $\overline{\psi}$ is the field produced by the profile n_0 and $\overline{\psi}_1$ is everything else; in (22), ψ_0 and ψ_1 are the first two terms in the expansion of ψ, the exact scalar field of the butterfly fibre.

Sustituting (19b) and (22) into (3) and only retaining terms to first order in the small parameter A, one observes

$$L[\psi_0] + AV^2 g_1 \psi_0 + AL[\psi_1] = 0 \ , \tag{23}$$

where L is the partial differential operator,

$$L = \nabla^2 - W^2 + V^2 g_0 \ , \tag{24}$$

corresponding to the profile n_0. Again, ∇^2 is the two dimensional

Laplacean operator. Since g_0 is axisymmetric, L will produce a

convenient set of functions, $\{F_n(R)\cos(n\theta), F_n(R)\sin(n\theta)\}$, in which to

expand ψ and where the form of F_n depends on the specific behaviour of

g_0.

Independently equating the co-efficient of each power of A in (23)

to zero yields a pair of coupled, partial differential equations:

$$L[\psi_0] = 0 \tag{25a}$$

and

$$L[\psi_1] = -V^2 g_1 \psi_0 \ . \tag{25b}$$

To recover the solution of the axisymmetric structure as $A \to 0$, it follows

that

$$\psi_0 = F_n(R) \ {\cos \atop \sin}(n\theta) \ , \tag{26}$$

and the solution for ψ_1 is

$$\psi_1 = \psi_s + \sum_{\ell=0}^{\infty} F_\ell(R)(a_\ell \cos(\ell\theta) + b_\ell \sin(\ell\theta)) \tag{27}$$

where ψ_s is any particular solution of the inhomogeneous equation (25b),

with the replacement (26) completed. Determination of ψ_s can be

difficult, particularly if g_1 is of such a form that the right-hand

expression of (25b) is a solution of (25a).

§5.6.2 Note on normalization

At this juncture, it is worth elaborating on a feature of this analysis, which is, at best, poorly explained in the literature. In defining any modal field, ψ, there is always an ambiguity of amplitude which is resolved by some normalization condition. Sometimes it is required that

$$\|\psi\|^2 = N , \tag{28}$$

where N is specified. More commonly, for an axisymmetric profile

$$\psi(R=1) = 1 .$$

In any perturbation analysis, a normalization condition is imposed in the definition of ψ_0 of the expansion (22). It is **always** true that

$$\psi_1 = P\psi_0 + \psi_c \tag{29}$$

where ψ_c is uniquely determined using continuity requirements but P remains arbitrary. However, by adding $A\psi_1$ to ψ_0, the new ψ no longer satisfies the required normalization constraint. By correctly choosing a unique value for P, this can be satisfied again.

For example, replacing (22) and (29) in condition (28) shows, as ψ_0 satisfies (28), that

$$P = -\frac{1}{N} \langle \psi_0, \psi_c \rangle.$$

§5.6.3 Employing the inverse-square W-profile

Thus far, the analysis is valid for any choice of axisymmetric profile. Specifically, the inverse-square W-profile produces for (19),

the division

$$g_0 = \begin{cases} 1 & , \ R<1 \\ -A/2R^2 & , \ R>1 \end{cases}$$

(30a)

(30b)

and

$$g_1 = \begin{cases} 0 & , \ R<1 \\ -\cos(2\theta)/2R^2 & , \ R>1 \ . \end{cases}$$

(31a)

(31b)

When this is exploited in (21), it confirms that there are no first order corrections to U and W. Thus, the propagation constants assume their values for the unperturbed inverse-square W-fibre, U_0 and W_0, respectively.

Their accuracy is shown in figure 5.2. This approximation does worsen for increasing values of A, but, for A=1, the relative error is less than 0.4% over the entire indicated range of V.

§5.6.4 Modal field

For convenience, denote with the subscripts I and E quantities, respectively, interior and exterior to the core-cladding interface. Because g_0 is discontinuous, it is particularly useful in the analysis of ψ to consider ψ_I and ψ_E separately.

Since it is the fundamental mode which is of interest, ψ will be symmetric about both the X- and Y-axes, as, from (1), it is clear that n^2 displays this behaviour. Thus, in (26), ψ_0 is merely F_0 and only the even cosine harmonics are required in the series (27). Considering the butterfly profile (1), it follows that, within the core, the refractive index is axisymmetric. The implications of this are plain if (31) is substituted into (25b): ψ_s is only non-zero within the cladding.

With these simplifications, from (26) and (27),

$$\psi_{I0} = J_0(UR) \,/\, J_0(U) \tag{32}$$

and

$$\psi_{I1} = \sum_{n=0}^{\infty} \alpha_n \, J_{2n}(UR) \, \cos(2n\theta) , \tag{33}$$

since the operator L of (24) corresponds to that of a step-profile.

From (24), within the cladding, (30) produces the operator of the inverse-square W-profile. Thus, from (26), (27), (59) and the symmetry simplifications,

$$\psi_{E0} = K_{\nu_0}(WR) \,/\, K_{\nu_0}(W) \tag{34}$$

and

$$\psi_{E1} = \psi_s + \sum_{n=0}^{\infty} \beta_n \, K_{\nu_n}(WR) \, \cos(2n\theta) , \tag{35}$$

where

$$\nu_n^2 = 4n^2 + \frac{AV^2}{2} .$$

Substituting (24), (30), (31), and (34) in (25b) shows that ψ_s is a solution of

$$(\nabla^2 - W^2 - \frac{\nu_0^2}{R^2}) \psi = V^2 \frac{\cos(2\theta) K_{\nu_0}(WR)}{2R^2 K_{\nu_0}(W)} ,$$

inspection of which shows

$$\psi_s = -V^2 \frac{K_{\nu_0}(WR)\cos(2\theta)}{8K_{\nu_0}(W)} . \tag{36}$$

Naturally, both ψ and $\partial\psi/\partial R$ must be continuous at R=1, and this will determine all but one of the constants $\{\alpha_n\}$ and $\{\beta_n\}$ in the expansions (33) and (35). As explained in §5.6.2, the remaining constant can be found from the normalization requirement.

Using (22) and (32)-(36), continuity shows that,

$$\alpha_\ell = 0 = \beta_\ell , \qquad \forall\; \ell \geqslant 2 , \qquad (37a)$$

$$\alpha_1 = \frac{V^2}{8J_0} \; \frac{\dfrac{K'_{\nu_0}}{K_{\nu_0}} + \dfrac{K'_{\nu_1}}{K_{\nu_1}}}{\dfrac{K'_{\nu_0}}{K_{\nu_0}}\left(1 - \dfrac{4}{U^2} - \dfrac{2WK'_{\nu_1}}{U^2 K_{\nu_1}}\right) + 2 + \dfrac{K'_{\nu_1}}{K_{\nu_1}}} \qquad (37b)$$

$$\beta_1 = \alpha_1 J_2 / K_{\nu_1} , \qquad (37c)$$

and

$$\beta_0 = \frac{\alpha_0 J_0}{K_{\nu_0}} , \qquad (37d)$$

where, for brevity, the arguments U and W are omitted from J_n and K_μ, respectively, and α_0 remains as the undetermined constant. Also,

$$\chi = U \frac{J_1(U)}{J_0(U)} = -W \frac{K'_{\nu_0}(W)}{K_{\nu_0}(W)}$$

which defines the eigenvalue equation for U and W. Thus, combining (22) and (32)-(37), the modal field, correct to order A, is constructed:

$$\psi = \begin{cases} \dfrac{J_0(UR)}{J_0}(1+A\alpha_0 J_0) + A\alpha_1 J_2(UR)\cos(2\theta) & , \quad R \leqslant 1 \\[4mm] \dfrac{K_{\nu_0}(WR)}{K_{\nu_0}}(1+A\alpha_0 J_0) + A\beta_1 K_{\nu_1}(WR)\cos(2\theta) - \dfrac{AV^2 K_{\nu_0}(WR)}{8K_{\nu_0}}\cos(2\theta), \quad R \geqslant 1, \end{cases} \qquad (38)$$

with α_1 and β_1 given by (37b) and (37c). This agrees with the result of §5.2.3, where the axisymmetric limit of the exact solution was recovered.

§5.6.5 Geometric birefringence

Using (38), the normalization integral, $\|\psi\|^2$, follows, correct to first order in A.

$$\|\psi\|^2 = \frac{\pi V^2}{2U^2 W^2} (2\chi^2 - AU^2) (1 + 2A\alpha_0 J_0) . \tag{39}$$

Thus, it is clear how, as explained §5.6.2, this can determine the value of α_0.

Substituting (38) and (39) directly into (17) and (18), the value of the normalized birefringence, correct to order A, is

$$B_p = \frac{2W^2 \chi U^2 A^2}{V^4 (2\chi^2 - AU^2)} \left(4\alpha_1 J_0(1 - \frac{\chi^2}{U^2}) - 1\right) .$$

The utility of this approximation is indicated in figure 5.4, where this perturbation solution is compared with the exact solution for A=0.5 and A=1.0. It is apparent that the perturbation expression overestimates B_p, and assumes its peak value at a higher value of V. Nevertheless, the accuracy is remarkable: for A=1, the relative error is 3.9%, 4.0% and −3.1% at V=2.5, 2.0 and 1.4, respectively.

§5.6.6 Scalar cut-off frequencies

Next, using the results of §1.A, estimates for the same cut-off frequencies as calculated in §5.4.1 and §5.4.2 are obtained.

For the fundamental mode, replacing (31) in (1.18) shows that no first order correction exists. The normalized cut-off is

$$V_{co} = \overline{V}_{co} \quad ,$$

where $\overline{V}_{co}$, given by (68), is the cut-off frequency of an inverse-square W-fibre characterized by A/2.

To distinguish between the two higher-order modes it is useful to write explicitly the corresponding modal fields on the axisymmetric fibre:

$$\overline{\psi} = \begin{cases} \dfrac{J_1(\overline{V}_{co}R)}{J_1(\overline{V}_{co})} \{^{\cos}_{\sin}\}\theta \; , & R<1 \\[2em] \dfrac{1}{\lambda_0}\dfrac{}{R} \{^{\cos}_{\sin}\}\theta \; , & R>1 \; , \end{cases} \tag{40}$$

where cos and sin refer to the LP^E_{11}- and LP^O_{11}-modes, respectively. The scalar cut-off frequency is the same for both modes on an axisymmetric structure, where they are degenerate. Also,

$$\nu_0^2 = \tfrac{1}{2}A\overline{V}_{co} + 1 \; .$$

Using (31) and (40) in (1.18) shows

$$V_{co} = \overline{V}_{co}\left(1 \pm A\frac{J_1^2(\overline{V}_{co})}{4\lambda_0(J_1^2(\overline{V}_{co}) - J_2(\overline{V}_{co})J_0(\overline{V}_{co}))}\right) \; ,$$

from which it is readily seen how the the butterfly fibre's axi-asymmetry, measured by A, does separate the cut-off values of the first two higher-order modes.

However, as A→0, corresponding to slight axisymmetry, the true scalar modes are not these LP-modes, but linear combinations of these (Snyder & Young, 1978) with different symmetry. Remember, on an axisymmetric waveguide, the higher-order modes are not plane polarized. In figure 5.3, it is clear how rapidly the LP-modes are established; the two higher-mode cut-off frequencies quickly separate.

Figure 5.3 also shows the accuracy of the perturbation result. For A=1, the relative errors in normalized cut-off frequencies of the LP_{01}-,

LP_{11}^O- and LP_{11}^E-modes, are 1.9%, 2.3% and 0.2%, respectively. The last result is exceptionally accurate.

§5.7   Incorporation of anisotropy

On an anisotropic waveguide the guidance of the mode polarized along the Y-axis is controlled by a refractive index profile which differs from that which guides the X-polarized mode. Denote these different profiles as $n^{(Y)}$ and $n^{(X)}$, respectively. The different modal parameters of the different polarization states can be obtained by separately solving for the modes of each refractive index profile.

The conventional method of treating anisotropy is to consider the difference, $n^{(X)}-n^{(Y)}$, as constant over the entire infinite cross-section. As explained in §P.4, this is an oversimplification which does not reflect the physical situation as V→0. Hence, the model needs improving.

§5.7.1 Model

Using an analysis of the stress, it is possible (e.g. Okamoto et al, 1981; Chu & Sammut, 1984) to calculate the detailed form of the anisotropy over the cross-section. However, with a simple model like the butterfly profile, it is better to use a simple model of the anisotropy. An exact replication of experimental results would require an improvement on the refractive index defined in (1).

The imposed anisotropy is

$$n^{(X)^2} - n^{(Y)^2} = \begin{cases} 2\,\delta n_{c\ell}^2 & , R<1 \\[2ex] \dfrac{2\,\delta n_{c\ell}^2 \cos^2\theta}{R^2} & , R>1 \end{cases} \tag{41}$$

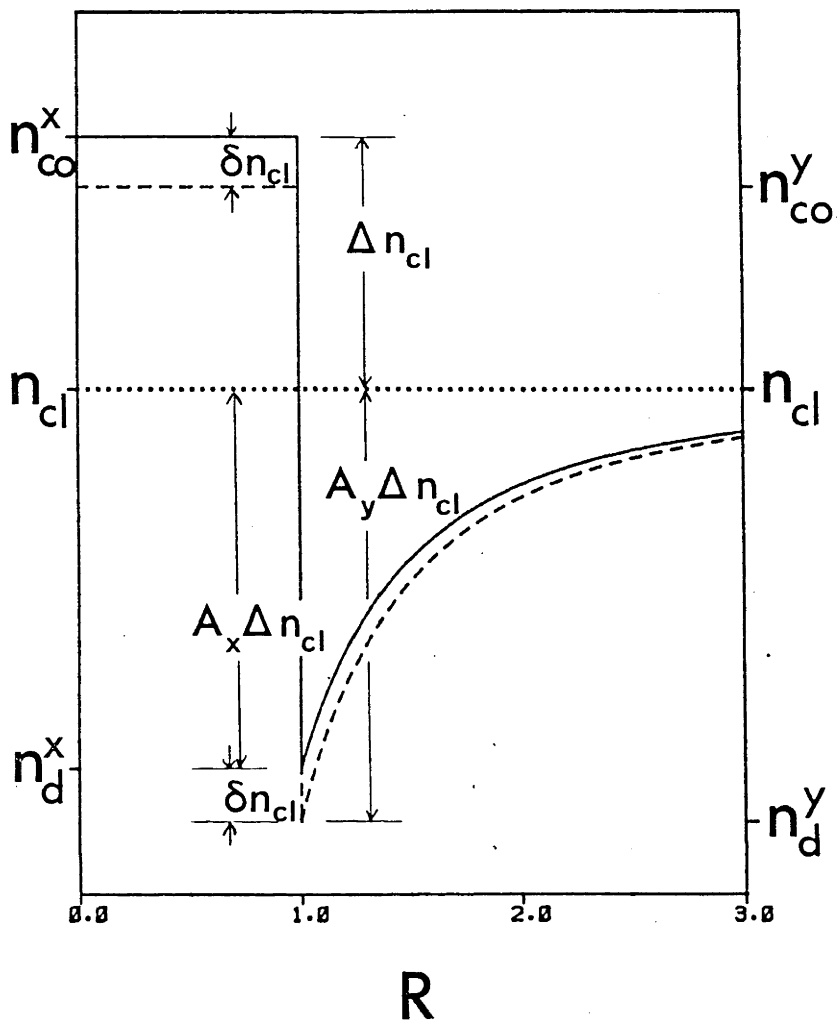This leads to the two profiles shown in figure 5.5. n(X) is the solid

Figure 5.5

The anisotropy, (41), imposed on the butterfly fibre. The X-profile is the solid curve; the Y-profile is the broken curve displaced by $\delta n_{c\ell}$ in the core.

curve; $n^{(Y)}$ the broken one. The anisotropy is the difference between these two. While constant in the core, the anisotropy vanishes as $R \rightarrow \infty$. Thus it reflects the physical conditions: there is no stress and resultant anisotropy on the outside, free-surface of a fibre. While the lack of radial continuity at $R=1$ is unphysical, it does not detract from the model's utility.

The behaviour of the butterfly profile is fully specified by the depth parameter. If this is A_X for the X-profile, then for the Y-profile

$$A_Y = \frac{A_X 2\Delta + 2\delta}{2\Delta - 2\delta}$$

$$= A_X + \frac{(\delta/\Delta)(A_X+1)}{1 - (\delta/\Delta)} > A_X .$$

(42)

Thus, the Y-profile is chacterized by a depth parameter greater than that which describes the X-profile. The next sections show how this causes the distinctive behaviour of an anisotropic fibre.

§5.7.2 Anisotropic birefringence

The anisotropy decreases with increasing distance from the axis. Thus, as the modal field spreads further into the cladding, the effective anisotropy decreases. In §P.4, the V-dependent correction factor to the anisotropic birefringence was defined as, (P.13)

$$H_B = \frac{\beta_x - \beta_y}{k(n^{(X)} - n^{(Y)})} .$$

This is used with the assumption of constant anisotropy. For the model (40), which has variable anisotropy, the normalizing denominator is the core's anisotropy, $(n^{(X)} - n^{(Y)}) = \delta n_{c\ell}$. β_x and β_y are the scalar propagation constants of the profiles described by A_X and A_Y, respectively. β, as found via U in §5.3, is a function only of A and
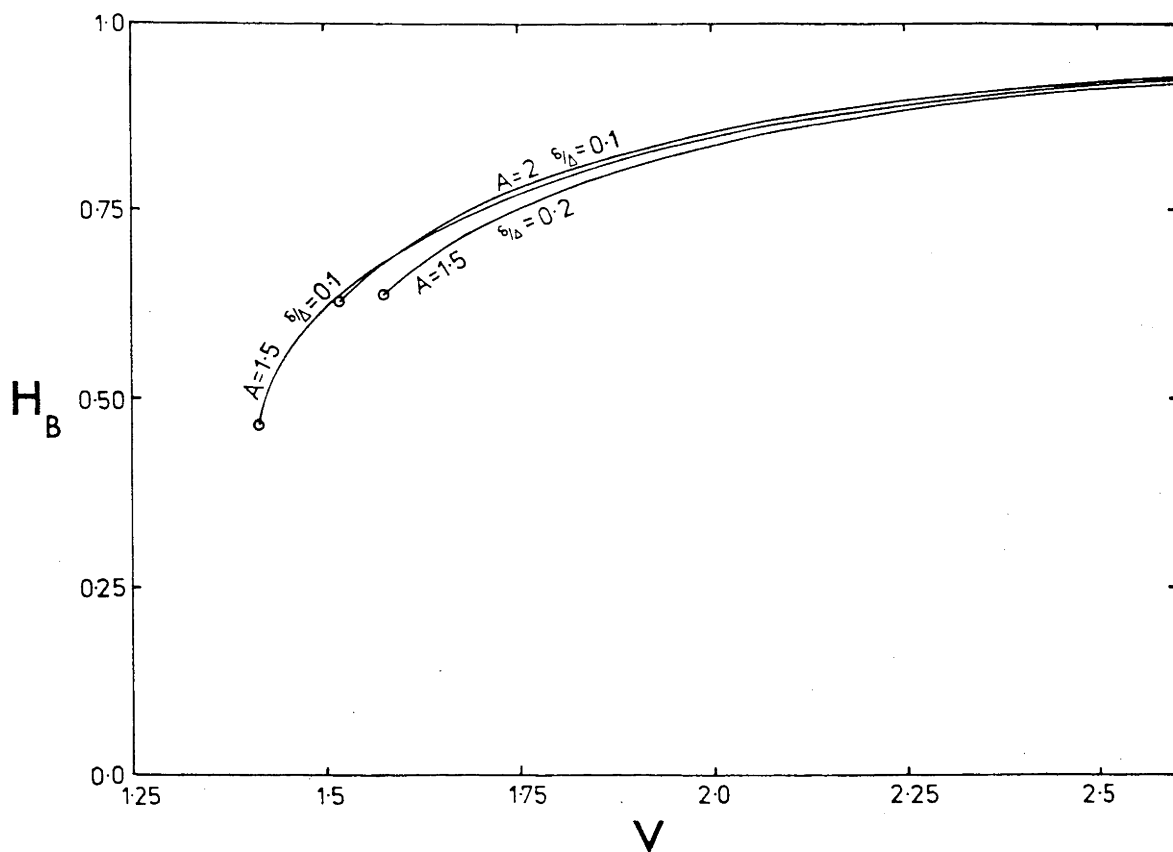
Figure 5.6

The birefringence correction function, H_B, of the butterfly profile for various combinations of parameters.

Table 5.3

The ratio of scalar cut-off frequencies of the two polarization states of the first three modes on an anisotropic butterfly fibre.

mode	experiment	$A_x = 1.5$	$A_x = 2.0$
LP_{01}	1.08	1.09	1.09
LP_{11}^0	1.09	1.06	1.06
LP_{11}^E	1.08	1.07	1.06

V. With the two different depth parameters, the results in figure 5.6 were obtained. The value of V is defined for the X-profile. The selected values of δ/Δ match the measurements of bow-tie fibres by Varnham (1984).

It is seen that $H_B(V)$ is very sensitive to the choice of δ/Δ, the relative anisotropy, but not so sensitive to the value of A_X. This is expected. A_X measures the strength of the geometric influences on H_B, whereas δ/Δ measures the anisotropic effects. In figure 5.6, the circles indicate when the Y-polarized mode is cut-off. Even at this point, the geometric birefringence is swamped by the anisotropic birefringence. For A=2 and $(\delta/\Delta)=0.1$, with the same normalization as used in figure 5.6 and $\Delta=1/3\%$, the geometric birefringence is less than 0.02 for all V.

Although the numbers differ, the general form of the curves in figure 5.6 agrees with previous attempts to evaluate H_B for the bow-tie fibre. Okamoto (1984), using a finite element analysis, calculated the detail of the anisotropy and then defined an equivalent step-fibre, whose modal field was used to find H_B. Varnham (1984) also evaluated an approximation which used the modal field of a circular step fibre.

A significant difference in behaviour between previous results and those of the butterfly profile is that this model has a fundamental mode which is cut-off. As a finite cut-off value is approached, ψ spreads further into the cladding than does the field of a step fibre with the same value of V. In figure 5.6, as V decreases, H_B decreases faster than the predictions based on the field of a step-fibre.

§5.7.3 Separation of cut-off frequencies

In §5.4.3 it was shown that the geometric birefringence causes only a small separation in the cut-off frequencies of the two polarization states of the same mode. This is much less than the experimental values found on a bow-tie fibre (Varnham, 1984, table 6.4). Splitting of the observed magnitude can be generated purely from the geometric birefringence of the butterfly profile, but only with an unreasonably large value of Δ (greater than 13%).

For the isotropic waveguide, the modal cut-off frequency is a function only of the depth parameter, A. Thus, the X- and Y-profiles, isotropic and characterized by the distinct depth parameters A_X and A_Y, will have different cut-off frequencies, $V_{co}^{(X)}$ and $V_{co}^{(Y)}$, respectively. Implicit in the definition of the normalized frequency, V, is the profile height parameter, Δ. For the X-profile this is, indeed, Δ, but for the Y-profile it is $(\Delta-\delta)$. Before comparison, $V_{co}^{(Y)}$ must be renormalized.

To assess the separation of the cut-off frequencies, consider the ratio, S, between the cut-off frequencies of the X- and Y-polarized modes;

$$S = \frac{V_{co}^{(X)}}{V_{co}^{(Y)}} \, .$$

The results in table 5.3 follow. For comparison, the experimental results are included. These show good agreement with the model's results. Based on the fields of the circular step-profile, previous models of the bow-tie fibre did not predict such large separation of the cut-off frequencies of the two polarization states of the same mode. Indeed, the fundamental mode of a step-fibre is not cut-off.

§5.A.1 Appendix: Mathieu functions

Mathieu functions, first described by Emile Mathieu in 1868, are solutions of

$$\frac{d^2 y}{dx^2} + (\lambda - 2q \cos 2x) \, y = 0 \, . \qquad (43)$$

Subsequently, they have been described in great detail; a complete treatment was written by McLachlan (1947). However, since the notation used to describe them is not standard, it is necessary to define certain quantities. Also, high-speed computers, not available in 1868, have altered the relevent methods of computation.

For a given value of q, there exists a countably infinite set of values, $\{\lambda_n\}$, for which a periodic solution of (43) exists. Such numbers are termed characteristic values. Corresponding to each value of λ_n, there is a unique function, a periodic Mathieu function. These functions can be grouped into four types: even solutions of period 2π, even solutions of period π, odd solutions of period 2π, and odd solutions of period π, denoted by $ce_{2n}(x,q)$, $ce_{2n+1}(x,q)$, $se_{2n+1}(x,q)$, and $se_{2n}(x,q)$, respectively. The associated characteristic values are $a_{2n}(q)$, $a_{2n+1}(q)$, $b_{2n+1}(q)$, and $b_{2n}(q)$, respectively. For convenience, the explicit dependence of quantities on q will not be displayed subsequently.

Being integrable, the functions can be represented as summations of the trigonometric functions with the appropriate symmetry and periodicity requirements. Explicitly, these are

$$ce_{2n}(x) = \sum_{k=0}^{\infty} A_{2k}^{(2n)} \cos (2kx) \quad , \qquad (44)$$

$$ce_{2n+1}(x) \; = \; \sum_{k=0}^{\infty} A_{2k+1}^{(2n+1)} \cos \, (2k+1)x \qquad , \qquad\qquad (45)$$

$$se_{2n+1}(x) \; = \; \sum_{k=0}^{\infty} B_{2k+1}^{(2n+1)} \sin \, (2k+1)x \quad , \qquad\qquad (46)$$

and

$$se_{2n}(x) \; = \; \sum_{k=0}^{\infty} B_{2k}^{(2n)} \sin \, 2kx \; . \qquad\qquad (47)$$

The periodicity properties readily show that the coefficients $A_j^{(i)}$ and $B_j^{(i)}$ satisfy definite recurrence relations (e.g. A&S, 20.2.5 to 20.2.11), which leave only the coefficient of the lowest harmonic as arbitrary.

This ambiguity of amplitude can be avoided by the imposition of a specific normalization property. At this point various conventions are adopted. Here, that which originated with Goldstein (1927), is chosen. Examination of (43) reveals that, if q vanishes, $ce_\ell(x)$ and $se_\ell(x)$ become $\cos(\ell x)$ and $\sin(\ell x)$, respectively. Let the Mathieu functions be normalized like these limiting trigonometric functions, i.e.

$$\int_0^{2\pi} ce_0^2(x) \; dx \; = \; \| ce_0 \|^2 \; = \; 2\pi \qquad\qquad (48)$$

and, for $j \geqslant 1$,

$$\| ce_j \|^2 \; = \; \pi \qquad\qquad (49)$$

and

$$\|se_j\|^2 = \pi , \qquad (50)$$

since se_0 vanishes identically. Ambiguity of sign is resolved by requiring that $A_j^{(i)}$ and $B_j^{(i)}$ all be positive. Also, consideration of Sturmian theory (e.g. Ince, 1926a, ch.10) and (43) shows that the periodic Mathieu functions are orthogonal on $[0,2\pi]$ with unit weighting function.

The evaluation of Mathieu functions presents a couple of numerical complications. The first, and certainly most intimidating, is the evaluation of the characteristic values. The second is the evaluation of the co-efficients for the series (44) to (47).

Concerning the latter, consider by way of example the function $ce_{2n}(x)$ with associated characteristic value a_{2n}. The co-efficents satisfy

$$A_2^{(2n)} = A_0^{(2n)} a_{2n} / q , \qquad (51a)$$

$$A_4^{(2n)} = A_2^{(2n)} (a_{2n} - 4)/q + 2A_0^{(2n)} \qquad (51b)$$

and

$$A_{2(m+1)}^{(2n)} = A_{2m}^{(2n)} (a_{2n} - 4m^2)/q + A_{2(m-1)} . \qquad (51c)$$

Inspection of this system reveals that the magnitude of the coefficients increases from $A_0^{(2n)}$ until $A_{2n}^{(2n)}$, and then declines, to ultimately vanish. Numerically, computation proceeds from a guess for $A_0^{(2n)}$, say A_0', which provides A_{2k}' from the recurrence relations, and then normalizing, to satisfy (48) and (49).

$$\sum_{k=0}^{\infty} (A'_{2k})^2 (1 + \delta_{k0}) \pi = S \pi$$

$$\Rightarrow \quad A_{2k}^{(2n)} = (1 + \delta_{n0}) A'_{2k} / \sqrt{S}$$

recalling definition (44). However, if an unsuitable value of A'_0 is selected, then S or A'_{2n} may become too large for the machine. To avoid this difficulty, the approximate behaviour of $A_{2k}^{(2n)}$ is examined.

It is straightforward to convert (51) into a solvable, first order, differential equation. If h is a small quantity and

$$A_{2k}^{(2n)} = \hat{A}(x=kh),$$

then

$$\hat{A}' = \frac{h \, a_{2n} - 4x}{2 \, q \, h^3}.$$

$$\Rightarrow \quad \hat{A} = C \exp(x(3 h^2 a_{2n} - 4n^2)/6q),$$

where C is an amplitude constant. This shows

$$\frac{A'_{2n}}{A'_0} \sim \exp (n(3 a_{2n} - 4n^2)/6q),$$

which provides a good guess for A'_0 such that A'_{2n} is approximately unity.

To simplify the computation of the characteristic values is not so easy. Basically, the procedure depends on the magnitude of q. If q is "large", the asymptotic forms, derived by Ince (1926b,1927), are employed; if q is "small", a series expansion in q is utilized; if q has an intermediate value, it is necessary to solve the continued fractions (e.g. Wall, 1948). As an example, details pertaining to q_{2n} will be presented.

When q=0, (43) reduces to the familiar simple harmonic equation with eigenvalues

$$\lambda = \ell^2 ,$$

where ℓ is an integer, and associated periodic solutions

$$\cos(\ell x) , \sin(\ell x) .$$

Using this limit for small values of q, (43) can be treated as a perturbation problem, with solutions of the form

$$a_{2n} = 4 n^2 + \sum_{j=1}^{\infty} \lambda_j q^{2j} \qquad (52)$$

and

$$ce_{2n} = \cos(2nx) + \sum_{j=1}^{\infty} c_j(x) q^{2j} . \qquad (53)$$

This is the method employed originally by Mathieu himself. Following him, expansions were obtained (e.g. McLachlan, 1947, §2.151) to several orders, but valid only for tiny values of q. However, modern computing resources allow numerical evaluation of a very many terms, the machine doing most of the work formerly done algebraicly. The key to this is the recognition, and subsequent proof by induction – a trivial exercise – that $c_j(x)$ is always of the form

$$c_{2j} = \sum_{k=1}^{j} U_{2j,k} \cos 2x(n + 2k) + \sum_{k=1}^{\min(j,[n/2])} L_{2j,k} \cos 2x(n - 2k)$$

$$c_{2j-1} = \sum_{k=1}^{j} U_{2j-1,k} \cos 2x(n+2k-1) + \sum_{k=1}^{\min(j,[n+1/2])} L_{2j-1,k} \cos 2x(n+1-2k) ,$$

where the entries of the triangular matrices U and L are found from simple recurrence relations. These relations are determined by substituting (52) and (53) in (43), and requiring the periodicity of c_j. The co-efficients in (52) are

$$\lambda_j = \begin{cases} U_{2j-1,1} & , n = 0 \\ U_{2j-1,1} + 2 L_{2j-1,1} & , n = 1 \\ U_{2j-1,1} + L_{2j-1,1} & , n \geqslant 2 , \end{cases}$$

and these also follow from the periodicity requirements. Thus, the series can be easily used almost to the theoretical limit of its convergence, as explained by Hunter and Guerrieri (1981). For a_0 this limit is 1.405. For succeeding characteristic values, the radius increases.

Next, the method for solving the continued fractions for a_{2n}, is outlined. The sequence a_{2n} are the roots of the infinite continued fraction (A&S, 20.2.21)

$$V(x) = V_0 - \frac{A_2}{V_2 -} \quad \frac{A_4}{V_4 -} \quad \cdots \quad \frac{A_{2j}}{V_{2j} -} \quad \cdots \qquad (54)$$
$$= 0 ,$$

where

$$V_{2j} = \begin{cases} (1 - x/4j^2)^2 / q & , j \geqslant 1 \\ -x/2q & , j = 0 \end{cases}$$

and

$$A_{2j} = \begin{cases} 1 / 4 & , j = 1 \\ 1 / 16j^2(j-1)^2 & , j \geqslant 2 . \end{cases}$$

To find the nth root of $V(x)$, it is better to rearrange the continued fraction (54). $V(x)$ has identical roots to

$$W(x) = \left(\frac{V_n - A_n}{V_{n-1}^-} \quad \cdots \quad \frac{A_1}{V_0} \right) - \left(\frac{A_{r+1}}{V_{r+1}^-} \quad \frac{A_{r+2}}{V_{r+2}^-} \quad \cdots \right),$$

where the first bracketed term is a terminating continued fraction.

Since there are infinitely many roots, an approximate value for a_{2n} is needed as a starting point for the numerical, root-finding routines. This estimate needs to be nearest to the root of $W(x)$ corresponding to the characteristic value being sought. The form of $a(q)$ (e.g. McLachlan, 1947, p40) does not permit a ready estimate for a lower and an upper bound on a_{2n}. Seeking an algebraic – this being the simplest – function which satisfies the known form of a_{2n} as $q \to 0$ and $q \to \infty$, it is found that the simplest suitable expression is

$$a_{2n} = -2q + 4n^2 + \frac{4q}{2-Bq},$$

where

$$B = \begin{cases} 5 / 12 & , n = 1 \\ 1 / 2(4n^2 - 1) & , \text{otherwise.} \end{cases}$$

This describes the approximate behaviour of a_{2n}, and well separates the different orders away from the asymptotic regimes, when the continued fractions can be avoided.

§5.A.2 Appendix: Inverse–square W–fibre

The W-fibre (Kawakami et al, 1976) has some interesting properties, notably decreased loss in a bend and a non-zero cut-off frequency for the fundamental mode. However, the analysis of the W-fibre is complicated by the necessity of dividing the cross-section into three

regions. The inverse-square W-fibre has two regions in its refractive

index profile, and consequently is easier to examine. It is also the

limiting form of the butterfly profile.

The inverse-square W-fibre has an axisymmetric refractive index

profile defined by the shape-function

$$g = \begin{cases} 1 & , \quad R<1 \\ B/R^2 & , \quad R>1 \end{cases} \tag{55}$$

where R is the radial co-ordinate, nondimensionalised by the core's

radius ρ. This profile is illustrated in figure 5.1(b).

Within the weak-guidance approximation, solutions are derived by

first solving the axisymmetric scalar wave equation (P.3) for the modal

field ψ,

$$\nabla^2 \psi + (V^2 g - W^2)\psi = 0 \tag{56}$$

where V, defined by

$$V^2 = k^2 n_{c\ell}^2 \rho^2 2\Delta , \tag{57}$$

is the normalized frequency, k the free-space wavenumber, and U^2 and W^2

are the usual, nondimensional propagation constants, (P.5). For the

regions inside and outside the core, (56) has distinct forms. If R<1,

the solution space for ψ_I is spanned by $\{\psi_{In}\}$, defined by

$$\nabla^2 \psi_I + U^2 \psi_I = 0$$
$$\Rightarrow \quad \psi_{In} = A_n J_n(UR) \begin{Bmatrix} \cos(n\theta) \\ \sin(n\theta) \end{Bmatrix} , \tag{58}$$

where A_n is a constant and J_n is the Bessel function of the first kind.

The second set of solutions, involving Bessel functions of the second

kind, is ignored since it is required that ψ remains finite at R=0. If

R>1, the solution space for the external modal field, ψ_E, is spanned by

the functions $\{\psi_{En}\}$, given by

$$\nabla^2 \psi_E - (W^2 + \frac{BV^2}{R^2}) \psi_E = 0$$

$$\Rightarrow \quad \psi_{En} = B_n K_{\nu_n}(WR) \begin{Bmatrix} \sin(n\theta) \\ \cos(n\theta) \end{Bmatrix}, \qquad (59)$$

where B_n is a constant, K_λ is the modified Bessel function of the third

kind of general fractional order, and ν_n is defined by

$$\nu_n^2 = BV^2 + n^2. \qquad (60)$$

Again the second set of solutions is ignored; this time because it is

required that ψ vanishes as $R \to \infty$.

Boundary conditions are that both ψ and $\partial\psi/\partial R$ are continuous at the

core-cladding iterface, R=1. Before imposing these, it is worth noting

that ψ, as an eigenfunction of a differential operator, is determined

only to within an arbitrary amplitude constant. For convenience, this

constant will be fixed by requiring $\psi=1$ when R=1, i.e.

$$A_n = \frac{1}{J_n(U)}. \qquad (61)$$

The continuity conditions and (58)-(61) give

$$B_n = \frac{1}{K_{\nu_n}(W)} \qquad (62)$$

and an equation to determine the propagation constants:

$$\frac{U J_n'(U)}{J_n(U)} = \frac{W K_{\nu_n}'(W)}{K_{\nu_n}(W)}, \qquad (63)$$

remembering

$$V^2 = U^2 + W^2. \qquad (64)$$

System (63) and (64) has a set of real-valued solutions, $\{U^{(n\ell)}\}$, for each n. However, as usual, only a finite number of such U are real for any finite value of V.

Of particular interest is the fundamental mode of the inverse-square W-fibre. This corresponds to the smallest value of U. The modal field is axisymmetric, n=0, and

$$\psi = \begin{cases} J_0(UR) \,/\, J_0(U) & , \quad R \lessdot 1 \\ K_{\nu_0}(WR) \,/\, K_{\nu_0}(W) & , \quad R \gtrdot 1 \end{cases} \qquad (65)$$

The eigenvalue equation, of which the desired U is the smallest root, is

$$W \frac{K'_{\nu_0}(W)}{K_{\nu_0}(W)} + U \frac{J'_0(U)}{J_0(U)} = 0 \qquad (66)$$

which can be readily solved, using a Newton-Raphson method, if a solution exists.

This last qualification is important because the profile (55) does, indeed, display the behaviour of the more familiar W-fibre in having a non-zero value for the cut-off V of the fundamental mode. For a profile characterized by the depth parametre B, there is the customary countable set of frequencies, V_c , at which modes become leaky. These can be calculated by setting $U = V_c = V$ in (56) and working from there, or, more simply, by setting $U = V_c = V$ in (58) and (61) and employing the asymptotic form of $WK'_\lambda(W)/K_\lambda(W)$ for small W (A&S, 9.6.9) in (59) and (62) to give

$$\psi_{En} \sim R^{-\nu_n} \begin{cases} \sin(n\theta) \\ \cos(n\theta) \end{cases} , \qquad (67)$$

and in (63) to produce

$$V_c \frac{J_n'(V_c)}{J_n(V_c)} = -\nu_n \,. \tag{68}$$

Again, this is easily solved using the Newton-Raphson method. A countable sequence of solutions V_c exists for any B, which appears in (68) via ν_n and (60). In particular, for n=0, (68) reduces to

$$V_c J_1(V_c) - \sqrt{B}\, J_0(V_c) = 0 \tag{69}$$

which has a solution for **all** B. The smallest solution defines the cut-off frequency of the fundamental mode. This behaviour differs from that of the conventional W-fibre. The fundamental mode is always cut-off on an inverse-square W-fibre; for a W-fibre, the refractive index depression must be sufficiently wide or deep before cut-off occurs. It is interesting to examine the behaviour of the smallest solution of (69). As B increases from 0, $V_c^{(0)}$ increases monotonically from 0 to approach the limiting value 2.405 as $B \to \infty$. As the first order estimate of the butterfly profile's fundamental mode's cut-off, this is shown as the dashed curve, labelled LP_{01}, in figure 5.3.

The limit $B \to \infty$ invalidates the assumption which produces the weak guidance formalism, because the total refractive index variation is no longer small.

It is useful to obtain the normalization integral for the modal field described above. This proceeds from

$$\|\psi\|^2 = \pi\, N_m^{n\ell} \tag{70}$$

Substitution of (58), (59), (61) and (62) in (70) gives

$$N_m^{n\ell} = \frac{V^2(1 + \delta_{n0})}{2U^2W^2}\,(\chi_n^2 - 2n\chi_n BU^2)\,,\qquad(71)$$

where the eigenvalue equation (63) was employed, as were recurrence relations for the Bessel functions, (60), and the definition

$$\chi_n = \frac{U\,J_{n+1}(U)}{J_n(U)}\,.$$

In particular, for the fundamental mode

$$N_m = \frac{V^2}{W^2}\left(\frac{J_1^2(U)}{J_2^2(U)} - B\right).$$

Any of the standard quantities can be calculated, using the formulae in table 13.2 in Snyder & Love (1983), since ψ, $\|\psi\|$, etc. have been obtained, and the weak guidance formalism is in use.

CHAPTER SIX

Bending Loss and Axi-Asymmetry

> Tigger explained what had happened at the same
> time that Roo was explaining about his Biscuit
> Cough and Kanga was telling them not both to
> talk at once, so it was some time before
> Christopher Robin guessed that Pooh and Piglet
> and Rabbit were all lost in the mist.
>
> A.A. Milne, "The House at Pooh Corner"

The well known expression - (20), below - for the radiation loss, caused by very gradual bending of a weakly guiding fibre, does not include the effect of the finite cross-section of the core. White (1979) derived an expression to incorporate this, but his analysis was in error. In this chapter, the correct expression is obtained, and then used to show how rotating the core of a non-axisymetric fibre changes the loss from the bend.

§6.1   Background

When an optical fibre is bent, power is lost from a mode which would be bound on a straight fibre. Since waveguides are bent when used, it is important to obtain some form of quantitative understanding of the behaviour of a mode, particularly the fundamental mode, within a bend. Also, it is interesting to determine how the state of polarization of the electric field and the axi-asymmetry of the profile affect the loss.

The first analysis of loss from a bent dielectric waveguide was undertaken by Marcatili (1969a), who examined a pseudo-rectangular cross-section with edges parallel to the plane of the bend. Within this approximation, the loss was explicity shown to be idependent of the polarization of the mode, but no details of the effect of rotating the cross-section in the plane of the bend were provided. Marcuse (1971)

examined a bent slab, an arrangement which permits an exact solution of the Maxwell equations. In this case, the independence of the attenuation of the modal power from the state of polarization is simply obtained.

Subsequently, others investigated the attenuation of power in a bent waveguide. Notable amongst these were Lewin (1974) and Kuester & Chang (1975) who showed that the loss is independent of polarization for all circular, clad fibres. However, their analysis is exceptionally cumbersome. More recent work has ignored polarization, choosing the direction for the electic field that makes the analysis easiest. For example, White (1979) chose E perpendicular to the plane of the bend.

The orientation and size of the axi-asymmetric fibre's core is known to affect the attenuation of power in a bend, but no satisfactory analysis has been completed. Unfortunately White (1979; reproduced in Snyder & Love, ch.23) made an error, which showed the orientation of the core to be irrelevant. Others have only explicitly considered axisymmetric profiles, especially the step- and W-profiles.

It is instructive to rework the analysis of White, correcting his error, to show how the loss does depend on the orientation of the core. Also, one can show that the volume current method reveals no dependence of the dominant loss mechanism on the state of polarization of the signal. Alas, no elegant, physical argument yet exists to establish this result.

§6.2 Calculating radiation from a bend

In calculating formulae for the attenuation of energy from a bent dielectric waveguide, basically two methods have been used. To describe the energy lost, the first utilizes a continuum of radiation modes.

These are coupled to the fibre's modal field, ψ. The second method, suggested by Snyder (1970) and used by White (1977), is the volume or induced current method.

§6.2.1 Volume current model of radiation

The volume current method models the radiation lost from a bend as the radiation from a closed loop of the waveguide's core embedded within an infinite body with the same refractive index as the cladding, $n_{c\ell}$. This allows the core to be considered as a perturbation within an otherwise uniform medium (refer Snyder & Love, 1983, ch.22). The attenuation of power is evaluated by comparing the total power radiated by the loop, which acts as an antenna, and the power of the corresponding bound mode on a straight fibre. For a bend with a large radius of curvature - typicaly 1 cm or greater - a very small fraction of energy is lost.

To measure the attenuation of the power within a bend, an attenuation constant, γ, is defined by

$$P = P_0 \, e^{-\gamma z}$$

where P_0 is the power entering the bend and z is the axial distance around the bend. Using the model outlined above,

$$\gamma = \frac{(\Delta P)}{P_0 \, 2\pi \, R_0 \, \rho} \tag{1}$$

where (ΔP) is the power radiated by the loop, P_0 is taken as the power in the corresponding bound mode of a straight fibre, and (ρR_0) is the radius of curvature of the bend. R_0 is the normalized value.

In a practical problem, the ratio of bend to core radius is typically of the order 10^4, or greater. Thus, the electromagnetic field within the loop is equated to the corresponding field on a straight waveguide. This is an approximation. A bend causes a shift in the modal field (Marcuse, 1976b); the energy tends to move away from the fibre's axis, towards the outer edge of the bend.

§6.2.2 Note on the field shift

Marcuse (1976a) and White (1977) examined the effect of the field shift on the attenuation constant, γ. For a large bending radius, R_o, they found the shift, and thus the change in γ, to be negligible. In particular, for the fundamental mode, the loss increases slightly as the peak intensity of the field moves away from the waveguide's axis, toward the outside of the bend, where energy is more susceptible to loss.

The field shift can be included in the model by using, instead of ψ, the corrected modal field obtained by the method outlined by Marcuse (1976b).

§6.3   Initial modal power

The analysis could proceed using the exact solution of the Maxwell equations, with an ensuing increase in complexity. However, as elsewhere, a weakly guiding fibre is considered. Since interest is in axi-asymmetric structures, the electric field of the propagating mode is approximated as an LP-mode:

$$E \approx A \, \psi \, e^{i\beta z} \, \hat{p} \tag{2}$$

where A is a dimensional amplitude constant, ψ is the modal field, $\hat{p}$ is a unit vector in the direction of polarization of the electric field,

and β is the mode's propagation constant. The power of this bound mode is given by

$$P_0 = \frac{1}{2} \rho^2 n_{c\ell}^2 A \sqrt{\frac{\varepsilon_0}{\mu_0}} \| \psi \|^2 \tag{3}$$

where μ_0 and ε_0 are, respectively, the permeability and permittivity of a vacuum, and ρ is the chosen length scale.

As elsewhere, the refractive index is given by

$$n^2 = n_{c\ell}^2 (1 + 2\Delta g). \tag{4}$$

§6.4   Radiated power

§6.4.1 Vector potential

Suppose the direction of polarization of E is such that $\hat{p}$ makes an arbitrary, but fixed, angle T with the plane of the bend (refer figure 6.1(a)), i.e.

$$\hat{p} = \sin T \, \hat{r} + \cos T \, \hat{R}_a \tag{5}$$

where $\hat{R}_a$ is a unit, outward radial vector in the XY-plane. In the analysis of White (1979), it was assumed that $T=\pi/2$.

For the volume current method, the electric field in the core is replaced by a volume density of currents, J, defined by

$$J = i \sqrt{\frac{\varepsilon_0}{\mu_0}} k \left(n_{c\ell}^2 - n^2 \right) E \, . \tag{6}$$

This quantity is described with respect to the toroidal co-ordinates (ζ, s, ξ) (refer figure 6.1(b)). The implicit time dependence shows that these currents are oscillating and consequently radiate, as in an antenna. To determine the total radiation, it is useful to define an

Figure 6.1

(a) A waveguide bent in the XY-plane. The electric field, **E**, is polarized at angle T to this plane.

(b) The toroidal coordinates (ζ, s, ξ) used to describe position within the bent waveguide; the spherical polar coordinates (R, θ, ϕ) used to describe a position in space.

(a)

(b)
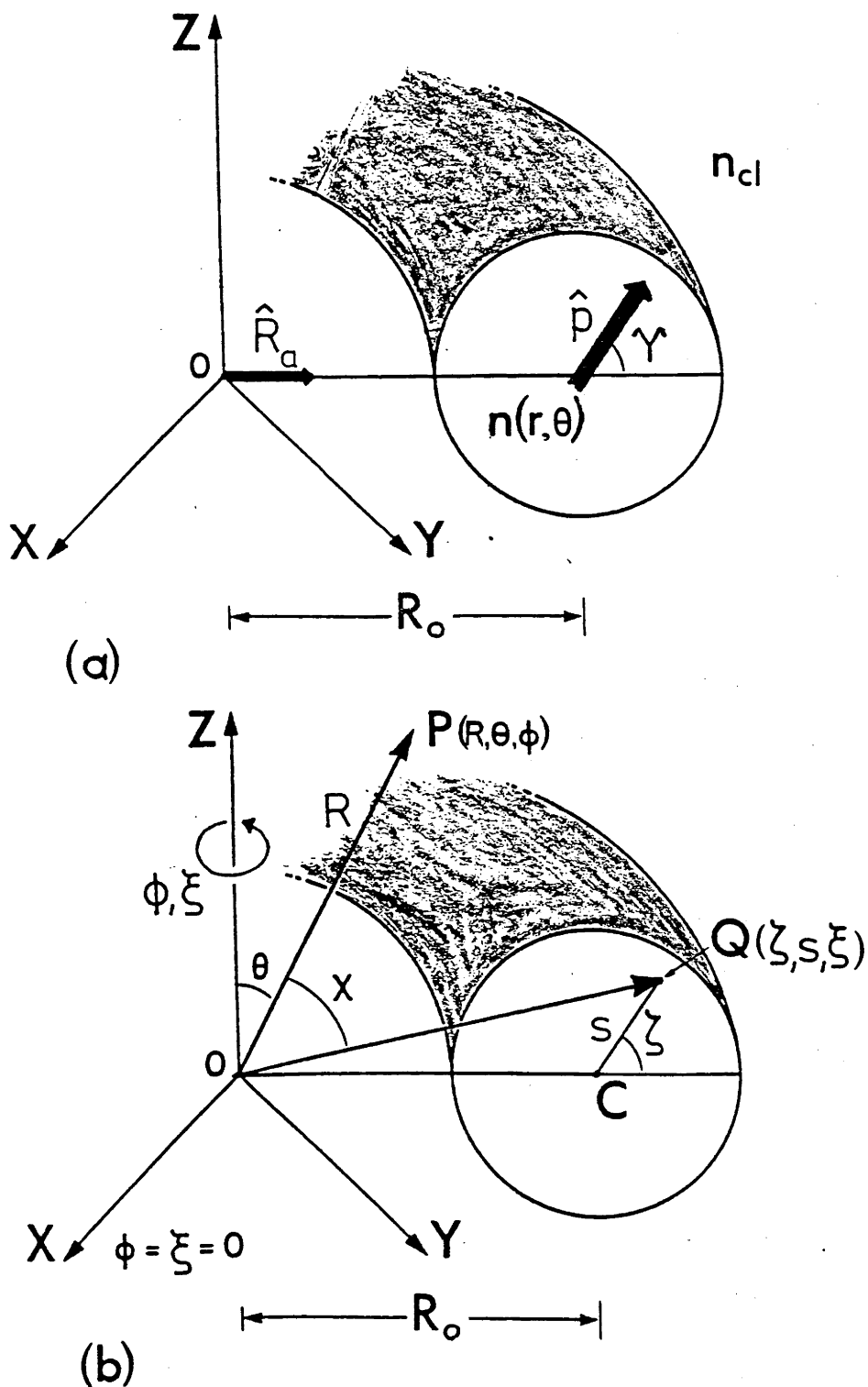
electromagnetic vector potential N by

$$N = \int_{R^3} dV' \; e^{-ikn_{c\ell}\rho|r'|\cos\chi} \; J(r')$$

or, in dimensionless form,

$$M = N \Big/ i \; \rho^3 \sqrt{\frac{\epsilon_0}{\mu_0}} \; k \; 2 \Delta \; n_{c\ell}^2 \; A$$

$$= \int_{R^3} dV' \; F_1(s,\xi) \; e^{-ikn_{c\ell}\rho|r'|\cos\chi} \tag{7}$$

where the integral, over all space, includes all currents, the angle χ is shown in figure 6.1(b) and

$$F_1(s,\xi) = -(R_0 + s \cos \xi)g\psi \tag{8}$$

where $g(s,\xi)$, the shape-function of the core, defines the loop. M is defined with respect to the spherical polar coordinates (R,θ,ϕ). Explicitly, the total radiated power is

$$P_{rad} = \frac{V^4 \; \rho^4}{32 \; \pi^2 k^2} \sqrt{\frac{\epsilon_0}{\mu_0}} \; \oint_C d\phi \int_0^\pi \sin\theta \; d\theta \; \left|\hat{R}_s \wedge M\right|^2 \tag{9}$$

where the integral is over the entire solid angle about the loop of core material. V is the usual normalized frequency, and $\hat{R}_s$ is the unit radial vector in the spherical polar system. The notation, used in the ϕ-integral, indicates that the range is a complete, but arbitrary, 2π-cycle.

If $g(s,\xi)$ characterizes the uniformly clad fibre, then g=0 for $s > s_0$, and (8) shows that $F_1=0$ in the same domain. Even if g is not of this form, there is still some value s_0 beyond which F is negligible, because ψ decreases exponentially away from the waveguide's axis, as

explained in §P.2.1. In the subsequent asymptotic expansions, little

error is introduced by terminating F_1, if necessary. In practice

$s_0 \ll R_0$.

As notational shorthand and to highlight relative magnitudes,

define

$$C_0 = V/\sqrt{2}\Delta \tag{10}$$

and

$$\varepsilon = W^2/2C_0^2 . \tag{11}$$

Within the weak guidance approximation, C_0 is large, and ε is very

small.

Proceeding further, it is necessary to examine **M**. Explicitly the

components are

$$M_i = \cos T \int_0^{s_0} ds \oint_C d\xi \oint_C d\zeta \cos \zeta K(\zeta,s,\xi) \tag{12a}$$

$$M_j = \cos T \int_0^{s_0} ds \oint_C d\xi \oint_C d\zeta \sin \zeta K(\zeta,s,\xi) \tag{12b}$$

and

$$M_k = \sin T \int_0^{s_0} ds \oint_C d\xi \oint_C d\zeta K(\zeta,s,\xi) , \tag{12c}$$

where

$$K(\zeta,s,\xi) = F_1(s,\xi) e^{-iC_0 s \cos\theta \sin\xi} e^{g(\zeta,s,\xi)}$$

and

$$g = C_0(1+\varepsilon)\left(R_0 + s \cos\xi\right)\zeta - C_0\left(R_0 + s \cos\xi\right)\cos(\zeta-\phi) ,$$

where various geometric identities were used to simplify the argument of

the exponential factor in the integrand of (7). The s- and ξ-integrals

cover the core's cross-section and depend on knowing g and ψ. However,

ζ is the circumnavigation of the loop and this can be done,

asymptotically, in the general case. For M_k, the ζ-integral is

$$I_\zeta^{(k)} = \oint_C d\zeta \, e^{iC_0(R_0 + s \cos \xi)(1+\epsilon)\zeta - C_0(R_0 + s \cos \xi)\cos(\zeta - \phi)} \quad .$$

Comparing this with the representation (A&S 9.1.22) of the Bessel function of the first kind for large order –

$$J_\nu(z) \sim \frac{1}{2\pi} e^{i\nu\pi/2} \oint_C dt \, e^{i\nu t - iz \cos t}$$

– and an improved Debye asymptotic form (Snyder & Love, eq(37-90b)) of $J_\nu(z)$ for large ν, valid when $\nu - z > \nu^{1/3} \gg 1$ –

$$J_\nu(z) \sim \frac{1}{\sqrt{2\pi}} \frac{1}{(\nu^2 - z^2)^{1/4}} \exp\left(\frac{-(\nu^2 - z^2)^{3/2}}{3 z^2}\right)$$

– shows that

$$I_\zeta^{(k)} \sim \frac{e^{iC_0(R_0 + s \cos \xi)(1+\epsilon)(\phi - \pi/2)}}{C_0^{1/2}(R_0 + s \cos \xi)^{1/2}(2\epsilon + \cos^2\theta)^{1/4}}$$

$$\times \exp\left(\frac{-C_0(R_0 + s \cos \xi) h(\theta)}{3}\right) , \tag{13}$$

where

$$h = (\cos^2\theta + 2\epsilon)^{3/2} / \sin^2\theta.$$

The identifications

$$\nu = C_0(1 + \epsilon)(R_0 + s \cos \xi)$$

and

$$z = C_0(R_0 + s \cos \xi) \sin\theta$$

were made, and it was recalled that $s_0 \ll R_0$. Thus, the conditions for the applicability of the Debye form are satisfied. From (12c) and (13),

$$M_k = M_0 \sin T$$

where

$$M_0 = \frac{\sqrt{2\pi} \, e^{iC_0(R_0 + s \cos\xi)(1+\epsilon)(\phi-\pi/2)}}{C_0^{1/2} (R_0 + s \cos\xi)^{1/2} (2\epsilon + \cos^2\theta)^{1/4}}$$

$$x \quad F_1(s,\xi) \, e^{-iC_0 s \cos\theta \sin\xi} \, e^{-C_0(R_0 + s \cos\xi)h/3}$$

$$= \sqrt{2\pi} \, F_1 \, e^{-iC_0 s \cos\theta \sin\xi} \, I_\zeta^{(k)} \, . \tag{15}$$

The evaluation of M_i and M_j is more difficult, which is why the selection of $T = \pi/2$ is usually made.

For M_i the ζ-integral is

$$I_\zeta^{(i)} = \oint_C d\zeta \, \cos\,\zeta \, e^{iC_0(R_0 + s \cos\xi)(1+\epsilon)\zeta - C_0(R_0 + s \cos\xi)\cos(\zeta-\phi)}$$

$$\sim \pi \, e^{i\nu(\phi-\pi/2)} \left(e^{i(\phi-\pi/2)} J_{\nu+1}(z) + e^{-i(\phi-\pi/2)} J_{\nu-1}(z) \right)$$

$$\sim (\sin\phi) \, I_\zeta^{(k)} \, , \tag{16}$$

since

$$\nu + 1 \approx \nu \approx \nu-1 \tag{17}$$

because ν is large. It is worth stressing the care needed in obtaining asymptotic results. For example, if the approximation (17) is made immediately after rewriting $\cos\zeta$ in terms of exponentials, the erroneous result

$$I_\zeta^{(i)} \sim -(\cos\,\phi) \, I_\zeta^{(k)}$$

follows. This gives an entirely different form of the dependence of the attenuation on T, leaving it sensitive to polarization.

Starting with M_j, an analogous procedure to that above yields

$$I_\zeta^{(j)} \sim -(\cos \phi) \, I_\zeta^{(k)} .$$

Thus, together with (12), (14), (15) and (16),

$$M = M_0 \left(\sin T \, \hat{z} + \cos T \, \left(\sin \phi \, \hat{x} - \cos \phi \, \hat{y} \right) \right).$$

Using this result, the integrand of (9) simplifies to

$$\left| \hat{R}_s \wedge M \right|^2 = \left| M_0 \right|^2 \left(1 - \cos^2\theta \, \sin^2 T \right) . \tag{18}$$

§6.4.2 Polarization-independent loss

In (9), $\left| M_0 \right|^2$ involves two integrals over the cross-section; let the descriptive polar coordinates be (s, ξ) and (s', ξ') with the obvious corresponding Cartesians (x, y) and (x', y'). The imaginary part of M_0 arises from the exponential factor in M_0, shown in (15). Since the complex conjugate of an integral with an integrand of this form is the integral of the complex conjugate,

$$\left| M_0 \right|^2 = \frac{2\pi e^{iC_0(1+\varepsilon)(\phi-\pi/2)(x-x')} \, F_1(s,\xi) F_1(s',\xi') e^{iC_0(y-y')\cos\theta} \, e^{-C_0 H}}{C_0 \left(R_0 + s \cos \xi \right)^{1/2} \left(R_0 + s' \cos \xi \right)^{1/2} \left(2\varepsilon + \cos^2\theta \right)^{1/2}} \tag{19}$$

where

$$H = -C_0(2R_0 + x + x') \, h(\theta)/3$$

Inappropriate approximation in deriving this expression is the origin of White's error. In (13), he ignored the contribution $(s \cos \xi)$, since it is small compared with R_0. However, while this is insignificant in the modulus of M_0, its omission from the phase factor drops a term of comparable magnitude to that retained. If all terms dependent on s and s' – excepting those in $F1$ – are removed, the "thin wire" approximation is recovered. This result (e.g. Snyder & Love, 1983, ch.23) is

$$\gamma = \frac{V^4 \; e^{-4R_0 W^3 \Delta/3 \, V^2}}{8 \pi^{1/2} \rho R_0^{1/2} W^{3/2} \|\psi\|^2} \left[\int_{S_\infty} dS \; g \; \psi \right]^2 \tag{20}$$

which does not include any effect of the finite cross-section, because the entire volume of current densities is concentrated along the axis of the waveguide.

Comparison of (9) and (19) reveals how the φ-integral and θ-integral separate. The former produces

$$I_\phi = \oint_C d\phi \; e^{iC_0(1+\varepsilon)(\phi-\pi/2)(x-x')}$$

$$= \frac{e^{iC_0(1+\varepsilon)\pi(x-x')}}{i \, (x-x') \, C_0} + \frac{e^{iC_0(1+\varepsilon)\pi(x-x')}}{i \, (x'-x) \, C_0} \; . \tag{21}$$

The latter is more difficult to evaluate. Examination of (19) shows that the integrand in (9) is dominated by the huge coefficient of $h(\theta)$ in the argument of the exponential. This argument is a maximum when $\theta = \pi/2$, so that a Laplace expansion about this value can be used to obtain an asymptotic form

$$I_\theta = \int_o^\pi d\theta \; \frac{\sin \theta (1-\cos^2\theta \, \sin^2 T)}{(2\varepsilon + \cos^2\theta)^{1/2}} \; e^{iC_0(x-x')\cos\theta} e^{-C_0(x+x')h(\theta)} e^{-2C_0 R_0 h(\theta)/3}$$

$$\sim \sqrt{\frac{\pi}{C_0 R_0}} \; \frac{e^{-C_0(x+x')(2\varepsilon)^{3/2}/3}}{(2\varepsilon)^{3/4}} \; e^{-2C_0 R_0 (2\varepsilon)^{3/2}/3} \; . \tag{22}$$

The significant feature here is the exponentially small quantity, $\exp\left(-2C_0 R_0 (2\varepsilon)^{3/2}/3\right)$. This is entirely independent of the profile and is identical to the thin wire expression in (20). It depends on the waveguide parameters V and W, i.e. β, the propagation constant; it is not influenced by the detail of the finite cross-section.

More significantly, (22) shows that γ is independent of the polarization angle T. It should be emphasized that this is a valid approximation only if R_0/s_0 is very large. As expected, this means the polarization does influence attenution as the bend becomes sharper and/or the field, ψ, spreads significantly beyond the core, i.e. the mode approaches cut-off.

To show the outcome of the above analysis, (1), (3), (4), (9), (15), (19), (21) and (22) are combined and the constants regrouped, to give,

$$\gamma = \frac{V^4 \, e^{-4R_0 W^3 \Delta/3 V^2}}{8\pi^{3/2} \rho R_0^{1/2} \, \|\psi\| \, W^{3/2} C_0} \int dx \, f(x) \int dx' \, f(x') \, \frac{e^{i\pi C_0(x-x')}}{2i(x-x')} \tag{23}$$

where

$$f(x) = \left(\int dy \, g(x,y) \, \psi(x,y) \right) \sqrt{1 + \frac{x}{R_0}} \, e^{-2W^3 x/3 C_0^2} . \tag{24}$$

§6.4.3 Influence of the cross-section

In (24), observe how the ϕ-integral, (21), has acted to convolve the two integrals over the cross-section. In White's analysis, $I_\phi = 2\pi$, and consequently the integrals over the cross-section separate. To determine the dominant terms of this convolution, recall that $C_0 \gg 1$, leading to the asymptotic result

$$\int dx \, g(x) \, \frac{e^{i\pi \varepsilon_0(x-x')}}{2i(x-x')} \sim \frac{g(x')}{\pi C_0}$$

which shows, from (23), that

$$\gamma \sim \frac{\Delta V^2 \, e^{-4R_0 W^3 \Delta/3 V^2}}{4\pi^{5/2} \, \rho \, R_0^{1/2} \, W^{3/2} \, \|\psi\|^2} \int dx \, g^2(x) . \tag{25}$$

This expression is at least an order of magnitude smaller than the thin wire result.

In practice, attenuation is expressed logarithmically, whence, from (25),

$$\ln \gamma = \frac{-4R_0 W^3 \Delta}{3V^2} - \tfrac{1}{2} \ln R_0 + D$$

where the constant D is independent of R_0. For $R_0 \gg 1$, the functional relationship between γ and R_0 is essentially linear. The details of D determine the intercept. It follows from (25) that the correction due to the finite cross-section influences only D, as the examples in §6.5 show. In particular, D is lower than predicted by the "thin wire" approximation and also does depend on the axi-axymmetry of the profile. It is observed (e.g. Neumann & Rudolph, 1975) that the actual loss from a bent fibre is lower than that predicted by (20).

§6.5 Examples

It is helpful to examine the influence of the finite cross-section for a step-fibre, and then the effect of rotating the axes of an axi-asymmetric profile with respect to the plane of the bend. Comparison of (20) and (25) shows that consideration of the finite cross-section is equivalent to multiplying the "thin-wire" expression by the correction factor

$$H = \frac{2\Delta \int dS \, g \, \psi \int dY' \, g \, \psi(X,Y')}{\pi^2 V^2 \left[\int dS \, g \, \psi \right]^2} \tag{26}$$

where the integrals are over the entire area in which $g\psi$ does not vanish, and the simplification, mentioned below (24), is made.

§6.5.1 Circular step waveguide

The thin wire approximation for a step-profile fibre gives the result (e.g. Snyder & Love, eq(23-13))

$$\gamma = \frac{\pi^{1/2} U^2}{2\rho R_0^{1/2} V^2 W^{3/2} K_1^2(W)} e^{-4R_0 W^3 \Delta/3 V^2} .$$

Substitution of ψ for a step fibre into (26) gives

$$H = \frac{4 \Delta U^2}{\pi^4 V^2 J_1^2(U)} \int_0^1 dR \, R \, J_0(UR) \int_0^{\pi/2} d\theta \int_{R\cos\theta}^1 dt \, \frac{t J_0(Ut)}{\sqrt{t^2 - R^2\cos^2\theta}} ,$$

which can be evaluated using numerical integration routines. Using the same field and shape-function in White's analysis gives (Snyder & Love, eq(23-22)) the following correction factor to the thin wire expression for loss,

$$\bar{H} = \frac{U^4}{V^4 W^2 K_1^2(W)} .$$

With $V=2.4$, this gives $\bar{H}=1.9$, while the correct value is $H=0.018\Delta$ and Δ itself is typically less than 10^{-2}. Thus, White's result overestimates the loss. The effect of the cross-section being finite in extent is to decrease the rate at which energy is lost from the bent waveguide.

§6.5.2 Clad-parabolic elliptical waveguide

To see explicitly the manner in which axi-axymmetry of the refractive index profile can influence the loss, consider the clad-parabolic, elliptical fibre. In particular, consider this waveguide well away from cut-off. There it can be well approximated by the unphysical, but simply analyzed, infinitely parabolic profile. For this second profile,

$$g = 1 - \varepsilon \, \bar{X}^2 = \frac{\bar{Y}^2}{\varepsilon} \, ,$$

where $(\bar{X}, \bar{Y})$ are Cartesian coordinates, defined with respect to the natural axes of the concentric, elliptical contours of constant refractive index. The fundamental mode field is (Snyder & Love, p355f)

$$\psi = \exp\left(\frac{-V}{2} \left(\sqrt{\varepsilon}\,\bar{X}^2 + \frac{\bar{Y}^2}{\sqrt{\varepsilon}}\right)\right).$$

Lengths are scaled by $\rho = \sqrt{\rho_x \rho_y}$, $\varepsilon = \rho_y / \rho_x$, where ρ_x and ρ_y are the semimajor and semiminor axes, respectively, of the core. The Gaussian decay of ψ shows how little error is introduced by truncating $g\psi$ at a finite value s_0.

From (20) it is straightforward to obtain the thin-wire approximation to the bend-loss attenuation coefficient:

$$\gamma_t = \frac{V^3 \, \pi^{1/2} \, e^{-4R_0 W^3 \Delta / 3V^2}}{2\,\rho R_0^{1/2} \, W^{3/2}} \left(1 - \left(\frac{\varepsilon + 1}{V\sqrt{\varepsilon}}\right)\right)^2 .$$

The factor which corrects this for the effect of the finite, asymmetric core depends on the orientation of this core with respect to the plane of the bend. Suppose the major axis of the elliptical cross-section makes angle η with the plane of the bend. From (26),

$$H = \frac{\Delta \varepsilon^{1/4}}{\pi^{1/2} \left(1 - \frac{\varepsilon+1}{V\sqrt{\varepsilon}}\right)^2 V^{3/2}} \, \Xi_\eta ,$$

where

$$\Xi_\eta = \frac{b^2 + \dfrac{bc}{a} + \dfrac{3c^2}{4a^2}}{\left(\varepsilon \sin^2\eta + \cos^2\eta\right)^{1/2}} \, ,$$

$$a = \frac{V\sqrt{\varepsilon}}{\varepsilon \sin^2\eta + \cos^2\eta} \, ,$$

$$b = 1 - \frac{\cos^2\eta + \varepsilon^2\sin^2\eta}{V\sqrt{\varepsilon}\ (\varepsilon\sin^2\eta + \cos^2\eta)}$$

and

$$c = \frac{(1-\varepsilon)^2\sin^2\eta\cos^2\eta\ (2\varepsilon + 3(\cos^2\eta + \sin^2\eta))}{\varepsilon\ (\varepsilon\sin^2\eta + \cos^2\eta)^2} - \frac{\sin^2\eta + \varepsilon^2\cos^2\eta}{\varepsilon} .$$

The two limiting cases are $\eta = 0$

$$\Xi_0 = \frac{2\pi^{3/2}\varepsilon^{1/4}}{V^{3/2}}\ (1 + \frac{1}{V}\ (\frac{1}{\varepsilon^{3/2}} - 2\varepsilon^{3/2}) + \frac{1}{V^2}(\frac{3}{4\varepsilon^3} - 1 + \varepsilon^3))$$

and $\eta = \pi/2$

$$\Xi_{\pi/2} = \frac{2\pi^{3/2}}{V^{3/2}\varepsilon^{1/4}}\ (1 + \frac{1}{V}\ (\varepsilon^{3/2} - \frac{2}{\varepsilon^{3/2}}) + \frac{1}{V^2}(\frac{1}{\varepsilon^3} - 1 + \frac{3\varepsilon^3}{4}))\ ,$$

showing that bend loss is different for different orientations of the core.

The infinite parabolic profile best models the clad-parabolic profile as $V \to \infty$. Taking this limit,

$$\frac{\Xi_{\pi/2}}{\Xi_0} \sim \frac{1}{\sqrt{\varepsilon}} .$$

Thus, as the cross-section is rotated so that its major axis becomes perpendicular to the plane of the bend, the loss increases by the factor $1/\sqrt{\varepsilon}$. This is physically obvious. The dominant contribution to γ comes from near $\theta = \pi/2$ in (22). The modal field spreads further into the cladding along the minor axis of the guide, and thus energy is more easily lost when this axis is aligned with $\theta = \pi/2$.

The other instructive limit of the above formula occurs as the elliptical cross-section becomes longer and thinner, i.e. $\varepsilon \to 0$. In this case

$$\frac{\Xi_{\pi/2}}{\Xi_0} \sim \frac{4}{3\,\varepsilon^{1/2}}$$

which is unbounded as $\varepsilon \to 0$.

Again the loss increases – this time dramatically – as the cross-section moves from parallel to perpendicular to the plane of the bend, and the physics is the same as explained in the previous paragraph.

The trends exhibited by this core's geometry are expected to be similar in other axi-asymmetric fibres. Notably, rotation of the core with respect to the plane of the bend will significantly alter the rate at which energy is lost in the bend.

§6.5.3 Pseudo-rectangular profile

The pseudo-rectangular profile (Kumar et al, 1983) exhibits the same sort of behaviour as the elliptical prifile above. In this case

$$g = \begin{cases} 1 & , \ |\bar{X}| < 1/\sqrt{\varepsilon} \text{ and } |\bar{Y}| < \sqrt{\varepsilon} \\ -1 & , \ |\bar{X}| > 1/\sqrt{\varepsilon} \text{ and } |\bar{Y}| > \sqrt{\varepsilon} \\ 0 & , \ \text{elsewhere} \end{cases}$$

and

$$\psi = \psi_s^{(X)}\left(\bar{X}\sqrt{\varepsilon}\right) \psi_s^{(Y)}\left(\bar{Y}/\sqrt{\varepsilon}\right)$$

where $(\bar{X},\bar{Y})$ Cartesian coordinates defined with respect to the natural axes of the rectangular cross-section. Lengths are scaled by $\rho = \sqrt{\rho_x \rho_y}$ –

giving a normalized frequency $V^2 = k^2 n_{c\ell}^2 2\Delta\rho_x\rho_y$ - while $\varepsilon = \rho_y/\rho_x$, where ρ_y and ρ_x are the half lengths of the short and long sides, respectively, and $\psi_s^{(j)}$ is the modal field of a planar waveguide with normalized frequency $V\sqrt{\varepsilon}$, if j=X, and $V/\sqrt{\varepsilon}$, if j=Y. The normalized propagation constants are defined in an analagous manner.

In the cladding, the modal field of a slab decays exponentially, so $g\psi$ can again be truncated. It follows from (26) that

$$H = \frac{\Delta\ \varepsilon^2}{8\pi^2 \cdot V^2 W_X^2 W_Y^2} \frac{1}{\left(\frac{W_X^2 W_Y^2}{U_X^2 U_Y^2} - 1\right)^2} \Xi_\eta$$

where η is the angle between the long side of the rectangular cross-section and the plane of the bend. The two limiting forms are

$$\Xi_0 = \frac{4}{\varepsilon W_Y^2} \left(\frac{1}{W_X} + \frac{W_Y^4}{U_Y^4}\left(1 + \frac{W_X}{U_X^2}\right)\right)$$

and

$$\Xi_{\pi/2} = \frac{4}{\varepsilon^2 W_X^2} \left(\frac{1}{W_Y} + \frac{W_X^4}{U_X^4}\left(1 + \frac{W_Y}{U_Y^2}\right)\right) .$$

As before, examination of the limit $\varepsilon\to0$ provides an insight into the effect of the axi-axymmetry on the loss:

$$\frac{\Xi_{\pi/2}}{\Xi_0} \sim \frac{2^5 V^7}{\pi^4 \varepsilon^{1/2}} .$$

Thus, the loss increases as the long, thin rectangular cross-section is rotated from parallel to perpendicular to the plane of the bend. As $V\to\infty$,

$$\frac{\Xi_{\pi/2}}{\Xi_0} \sim \frac{1}{\varepsilon^2}$$

and the trend continues. Of course, as $V \to \infty$, the exponential factor in (23) vanishes, and the loss is small. This, too, is expected. The power is confined to the core.

§6.6   Comments

The examples of §6.5 showed how the geometry of the core influences the attenuation of power in a bend; as the axi-asymmetric profile rotates, γ changes.

The geometry of the profile has another effect on γ. In §6.4.2, γ was shown to be independent of the state of polarization of the mode, **within the weak guidance approximation.** Below (22), it was mentioned that the argument of the dominant, exponential factor depends only on β, not the detail of the profile. For an axi-asymmetric profile, birefringence, i.e. $\beta_x \neq \beta_y$, causes the attenuation constants of the X- and Y-polarized modes, γ_x and γ_y, respectively, to differ.

If the birefringence is small, this is not significant. However, Okamoto (1984) showed that large, anisotropic birefringence causes sufficient difference between γ_x and γ_y that effective single-polarizatin operation is possible. The dominant influence on this difference in bend loss is independent of the detail of g.

CHAPTER SEVEN

Alternate Formalism:

"Fourier Fibre Optics"

> The Old Grey Donkey, Eeyore, stood by
> himself in a thistly corner of the
> Forest, his front feet well apart, his
> head on one side, and thought about
> things. Sometimes he thought, "Why?" and
> sometimes he thought, "Wherefore?" - and
> sometimes he thought, "Inasmuch as
> which?" - and sometimes he didn't quite
> know what he **was** thinking about.
>
> A.A. Milne, "Winnie-the-Pooh"

The weak guidance formalism, used in the orthodox analysis of dielectric waveguides, employs the scalar wave equation, which is a linear, second-order differential equation for the modal pattern, or near field, ψ, which is the distribution of energy in the cross-section of the waveguide. It is possible to rework the formalism in terms of the far field, Ψ, which is the Fourier transform of ψ and the pattern seen when the light is projected from the waveguide onto a distant screen. This new formalism produces a homogeneous integral equation, which needs to be solved for the propagating mode (Pask, 1982). If only axisymmetric refractive index profiles are considered, the analysis greatly simplifies. In this case symmetric Fredholm equations of the second kind are recovered. It is interesting how the structure - notably the location of the zeroes - of the kernel of this equation influences the detail of Ψ. Two examples are shown. An appealing general result is suggested, although a rigorous proof of this description of the behaviour is not yet available.

§7.1   Motivation

Particularly for the fundamental mode, the transverse field distribution, ψ, is very insensitive to the detailed structure of the refractive index profile, n. For example, ψ does not change sign. This insensitivity to the detailed structure is exploited in the derivation of various schemes which identify equivalent waveguides.

ψ^2 corresponds to the intensity of the electromagnetic wave as it propagates along the fibre. As such, it represents a quantity which can be measured. However, the insensitivity means that the fine detail of n can be found only by exceptionally careful and accurate measurements of ψ. Some properties, e.g. dispersion, depend critically on the fine structure of n. For this reason, it is useful to develop a characterization which depends on this fine structure. The far field, Ψ, does. This is rich in structure, being a pattern which **can** have many zeroes and local intensity peaks. Relationships between these zeroes and intensity peaks are very dependent on the form of n.

Within the laboratory, Ψ^2 is easier to measure than ψ^2 (Gambling et al, 1976; Brinkmeyer, 1979). While the latter is the signal's intensity within the waveguide, the former is the intensity pattern seen when the travelling signal is projected onto a distant screen. Indeed, this very simplicity of examination has influenced some characterizations (Pask & Sammut, 1980; Matsumura & Suganuma, 1980) of equivalent step index fibres to employ Ψ^2.

As Pask (1982) observed, the Fourier representation can be considered the more natural way of describing fibre optics. Recently the discussion of Petermann's "strange" spot-size (Petermann, 1983; Pask, 1984) involved the use of Ψ, rather than ψ. Thus, the derivation of a formalism to describe Fourier fibre optics is desirable.

In a Fourier domain, the behaviour of the transform of the refractive index distribution is of interest, too. Subsequently the transform, G, of the shape-function, g, is examined. It will be seen that there may be a simple correlation between the zeroes of G, and the zeroes of Ψ.

§7.2   Derivation of the integral equation

The refractive index profile $n(\mathbf{r})$ at position $\mathbf{r}=(X,Y)$ is

$$n^2(\mathbf{r}) = n_{c\ell}^2\left(1 + 2\Delta g(\mathbf{r})\right) , \qquad (1)$$

where $n_{c\ell}$ is the cladding index and Δ is the customary profile height

parameter.   The scalar wave equation (P.3) is

$$\left(\nabla^2 + V^2 g(\mathbf{r}) - W^2\right) \psi = 0 \qquad (2)$$

where V and W have their usual meanings, all lengths are scaled, and ∇^2

is the two dimensional Laplacean operator.   Using (2), a particularly

elegant form of integral equation can be obtained, a form with very well

understood properties.

§7.2.1 Transform of the differential equation

To transfer to the Fourier domain, with variable $\mathbf{p}$,   the two-

dimensional Fourier transform is defined by

$$G(\mathbf{p}) = \mathcal{F}_2(g(\mathbf{r}),\mathbf{p}) \qquad (3)$$

$$= \frac{1}{2\pi} \int_{R_2} d\mathbf{r}\; g(\mathbf{r})\, e^{-i\mathbf{p}.\mathbf{r}}$$

whence

$$\Psi(\mathbf{p}) = \mathcal{F}_2(\psi(\mathbf{r}),\mathbf{p}) \qquad (4)$$

From physical considerations, it is clear that ψ, $\partial\psi/\partial X$, and $\partial\psi/\partial Y$

vanish as $|\mathbf{r}|\to\infty$.   Thus (refer Davies, 1978, §11.1),

$$\mathcal{F}_2\left(\nabla^2 \psi(\mathbf{r}), \mathbf{p}\right) = -p^2 \Psi(\mathbf{p}) \ ,$$

where the orthodox notation $|\mathbf{z}| = z$ is employed. Using the two-dimensional analogue of the convolution-product result, (2) is transformed into the integral equation

$$\left(p^2 + W^2\right) \Psi(\mathbf{p}) = \lambda_0 \int_{R^2} d\boldsymbol{\zeta} \ \Psi(\boldsymbol{\zeta}) \ G(\mathbf{p} - \boldsymbol{\zeta}) \ , \qquad (5)$$

where

$$\lambda_0 = V^2 / 4\pi^2 \ .$$

This is the expression derived by Pask (1982). Apart from the factor multiplying Ψ in the left-hand expression, (5) has the standard form of a Weiner-Hopf equation.

It is interesting to note that the roles of V and W have been interchanged. In (2), W appears in the solution as an eigenvalue, when V is specified, while in (5), V is determined as an eigenvalue, given W.

§7.2.2 Effect of axisymmetry

If n is an axisymmetric refractive index profile, then

$$g(\mathbf{r}) = g(r)$$

and examination of (3), shows

$$G(\mathbf{p}) = G(p) \ .$$

Under this condition, the Fourier transforms reduce to zeroeth order Hankel transforms (refer Davies, §15.1) and (3) becomes

$$G(p) = \int_0^\infty g(r) J_0(pr) r \, dr \qquad (6)$$

where J_0 is the zeroeth order Bessel function of the first kind.

For HE_{1m}-modes, including the fundamental (HE_{11}) mode, ψ is also axisymmetric, and thus Ψ, given by a similar expression to (6), is a function of p only. Under these circumstances (5) can be greatly simplified. The integral on the right-hand side of (5) can be written explicitly, using polar co-ordinates with θ being the angle between **p** and ξ,

$$I_R = \int_{R^2} d\xi \; \Psi(\xi) \; G(\mathbf{p}-\xi)$$

$$= \int_0^\infty \xi d\xi \int_0^\infty d\theta \; G\left[(p^2+\xi^2-2p\xi\cos\theta)^{1/2}\right]\Psi(\xi)$$

$$= \int_0^\infty \xi d\xi \; \Psi(\xi) \int_0^{2\pi} d\theta \int_0^\infty dr \; rg(r) \; J_0\left(r(p^2+\xi^2-2p\xi\cos\theta)^{1/2}\right) \qquad (7)$$

using (6). Both the θ- and r-integrals are convergent, allowing an interchange of the order of integration. Using Gradshtein & Ryzhik (6.684.1), the θ-integration in (7) can be performed, giving

$$I_R = 2\pi\int_0^\infty \xi d\xi \; \Psi(\xi) \int_0^\infty rdr \; g(r) J_0(rp) J_0(r\xi) \; .$$

Substituting this into (5) produces

$$(p^2 + W^2)\Psi(p) = 2\pi\lambda_0\int_0^\infty \xi d\xi \; \Psi(\xi) L(p,\xi) \qquad (8a)$$

where

$$L(p,\xi) = \int_0^\infty dr \; rg(r)J_0(rp)J_0(r\xi) \tag{8b}$$

is a symmetric kernel.

The system (8) defines a linear, homogeneous integral equation. By changing variables to

$$s = p^2 \;\; ; \;\; t = \xi^2$$

and defining

$$\phi(x) = \left(x+W^2\right)^{1/2}\Psi(\sqrt{x})$$

and

$$K(s,t) = \frac{L(\sqrt{s}, \; \sqrt{t})}{\left((s+W^2)(t+W^2)\right)^{1/2}} \; , \tag{9}$$

(8) becomes

$$\phi(s) = \lambda \int_0^\infty dt \; \phi(t)K(s,t) \tag{10}$$

where

$$\lambda = V^2/4\pi$$

is called a characteristic value. The dependence on W has been absorbed into ϕ and K. (10) is a homogeneous Fredholm integral equation of the second kind with a symmetric kernel, an equation extensively examined in the literature.

§7.2.3   Properties of the integral equation

It follows from the properties of $g(r)$ and J_0 that K is in the Hilbert space of Lebesgue square integrable functions, $L^2(\mathbb{R}^{+2})$. Also, if W does not vanish, it follows from (9) that K is continuous on $\mathbb{R}^{+2}$.

(If W=0, the mode is at cut-off, and an alternative description becomes necessary.) Given these properties of K, then ϕ will also satisfy these requirements.

For ease of description, on $L^2(\mathbf{R}^+)$ define the integral operator $\mathbf{K}$, by

$$(\mathbf{K}u)(x) = \int_0^\infty dt\ K(x,t)u(t)\ .$$

Solutions of (10) are the eigenfunctions and corresponding characteristic values of $\mathbf{K}$.

It is useful to know whether $\mathbf{K}$ is a positive definite operator. If $u,v \in L^2(\mathbf{R}^+)$, the inner product on this space is defined by

$$\langle u,v \rangle = \int_{\mathbf{R}^+} dx\ u(x)v(x)\ .$$

For all u,

$$\langle u,\mathbf{K}u \rangle = \int_0^\infty u(x)dx \int_0^\infty u(t)dt\ K(x,t)$$

$$= \int_0^\infty g(r)rdr\ \left[\int_0^\infty dxu(x)\ \frac{J_0(r\sqrt{x})}{\left(x+W^2\right)^{1/2}}\right]^2$$

$$\geqslant 0$$

provided g is everywhere non-negative. In this case $\mathbf{K}$ is positive definite. If g assumes positive and negative values, the inequality may hold, but it will depend upon the position of these regions of negativity, relative to the weighting provided by the squared x-integral. This is a complicated condition.

A positive definite, Fredholm operator satisfies the requirements of Mercer's theorem (refer Courant & Hilbert, p158), and possesses a complete set of orthogonal eigenfunctions $\{\phi_0,...\}$ and an ordered sequence of positive characteristic values,

$$0 < \lambda_0 \leqslant \lambda_1 \leqslant ... .$$

Thus, given W, there exists an unbounded sequence of V's for which W is a solution. Further, the modal fields corresponding to these can be recovered from the eigenfunctions of (10), as

$$\psi(r) = \int_0^\infty dp \; p \; \frac{J_0(pr)\phi(p^2)}{\left(p^2 + W^2\right)^{1/2}} \; .$$

The scalar propagation problem has been formulated in terms of an integral equation. However, there are not as many general, theoretical results about the form of the solutions of integral equations as there are about the form of the solutions of differential equations. For example, there is no analogue of the Sturm-Liouville theory.

§7.3   Example: Smoothed-out profiles

To obtain an insight into the behaviour of Ψ, a couple of examples are presented. The first is the set of "smoothed-out" profiles defined by

$$g_m(r) = \frac{\Gamma(m+1,(m+1)r^2)}{\Gamma(m+1)} \; , \qquad (11)$$

where $\Gamma(x,y)$ is the incomplete gamma function (refer A&S, 6.5.3). These profiles are of interest because the shape varies from Gaussian to step, as m varies from 0 to ∞, but the profile volume is constant (see figure 7.1). It is interesting to determine how this change in g
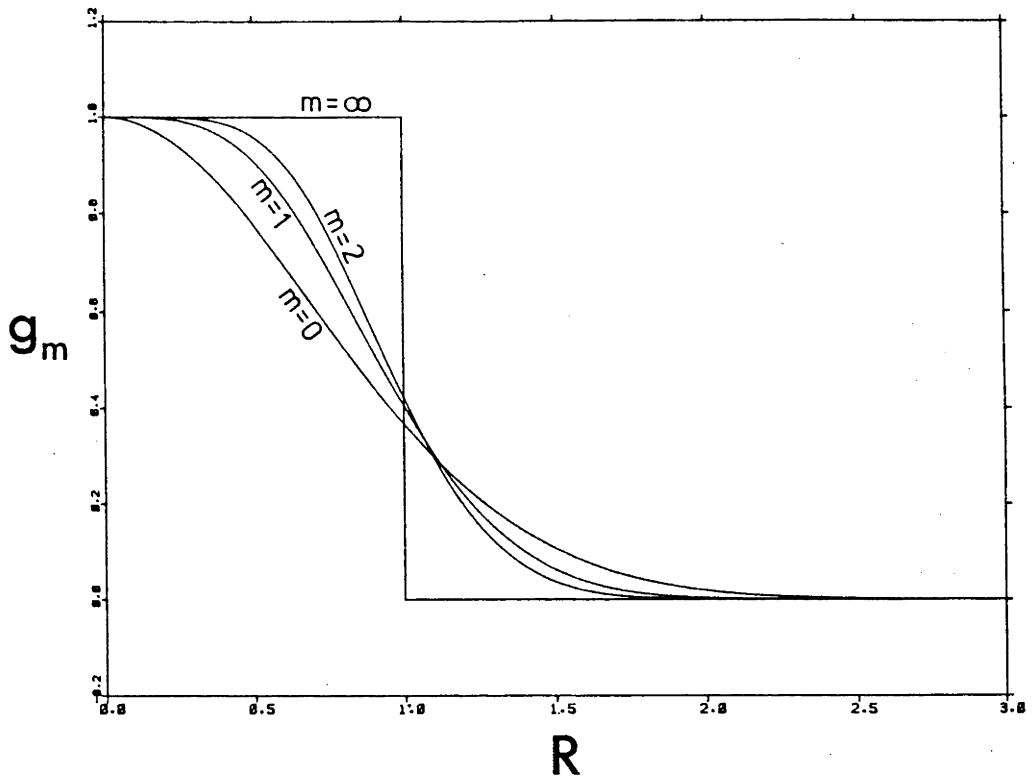
Figure 7.1

The family of equal volume, smoothed-out profiles, defined in (11), vary from Gaussian to step as m varies from 0 to ∞.
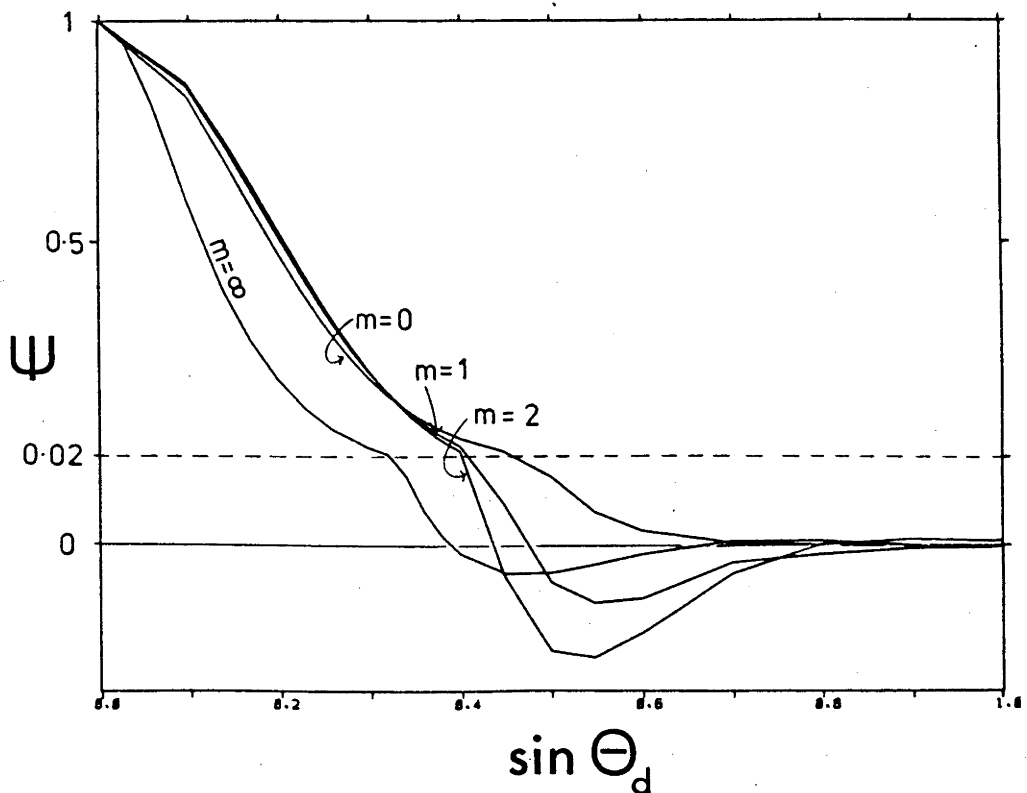

Figure 7.2

Far field patterns for the smoothed-out profiles. Here the canonical normalized frequency is $\bar{V}=2.4$. θ_d is the observation angle.

influences the detail of Ψ, recalling the motivation as to whether the location of the zeroes of Ψ corresponds to detail of n. The fundamental mode, corresponding to Ψ_0, is of particular interest.

§7.3.1 Integral equation

Pask (1982) showed that, with g given in (11), G(p) defined by (6) becomes

$$G(p) = \frac{\pi}{m+1} e^{-p^2/4(m+1)} L_m^{(1)}(p^2/4(m+1)) \qquad (12)$$

where $L_n^{(c)}$ is a generalized Laguerre polynomial (A&S, 22.3.9). Thus, G has m zeroes. Using (12), together with (5), (6) and (7), the preliminary symmetric kernel, $L(p,\xi)$ of (8b), is

$$L(p,\xi) = e^{-p^2/4(m+1)} e^{-\xi^2/4(m+1)} \sum_{\ell=0}^{\infty} \left(\frac{p^2\xi^2}{4(m+1)}\right)^\ell \frac{1}{\ell!^2} L_m^{(2\ell+1)}\left(\frac{p^2+\xi^2}{4(m+1)}\right)$$

and, after the variable change

$$s = p^2/4(m+1); \qquad t = \xi^2/4(m+1) ,$$

the integral equation (8a) becomes

$$(s+\alpha)\Phi(s) = \lambda \int_0^\infty dt \; \Phi(t)K(s,t) \qquad (13a)$$

where

$$\alpha = W^2/4(m+1) ,$$

$$\Phi(t) = \Psi(\sqrt{4(m+1)t}) ,$$

and

$$K(s,t) = e^{-s}e^{-t} \sum_{\ell=0}^{\infty} \frac{(st)^{\ell}}{\ell!^2} L_m^{(2\ell+1)}(s+t) \ . \tag{13b}$$

As can be readily appreciated, (13) cannot be solved in a simple, analytic form. Since interest is in the structure of Ψ, notably its zeroes and local maxima, and since this structure is the same for Φ, it is useful to examine an approximate form for Φ, an approximation which might aid in discerning the features of Ψ.

§7.3.2 Approximate solution

For a first approximation of Φ, the iterative method of Svartholm (e.g. Sneddon, p385) is used. This procedure commences with an arbitrary function, usually including free parameters which can be optimized to improve the approximation. The kernel is applied iteratively so that the process converges on the dominant eigenfunction:

$$\phi_0 = \lim_{n \to \infty} \left((\lambda_0 K)^n h\right)$$
,

where h is an arbitrary function.

Pask (1982) commenced with the form

$$\phi_0 \approx \chi_0 = e^{-bx}$$

and optimized the choice of b by requiring Λ_0, the first approximation of λ_0, to be stationary with respect to b. Thus,

$$\frac{\partial \Lambda_0}{\partial b} = 0 \quad \Rightarrow \quad (m+1)(4\alpha-1) = \left(1+\frac{1}{(m+1)b}\right)^{m+2} - (m+2)\left(1+\frac{1}{b(m+1)}\right) \ .$$

This produced a first iterated solution

$$\chi_1 = \frac{e^{-bx/(1+b)}}{(x+\alpha)(1+b)} \sum_{n=0}^{m} \left(\frac{b}{1+b}\right)^n L_n\left(\frac{bx}{1+b}\right) ,$$

which is a polynomial of degree m multiplied by a positive function. Thus, for a refractive index of form (11), characterized by m, this approximation implies that there are m zeroes in Ψ. Of course, not all would be visible in the far field pattern. A **finite** value of p corresponds to $\sin\theta = 1$, or an observation angle of 90°. For the far field, $\Psi(p)$,

$$p = ka \sin\theta ,$$

so that for p>ka, the zeroes do not appear.

It is readily appreciated that to proceed analytically with this iteration, and obtain χ_2 is not easy. However, for the cases m=1 and m=2, it was possible to obtain an explicit form for χ_2 which showed the same behaviour – a polynomial of degree m multiplied by a positive function. Using numerical integration, the second iteration was evaluated up to m=4, and the zeroes of χ_2 were seen to be very close to those of χ_1.

This relation between m in (11), which is also the number of zeroes of G_m in (12), and the number of zeroes of Ψ is consistent with the two cases m=0, for which it is known that Ψ has no zeroes, and m=∞, the step, for which Ψ is known (Gambling et al, 1976b) to have an infinite number of zeroes. Whether this relation involving m and the number of zeroes of Ψ is true, or whether it is a coincidence due to the approximation needs to be investigated further.

§7.3.3 Exact solution

Conventionally, numerical solutions of integral equations like (13) are obtained using the Nyström method (e.g. Baker, §3.2), which converts the integral equation into a finite dimensional matrix eigenvalue problem. However, for (13) it was found that convergence was slow. Up to 60x60 matrices were used without satisfactory results, and thereafter errors involved in numerical matrix manipulation caused difficulties.

Thus, another technique of solution was developed, and the details are presented in §7.A. The expansion of the eigenfunctions in terms of simple polynomials produced a different finite dimensional matrix problem. Employing this method, convergence was rapid; 12x12 matrices produced satisfactory results. The primary eigenfunctions were obtained, and the far field patterns corresponding to several values of m in (11) are shown in figure 7.2. The number of zeroes is again m, consistent with the iterative approximation.

§7.4 Example: Non-standard power law profiles

The next example considered is another family of profiles which varies continuously from a step to a Gaussian like cross-section. These are characterized by a power-law expression

$$g_q(r) = \begin{cases} (1-r^2/(q+1))^q, & r \leqslant \sqrt{q+1} \\ 0 & , r > \sqrt{q+1} \end{cases} \tag{15}$$

The step profile corresponds to g_0. For $q \gg 1$ (A&S, 4.2.21)

$$g_\infty \sim e^{-r^2},$$

corresponding to the Gaussian profile. If $m=1/q$, the characterization is identical to that of §7.3. These profiles are shown in figure 7.3.
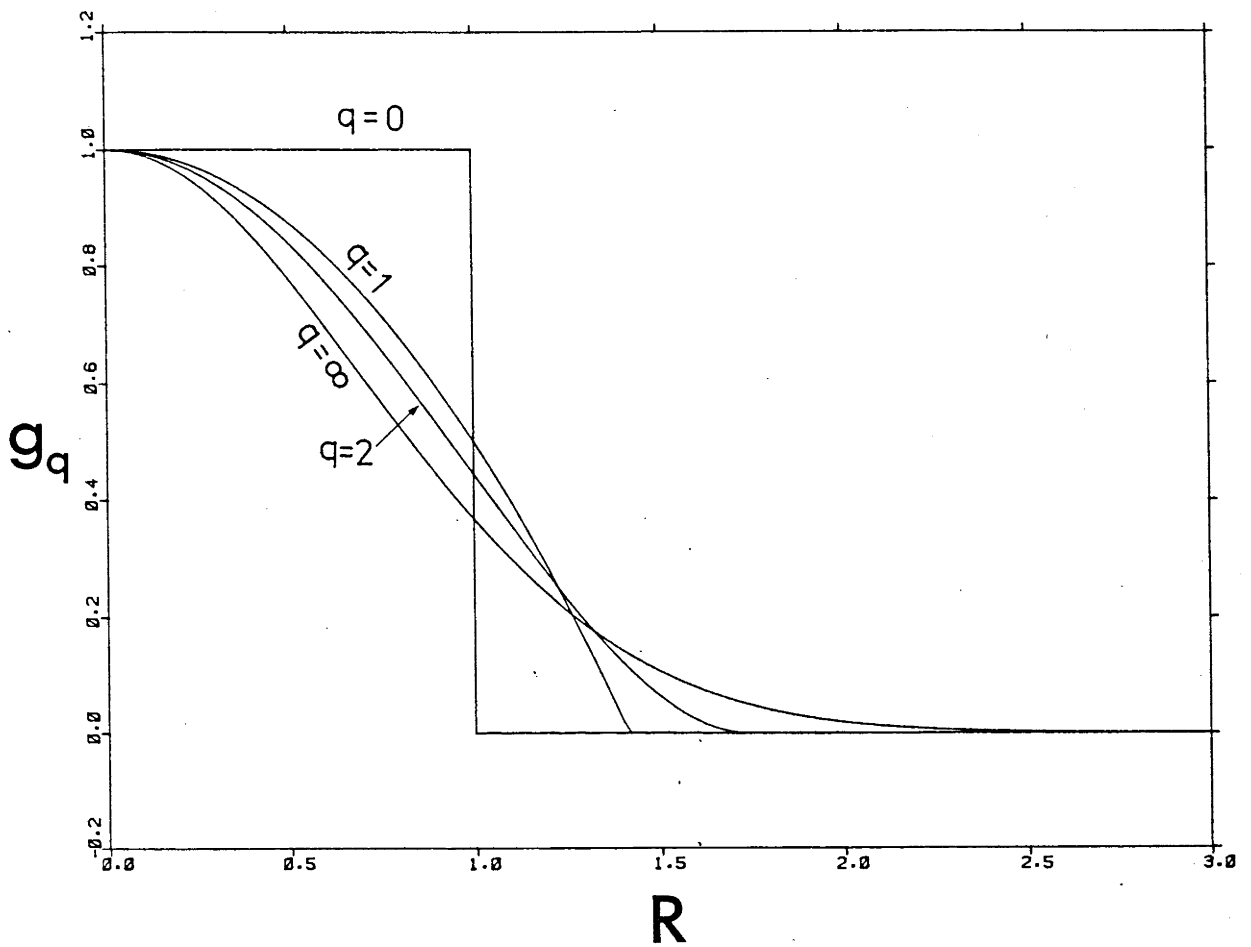
Figure 7.3

The family of non-standard power-law profiles, defined in (15), varies from step to Gaussian as q varies from 0 to ∞.

§7.4.1   Integral equation

Using (6), the transform of the refractive index, another

observable field (refer Brinkmeyer, 1979), is

$$G_q(p) = 2^q \Gamma(q+1) \frac{J_{1+q}(p\sqrt{q+1})}{(p\sqrt{q+1})^{q+1}}$$

$$= 2^{1/m} \Gamma(\frac{m+1}{m}) \frac{J_{1+1/m}(p\sqrt{(m+1)/m})}{(p\sqrt{\frac{m+1}{m}})^{(m+1)/m}}$$

which has an infinite number of zeroes, if m is a positive integer.

Proceeding analogously to §7.3.1, it is found that

$$L(p,\xi) = \sum_{k=0}^{\infty} \Gamma(q+2k+2)\overline{G}_k(q+1,1,i) \frac{J_{q+2k}(p\sqrt{q+1})J_{q+2k}(\xi\sqrt{q+1})}{p^{q+1}\xi^{q+1}(1+q)^{q+1}} 4^{q+1} \Gamma(q+2) \quad (16)$$

where $\overline{G}_k(x,n,p)$ is a Jacobi polynomial (A&S, 22.2.2). After the

variable change

$$s^2 = qp^2 \; ; \quad t^2 = q\xi^2 \, ,$$

(10) becomes

$$\phi(s) = \mu \int_0^{\infty} ds \, s\phi(s)K(s,t) \, , \qquad (17a)$$

where

$$\mu = \frac{v^2 4^q \Gamma(q+2)}{\pi} \, ,$$

$$\phi(x) = \sqrt{x^2+\alpha} \, \Psi(x/\sqrt{q+1}) \, ,$$

$$K(s,t) = \frac{1}{\sqrt{s^2+\alpha} \, \sqrt{t^2+\alpha}} \frac{L(s/\sqrt{q+1},t/\sqrt{q+1})}{\Gamma(q+2)4^{q+1}} \qquad (17b)$$

and

$$\alpha = qW^2 .$$

Consider the kernel in (16) with either p=0 or ξ=0. Because of symmetry, the choice does not matter. In this example, it is clear (A&S 9.1.10) that the resulting function of one variable has an infinite number of zeroes.

§7.4.2 Solution

The kernel defined by (16) and (17) consists of an infinite sum of terms, each of which has its functional dependence on s and t completely separated. On truncating this infinite sum, the problem can be reduced to an eigenvalue–eigenvector equation involving a finite, real, symmetric matrix. Thus, a satisfactory solution for (17a) can be obtained using the method for degenerate kernels (e.g. Mikhlin, 1957, §4). In this case, Ψ has an infinite number of zeroes. However, it is clear from (14) that not all the zeroes will be visible in the far field pattern.

§7.5   Conjecture

In §7.3 it was shown that the kernel vanishes on m contours in the semi-domain s < t (refer figure 7.4(a)) and has a primary eigenfunction with, seemingly, m zeroes. In §7.4, a kernel with an infinite number of such contours (figure 7.4(b)) was shown to possess a primary eigenfunction with an infinite number of zeroes. This result points to the lack of rigorous results in the theory of integral equations. There does not appear to be any general theory which relates the oscillatory nature of a kernel to that of the primary eigenfunction (except if the kernel is everywhere positive, as explained in §8.3).

Figure 7.4

(a) A qualitative indication of the contours where the kernel (13 b) vanishes.   There are m.

(b) A qualitative indication of the contours where the kernel (17b) vanishes.   There are an infinite number.
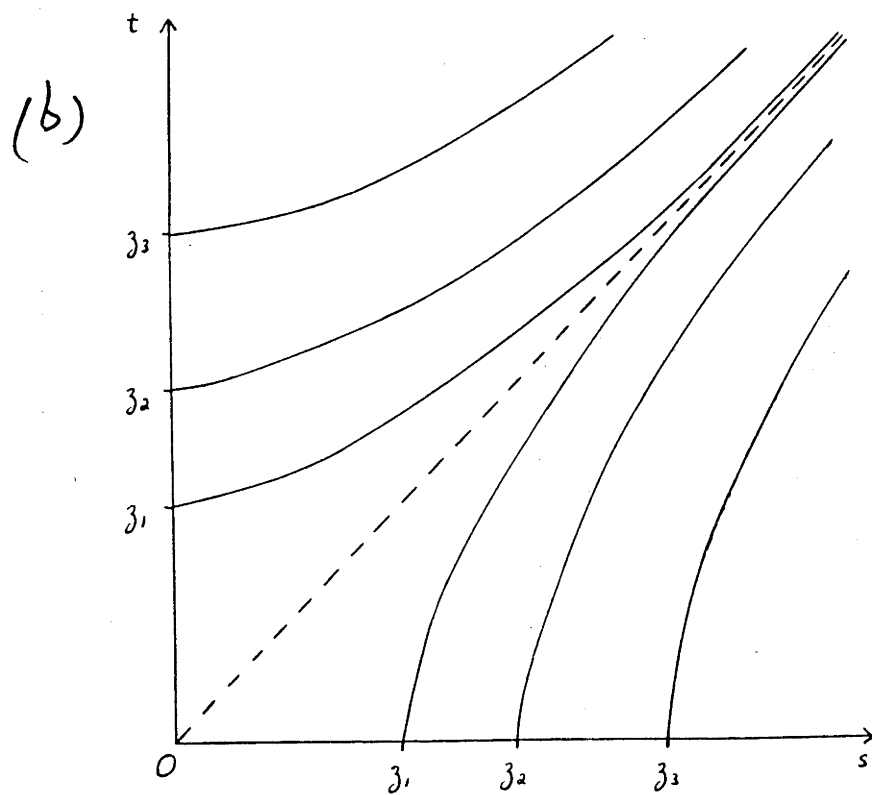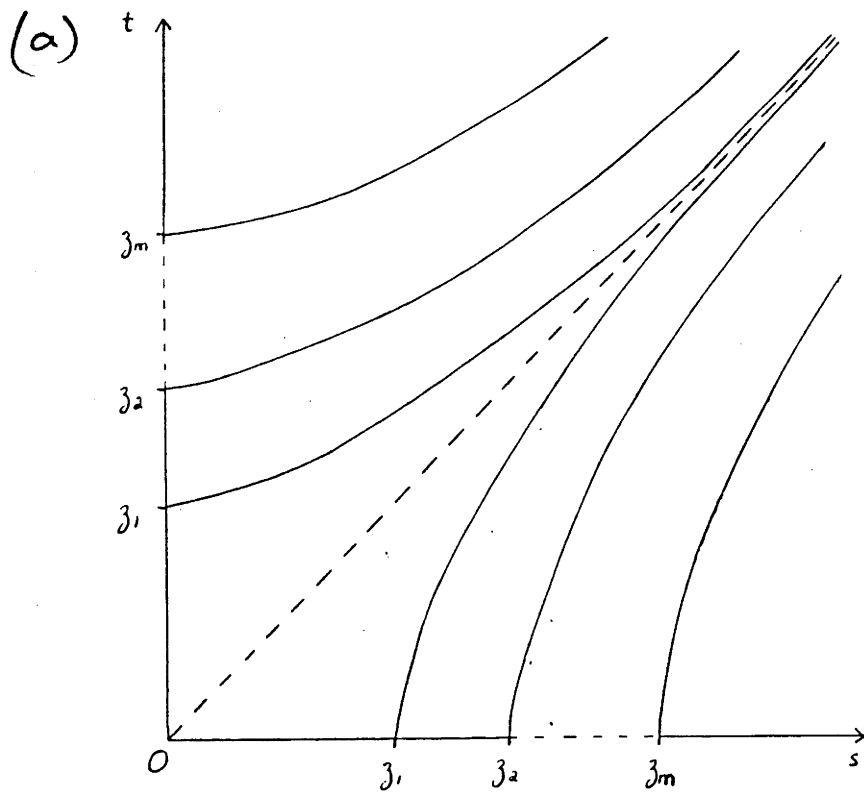
Recalling that the motivation for this research was to find the way ψ responds to the fine details of n, it is to be expected that a slower variation in n, corresponding to less oscillations in the kernel, would produce a smoother form of ψ. The Fourier transform magnifies the effect of these variations; faster variations in ψ cause more rapid oscillations in Ψ.

In the theory of differential equations, Sturm-Liouville theorems relate the form of the differential operator and its domain of definition, to the oscillations of the eigenfunctions. It is an interesting, but unresolved, question whether a theory exist to link the structure of an integral operator with that of its eigenfunctions.

§7.A   Appendix: A method for solving certain integral equations

Presented here is an analytic method of solution for homogeneous Fredholm integral equations of the second kind –

$$\phi(x) = \lambda \int_\Omega dt\ K(x,t)\phi(t) \tag{18}$$

– when the kernel is an infinite sum of polynomials:

$$K(x,t) = f(x)f(t) \sum_{\ell=0}^{\infty} (xt)^\ell P_\ell(x+t) \tag{19}$$

which is convergent, and where

$$P_\ell(z) = \sum_{k=0}^{\infty} a_{\ell k} z^k \ ,$$

a polynomial of degree m. It is possible to resum (19) as

$$K(x,t) = \sum_{\ell=0}^{\infty} \chi_{\ell}(x) \sum_{k=0}^{\infty} c_{\ell k} \chi_k(t)$$

where

$$\chi_j(z) = f(z)z^j$$

and

$$c_{ij} = \begin{cases} 0 & , \; j+m < i < \max(0,j-m) \\ \sum_{p=\max(0,j-i)}^{i+m} a_{j-p,i-j+2p} \dfrac{(i-j+2p)!}{p!(i-j+p)!} & , \; \text{elsewhere} \end{cases} .$$

Because (19) is convergent, it is apparent that the series for c_{ij} is convergent.

Using standard tensor notation, the operator $\mathbf{K}$ can be written as

$$\mathbf{K} = \sum_{\ell,k=0}^{\infty} c_{\ell k} \chi_{\ell} \otimes \chi_k \; . \tag{20}$$

Being real and positive definite, $\mathbf{K}$ has a complete, orthonormal set of eigenfunctions, $\{\phi_n\}$, with associated real characteristic values, $\{\lambda_n\}$. Thus,

$$\mathbf{K} = \sum_{n=0}^{\infty} \lambda_n \phi_n \otimes \phi_n$$

$$= \sum_{n,r,s=0}^{\infty} \lambda_n \tau_{nr} \tau_{ns} \chi_n \otimes \chi_s \; , \tag{21}$$

where

$$\phi_n = \sum_{k=0}^{\infty} \tau_{nr} \chi_r$$

is the expansion of ϕ_n in terms of the basis $\{\chi_n\}$. From (20) & (21), it

follows that

$$c_{\ell k} = \sum_{j=0}^{\infty} \lambda_j \tau_{j\ell} \tau_{jk}$$

$$\Rightarrow \quad C = T^{\dagger} \Lambda T \quad , \tag{22}$$

where the matrices C, T, and Λ have elements c_{ij}, τ_{ij}, and $\lambda_i \delta_{ij}$, respectively, and $\dagger$ denotes matrix transpose.

Although $\{\phi_n\}$ is orthonormal, $\{\chi_n\}$ is not. Thus

$$\langle \chi_i, \chi_j \rangle = G_{ij}$$

$$= \int_{\Omega} dy \, f^2(y) y^{i+j}$$

$$= g_{i+j} \quad ,$$

which gives

$$\langle \phi_{\ell}, \phi_n \rangle = \delta_{\ell n} = \sum_{i,j=0}^{\infty} \tau_{\ell i} \tau_{nj} G_{ij}$$

$$\Rightarrow \quad I = TGT^{\dagger} \quad . \tag{23}$$

This is a second matrix equation, to be solved together with (22). The system (22) and (23) can be simplified further. Because $K(x,t)$ is symmetric, C is symmetric and can be decomposed as

$$C = SS^{\dagger} \quad ,$$

where S is an upper triangular matrix. Thus, from (22)

$$T = \Lambda^{1/2} US \quad ,$$

where U is a unitary matrix which remains to be determined. Define

$$R = SGS^{\dagger} ,$$

so that substitution of (24) in (23) produces

$$\Lambda^{1/2} URU^{\dagger} \Lambda^{-1/2} = I$$

$$\Rightarrow \qquad R = U^{\dagger} \Lambda U ,$$

which follows because R is a real, symmetric, non-singular matrix.

Thus the solution of (18) is reduced to finding the eigenvalues and eigenvectors of R. Because of the properties of this matrix, there are suitable numerical routines to do this.

In principle, **this method is analytic.** However, because R is of infinite order, it is necessary to truncate R,S,G, etc.

CHAPTER EIGHT

Eigenfunctions of Integral Operators

So Pooh and I go whispering, and Pooh looks very
bright,
And says, "Well, I say sixpence, but I don't
suppose I'm right."
And then it doesn't matter what the answer ought
to be,
'Cos if he's right, I'm Right, and if he's
wrong, it isn't Me.

A.A.Milne, "Now We Are Six"

The venerable Sturm-Liouville theorems (e.g. Ince, 1926a, ch 10) provide

an indication of the oscillatory behaviour of the eigenfunctions of

linear, second-order differential operators. However, as noted in §7.2,

no analogous theory exists for linear integral operators. In the

previous chapter it was observed that the zeroes of the eigenfunctions

might be related to the zeroes of the kernel of the integral operator.

In this chapter, a more general examination of the relationship between

the structure of the kernel and the eigenfunctions' zeroes is presented,

and a suggestion about a general correspondence will be offerred. The

contours on which $K(s,t)$ vanishes in the (s,t) domain divide sub-domains

where K has opposite sign. These contours are deemed critical: the

number and form may fix the zeroes of ϕ.

§8.1   Statement of the problem

§8.1.1 Notation and definitions

Consider the integral operator, K, defined on the

interval $[a,b]=\Omega$ by the kernel $K(s,t)$. Interest is with the

eigenfunctions, $\{\phi_n\}$, and characteristic values, $\{\lambda_n\}$, of **K**. In

particular, it is desired to know $\{z \in \Omega : \phi_0(z)=0\}$, i.e. the location of

the zeroes of the primary, or fundamental, eigenfunction.

On the domain Ω^2, K(s,t)=0 on the curves $C_1,\ldots C_m$. If Ω is

infinite, m may be infinite. These contours in Ω^2 will be called the

ISONULLS of **K**, and are defined by the implicit relation

$$K(s,t) = 0.$$

Because K is symmetric, C_n is symmetric when reflected in the line s=t.

Assuming **K** is symmetric and positive-definite, i.e. self-adjoint,

it follows that there exists a complete, orthonormal set $\{\phi_n\}$, and a

sequence

$$\lambda_0 \leqslant \lambda_1 \leqslant \ldots$$

for the characteristic values. Subsequently, such restrictions will be

assumed to apply to **K**.

§8.1.2 Some examples

If $\Omega{=}R$ and K is the symmetric kernel

$$K(s,t) = e^{s^2/2} e^{t^2/2} (2-\text{erfc}(s)) \, \text{erfc}(t) \, , \, s \leqslant t,$$

where erfc is the complementary error function (A&S, 7.1.2), then

(Courant & Hilbert, p153) ϕ_n is the nth order Hermite function. In this

case, the kernel is everywhere positive, and the nth eigenfunction has n

zeroes.

A similar result occurs for the semi-infinite interval $\Omega{=}R^+$. The

symmetric kernel

$$K(s,t) = e^{s/2} e^{t/2} E_1(t) \, , \quad 0 \leqslant s \leqslant t,$$

produces (Courant & Hilbert, p153) ϕ_n as the nth order Laguerre

function. Here E_1 is the first order exponential integral (A&S, 5.1.1). Again an operator which is everywhere positive has an nth eigenfunction with n zeroes.

A similar result can be seen on the finite domain $\Omega=[-1,1]$. If the kernel is given by

$$K(s,t) = \frac{1}{\sqrt{1-\cos(s+t)}} \overline{K}\left(\sqrt{\frac{2\sin(t)\sin(s)}{1-\cos(s+t)}}\right) \ ,$$

which is also everywhere positive, the eigenfunctions are (Hansen, 1975, 46.8.11) renormalized Legendre polynomials. $\overline{K}$ is a complete elliptic integral (A&S, 17.3.1). Again the nth eigenfunction has n zeroes.

For variety, it is apparent (Watson, 1966, p144) that the weakly singular kernel, defined on $\Omega=R^+$ by

$$K(s,t) = \frac{J_0(s+t)}{\sqrt{st}} \ ,$$

has $J_k(t)/\sqrt{t}$ as eigenfunctions. Here there are an infinite number of isonulls, and each eigenfunction has an infinite number of zeroes.

These examples suggest a general theory, linking the number of isonulls and the number of zeroes of the eigenfunctions, awaits discovery.

§8.1.3 A suggested answer

For some class of operators, a suggested correlation between the zeroes of the primary eigenfunction and the structure of the kernel is:

the number of zeroes of ϕ_0 is the same

as the the number of isonulls cutting

either the S- or the T-axis.

Because of the symmetry of K, these two numbers are the same. Of course, a change of variables may change the co-ordinate axes such that no isonulls cut them. So there needs to be some preferred axes for K.

What class of operators displays this behaviour? Firstly, neither axis can be an isonull. Secondly, for simplicity of examination, all isonulls will be assumed to correspond to simple changes of sign.

§8.2   Strongly positive operators

In the examples of §8.1.2, the primary eigenfunction of a kernel which was positive everywhere had no zeroes. This is a special case of a more general result in operator theory - Jentzch's theorem (e.g. Hochstadt, 1973, p256). It is a consequence of the results of Kreĭn (1962) and Krasnosel'skii (1964).

The theorem, as recorded, applies to a compact, i.e. closed and bounded, domain, Ω. If $K \varepsilon C^0(\Omega^2)$ and $K(\Omega^2) > 0$, and since $\mathbb{K}$ is assumed positive definite and thus has only positive eigenvalues, then

$$0 < \lambda_0 < \lambda_i \ , \quad i \geqslant 1 \ ,$$

and

$$\phi_0(\Omega) > 0.$$

Hence, if Ω is bounded and K is positive everywhere, the primary eigenfunction is positive everywhere. Furthermore, this eigenfunction is unique, to within a normalization constant. Since ϕ_n, $n > 0$, is orthogonal to ϕ_0, all higher order eigenfunctions must have at least one zero.

On the bounded Ω, such an operator $\mathbb{K}$ is termed strongly positive with respect to the continuous, non-negative functions, which form a

solid cone. However, if Ω is not bounded, the non-negative functions do

not form a solid cone within the Banach space $C^0(\Omega)$, K is not strongly

positive, and Jentzch's theorem is not immediately applicable.

That this should be so is readily appreciated. K and ϕ must vanish

at infinity, and thus are not bounded away from zero on the

unbounded Ω, as they were for compact Ω. However, if K is truncated to

a bounded domain Ω_n which becomes Ω as $n \to \infty$, then $K_n \to K$ and, since $\lambda_0 > 0$,

$\lambda_0^{(n)} \to \lambda_n$. The eigenfunctions $\phi_0^{(n)}$ will converge to ϕ_0, but, while

$$\phi_0^{(n)}(\Omega_n) > 0 ,$$

only the weak inequality

$$\phi_0(\Omega) \geqslant 0$$

applies to ϕ_0. As mentioned, ϕ_0 will vanish at infinity. But will it

vanish, having a degenerate zero at some finite value? It seems

unlikely.

§8.3   Another result

For some positive kernels, more can be said about the behaviour of

the eigenfunctions.

In particular, oscillating kernels (see, e.g., Shaposhnikova et al,

1975, p83) have eigenfunctions such that the number of zeroes of ϕ_n is

n, and the zeroes of ϕ_n and ϕ_{n+1} interlace. Oscillating kernels are

defined on compact domains and need not be positive everywhere, so long

as they are non-negative. Also, using a discrete set of points

from Ω as arguments in K(s,t), it must be possible to define oscillating

matrices.

§8.4   Simply factorred kernel

§8.4.1 Lemma

Again commence by assuming Ω is bounded. Suppose K can be factorred as

$$K(s,t) = h(s) \, K_1(s,t) \, h(t) \, ,$$

where h has a finite number of simple zeroes on Ω and K_1 is everywhere positive. Also, define

$$\Phi = h\phi \, .$$

The operator $\mathbb{K}_1$, defined by the kernel

$$K_2(s,t) = h^2(s) \, K_1(s,t) \, ,$$

is positive, though not strongly positive. K_2 vanishes at the zeroes of h. However, although K_2 is not necessarily symmetric, the results

$$\lambda_0 > 0$$

$$\phi_0(\Omega) \geqslant 0$$

follow, using the theory developed by Krasnosel'skii (1964, ch2).

Since Φ is non-negative, ϕ changes sign with h. Hence, the zeroes of ϕ_0 include all the zeroes of h. There are no other zeroes of ϕ_0. This can be seen by assuming one exists, say z_1, and noting the contradiction in

$$0 = \Phi(z_1) = \lambda_0 \int_\Omega h^2(z_1) \, K_1(z_1,t) \, \Phi(t) \, dt \, ,$$

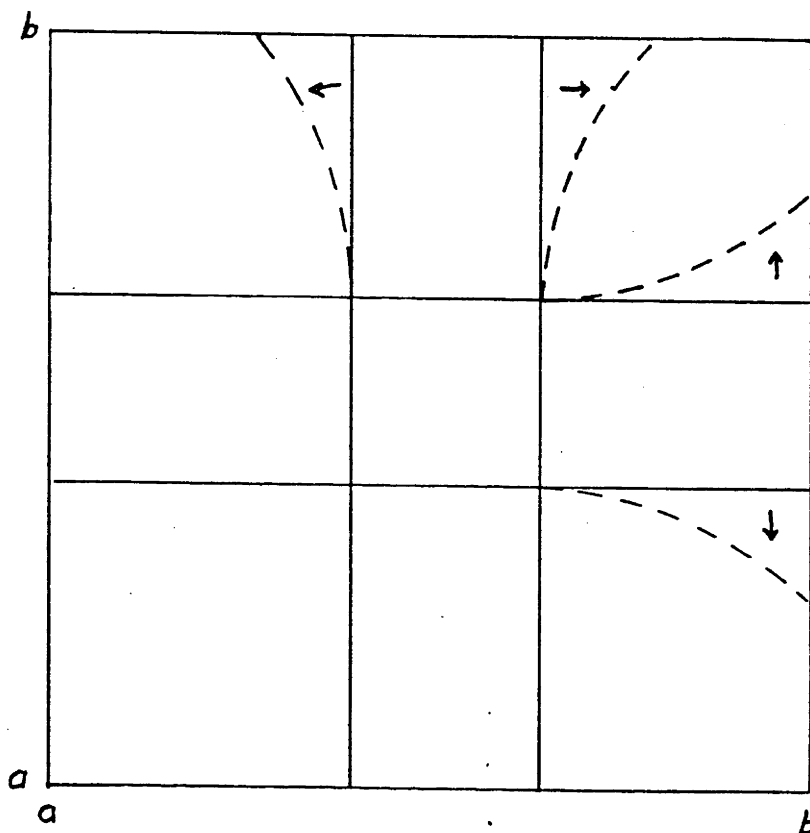where the integrand does not vanish identically and is non-negative.

Figure 8.1

The rectangular pattern of the isonulls of the kernel described in §8.4. The dotted portions indicate a pattern of isonulls which can be considered as a perturbation of the original, simpler pattern.

Again it is necessary to extend the result to an unbounded interval Ω. By analogy with the previous section, this can be achieved by the careful use of sequences. Thus, for an operator whose kernel has isonulls arranged as in figure 8.1 the primary eigenfunction has zeroes at exactly the same positions.

§8.4.2 Extension

The eigenfunctions of a symmetric operator vary continuously with the parameters of the kernel (see, e.g. Courant & Hilbert, p151). These parameters determine the isonulls. Thus, a perturbation of the isonulls away from the rectangular pattern – for example, the dotted curves in figure 8.1 – should not alter the number of zeroes of the primary eigenfunction, but, in general, the location of the zeroes will shift.

Of course, as the isonulls are deformed more and more, one of the zeroes may disappear, having shifted to infinity, or two may coalesce. One need consider only the way the number of zeroes in the primary eigenfunction of §7.3 changes as m, the parameter of the kernel, varies smoothly from one integer value to the next.

§8.5 One contour

Using variational theory, some very specific results can be established. One useful observation is proven below.

§8.5.1 Lemma

This time there is no need to assume Ω is bounded. However, Ω must be at least semi-bounded, i.e. either a or b finite. Subsequently, a is assumed finite. If a is infinite, a similar argument produces the corresponding result.

Suppose $K(s,t)$ is of the form such that its only isonull, C_1, is of the type indicated in figure 8.2, and is defined by the points $(s,f(s))$. It is required that

$$y_0 = \sup \{s \in \Omega: (s,f(s)) \in C_1\}$$

be bounded away from b, and $K(a,a) > 0$, thus causing $K(b,b) < 0$. The opposite sign arrangement does **not** work.

To show that the primary eigenfunction does have a zero, a contradiction is sought. For this contradiction, it is assumed that $\phi_0(\Omega) > 0$, and define

$$h(x) = \begin{cases} \phi_0 & , \quad x < y_0 \\ -\phi_0 & , \quad x > y_0 . \end{cases} \tag{1}$$

To maintain continuity, this jump in the function can be disguised by a third section, defined on an arbitrarily thin region, but the result is not altered. A general theorem (e.g. Courant & Hilbert, p132) for integral operators is that, for all functions h,

$$\langle \phi_0, K\phi_0 \rangle \geqslant \langle h, Kh \rangle . \tag{2}$$

In particular, this is true for h defined in (1). Substituting in (2) shows the only non-zero portion of the consolidated integral to be

$$2 \int_a^{y_0} ds \int_{y_0}^b dt \, K(s,t) \, \phi_0(s) \, \phi_0(t) \, > 0 .$$

This is a contradiction, because over this domain $K < 0$ and it is postulated ϕ_0 is everywhere positive. Thus, ϕ_0 must have at least one zero.
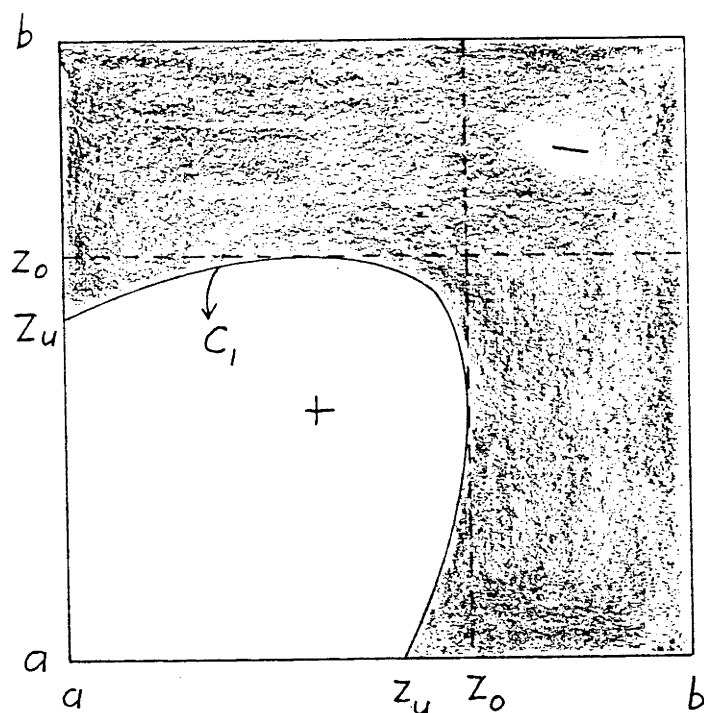
Figure 8.2

The structure of the kernel examined in §8.5. The sign of K(s,t) is negative in the shaded region. While b is shown to be finite, it need not be so. z_0 is the greatest value of s(or t) for which there is a value t(or s), producing the point (s,t) on C_1.
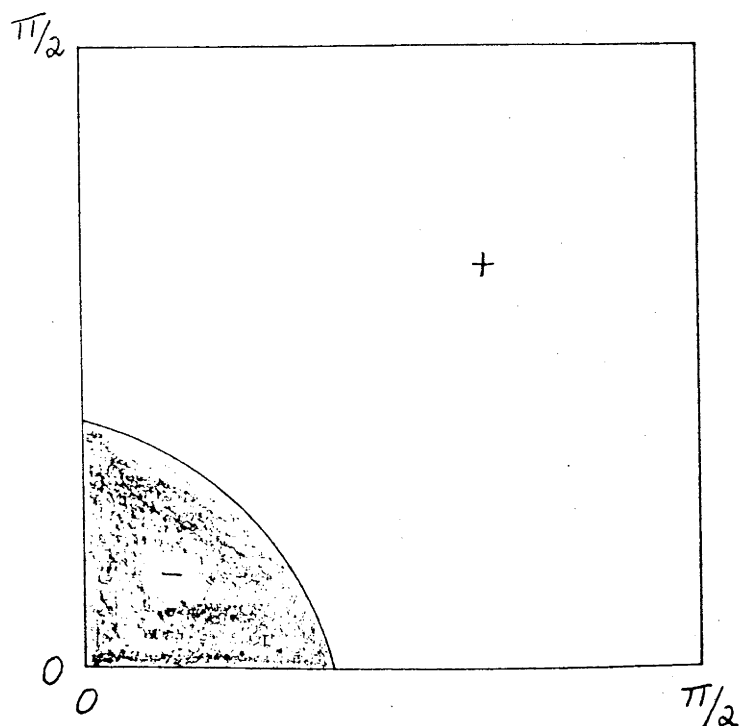

Figure 8.3

The structure of the kernel examined in §8.6. Again the sign of K(s,t) is negative in the shaded region.

§8.5.2 Extension

One can see by continuing with the trial function h, that y_0 is an upper bound on z_0. Thus, one could, perhaps, vary the parameters of K so that C_1 is no longer bounded.

Using property (2) of the primary eigenfunction, it is possible to show further results. Assumptions on the form of C_1 lead to various consequences on the position of the zero, z_0, of ϕ_0. For example, if f is a bijective function on $[a,y_0]$, then z_0 exceeds y_1, where y_1 is the intersection of C_1 with the line s=t.

Of course, the above has not established whether z_0 is unique!

§8.6 Complicating example

The preceeding sections may have implied that a kernel with one isonull defines an operator whose primary eigenfunction has one zero. However, this is not always true. If $\Omega=[0,\pi/2]$ and

$$K(s,t) = \cos(2\cos(s)\cos(t)) ,$$

which has the structure shown in figure 8.3 , the primary eigenfunction (refer A&S, 20.7.20) is the Mathieu function $ce_0(z,1)$, which is always positive. The succeeding eigenfunctions, ϕ_n, have n zeroes on $[0,\pi/2]$. This kernel has an isonull as in figure 8.2, but the sign of K in the two sub-domains is reversed. Thus, some significance exists in the way in which the sign of K is arranged.

§8.7   Conjecture

What is the underlying, general theory linking the structure of the
kernel, $K(s,t)$, of an integral operator, **K**, with the behaviour of the
eigenfunctions, $\{\phi_n\}$? For a self-adjoint operator, a suggestion
follows.

If the domain of definition, $\Omega^2 = [a,b]^2$, is bounded, and K vanishes
at only a finite number of points on the boundary of Ω^2, then suppose K
is positive at either (a,a) or (b,b) (or both, of course). Linearly
transform (s,t) so that this "positive corner" of Ω^2 is relocated at
$(0,0)$. The other corner becomes $(b-a,b-a)$. If Ω is only semi-bounded,
i.e. one of a or b is infinite, a similar procedure can be followed.
Suppose b is infinite (If a is infinite, an analogous result is
immediate.), $K(a,a)$ is positive, and $K(a,t)$ vanishes at only a countable
number of points in Ω. Translate the origin so that (a,a) becomes
$(0,0)$. If b were the finite limit of Ω, $(0,0)$ would correspond to
(b,b), at which it would be required that K were positive.

It is postulated that

the number of isonulls cutting either axis

equals the number of zeroes of the primary

eigenfunction, say m.

By symmetry this number is the same for both the S- and T-axes. For
succeeding eigenfunctions there is probably a systematic relation, but,
whether the number of zeroes of ϕ_n is $(m+n)$ or $\max(m,n)$, is not obvious.
Examination of the numerical results of §7.3 suggests the former.

EPILOGUE

When we asked Pooh what the opposite of an
Introduction was, he said "The what of a what?"
which didn't help us as much as we had hoped,
but luckily Owl kept his head and told us that
the Opposite of an Introduction, my dear Pooh,
was a Contradiction; and, as he is very good at
long words, I am sure that that's what it is.

A.A.Milne, "The House at Pooh Corner"

REFERENCES

M.ABRAMOWITZ & I.A.STEGUN (eds) (1965), *Handbook of Mathematical Functions*, Dover, New York

M.J.ADAMS (1981), *An Introduction to Optical Waveguides*, John Wiley & Sons, Chichester

M.J.ADAMS, D.N.PAYNE & C.M.RAGDALE (1979), *Electron Lett*, **15**, 298

C.T.H.BAKER (1977), *The Numerical Treatment of Integral Equations*, Clarendon, Oxford

R.D.BIRCH, D.N.PAYNE & M.P.VARNHAM (1982), *Electron Lett*, **18**, 1036

R.J.BLACK (1984), *PhD Thesis*, Australian National University, Canberra

R.J.BLACK & C.PASK (1984), *J Light Tech*, **2**, 268

M.BORN & E.WOLF (1970), *Principles of Optics*, 4th edn, Pergamon, Oxford

E.BRINKMEYER (1979), *Appl Opt*, **18**, 932

L.J.CHU (1938), *J Appl Physics*, **9**, 583

P.L.CHU & R.A.SAMMUT (1984), *J Light Tech*, **2**, 650

E.T.COPSON (1965), *Asymptotic Expansions*, Cambridge University Press, Cambridge

R.COURANT & D.HILBERT (1953), *Methods of Mathematical Physics*, vol 1, Interscience, New York

J.R.COZENS & R.B.DYOTT [- CITERNE] (1979), *Electron Lett*, **15**, 558, and comment with J.CITERNE (1980), ibid., **16**, 13

B.DAVIES (1978), *Integral Transforms & their Applications*, Springer-Verlag, New York

R.B.DYOTT & J.R.STERN (1971), *Electron Lett*, **7**, 82

R.B.DYOTT, J.R.COZENS & D.G.MORRIS (1979), *Electron Lett*, **15**, 380

A.ERDELYI (1940), *Compositio Mathematica*, **7**, 340

A.ERDELYI (1956), *Asymptotic Methods*, Dover, New York

A.ERDELYI, W.MAGNUS, F.OBERHETTINGER & F.G.TRICOMI (1954), *Tables of Integral Transforms*, 2 vols, McGraw-Hill, New York

A.ERDELYI, W.MAGNUS, F.OBERHETTINGER & F.G.TRICOMI (1955), *Higher Transcendental Functions*, 3 vols, McGraw-Hill, New York

L.EYGES (1978), *Appl Opt*, **17**, 1673

L.EYGES, P.GIANINO & P.WINTERSTEINER (1979), *J Opt Soc Am*, **69**, 1226

W.A.GAMBLING & H.MATSUMURA (1977), *Electron Lett*, **13**, 691

W.A.GAMBLING, D.N.PAYNE, H.MATSUMURA & R.B.DYOTT (1976a), *IEE J Micro Opt & Acoust*, **1**, 13

W.A.GAMBLING, D.N.PAYNE, H.MATSUMURA & R.B.DYOTT (1976b), *Electron Lett*, **12**, 546

W.A.GAMBLING, H.MATSUMURA & C.M.RAGDALE (1978), *Electron Lett*, **14**, 618

D.GLOGE (1971), *Appl Opt*, **10**, 2252

J.E.GOELL (1969), *Bell Syst Tech J*, **48**, 2133

S.GOLDSTEIN (1927), *Trans Cambr Phil Soc*, **23**, 303

I.S.GRADSHTEIN & E.M.RYZHIK (1965), *Tables of Integrals Series and Products*, 4th edn, Academic Press, New York

E.R.HANSEN (1975), *A Table of Series and Products*, Prentice-Hall, Englewood Cliffs

H.HOCHSTADT (1973), *Integral Equations*, John Wiley & Sons, New York

G.B.HOCKER & W.K.BURNS (1977), *Appl Opt*, **16**, 113

A.HONDROS & P.DEBYE (1910), *Ann Phys*, **32**, 465

C.HUNTER & B.GUERRIERI (1981), *Stud Appl Math*, **64**, 113

C.D.HUSSEY & C.PASK (1981), *Electron Lett*, **17**, 664

C.D.HUSSEY & C.PASK (1982), *Proc IEE*, **H129**, 123

L.D.HUTCHESON, I.A.WHITE & J.J.BURKE (1980), *Opt Lett*, **5**, 276

E.L.INCE (1926a), *Theory of Ordinary Differential Equations*, republished by Dover, New York

E.L.INCE (1926b), *Proc Roy Soc Edin*, **46**, 316

E.L.INCE (1927), *Proc Roy Soc Edin*, **47** 294

I.P.KAMINOW & V.RAMASWAMY (1979), *Appl Phys Lett*, **34**, 268

K.C.KAO & G.A.HOCKMAN (1966), *Proc IEE*, **113**, 1151

S.KAWAKAMI, M.MIYAGI & S. NISHIDA (1975), *Appl Opt*, **14**, 2588

S.KAWAKAMI, S.NISHIDA & M.SUMI (1976), *Proc IEE*, **123**, 586

S.KITAYAMA, S.SEIKAI, N.UCHIDA & M.AKIYAMA (1981), *Electron Lett*, **17**, 419

M.A.KRASNOSEL'SKII (1964), *Positive Solutions of Operator Equations*, Nordhoff International, Groningen

M.G.KREIN & M.A.RUTMAN (1962), *Linear operators leaving invariant a cone in a Banach space*, ser 1 vol 10, Translations by Am Math Soc

A.KUMAR & R.K.VARSHNEY (1984), *Opt Quant Electron*, **16**, 349

A.KUMAR, K.THYAGARAJAN & A.K GHATAK (1983), *Opt Lett*, **8**, 63

A.KUMAR, R.K.VARSHNEY & K.THYAGARAJAN (1984), *Electron Lett*, **20**, 112

E.F.KUESTER & D.C.CHANG (1975), *IEE J Quant Electron*, **QE-11**, 903

L.D.LANDAU & E.M.LIFSHITZ (1960), *Electrodynamics of Continuous Media*, Pergamon, Oxford

L.D.LANDAU & E.M.LIFSHITZ (1971), *The Classical Theory of Fields*, 3rd edn, Pergamon, Oxford

L.LEWIN (1974), *IEEE Trans Microwave Theory & Tech*, **MTT-22**, 718, and correction (1975), ibid., **MTT-23**, 779

L.LEWIN, D.C.CHANG & E.F.KUESTER (1977), *Electromagnetic Waves and Curved Structures*, Peter Peregrinus on behalf of I.E.E., Stevenage

J.D.LOVE & C.D.HUSSEY (1984), *Opt Quant Electron*, **16**, 41

J.D.LOVE, R.A.SAMMUT & A.W.SNYDER (1979), *Electron Lett*, **15**, 615

E.A.J.MARCATILI (1969a), *Bell Syst Tech J*, **48**, 2073

E.A.J.MARCATILI (1969b), *Bell Syst Tech J*, **48**, 2103

D.MARCUSE (1971), *Bell Syst Tech J*, **50**, 2551

D.MARCUSE (1972), *Light Transmission Optics*, Van Nostrand, Princeton

D.MARCUSE (1976a), *J Opt Soc Am*, **66**, 216

D.MARCUSE (1976b), *J Opt Soc Am*, **66**, 311

D.MARCUSE (1978), *J Opt Soc Am*, **68**, 103

D.MARCUSE (1982), *Appl Opt*, **21**, 4208

E.MATHIEU (1868), *J Math Pures Appl*, **13**, 137

H.MATSUMURA & T.SUGANUMA (1980), *Appl Opt*, **19**, 3151

N.W.McLACHLAN (1947), *Theory an Aplications of Mathieu Functions*, Clarendon, Oxford

S.G.MIKHLIN (1957), *Integral Equations*, Pergamon, London

A.A.MILNE (1926), *Winnie-the-Pooh*, Methuen, London

A.A.MILNE (1927), *Now We Are Six*, Methuen, London

A.A.MILNE (1928), *The House at Pooh Corner*, Methuen, London

E.G.NEUMANN & H.D.RUDOLPH (1975), *IEEE Trans Microwave Theory & Tech*, **MTT-23**, 142

K.OKAMOTO (1984), *Appl Opt*, **23**, 2638

K.OKAMOTO, T.HOSADA & T.EDAHIRO (1981), *J Quant Electron*, **QE-17**, 2123

K.OKAMOTO, M.P.VARNHAM & D.N.PAYNE (1983), *Appl Opt*, **22**, 2370

T.OKOSHI (1981), *J Quant Electron*, **17**, 879

T.OKOSHI, K.OYAMADA, M.NISHIMURA & H.YOKOTA (1982), *Electron Lett*, **18**, 824

C.PASK (1982), unpublished work, some of which was presented at Optics 82, Max Born Centenary Conference, Edinburgh, 1982

C.PASK (1984), *Electron Lett*, **20**, 144

C.PASK & R.A.SAMMUT (1980), *Electron Lett*, **16**, 310

F.PAYNE (1982), *Opt Quant Electron*, **14**, 525

K.PETERMANN (1976), *Electron Lett*, **12**, 107

K.PETERMANN (1977), *Opt Quant Electron*, **9**, 167

K.PETERMANN (1983), *Electron Lett*, **19**, 713

V.RAMASWAMY, R.D.STANDLEY, D.SZE & W.G.FRENCH (1978), *Bell Syst Tech J*,
       57, 635

S.C.RASHLEIGH (1982), *Opt Lett*, **7**, 294

S.C.RASHLEIGH & R.H.STOLEN (1983), *Laser Focus*, **19**, no.5, 155

Lord RAYLEIGH (J.W.STRUTT) (1897), *Philos Mag*, **43**, 125

S.R.RENGARAJAN & J.E.LEWIS (1980), *Electron Lett*, **16**, 263

R.A.SAMMUT (1979), *Electron Lett*, **15**, 590

R.A.SAMMUT (1980a), *Electron Lett*, **16**, 156, and correction, ibid., 863

R.A.SAMMUT (1980b), *Electron Lett*, **16**, 728

R.A.SAMMUT (1982a), *Electron Lett*, **18**, 221

R.A.SAMMUT (1982b), *Opt Quant Electron*, **14**, 419

R.A.SAMMUT (1983), private communication

R.A.SAMMUT & C.PASK (1983), *Electron Lett*, **19**, 105

R.A.SAMMUT, C.HUSSEY, J.D.LOVE & A.W.SNYDER (1981), *Proc IEE*, **H128**, 173

S.SARKAR, K.THYAGARAJAN & A.KUMAR (1984), *Opt Communic*, **49**, 178

Y.SASAKI, K.OKAMOTO, T.HOSAKA & H.SHIBATA (1982), *Proc Opt Fibre Conf
       1982*

W.O.SCHLOSSER (1972), *Bell Syst Tech J*, **51**, 487

T.O.SHAPOSHNIKOVA, R.S.ANDERSSEN & S.G.MIKHLIN (eds) (1975), *Integral
       Equations - a reference text*, Noordhoff International, Leyden

J.R.SIMPSON, R.H.STOLEN, F.M.SEARS, W.PLEIBEL, J.B.MACCHESNEY &
       R.E.HOWARD (1983), *J Lightguide Tech*, **1**, 370

I.N.SNEDDON (1951), *Fourier Transforms*, McGraw-Hill, New York

A.W.SNYDER (1969), *IEEE Trans Microwave Theory & Tech*, **MTT-17**, 1130

A.W.SNYDER (1970), *IEEE Trans Microwave Theory & Tech*, **MTT-18**, 608

A.W.SNYDER (1981), *Proc IEEE*, **69**, 6

A.W.SNYDER & J.D.LOVE (1983), *Optical Waveguide Theory*, Chapman & Hall,
       London

A.W.SNYDER & F.F.RUHL (1983), *J Opt Soc Am*, **73**, 1165

A.W.SNYDER & R.A.SAMMUT (1979), *J Opt Soc Am*, **69**, 1663

A.W.SNYDER & W.R.YOUNG (1978), *J Opt Soc Am*, **68**, 297

A.W.SNYDER, J.D.LOVE & R.A.SAMMUT (1982), *J Opt Soc Am*, **72**, 1131

W.STEWART (1980), *Electron Lett*, **16**, 380

J.J.THOMSON (1893), *Recent Researches in Electricity and Magnetism*, Clarendon, Oxford

C.C.TIMMERMANN (1977), *Appl Opt*, **16**, 1793

A.R.TYNES, R.M.DEROSIER & W.G.FRENCH (1979), *J Opt Soc Am*, **69**, 1587

M.P.VARNHAM (1984), *PhD Thesis*, University of Southampton, Southampton

M.P.VARNHAM, D.N.PAYNE, A.J.BARLOW & R.D.BIRCH (1983a), *J Lightwave Tech*, **1**, 332

M.P.VARNHAM, D.N.PAYNE, R.D.BIRCH & E.J.TARBOX (1983b), *Electron Lett*, **19**, 246

H.S.WALL (1948), *Analytic Theory of Continued Fractions*, Van Nostrand, New York

G.N.WATSON (1966), *A Treatise on the Theory of Bessel Functions*, 2nd edn, Cambridge University Press, Cambridge

I.A.WHITE (1977), *PhD Thesis*, Australian National University, Canberra

I.A.WHITE (1979), *IEE J Micro Opt & Acoust*, **3**, 186

C.YEH (1962), *J Appl Physics*, **33**, 3235

C.YEH [- CITERNE] (1976), *Opt Quant Electron*, **8**, 43, and correspondence with J.CITERNE (1980), ibid., **12**, 529

C.YEH, K.HA, S.B.DONG & W.P.BROWN (1979), *Appl Opt*, **18**, 1490